Numerical methods for Lagrangian and Arbitrary-Lagrangian-Eulerian Hydrodynamic Contribution to the simulation of High-Energy-Density-Physics Problems

Jérôme Breil

université de BORDEAUX

HABILITATION À DIRIGER DES RECHERCHES

PRÉSENTÉE à

L'UNIVERSITÉ DE BORDEAUX

ÉCOLE DOCTORALE DE MATHÉMATIQUES ET D'INFORMATIQUE

Spécialité : Mathématiques Appliquées et Calcul Scientifique

Par **Jérôme BREIL**

Numerical methods for Lagrangian and Arbitrary-Lagrangian-Eulerian Hydrodynamic Contribution to the simulation of High-Energy-Density-Physics Problems

---

Soutenue le : 24 juin 2016

Après avis des rapporteurs :

Andrew Barlow	Senior Scientist, AWE
Michael Dumbser	Professeur, University of Trento
Boniface Nkonga	Professeur, Université de Nice Sophia-Antipolis

Devant la commission d'examen composée de :

Andrew Barlow	Senior Scientist, AWE	Rapporteur
Dimitri Batani	Professeur, Université de Bordeaux	Examinateur
Jean-François Clouet	Directeur de recherche, CEA DAM	Examinateur
Bruno Després	Professeur, Université Paris VI	Président
Michael Dumbser	Professeur, University of Trento	Rapporteur
Boniface Nkonga	Professeur, Université de Nice Sophia-Antipolis	Rapporteur
Vladimir Tikhonchuk	Professeur, Université de Bordeaux	Examinateur

– 2016 –

A Kazuyo, Luca, Kenzo et Sacha.

Acknowledgments

With this document I wanted to highlight and give an end point to my last ten year of research in the CELIA laboratory at the University of Bordeaux. All the work presented here could not have been achieved without the collaboration of many people and I would like to express my gratitude here.

First of all, I would like to warmly thank Andrew Barlow, Michael Dumbser and Boniface Nkonga for having accepted to review this thesis and for their excellent report. Then, I would like also to thank Bruno Després for having accepted to be the president of this Jury. Also I want to thank Jean-François Clouet, Dimitri Batani, and Vladimir Tikhonchuk for being member of the jury.

In 2003, after my Post doc in Japan, I had the opportunity to join the CELIA laboratory. At that time I worked with Pierre-Henri Maire and Jean Ovadia who make me discovered Lagrangian hydrodynamics. We have developed, in a very short time, the hydrodynamic engine of the CHIC code at that time. I can say here that I am particularly indebted to Pierre-Henri Maire with whom I had a very fruitful research. I have a long term contract with him and I hope it will continue.

I am also very grateful to Rémi Abgrall and Vladimir Tikhonchuk who are not only two very gifted scientist in their specific domain but are also very good for motivating and for making people work together.

At CELIA I mentored several Postdoc and PhD student. Stéphane Galéra was not really a Postdoc as we were working so closely but I want to thank him here for his collaboration to this work. Then I had the opportunity to work and exchange with very talented Postdoc students: Marie Billaud, Thibault Harribey, Pascal Jacq and Antoine Lemoine. I was also co-director of Jan Velechovsky PhD thesis for the numerical part with V. Tikhonchuk and R. Liska. Then, after this first experience as PhD supervisor, Gabriel Georges will defend his thesis and he will be my first PhD student after my own HDR defense. With Gabriel it is a long story as I mentored him during his second and last year engineer school project. I can say that it was always a pleasure to work with him and I have here the opportunity to tell him again that he really did a good job during his PhD. I hope he enjoyed like I did his thesis I supervised with Pierre-Henri Maire.

Mikhail Shashkov is like Pierre-Henri Maire, when you have the opportunity to work with this kind of researcher you can shine through them. Mikhail is a very high level scientist from LANL with whom I really enjoy collaborating. Raphaël Loubère was also part of the team as he was former Shashkov Postdoc and we also actively collaborate since he come back to France at CNRS in Toulouse. In the same Shashkov team I don't want to forget my Czech colleagues

Richard Liska, Pavel Vachal and Milan Kuchařík who give me the opportunity to visit Prague many time for meeting and collaboration. Our last collaboration being Jan's thesis between Bordeaux and Prague.

In CELIA I could met also great scientist with whom I could collaborate but also with time became friend. I want to thank first, Philippe Nicolaï for having pushing me working more on physics. I am also indebted with him as with him I could start collaboration with ILE on MHD and it give me the opportunity to visit Hideo Nagatomo at ILE who is a talented scientist in Japan. I want also to thank Marina Olazabal, who come from applied Mathematics and with whom I worked on very Rayleigh-Taylor unstable subject. With her collaboration is always easy as we can speak the same language. I have also the opportunity to thank here Jean-Luc Feugeas, with whom we worked on several different subject but the CECLAD code was one of our best collaboration.

Now I want to make a bigger step in the past and thank Jean-Paul Caltagirone who was my PhD director and with whom I never cut the link. I want also to thank Stéphane Glockner an old friend from my old PhD lab as we finally succeed to work again together. In fact it is not really true as Antoine Lemoine did all the job (and more) during his Postdoc with us.

Another team is the Cachan team with Joris Costes and Jean-Michel Ghidaglia. I want to thank them for giving me the opportunity to work with them and also for inviting me to the Cargèse conference.

Some last word to the CHIC user team of CELIA: Alexis Casner, Benoit Chimier, Guillaume Duchateau, Ludovic Hallo, Edouard Lebel, Xavier Ribeyre and Guy Schurtz with whom I interact. The Math team with Bruno Dubroca, Denise Aregba and Stéphane Brull. Then I don't want to forget the Multimat team with Jean-Philippe Braeunig, Stéphane Delpino, Philippe Hoch and Renaud Motte from DIF in Paris with whom I interact also late at night. And for the last but not the least I want to finish with the ILE team Hideo Nagatomo and Atsushi Sunahara, and the LLNL team Mike Owen, Robert Rieben and Dave Starinshak. I really want to thank them for welcoming me in their respective institute during my visit in Japan and in US.

Of course all this work could not have been done without Kazuyo who take care of our three Samurai Luca, Kenzo and Sacha while I was working on this HDR. I want to thank her for her patience and support as without her all this work could not have been finished.

和代、ありがとうございました。

Résumé

Méthodes numériques pour l'hydrodynamique Lagrangienne et leurs contributions à la simulation de la physique des hautes densités d'énergie

Ce document présente une partie des travaux effectués au laboratoire CELIA (CEA, CNRS, Université de Bordeaux) dans le domaine de la physique des hautes densités d'énergie (HDE). Le groupe de plasma chaud du CELIA est particulièrement impliqué dans la HDE, la fusion par confinement inertiel (ICF) et l'astrophysique de laboratoire. Les écoulements rencontrés en HDE sont souvent multi-matériaux et caractérisé par la présence de choc et de grande déformation du domaine de calcul. Les schémas numériques basés sur le formalisme Lagrangien sont bien adaptés à la modélisation de ce type d'écoulement car le maillage suit le fluide en mouvement. Ceci permet d'obtenir des résultats précis autour des chocs, ainsi qu'un suivi naturel des interfaces multi-matériaux. Le document est structuré comme suit. Tout d'abord, nous rappelons les principales caractéristiques de notre schéma Lagrangien centré. la stratégie ALE et Reale sont présentés en décrivant les différentes phases de notre algorithme ALE multi-matériaux. Le schéma de diffusion utilisé pour coupler les différents modèles physiques est présenté dans sa dernière extension le schéma CCLADNS pour les maillages non-conformes et non-orthogonaux en 2D et 3D. Enfin, le code CHIC est introduit et des études théoriques ainsi que des simulations d'expériences sont présentés.

Mots clés : Hydrodynamique Lagrangienne, Méthode ALE, Méthode de reconstruction d'interface, Méthodes Volumes Finis, Maillages Non-Structurés, Thermique Anisotrope, HDE

Abstract

Numerical methods for Lagrangian and Arbitrary-Lagrangian-Eulerian Hydrodynamic and their contribution to the simulation of High-Energy-Density-Physics Problems

This document presents a part of the works done at CELIA Laboratory (CEA, CNRS, Université Bordeaux) in the field of High Energy Density Physics (HEDP). The CELIA plasma physics group is particularly involved in HEDP, Inertial Confinement Fusion (ICF) and Laboratory astrophysics. Flows encountered in HEDP are multi-material and characterized by strong shock waves and large changes in the domain shape due to rarefaction waves. Numerical schemes based on the Lagrangian formalism are good candidates to model this kind of flows since the computational grid follows the fluid motion. This provides accurate results around the shocks as well as a natural tracking of multi-material interfaces. The document is structured as follows. First, we recall the main features of the compatible cell-centered Lagrangian discretization. ALE and ReALE strategy are presented by describing the different phases of our multi-material ALE algorithm. Diffusion scheme used to couple all the physical models is presented with the last extension of the CCLADNS scheme for non-conformal and non-orthogonal meshes in 2D and 3D. Finally CHIC code is introduced and some theoretical studies and experiments are presented.

Keywords : Lagrangian Hydrodynamic, ALE, Interface Reconstruction, Finite Volume Methods, Unstructured Grids, Anisotropic Heat Transfer, HEDP

Contents

Introduction

After COP21[1], held in Paris in 2015, the necessity to strongly reduce the emission of greenhouse gases requires increased effort if we want to keep open the possibility of limiting the rise in global mean temperature to 2°C. On the other hand, according to the BP's Energy Outlook[2], the world primary energy consumption is projected to grow from 2011 to 2030, adding 36% to the global consumption by 2030. The crucial question of availability of energy in the next decades requires several strong issues to be addressed among which the foreseen retirement of a large part of the power plant fleet and the lack of availability of fossil fuel. The safety issues in the nuclear industry which reduce the public acceptance need also to be addressed. The conjunction of these effects will cause a large gap between demand and supply of energy to be bridged in the 2040-2050 decade. The development of novel energy sources and associated power plants offers new perspectives for harmonious economic growth worldwide and large markets for our industries. Among the solutions proposed for carbon free energy production, fusion of light isotopes of hydrogen is appealing from the points of view of safety, abundance of primary resource (deuterium and lithium for the on-line production of tritium) and amenability to large scale, cost-effective, industrial production. Magnetic fusion, where the thermonuclear plasma is confined by means of magnetic fields in a toroidal geometry, benefits from a wide international collaboration and is expected to succeed in demonstrating plasma self heating on the ITER facility, now under construction in Cadarache (France). The other approach is Inertial Confinement Fusion (ICF) where small amounts of DT fuel are ignited in a vacuum chamber several times (> 10) per second. Laser beams provide the energy required for compression and ignition of the target. Up to now, the main scheme chosen for ICF is the indirect drive. This scheme, which rely on the conversion of laser energy into thermal radiation by the walls of a high-Z hohlraum, has been mainly developed in defence laboratories both in the United States and Europe, and the corresponding models, numerical codes, and material data remain largely classified. The indirect drive approach of Inertial Fusion has motivated the construction of two large-scale laser facilities: NIF[3] , in the U.S., which has been commissioned in 2009, and LMJ[4], under construction in France. The direct drive approach is much more suitable to energy production, from its relative simplicity and the higher target gains it provides. This approach is studied in academic institutions in Europe, United States, and Asia. According to numerical modeling and recent experiments, robust direct drive ignition can be obtained using one of the advanced schemes recently proposed and now under development: Fast Ignition and Shock Ignition.

From the facility conception, its construction and up to its scientific exploitation which will last for tens of years, numerical simulation using dedicated codes is present at each level. Massively parallel machines are generally built in continuity and interaction with such facilities (the TERA 100 machine and future EXA machine TERA 1000 at CEA being built in association with the

[1] www.cap-cop21.com
[2] www.bp.com
[3] https://lasers.llnl.gov/
[4] www-lmj.cea.fr

LMJ as example). These machines are used to run simulation codes solving the most up-to-date physical models on a huge mass of data on millions of cells or particles in the computational domain. Such machines are usually some of the most efficient computers on the planet.
In Europe the HiPER[5] (High Power Energy Research) project aims at demonstrating the feasibility of Inertial Fusion for Energy (IFE). The long-term goal is the construction of an experimental facility including all of the relevant technology. Intermediate phases will develop and down select technical solutions on the basis of a cost-risk analysis. This project could take benefit of the recent record yield shot of NIF where the scientific break-even has been achieved [84]. Within this project, the laser plasma physics group from CELIA works on dedicated physical experiments which require simulation for all the different phase of the experimental campaign. Before the submission of the proposal to scientific committee some crude simulations usually using 1D code or simplified 2D model are performed. Then, after acceptation more precise simulations are performed to help the experimentalist to design their experiment. On big facilities the number of experiments are usually restricted and simulation codes are the best tool to optimize this preparation phase. Finally, after the experimental campaign additional simulations are usually necessary for the interpretation of the experimental results.
This workflow performed for IFE is the same for other applications in the High Energy Density Physics (HEDP) domain like material science, Laboratory astrophysics ...
This document aims at presenting a part of the works done in the Arbitrary-Lagrangian-Eulerian (ALE) code : the CHIC (Code d'Hydrodynamique d'Implosion du CELIA) code which has been designed to simulate multi-material compressible hydrodynamics in an ICF context. Generally, ALE code is the computational engine onto which many physics modules are plugged-in. These are: laser propagation, energy diffusion, radiation transfer, plasma effects, etc. Although these modulus are important to produce physical relevant simulations, the ALE engine remains the fundamental brick that needs special care to begin with. The second one is the diffusion scheme where all the physics is connected. This platform was used for developing and implementing new ideas in numerical schemes and physical models for the academics.
A generic ALE code for hydrodynamics can be decomposed into three successive phases:

1. Lagrangian phase. For this first phase the numerical scheme computes the evolution in time and space of materials described in a Lagrangian formalism (Simulation on moving mesh). As the mesh deforms with the materials, it can be arbitrarily stretched, compressed and consequently of very bad geometrical quality; non-convex, tangled or high aspect ratio cells may appear.

2. Mesh regularization or smoothing phase. Given the Lagrangian mesh a regularization technique provides a new regularized mesh that one chooses to proceed which.

3. Conservative remapping phase. The remapping phase transfers the physical variables from the Lagrangian mesh onto the regularized grid. This remapping must be conservative in mass, momentum and total energy and the remapping must be at least as accurate as the numerical scheme is.

In the Lagrangian phase, a computational cell moves with the flow velocity. This ensures that there is no mass flux crossing the boundary of the Lagrangian moving cell. Thus, Lagrangian methods can capture contact discontinuity sharply in multi-material fluid flows. However they are also known to suffer from a lack of robustness correlated with the mesh motion driven by the materials. In order to gain some robustness, one generally adds phases 2 and 3. Phase 2 provides a better shaped mesh, it is only a geometrical operation, whereas phase 3 is a pure

[5] www.hiper-laser.org

conservative interpolation operation: The physical data are transferred on this new mesh to prepare next Lagrangian time step. Remark that if the remapping is systematically made onto the initial mesh the numerical method is by construction an Eulerian one (as Lagrange+Remap). In other words phases 1+3 provides an Eulerian code. If the regularized phase does generate neither the initial mesh, nor the Lagrangian one then the overall code is of ALE nature. Finally implementing these three phases leads to having three codes into one platform: Lagrangian, Eulerian and ALE. In the following we detail these three phases.

Lagrangian phase.

In the Lagrangian framework, one has to discretize not only the gas dynamics equations but also the vertex motion in order to move the mesh. Moreover, the numerical fluxes of the physical conservation laws must be determined in a compatible way with the vertex velocity so that the Geometric Conservation Law (GCL) is satisfied, namely the rate of change of a Lagrangian volume has to be computed coherently with the node motion. This critical requirement is the cornerstone of any Lagrangian multidimensional scheme. The most natural way to solve this problem employs a staggered discretization in which position, velocity and kinetic energy are centered at points, while density, pressure and internal energy are within cells. Since the seminal works of Von Neumann and Richtmyer [160], and Wilkins [163], many developments have been made in order to improve the accuracy and the robustness of staggered hydrodynamics [44, 47, 40]. More specifically, the construction of a compatible staggered discretization leads to a scheme that conserves total energy in a rigorous manner [45, 41].

The use of staggered schemes in ALE formalism generates several problematic situations due to the staggered placement of variables. That is why the desire to possess a cell-centered Lagrangian scheme was tempting. The first try is due to J. Dukowicz around 1985 [56]. He developed a Godunov like Lagrangian scheme that however suffered from internal inconsistency between flux computation and vertex displacement. Another alternative to the staggered discretization is to derive a Lagrangian scheme based on the Godunov method [70]. In comparison to staggered discretization, Godunov-type methods exhibit the good property of being naturally conservative, they do not need artificial viscosity and they allow a straightforward implementation of conservative remapping methods when they are used in the context of the ALE strategy. In the Godunov-type method approach, all conserved quantities, including momentum, and hence cell velocity are cell-centered. The main issue associated with the Godunov-type schemes is to define a flux discretization that is compatible with the node displacement so that the GCL is satisfied at the discrete level. Recently, such compatible discretizations have been provided [113, 114]. These works are based on schemes, in which interface fluxes and nodal velocities are computed coherently thanks to an approximate Riemann solver located at the nodes. This cell-centered Lagrangian scheme seems to be one of the best Lagrangian scheme available nowadays [99].

ALE code: mesh regularization, reconnection and remapping.

The ALE description has been initially introduced in the seminal paper of Hirt [76] to solve in a certain extent the shortcomings of purely Lagrangian and purely Eulerian descriptions by combining the best features of both aforementioned approaches. The main feature of the ALE methodology is to move the computational grid with a prescribed velocity field to improve the accuracy and the robustness of the simulation. ALE methods have been used for several decades to face successfully the difficulties inherent to the simulation of multi-material fluid flows with large distortions [7, 15, 78, 22, 58, 117, 54]. Usually, ALE methods can be implemented in two manners. The first one, which is termed direct ALE, consists in an unsplit moving mesh discretization of the gas dynamics equations wherein the grid velocity is typically deduced from

boundaries motion [127, 107]. In this approach convective terms are solved directly. The second one, is named indirect ALE. In an indirect ALE approach after an explicit Lagrangian phase a rezoning phase, in which nodes of the Lagrangian grid are moved to improve the geometric quality of the grid, and a remapping phase, wherein the physical variables are conservatively interpolated from the Lagrangian grid onto the new rezoned one [120] are applied. Again , when the rezoned mesh coincides with the initial mesh, indirect ALE algorithm corresponds to an Eulerian algorithm wherein advection terms are solved through the use of the remapping phase.

As already noticed the regularization phase consists in improving the geometrical quality of the Lagrangian mesh by some motion of vertexes. Classical techniques use the regularization effect of an elliptic operator [89] as in so-called Winslow method. Such techniques do not modify the mesh connectivity. Moreover an edge in its virtual displacement from its Lagrangian location to its regularized location can not move away from the convex hull defined by the neighbor Lagrangian cells. If so then a simple swept region based remapping technique can be employed [89]. This remapping technique computes the flux crossing an edge during its virtual motion. This flux is further associated to one of the two neighbor cells sharing this particular edge. Several mesh regularization techniques modify the mesh connectivity. The regularized mesh is consequently not anymore related to the Lagrangian one. Usually, in this case the remapping method must compute the exact intersection between the two arbitrarily different meshes [64, 65] but recent development allow a swept remapping method [75]. The exact intersection technique does not assume any special property shared by the meshes. It geometrically intersects one regularized cell and the Lagrangian mesh. Using such remapping method we can construct an ALE code with polygonal mesh reconnection, see as instance [103, 35, 75]. Such a code uses the Voronoi mesh machinery to allow mesh reconnection during the simulation. This, according to us, opens new perspectives to ALE codes.

Furthermore, in the context of multi-material computations using ALE method, grid and fluid move separately. The material interface which is naturally described in the Lagrangian framework may have moved and cells containing two or more materials could appear. These cells contain material interfaces which need special numerical treatment. Originally the Volume Of Fluid (VOF) method introduced in [77], track materials using volume fractions which is the ratio between the volume of the material in the cell and the volume of the cell. A number of numerical methods exist for solving the interface using piecewise linear interface reconstruction as the Piecewise Linear Interface Calculation (VOF PLIC) [165, 32] and the Moment Of Fluid (MOF) [5, 61] which is used in this work.

In Europe, very few codes exist to simulate ICF experiments. In particular we can cite the MULTI code [135] and the DUED code [13]. At CELIA the 2D ALE code named CHIC has been developed ([33] see also Appendix D) in a relatively short time and it possesses some of the most recent techniques for Lagrangian schemes, regularization, remapping, interface reconstruction, diffusion scheme etc... The CELIA group, in few years, has provided to the physics community a versatile simulation tool dedicated to laser-plasma interaction. The physics simulated using these up-to-date numerical bricks has been published in many journal articles [11, 74, 137, 126, 34] and created several collaborations with the scientific ALE community [103]. A version of the cell-centered code with mesh reconnection has been also realized in [103, 35, 75]. The diffusion scheme which is used in the CHIC code is also a cell-centered diffusion scheme [36, 116, 37] which enables a natural link to the cell-centered Lagrangian hydrodynamics scheme. Let us mention that such cell-centered Lagrangian schemes and associated ALE codes are not yet implemented in industrial codes. Nevertheless most of groups and research entities, especially in Europe and in the US are nowadays interested in this new field of cell centered Lagrangian scheme [16, 142].

The document is structured as follows. First, we recall the main features of the compatible cell-centered Lagrangian discretization in Chapter 1. ALE and ReALE strategy are presented in Chapter 2 by describing the different phases of our multi-material ALE algorithm. In Chapter 3 diffusion scheme used to couple all the physical models is presented with the last extension of the CCLADNS scheme for non-conformal and non-orthogonal meshes in 2D and 3D. Chapter 4 is devoted to the CHIC code where some theoretical studies and experiments are presented. Each chapter has is own Section for numerical results which are used to demonstrate the accuracy and the robustness of the methodology presented. Finally concluding remarks and perspectives about future works are given.

Selected publications

- P.-H. Maire, R. Abgrall, J. Breil, J. Ovadia, *A cell-centered lagrangian scheme for two-dimensional compressible flow problems*, SIAM J. of Scient. Comput., 29, 4, 1781-1824, 2007.
- J. Breil, P.-H. Maire, *A cell-centered diffusion scheme on two-dimensional unstructured meshes*, J. Comput. Phys., 224, 2, 785-823, 2007.
- J. Breil, S. Galera, P.-H. Maire, *Multi-material ALE computation in inertial confinement fusion code CHIC*, Comput. Fluids, 46, 1, 161-167, 2011.
- J. Breil, S. Galera, P.-H. Maire, *A two-dimensional VOF interface reconstruction in a multi-material cell-centered ALE scheme*, Int. J. Numer. Meth. Fluids, 65, 11-12, 1351-1364, 2011.
- M. Olazabal-Loumé, J. Breil, L. Hallo, X. Ribeyre, *Linear and non-linear high mode perturbations amplification at ablation front in HiPER targets*, Plasma Phys. Control. Fusion, 53, 015015, 2011.
- J. Breil, T. Harribey, P.-H. Maire, M. Shashkov, *A multi-material ReALE method with MOF interface reconstruction*, Comput. Fluids, 83, 115-125, 2013.
- M. Billaud Friess, J. Breil, P.-H. Maire and. Shashkov, *A multi-material CCALE-MOF approach in cylindrical geometry*, Commun. Comput. Phys., 15, 330-364, 2014.
- G. Gabriel, J. Breil, P.-H. Maire, *A 3D GCL compatible cell-centered Lagrangian scheme for solving gas dynamics equations*, J. Comput. Phys., 305, 921-941, 2016.

Chapter 1

A multi-dimensional cell-centered finite volume scheme for solving Lagrangian hydrodynamic on unstructured grids

The implosion of an ICF target generates very complex physical and hydrodynamical problems, see e.g. [97] and [140]. This is an unsteady, multi-material flow, where very strong shock waves occurring inside a geometry that is characterized by very large aspect ratio. Because of this thermodynamical and geometrical constraints, it is generally accepted that the simulation of these phenomena consists in solving numerically the equation of fluid dynamics in Lagrangian coordinates. The Lagrangian formalism uses a mesh that moves with the flow, but the partial derivative operators are written in Eulerian coordinates. This form of the equation is well suited to this type of problems because the problem of numerical diffusion linked to the transport operator is elegantly avoided. This is of fundamental importance for interface simulation.
Our aim is to propose a Lagrangian cell-centered scheme for multi-dimensional gas dynamics equations. Before describing our method, let us briefly give an historical overview on the Lagrangian schemes.
Lagrangian schemes are characterized by a mesh that follows the fluid flow. By this mean, these methods deal with interfaces in a natural manner. The main numerical difficulty lies in the node motion discretization, especially for multi-dimensional situations. The most natural way to overcome this difficulty is to use a staggered discretization, where the momentum is defined at the nodes and the other variables (density, pressure and specific internal energy) are cell-centered. This type of scheme was first introduced by Von Neumann and Richtmyer in [160] for one-dimensional flows. The bidimensional extension was proposed by Wilkins in [163]. It is based on an internal energy formulation. The entropy production inherent to shock waves is ensured by an artificial viscosity. In its initial version, this scheme was not conservative and it admitted numerical spurious modes. However, in spite of these drawbacks, this scheme has been widely used in the domain of multi-material flow simulations during last forty years. Moreover, since a decade, many improvements have been done in order to solve the previous problems. In their paper [44], Caramana and Shashkov show that with an appropriate discretization of the subzonal forces resulting from subzonal pressures, hourglass motion and spurious vorticity can be eliminated. By using the method of support operators proposed in [47], they constructed a staggered scheme which ensures the conservation of total energy. Moreover, the discretization of artificial viscosity has been considerably improved. First, by introducing formulations for multi-dimensional shock wave computations in [47] and then by using a discretization based

on a mimetic finite difference scheme in [40]. With all these improvements, the staggered Lagrangian scheme is an accurate and robust method, which can produce impressive results, even on unstructured polygonal grids, see for instance [105].

An alternative to the staggered discretization is to use a conservative cell-centered discretization. This method for Lagrangian gas dynamics in one dimension, has been introduced by Godunov, see [70] and [139]. The multi-dimensional extension of this method has been performed during the eighties, [22] and [58]. This multi-dimensional scheme is a cell-centered finite volume scheme on moving structured or unstructured meshes. It is constructed by integrating directly the system of conservation laws on each moving cell. The primary variables, density, momentum and total energy are defined in the cells. The flux across the boundary of the cell is computed by solving exactly or approximately a one-dimensional Riemann problem in the direction normal to the boundary. The main problem with this type of method lies in the fact that the node velocity needed to move the mesh cannot be directly calculated. In [22], the node velocity is computed via a special least squares procedure. It consists in minimizing the error between the normal velocity coming from the Riemann solver and the normal projection of the vertex velocity. It turns out that it leads to an artificial grid motion, which requires a very expensive treatment [59]. Moreover, with this approach the flux calculation is not consistent with the node motion.

In the cell-centered methods that have been proposed in [83] and [4] the gradient and divergence operators are expressed in the Lagrangian coordinates. This type of discretization needs to compute the Jacobian matrix associated to the map between Lagrangian and Eulerian spaces. However, these methods are purely Lagrangian and cannot be interpreted as moving mesh methods. This drawback has motivated an other approach proposed by Després and Mazeran. In [53], they made a theoretical analysis of the Lagrangian gas dynamics equations written in a fully Lagrangian form and they derived a new conservative and entropy consistent two-dimensional Lagrangian scheme of the finite volume type. It is a moving grid scheme based on a nodal solver. The node velocity is computed in a coherent manner with the face fluxes. The numerical results shown in [53] are quite impressive, in particular, those related to the difficult Saltzmann's test case. However, it appears that in the case of one-dimensional flows, this scheme leads a to nodal velocity, which depends on the cell aspect ratio. This drawback has motivated our study to develop a new cell-centered scheme that retains the good feature of Després-Mazeran scheme but resolves the aspect ratio problem using the EUCCLHYD (Explicit Unstructured Cell-Centered Lagrangian HYDrodynamics) scheme developed by Maire, Abgrall, Breil and Ovadia [113, 114, 110]. This scheme has been extended to cylindrical geometry [109, 27] and for three dimensional geometry in [118, 66].

The spatial second-order extension is obtained by a piecewise linear monotonic reconstruction of the pressure and velocity, given by their mean values over mesh cells. This reconstruction utilizes a least-squares procedure, see [111, 66, 114]. We define slope limiters in such a way that the values of the linear function at the cell vertices are within the bounds defined by the maximum and the minimum of the mean values over the set consisting of cell c and its nearest neighbors. Finally, instead of using the mean values of the pressure and the velocity in our nodal solver, we use their nodal extrapolated values deduced from the linear reconstruction. The time discretization is explicit and is based on a classical two-step Runge-Kutta procedure.

Here, we first present in Section 1.1 the Lagrangian scheme based on the Godunov solver in 1D. Then, the scheme in 2D is briefly introduced in Section 1.2. We derive space approximations based on face and node fluxes. The cylindrical extension from [27] is presented in Section 1.3. This extension is a modified version of the area weighted finite volume scheme of [109] and can recover the 2D scheme of Section 1.2 for planar geometry. To build this scheme, an area-

weighted formulation of the Lagrangian system of equations is proposed. Then, this system of equations is discretized using a cell-centered finite volume (FV) scheme. Contrary to [109] in which fluxes are directly deduced from the GCL constraint, here a simpler formulation that gives similar results is retained. These two main choices lead to a robust first-order scheme conservative for the total energy that has the great advantage to preserve spherical symmetry for one-dimensional flow on uniform angular polar grids. In Section 1.4 the 3D scheme is presented and is shown to be consistent with the Geometric Conservation Law (GCL). Second order in space using piecewise linear monotonic reconstruction and time through a Runge-Kutta procedure is introduced in Section 1.5. Finally, we validate our schemes with several test cases in Section 1.6. They are representative test cases for compressible fluid flows and demonstrate the robustness and the accuracy of the different Lagrangian schemes.

1.1 Lagrangian scheme in 1D

In Lagrangian hydrodynamic methods, a computational cell moves with the flow velocity its mass being time-invariant. Thus, Lagrangian methods can capture contact discontinuity sharply in multi-material fluid flows. Here the Lagrangian scheme is based on a cell-centered discretization of Lagrangian hydrodynamics equations. This scheme is written in total energy form. Here is the gas dynamics equation written in 1D,

$$\left\{\begin{array}{rcl} \rho d_t \tau - \partial_x u &=& 0, \\ \rho d_t u + \partial_x p &=& 0, \\ \rho d_t e + \partial_x p u &=& 0, \end{array}\right. \tag{1.1}$$

where ρ, u, p and e are respectively the density, velocity, pressure and the total energy. $\tau = 1/\rho$ is the specific volume. From total energy we can get internal energy from $\varepsilon = e - \frac{1}{2}u^2$. As the mesh is moving we have to add the local kinetic equation : $d_t x = u$.

1.1.1 Riemann solver

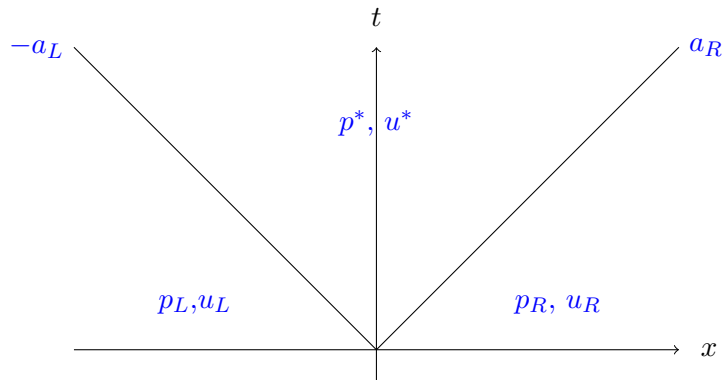

Figure 1.1: Structure of the Riemann problem for the Godunov solver.

In order to find an approximation of the flux of (1.1) we use the Godunov Riemann solver (see Fig. 1.1). The Riemann invariants lead to the following system:

$$\left\{\begin{array}{l} z_l(u^* - u_l) + p^* - p_l = 0, \\ z_r(u^* - u_r) - p^* + p_r = 0, \end{array}\right. \tag{1.2}$$

where $z = \rho a$ is the acoustic impedance and a the isentropic sound speed. Finally (u^*, p^*) are such that

$$\begin{cases} u^* = \dfrac{p_l - p_r + z_r u_r + z_l u_l}{z_r + z_l}, \\ p^* = \dfrac{z_r p_l + z_l p_r + z_l z_r (u_l - u_r)}{z_r + z_l}. \end{cases} \tag{1.3}$$

1.1.2 First order numerical scheme

The problem is solved on the interval $[0; L]$ which is discretized in N elements $C_1, \dots, C_N$. Furthermore, we can define the j^{th} cell center as $x_j = \frac{1}{2}(x_{j+\frac{1}{2}} + x_{j-\frac{1}{2}})$.
We perform first the integration in space on $\Delta x_j = [x_{j-1/2}, x_{j+1/2}]$:

$$\begin{cases} \rho \dfrac{d}{dt} \displaystyle\int_{x_{j-\frac{1}{2}}}^{x_{j+\frac{1}{2}}} \tau(x,t)\,\mathrm{d}x - \Big[u(x_{j+\frac{1}{2}},t) - u(x_{j-\frac{1}{2}},t)\Big] = 0, \\ \rho \dfrac{d}{dt} \displaystyle\int_{x_{j-\frac{1}{2}}}^{x_{j+\frac{1}{2}}} u(x,t)\,\mathrm{d}x + \Big[p(x_{j+\frac{1}{2}},t) - p(x_{j-\frac{1}{2}},t)\Big] = 0, \\ \rho \dfrac{d}{dt} \displaystyle\int_{x_{j-\frac{1}{2}}}^{x_{j+\frac{1}{2}}} e(x,t)\,\mathrm{d}x + \Big[pu(x_{j+\frac{1}{2}},t) - pu(x_{j-\frac{1}{2}},t)\Big] = 0. \end{cases} \tag{1.4}$$

Let be $\varphi_j = \dfrac{1}{\Delta x_j} \displaystyle\int_{x_{j-\frac{1}{2}}}^{x_{j+\frac{1}{2}}} \varphi(x,t)\,\mathrm{d}x$, now we integrate in time :

$$\begin{cases} \rho \Delta x_j \displaystyle\int_{t_n}^{t_{n+1}} \frac{d\tau_j}{dt}\,\mathrm{d}t - \int_{t_n}^{t_{n+1}} \Big[u(x_{j+\frac{1}{2}},t) - u(x_{j-\frac{1}{2}},t)\Big]\,\mathrm{d}t = 0, \\ \rho \Delta x_j \displaystyle\int_{t_n}^{t_{n+1}} \frac{du_j}{dt}\,\mathrm{d}t + \int_{t_n}^{t_{n+1}} \Big[p(x_{j+\frac{1}{2}},t) - p(x_{j-\frac{1}{2}},t)\Big]\,\mathrm{d}t = 0, \\ \rho \Delta x_j \displaystyle\int_{t_n}^{t_{n+1}} \frac{de_j}{dt}\,\mathrm{d}t + \int_{t_n}^{t_{n+1}} \Big[pu(x_{j+\frac{1}{2}},t) - pu(x_{j-\frac{1}{2}},t)\Big]\,\mathrm{d}t = 0. \end{cases} \tag{1.5}$$

Now with $\varphi^n = \varphi(t_n)$ and $\varphi^*_{j+\frac{1}{2}} = \dfrac{1}{\Delta t} \displaystyle\int_{t_n}^{t_{n+1}} \varphi(x_{j+\frac{1}{2}},t)\,\mathrm{d}t$, the system becomes :

$$\begin{cases} m_j(\tau_j^{n+1} - \tau_j^n) - \Delta t(u^*_{j+\frac{1}{2}} - u^*_{j-\frac{1}{2}}) = 0, \\ m_j(u_j^{n+1} - u_j^n) + \Delta t(p^*_{j+\frac{1}{2}} - p^*_{j-\frac{1}{2}}) = 0, \\ m_j(e_j^{n+1} - e_j^n) + \Delta t(p^*_{j+\frac{1}{2}} u^*_{j+\frac{1}{2}} - p^*_{j-\frac{1}{2}} u^*_{j-\frac{1}{2}}) = 0, \end{cases} \tag{1.6}$$

with $m_j = \rho_j \Delta x_j$, $(pu)^* = p^* u^*$ and where (p^*, u^*) are the solution of the Riemann solver (1.3).

1.1.3 Discrete form for entropy

In this section, we show that the scheme (1.6) is entropic. Here, we consider a macroscopic expression of the entropy (see [69]). In this case, the second law of thermodynamics writes

$$T\frac{ds}{dt} = \frac{d\varepsilon}{dt} + p\frac{d\tau}{dt}.$$

Thanks to (1.6) we can compute a discrete form for internal energy using the difference between the total energy and the kinetic energy.

Proposition 1: *The numerical scheme defined by (1.6) is entropic. More precisely, it satisfies the following inequality*

$$m_j T_j \frac{ds_j}{dt} = \rho_j c_j \Big(u^*_{j+\frac{1}{2}} - u_j\Big)^2 + \rho_{j+1} c_{j+1} \Big(u^*_{j-\frac{1}{2}} - u_j\Big)^2 \geq 0. \tag{1.7}$$

Proof.

$$m_j \frac{d\varepsilon_j}{dt} = m_j \frac{d\Big(e_j - \frac{1}{2}u_j^2\Big)}{dt} = p^*_{j-\frac{1}{2}} u^*_{j-\frac{1}{2}} - p^*_{j+\frac{1}{2}} u^*_{j+\frac{1}{2}} - p^*_{j-\frac{1}{2}} u_j + p^*_{j+\frac{1}{2}} u_j.$$

Therefore we obtain for the internal energy

$$m_j(\varepsilon_j^{n+1} - \varepsilon_j^n) + \Delta t \Big(p^*_{j+\frac{1}{2}}(u^*_{j+\frac{1}{2}} - u_j) - p^*_{j-\frac{1}{2}}(u^*_{j-\frac{1}{2}} - u_j)\Big) = 0.$$

We obtain the entropy variation

$$m_j T_j \frac{ds_j}{dt} = m_j \Big(\frac{d\varepsilon_j}{dt} + p_j \frac{d\tau_j}{dt}\Big) = p_j(u^*_{j+\frac{1}{2}} - u^*_{j-\frac{1}{2}}) + p^*_{j+\frac{1}{2}}(u_j - u^*_{j+\frac{1}{2}}) + p^*_{j-\frac{1}{2}}(u^*_{j-\frac{1}{2}} - u_j)$$

which is equivalent to

$$m_j T_j \frac{ds_j}{dt} = p_j(u^*_{j+\frac{1}{2}} - u_j + u_j - u^*_{j-\frac{1}{2}}) + p^*_{j+\frac{1}{2}}(u_j - u^*_{j+\frac{1}{2}}) + p^*_{j-\frac{1}{2}}(u^*_{j-\frac{1}{2}} - u_j),$$

So

$$m_j T_j \frac{ds_j}{dt} = (p_j - p^*_{j+\frac{1}{2}})(u^*_{j+\frac{1}{2}} - u^*_j) + (p^*_{j-\frac{1}{2}} - p_j)(u^*_{j-\frac{1}{2}} - u_j).$$

From relation (1.2), it comes that

$$\rho_j c_j (u^*_{j+\frac{1}{2}} - u_j) + p^*_{j+\frac{1}{2}} - p_j = 0.$$

Finally, Proposition 1 is shown. □

1.2 Lagrangian scheme in 2D

Let us introduce the notation employed for the 2D scheme, which are similar to those employed in [110, 111]. Considering a set $\{\Omega_c\}_{c\in\mathbb{N}}$ of non-overlapping polygonal cells that approximates the volume $V(t)$, each cell noted Ω_c is assigned a single index c. Each vertex of the cell c is labeled with the index p and localized thanks to its coordinates $\mathbf{X}_p = (X_p, Y_p)^t$. We introduce $\mathcal{P}(c)$ the list of the vertices belonging to the cell Ω_c and $\mathcal{C}(p)$ the list of the cells sharing the vertex p. These two sets are counter-clock-wise ordered. We introduce p^- and p^+ which denote the previous and the next nodes with respect to p in $\mathcal{P}(c)$, L^-_{pc} and L^+_{pc} are the half length of the edges $[pp^-]$ and $[pp^+]$, $\mathbf{N}^-_{pc}$ and $\mathbf{N}^+_{pc}$ are the unit outward normals to those edges. Finally, $L_{pc}\mathbf{N}_{pc}$ is the corner normal which is given by $L_{pc}\mathbf{N}_{pc} = L^-_{pc}\mathbf{N}^-_{pc} + L^+_{pc}\mathbf{N}^+_{pc}$. All these geometrical quantities are displayed in Fig. 1.2.

We present here the Explicit Unstructured Cell-Centered Lagrangian HYDrodynamics (EUCCLHYD) scheme [114, 113] based on a node-centered approximate Riemann solver. Let us recall briefly the main features of the first-order scheme. The gas dynamics equations written under integral form reads:

$$m\frac{d}{dt}\left\langle \frac{1}{\rho} \right\rangle - \int_L \mathbf{N}\cdot\mathbf{U}dL = 0, \tag{1.8}$$

$$m\frac{d}{dt}\langle \mathbf{U} \rangle + \int_L P\mathbf{N}dL = 0, \tag{1.9}$$

$$m\frac{d}{dt}\langle E \rangle + \int_L P\mathbf{N}\cdot\mathbf{U}dL = 0, \tag{1.10}$$

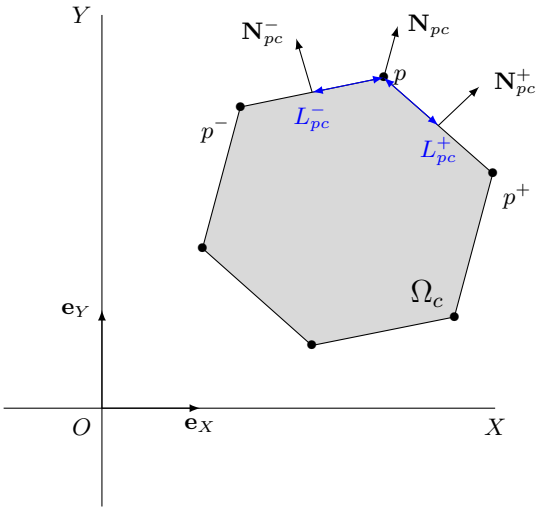

$$L_{pc}\mathbf{N}_{pc} = L_{pc}^+\mathbf{N}_{pc}^+ + L_{pc}^-\mathbf{N}_{pc}^-$$

Figure 1.2: Notations for the cell-centered scheme.

where $m = \int_V \rho dV$ represents the mass of the volume V. $\dfrac{d}{dt}$ is the material derivative and $\rho, \mathbf{U}, P, E$ are respectively the density, velocity, pressure and total energy. Each physical variable per unit of mass $(E, \mathbf{U})$ is noted as ϕ, and has its mass averaged value defined by $\langle\phi\rangle = \frac{1}{m}\int_V \rho\phi dV$.
The first-order spatial approximation of (1.8)-(1.10) is obtained considering local integrals on each cell Ω_c. Then, we have

$$m_c \frac{d}{dt}\mathbf{U}_c + \sum_{p\in\mathcal{P}(c)} \mathbf{F}_{pc} = \mathbf{0}, \tag{1.11}$$

$$m_c \frac{d}{dt}E_c + \sum_{p\in\mathcal{P}(c)} \mathbf{F}_{pc}\cdot\mathbf{U}_p = 0. \tag{1.12}$$

In addition, the mesh is moved through the local kinematic equation given at each node by

$$\frac{d\mathbf{X}_p}{dt} = \mathbf{U}_p \text{ for } t > 0 \quad \text{and} \quad \mathbf{X}_p(0) = \mathbf{X}_p^0, \tag{1.13}$$

with $\mathbf{U}_p$ and $\mathbf{X}_p^0$ respectively the velocity and the position of a node p at initial time. In the previous equations (1.11)-(1.12), $\mathbf{F}_{pc}$ is the numerical flux at each node p of each cell c defined by

$$\mathbf{F}_{pc} = L_{pc}P_c\mathbf{N}_{pc} - \mathbb{M}_{pc}(\mathbf{U}_p - \mathbf{U}_c), \tag{1.14}$$

with $\mathbf{U}_p$ the velocity at the point p and P_c the mean value of the pressure in the cell c. The 2×2 matrices $\mathbb{M}_{pc}$ and $\mathbb{M}_p$ are defined as

$$\mathbb{M}_{pc} = \mathsf{Z}_c\left(L_{pc}^-\mathbf{N}_{pc}^-\otimes\mathbf{N}_{pc}^- + L_{pc}^+\mathbf{N}_{pc}^+\otimes\mathbf{N}_{pc}^+\right), \text{ and } \mathbb{M}_p = \sum_{c\in\mathcal{C}(p)} \mathbb{M}_{pc}. \tag{1.15}$$

Here, Z_c denotes the "swept mass flux" associated to the isentropic sound speed a_c that is

$$\mathsf{Z}_c = \rho_c a_c. \tag{1.16}$$

In fact, Z_c corresponds to the acoustic impedance. As it has been demonstrated in [111] the total energy and momentum conservation is equivalent to

$$\sum_{c\in\mathcal{C}(p)} \mathbf{F}_{pc} = \mathbf{0}. \tag{1.17}$$

Finally using (1.14), the nodal velocity $\mathbf{U}_p$ is deduced from (1.17) by solving the linear system

$$\mathbb{M}_p\mathbf{U}_p = \sum_{c\in\mathcal{C}(p)} (L_{pc}P_c\mathbf{N}_{pc} + \mathbb{M}_{pc}\mathbf{U}_c). \tag{1.18}$$

In [110], the numerical fluxes used in the discretization of (1.8) and (1.10) are chosen for satisfying the local geometric conservation law (GCL) constraint (1.32). Since (1.32) is explicitly solved, there is no need to solve (1.8). Thus, each cell volume V_c is directly deduced from (1.32) using the conservation of the local GCL constraint.

1.3 Lagrangian scheme in axisymmetric geometry

In this part, an extension of the cell-centered Lagrangian scheme EUCCLHYD [110, 113] is presented for the numerical simulation of compressible flows in pseudo-Cartesian geometries for unstructured meshes as in [109]. This choice has the great advantage to treat both axisymmetric and Cartesian geometries [27]. In this section, a simpler formulation of the scheme introduced in [109] for first-order approximation is proposed. To this end, an area weighted formulation of classical Lagrangian equations is first introduced. Then these equations are discretized with a node-centered approximate Riemann solver.

1.3.1 Governing equations

During the Lagrangian phase, the rates of change of volume, mass, momentum and total energy are computed assuming that discretized volumes move following the flow. Thus, each arbitrary volume $V(t)$ depending on the time $t > 0$ moves satisfying the following system of equations

$$\frac{d}{dt}\int_V \rho dV = 0, \tag{1.19}$$

$$\frac{d}{dt}\int_V dV - \int_V \nabla\cdot\mathbf{U}dV = 0, \tag{1.20}$$

$$\frac{d}{dt}\int_V \rho\mathbf{U}dV + \int_V \nabla P dV = 0, \tag{1.21}$$

$$\frac{d}{dt}\int_V \rho E dV + \int_V \nabla\cdot(P\mathbf{U})dV = 0, \tag{1.22}$$

where $\dfrac{d}{dt}$ is the Lagrangian derivative and $\rho, \mathbf{U}, P, E$ are respectively the density, velocity, pressure and total energy. In addition, this system is closed thanks to an equation of state (EOS) as

$$P = P(\rho, \varepsilon), \tag{1.23}$$

with the internal energy ε defined as $\varepsilon = E - |\mathbf{U}|^2/2$. At last, we have local kinematic equation

$$\frac{d\mathbf{X}}{dt} = \mathbf{U}, \quad \mathbf{X}(0) = \mathbf{X}^0, \tag{1.24}$$

with $\mathbf{X}$ the location of a point of the control volume surface $S(t)$, at time $t > 0$ and $\mathbf{X}^0$ its initial value. This equation is equivalent to (1.20) also known as geometric conservation law (GCL).

1.3.2 Area-weighted formulation

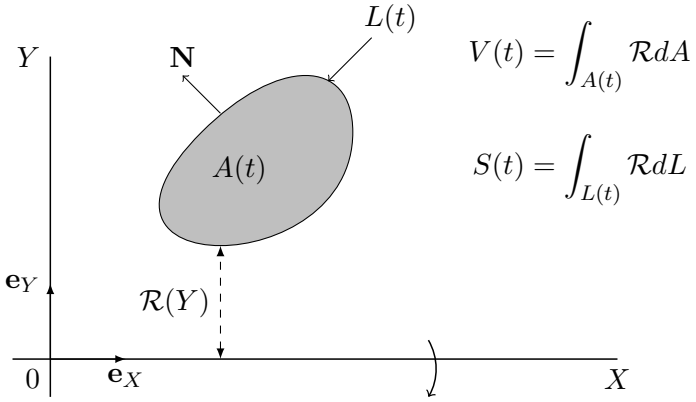

Figure 1.3: Notations related to the pseudo-cartesian grid.

For defining the differential operators used in the system of Lagrangian equation (1.19)-(1.22) a pseudo-Cartesian reference frame $\{0, X, Y\}$ for the orthonormal basis $(\mathbf{e}_X, \mathbf{e}_Y)$ is used (see FIG. 1.3). Thus each point is localized by means of its positions X and $\mathcal{R}(Y) = 1 - \alpha + \alpha Y$ the pseudo-radius. When $\alpha = 0$, the Lagrangian equations for Cartesian geometry are recovered, otherwise for $\alpha = 1$ this corresponds to axisymmetric equations. In this way, axisymmetric geometry is obtained from Cartesian one through a rotational symmetry about the X-axis. This implies that the volume $V(t)$ is generated by the rotation of the area $A(t)$ about the X-axis. In consequence, the element volume dV writes as $dV = \mathcal{R} dA$ with $dA = dX dY$ the element area in the pseudo-Cartesian frame. In the same manner, the control surface $S(t)$ delimiting $V(t)$ is obtained through the rotation of $L(t)$ the boundary of $A(t)$ and the surface element is given by $dS = \mathcal{R} dL$. Note that we have omitted the 2π factor in the evaluation of the element volume.

In a such framework, the velocity divergence and the pressure gradient read as follows

$$\nabla \cdot \mathbf{U} = \frac{1}{\mathcal{R}} \left[\frac{\partial(\mathcal{R}u)}{\partial X} + \frac{\partial(\mathcal{R}v)}{\partial Y} \right], \text{ where } \mathbf{U}^t = (u, v) \tag{1.25}$$

and

$$\nabla P = \left(\frac{\partial P}{\partial X} \mathbf{e}_X + \frac{\partial P}{\partial Y} \mathbf{e}_Y \right). \tag{1.26}$$

Using the previous definitions and after some calculations using the Green's formula, it is possible to rewrite (1.19)-(1.22) at least in two different ways. The first one, obtained without any approximation is the *control volume formulation*. When discretized this formulation leads to a conservative scheme for both equations of energy and momentum, and satisfies the local semi-discrete entropy inequality. However, as shown in [109] it does not preserve symmetries. Consequently, an *area-weighted formulation* is adopted here leading to a conservative scheme for energy equation that respect spherical geometries. This formulation is deduced from the control volume one assuming that momentum equation (1.21) is written in Cartesian geometry.

Like this, the area-weighted formulation for the Lagrangian equations reads

$$m\frac{d}{dt}\left\langle\frac{1}{\rho}\right\rangle - \int_L \mathbf{N}\cdot\mathcal{R}\mathbf{U}dL = 0, \tag{1.27}$$

$$m\frac{d}{dt}\langle\mathbf{U}\rangle + \overline{\mathcal{R}}\int_L P\mathbf{N}dL = 0, \tag{1.28}$$

$$m\frac{d}{dt}\langle E\rangle + \int_L P\mathbf{N}\cdot\mathcal{R}\mathbf{U}dL = 0, \tag{1.29}$$

where $m = \int_V \rho dV$ represents the mass of the volume V. Each physical variable per unit of mass $(E, \mathbf{U})$ is noted as ϕ, and has its mass density mean value defined by $\langle\phi\rangle = \frac{1}{m}\int_V \rho\phi dV$. The average $\overline{\mathcal{R}}$ corresponds to ratio $\overline{\mathcal{R}} = \frac{V}{A}$. In such case, as $m = \rho V$, the momentum equation is solved in Cartesian geometry. For Cartesian case $V = A$, we recover $\overline{\mathcal{R}} = 1$. Further details on the derivation of this system are available in [109].

1.3.3 Numerical scheme

Thereafter, we present briefly the first order cell-centered Lagrangian scheme. To this goal, similar notations as [64, 109, 111] are employed in the sequel. Let us consider a set $\{\Omega_c\}_{c\in\mathbb{N}}$ of non-overlapping polygonal cells that approximates $A(t)$. Each cell noted Ω_c is assigned a single index c. Each vertex of the cell c is labeled with the index p and is localized thanks to its coordinates $\mathbf{X}_p = (X_p, Y_p)^t$ in the pseudo-Cartesian frame. In addition, we introduce $\mathcal{P}(c)$ the list of the vertices belonging to the cell Ω_c and $\mathcal{C}(p)$ the list of the cells sharing the vertex p. These two sets are counterclockwise ordered. Let us introduce p^- and p^+ the previous and the next nodes with respect to p in $\mathcal{P}(c)$. We denote by L_{pc}^-, L_{pc}^+ the half length of the edges $[pp^-], [pp^+]$. Similar notations are used for the outward normals $\mathbf{N}_{pc}^+$ and $\mathbf{N}_{pc}^-$. Finally, the corner normal $L_{pc}\mathbf{N}_{pc}$ is given by $L_{pc}\mathbf{N}_{pc} = L_{pc}^+\mathbf{N}_{pc}^+ + L_{pc}^-\mathbf{N}_{pc}^-$. All these notations have been displayed in FIG. 1.4.

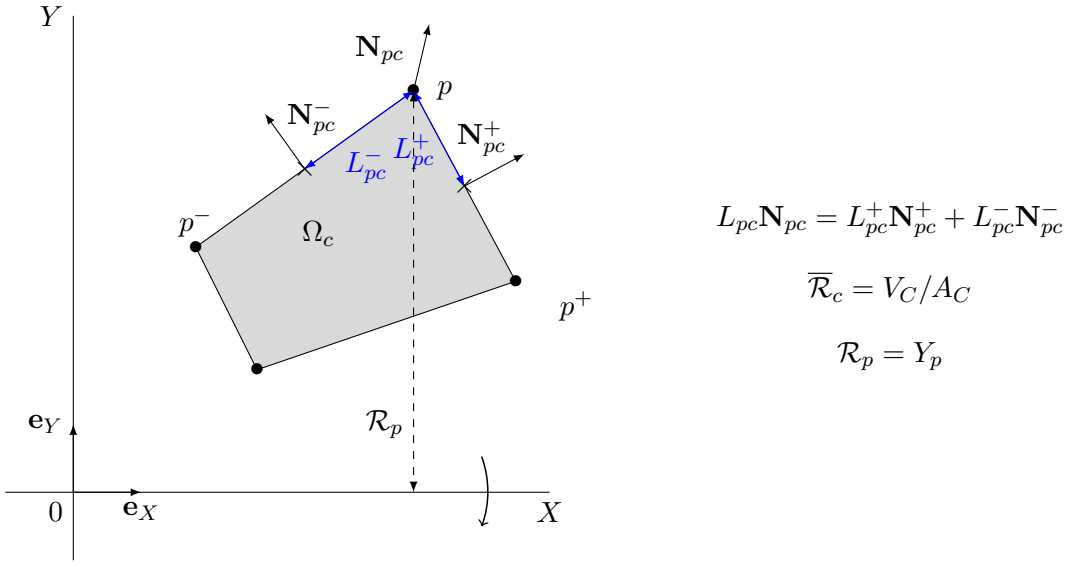

$$L_{pc}\mathbf{N}_{pc} = L_{pc}^+\mathbf{N}_{pc}^+ + L_{pc}^-\mathbf{N}_{pc}^-$$

$$\overline{\mathcal{R}}_c = V_C/A_C$$

$$\mathcal{R}_p = Y_p$$

Figure 1.4: Notations for the cell-centered scheme.

The first order spatial approximation of (1.27)-(1.29) is obtained considering local integrals on each cell Ω_c rotated about the X-axis. The mass m_c of the cell Ω_c is $m_c = \int_{\Omega_c}\rho dV$ and each

flow variable ϕ (as total energy, velocity) is averaged over each cell through the formula

$$\phi_c = \frac{1}{m_c}\int_{\Omega_c} \rho\phi dV,$$

named cell-centered value. Then, we have

$$m_c\frac{d}{dt}\mathbf{U}_c + \overline{\mathcal{R}}_c \sum_{p\in\mathcal{P}(c)} \mathbf{F}_{pc} = \mathbf{0}, \tag{1.30}$$

$$m_c\frac{d}{dt}E_c + \sum_{p\in\mathcal{P}(c)} \mathbf{F}_{pc}\cdot\mathcal{R}_p\mathbf{U}_p = 0. \tag{1.31}$$

In addition, the mesh is moved through the local kinematic equation given at each node by

$$\frac{d\mathbf{X}_p}{dt} = \mathbf{U}_p \text{ for } t > 0 \quad \text{and} \quad \mathbf{X}_p(0) = \mathbf{X}_p^0, \tag{1.32}$$

with $\mathbf{U}_p$ and $\mathbf{X}_p^0$ respectively the velocity and the position of a node p at initial time. In the previous equations, $\mathbf{F}_{pc}$ is the numerical flux at each node p of each cell c defined by

$$\mathbf{F}_{pc} = L_{pc}P_c\mathbf{N}_{pc} - \mathbb{M}_{pc}(\mathbf{U}_p - \mathbf{U}_c), \tag{1.33}$$

with $\mathbf{U}_p$ the velocity at the point p and P_c the mean value of the pressure in the cell c. The 2×2 matrix $\mathbb{M}_{pc}$ is defined as

$$\mathbb{M}_{pc} = \mathsf{Z}_c\left(L_{pc}^-\mathbf{N}_{pc}^-\otimes\mathbf{N}_{pc}^- + L_{pc}^+\mathbf{N}_{pc}^+\otimes\mathbf{N}_{pc}^+\right). \tag{1.34}$$

Where, we introduce the "swept mass flux" [57] associated to the isentropic sound speed a_c that is

$$\mathsf{Z}_c = \rho_c a_c. \tag{1.35}$$

This is nothing but the acoustic impedance. As it has been demonstrated in [111] the total energy and momentum conservation is equivalent to

$$\sum_{c\in\mathcal{C}(p)} \mathbf{F}_{pc} = \mathbf{0}. \tag{1.36}$$

Finally using (1.33), the nodal velocity $\mathbf{U}_p$ is deduced from (1.36) by solving the linear system

$$\mathbb{M}_p\mathbf{U}_p = \sum_{c\in\mathcal{C}(p)} (L_{pc}P_c\mathbf{N}_{pc} + \mathbb{M}_{pc}\mathbf{U}_c), \tag{1.37}$$

where

$$\mathbb{M}_p = \sum_{c\in\mathcal{C}(p)} \mathbb{M}_{pc}.$$

In [109], the numerical fluxes used in the discretization of (1.27) and (1.29) are chosen for satisfying the local GCL constraint (1.32). Here, we rather adopt a simpler approach. Since (1.32) is explicitly solved for moving the mesh in time, there is no need to solve (1.27). Thus, each cell volume V_c is directly deduced from (1.32). Thereby, it is possible to choose for the numerical flux in (1.29) a simple form as in (1.31) with $\mathcal{R}_p = 1-\alpha+\alpha Y_p$. Concerning the momentum equation, the mean value of $\mathcal{R}_c$ in cell c is equal to the discrete ratio $\overline{\mathcal{R}}_c = \dfrac{V_c}{A_c}$. Let us note that this new formulation of the area-weighted discretization for $\alpha = 0$ recover exactly the same as the one developed in Section 1.2 for two-dimensional Cartesian geometry. However, the present spatial discretization does not satisfy rigorously the GCL compatibility requirement for the numerical fluxes as in [109]. Nevertheless, this area-weighted discretization satisfies rigorously the GCL compatibility requirement for one-dimensional spherical flows on equiangular polar grids [27].

1.4 Lagrangian scheme in 3D

The 3D extension of Finite Volume Lagrangian schemes were recently proposed in [118, 48, 104, 46, 162, 29] leading to two main difficulties: the GCL compatibility and the limiting of a reconstructed field in the 3D space.
The GCL compatibility is crucial and imposes the cell volume computed geometrically to coincide with the volume evaluated by the discretization of the volume conservation equation. The difficulty comes from the polyhedral cell and its non-planar faces. The two main solutions are to parametrize the cell [48], which means that a mapping is defined between the cell and a reference element, or to decompose the cell into tetrahedrons [118, 38]. However, the decomposition of a polyhedral cell is not unique in 3D and more complex than in the 2D framework.
We propose here, a systematic and symmetric decomposition of polyhedral cells. It relies on the decomposition of a non planar face into planar triangular faces by adding a supplementary point on the face which is the barycenter of the face vertices. The kinematics of this supplementary point is solved by prescribing its velocity as being the barycenter of the vertices velocity. This amounts to assume a linear representation of the velocity field over the faces with respect to the space variable. Moreover, this decomposition enables to define a discrete divergence operator leading to the respect of the GCL.

The spatial domain $\omega(t)$ is paved with a set of non-overlapping polyhedrons denoted ω_c such that $\omega(t) = \bigcup_c \omega_c$. A polyhedron is a volume delimited by polygonal faces. These faces can be non-planar in the 3D space and a special treatment is required in order to define their outward normal and area. A first method is to parametrize the cell, which means that a mapping is defined between the cell and a reference element. In [48] for example, an isoparametric transformation is adopted for representing the hexahedrons. The problem of the parametrization is that the reference element is restricted to be a hexahedron or a tetrahedron. A second method to handle polyhedral cells is to split them into tetrahedrons by splitting the cell faces into triangles [38, 118]. In [118] for example, the quadrangular faces of a hexahedron are split by using one of their diagonals. This is easy to implement but introduces a loss of symmetry due to the choice of the diagonal. The splitting introduced by Burton [38] adapts to any polyhedral cell and preserves symmetries. However, it is computationally expensive since it needs to determine the faces barycenter as well as the edges midpoints. In this work, we propose to split the cells by adding only one point p_f^* for each of its faces as shown in Fig. 1.5. This splitting is midway between [38] and [118], it works for any polyhedral cell and preserves symmetry. This splitting enables to define unique area S_{t_r} and outward normal n_{t_r} for the triangular partition t_r. Moreover, using this geometric splitting the solution is asked to respect the GCL.

The following topological sets are defined :

- $\mathcal{T}(c)$ is the set of triangles t_r on the cell c,
- $\mathcal{T}(p)$ is the set of triangles t_r sharing the point p,
- $\mathcal{T}(f)$ is the set of triangles t_r partitioning the face f,
- $\mathcal{T}_f(p)$ is the set of triangles t_r of face f sharing point p,
- $\mathcal{P}_b(t_r)$ is the set of points p constituting the triangle t_r, including the face barycenter p_b,
- $\mathcal{P}(f)$ is the set of points p constituting the face f, without the face barycenter p_b,
- $\mathcal{P}(t_r)$ is the set of points p constituting the triangle t_r, without the face barycenter p_b,

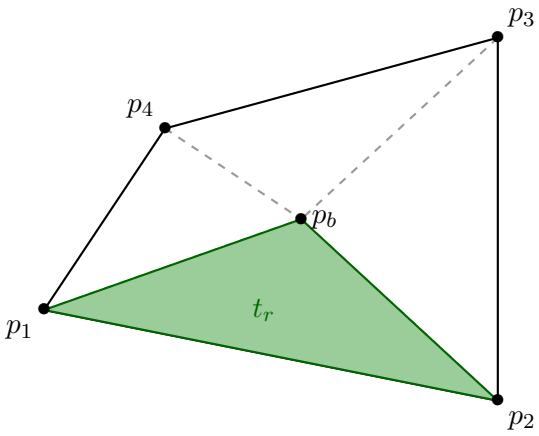

Figure 1.5: Geometric splitting of a quadrangular face f based on the barycenter p_b and creating the triangles t_r.

and the cell boundary is discretized as follows

$$\Sigma_c = \bigcup_{t_r \in \mathcal{T}(c)} t_r. \tag{1.38}$$

1.4.1 GCL discretization

Starting now from the GCL written for a cell Ω_c of boundary Σ_c the GCL writes

$$\frac{d}{dt}\int_{\Omega_c} \mathrm{d}\omega - \int_{\Sigma_c} \mathbf{U}\cdot\boldsymbol{n}\,\mathrm{d}\sigma = 0. \tag{1.39}$$

The left-hand side integral is the cell volume V_c and Σ_c is discretized following (1.38), thus the previous equation becomes

$$\frac{dV_c}{dt} - \sum_{t_r\in\mathcal{T}(c)} \left(\int_{t_r} \mathbf{U}\,\mathrm{d}\sigma\right)\cdot\boldsymbol{n_{t_r}} = 0, \tag{1.40}$$

where $\boldsymbol{n_{t_r}}$ is constant over the triangle t_r. Then considering a linear velocity field on each triangle t_r, the mean velocity $\boldsymbol{U}^*_{t_r}$ on the triangle is defined such that

$$\boldsymbol{U}^*_{t_r} = \frac{1}{S_{t_r}}\int_{t_r} \mathbf{U}\,\mathrm{d}\sigma = \frac{1}{S_{t_r}}\left(\frac{1}{3}\sum_{p\in\mathcal{P}_b(t_r)} \boldsymbol{U}_p\right). \tag{1.41}$$

Finally the GCL writes

$$\frac{dV_c}{dt} - \sum_{t_r\in\mathcal{T}(c)} S_{t_r}\boldsymbol{n_{t_r}}\cdot\left(\frac{1}{3}\sum_{p\in\mathcal{P}_b(t_r)} \boldsymbol{U}_p\right) = 0. \tag{1.42}$$

Denoting by p, p^+ and p^{++} the three points of the triangle t_r, such that the triangle t_r has the same orientation than the face f it is related to as shown in Fig. 1.6. This supplementary node

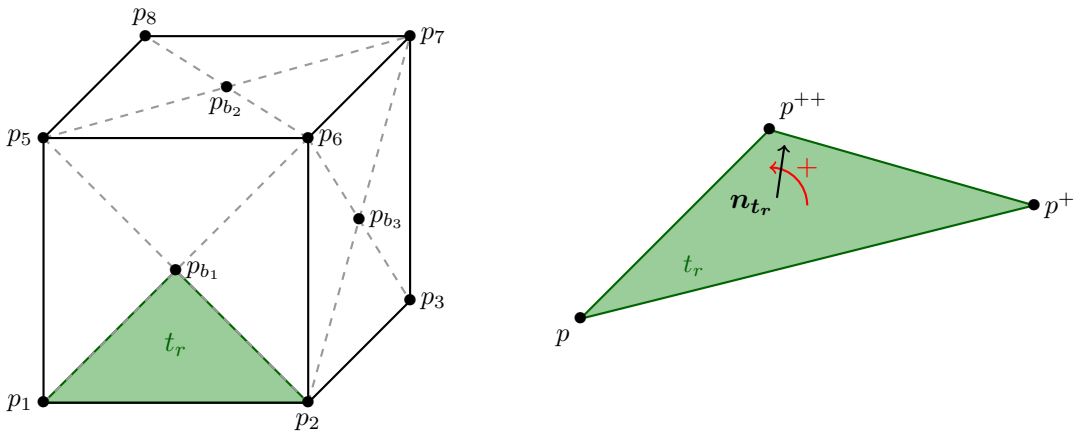

Figure 1.6: Face splitting for the simple case of an hexahedral cell with square faces (left). Orientation of the triangle t_r delimited by the nodes p, p^+ and p^{++} (right).

denomination is introduced in order to highlight cyclic simplifications but one has to keep in mind that one of these node is p_f^*. As t_r is a triangle, the following relation can be written

$$S_{t_r}\boldsymbol{n_{t_r}} = \frac{1}{2}\sum_{p\in\mathcal{P}_b(t_r)}\left(\boldsymbol{X_p^+}\times\boldsymbol{X_p^{++}}\right). \tag{1.43}$$

In this relation, $\boldsymbol{X_p}$ denotes the coordinates of node p. It enables to write the GCL as

$$\begin{aligned}\frac{dV_c}{dt} =& \frac{1}{6}\sum_{t_r\in\mathcal{T}(c)}\left[\sum_{p\in\mathcal{P}_b(t_r)}\boldsymbol{U}_p\right]\cdot\left[\sum_{p\in\mathcal{P}_b(t_r)}\left(\boldsymbol{X_p^+}\times\boldsymbol{X_p^{++}}\right)\right],\\ =& \frac{1}{6}\sum_{t_r\in\mathcal{T}(c)}\left[\sum_{p\in\mathcal{P}_b(t_r)}\boldsymbol{U}_p\cdot\left(\boldsymbol{X_p^+}\times\boldsymbol{X_p^{++}}\right)+\sum_{p\in\mathcal{P}_b(t_r)}\boldsymbol{U}_p\cdot\left(\boldsymbol{X_p}\times\left(\boldsymbol{X_p^+}-\boldsymbol{X_p^{++}}\right)\right)\right].\end{aligned} \tag{1.44}$$

1.4.2 Comparison between geometrical volume variation and GCL

Using the previous face splitting, a polyhedral cell can be decomposed into tetrahedrons. Let $\mathscr{T}_{t_r}$ be the tetrahedron such that its basis is the triangle t_r and its remaining vertex is the space origin (refer to Fig. 1.7). The cell volume v_c is then computed as

$$v_c = \sum_{t_r\in\mathcal{T}(c)} v_{\mathscr{T}_{t_r}}, \tag{1.45}$$

where $v_{\mathscr{T}_{t_r}}$ is the signed volume of the tetrahedron $\mathscr{T}_{t_r}$. Using O the space origin, all the tetrahedrons can be represented by $\mathscr{T}_{t_r} = \{O, p, p^+, p^{++}\}$. Moreover, this denomination is chosen such that the triangle t_r has the same orientation than the face f it is related to as shown in Fig. 1.7.

The signed volume of the tetrahedron $V_{\mathscr{T}_{t_r}}$ is such as

$$V_{\mathscr{T}_{t_r}} = \frac{1}{6}\boldsymbol{X_p}\cdot\left(\boldsymbol{X_p^+}\times\boldsymbol{X_p^{++}}\right). \tag{1.46}$$

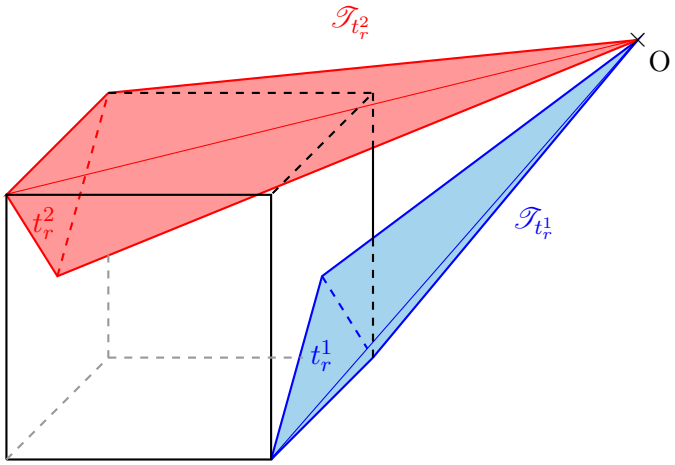

Figure 1.7: Splitting of the cell into tetrahedrons $\mathscr{T}_{t_r}$. The basis of $\mathscr{T}_{t_r^1}$ in blue (respectively $\mathscr{T}_{t_r^2}$ in red) is the triangle t_r^1 (respectively t_r^2) and its remaining vertex is the space origin. $\mathscr{T}_{t_r^1}$ has a negative volume and $\mathscr{T}_{t_r^2}$ has a positive one.

Time derivating this tetrahedron volume gives

$$\frac{dV_{\mathscr{T}_{t_r}}}{dt} = \sum_{p\in\mathcal{P}_b(t_r)} \frac{d\boldsymbol{X_p}}{dt}\cdot\nabla_{\boldsymbol{X_p}} V_{t_r} = \frac{1}{6}\sum_{p\in\mathcal{P}_b(t_r)} \boldsymbol{U}_p\cdot\left(\boldsymbol{X}_{\boldsymbol{p}}^{+}\times\boldsymbol{X}_{\boldsymbol{p}}^{++}\right), \tag{1.47}$$

and summing this result for each tetrahedron composing the cell c leads to the geometric formulation of the volume variation relation

$$\frac{dV_c}{dt} = \frac{1}{6}\sum_{\mathscr{T}_{t_r}\in\mathcal{T}(c)}\sum_{p\in\mathcal{P}_b(t_r)} \boldsymbol{U}_p\cdot\left(\boldsymbol{X}_{\boldsymbol{p}}^{+}\times\boldsymbol{X}_{\boldsymbol{p}}^{++}\right). \tag{1.48}$$

This last relation is the semi-discrete form of the time rate of change of the cell volume. The term between brackets is similar to the corner area vector related to node p defined by Després et al. [48].

The equality between (1.44) and (1.48) is respected provided that

$$\sum_{t_r\in\mathcal{T}(c)}\sum_{p\in\mathcal{P}_b(t_r)} \boldsymbol{U}_p\cdot\left(\boldsymbol{X_p}\times\left(\boldsymbol{X}_{\boldsymbol{p}}^{+}-\boldsymbol{X}_{\boldsymbol{p}}^{++}\right)\right) = 0. \tag{1.49}$$

Since only the numbering p^+, p^{++} depends on the triangle t_r one can permute the two sums

$$\sum_{p\in\mathcal{P}_b(c)} \boldsymbol{U}_p\cdot\left(\boldsymbol{X_p}\times\sum_{t_r\in\mathcal{T}(p)}\left(\boldsymbol{X}_{\boldsymbol{p}}^{+}-\boldsymbol{X}_{\boldsymbol{p}}^{++}\right)\right) = 0, \tag{1.50}$$

and this final relation is always respected since $\sum_{t_r\in\mathcal{T}(p)}\left(\boldsymbol{X}_{\boldsymbol{p}}^{+}-\boldsymbol{X}_{\boldsymbol{p}}^{++}\right)$ is a closed contour.

As a conclusion, the cell volume obtained from the discrete GCL (1.42) is equivalent to the volume calculated geometrically provided that the velocity field is linear on each triangle.

1.4.3 Definition of the discrete divergence operator

To achieve the discretization of (1.48), it remains to define the kinematics of the supplementary node p_f^* by determining its velocity $\mathbf{U}_{p_f^*}$. This velocity could be computed if a solver was defined at node p_f^*. However, in order to avoid the addition of supplementary degrees of freedom, the node p_f^* is defined as the face barycenter. Using the assumption of a linear velocity field with respect to $\boldsymbol{x}$ over the face leads to define $\mathbf{U}_{p_f^*}$ as the barycenter of the face vertices velocity

$$\mathbf{U}_{p_f^*} = \frac{1}{N_{p,f}} \sum_{q \in \mathcal{P}(f)} \mathbf{U}_q,$$

where $N_{p,f}$ is the number of nodes on the face f (without p_f^*).

This assumption of a linear velocity on the face f enables to eliminate the node p_f^* from the summations of (1.48). Let us start from the following semi-discrete form of the GCL

$$\frac{dv_c}{dt} = \sum_{t_r \in \mathcal{T}(c)} \sum_{p \in \mathcal{P}^*(t_r)} \mathbf{U}_p \cdot \left(\frac{1}{3} S_{t_r} \boldsymbol{n}_{t_r} \right),$$

Since the node p_f^* belongs to the set $\mathcal{P}^*(t_r)$, the previous relation can be written as

$$\frac{dv_c}{dt} = \sum_{p \in \mathcal{P}(c)} \sum_{f \in \mathcal{F}(c,p)} \mathbf{U}_p \cdot \frac{1}{3} \left(\sum_{t_r \in \mathcal{T}(c,f,p)} S_{t_r} \boldsymbol{n}_{t_r} + \frac{1}{N_{pf}} \sum_{t_r \in \mathcal{T}(c,f)} S_{t_r} \boldsymbol{n}_{t_r} \right),$$

This last relation can finally be written under the form

$$\frac{dv_c}{dt} = \sum_{p \in \mathcal{P}(c)} \mathbf{U}_p \cdot \left[\sum_{f \in \mathcal{F}(c,p)} S_{pf} \boldsymbol{n}_{pf} \right], \tag{1.51}$$

by introducing the face area vector $S_{pf}\boldsymbol{n}_{pf}$ such that

$$S_{pf}\boldsymbol{n}_{pf} = \frac{1}{3} \left(\sum_{t_r \in \mathcal{T}(c,f,p)} S_{t_r} \boldsymbol{n}_{t_r} + \sum_{t_r \in \mathcal{T}(c,f)} \frac{1}{N_{p,f}} S_{t_r} \boldsymbol{n}_{t_r} \right). \tag{1.52}$$

The $S_{pf}\boldsymbol{n}_{pf}$ is named face area vector as the contribution of face f to the corner area vector [53]. In the present work, this corner area vector writes $\boldsymbol{n}_p = \sum_{f \in \mathcal{F}(c,p)} S_{pf}\boldsymbol{n}_{pf}$. The numerical fluxes will be applied on these face area vectors which will ensure that the scheme satisfies the GCL.

The discrete divergence operator is defined as

$$(\nabla \cdot \boldsymbol{\psi})_{\omega_c} = \frac{1}{v_c} \int_{\omega_c} \nabla \cdot \boldsymbol{\psi} \, \mathrm{d}v = \frac{1}{v_c} \int_{\partial\omega_c} \boldsymbol{\psi} \cdot \boldsymbol{n} \, \mathrm{d}s.$$

Using the definition of the GCL (1.39) and the semi-discrete equation (1.51), this operator thus writes

$$(\nabla \cdot \boldsymbol{\psi})_{\omega_c} = \frac{1}{v_c} \sum_{p \in \mathcal{P}(c)} \sum_{f \in \mathcal{F}(c,p)} \boldsymbol{\psi}_p \cdot S_{pf}\boldsymbol{n}_{pf}, \tag{1.53}$$

for a vector $\boldsymbol{\psi}$ in the cell ω_c, if $\boldsymbol{\psi}_p$ is the value of this vector at the node p. In the same manner, the discrete gradient operator is defined as

$$(\nabla \varphi)_{\omega_c} = \frac{1}{v_c} \sum_{p \in \mathcal{P}(c)} \sum_{f \in \mathcal{F}(c,p)} \varphi_p S_{pf}\boldsymbol{n}_{pf}, \tag{1.54}$$

for any scalar φ in ω_c where φ_p is the value of φ at node p.

1.4.4 Discretization of the Euler equations

In a Lagrangian scheme, the mass conservation equation is easily respected since it imposes the cell mass m_c to be constant. Now, applying the previous discrete operators (1.53) and (1.54) to the semi-discrete momentum and total energy conservation equations writes

$$\begin{aligned} m_c \frac{d\mathbf{U}_c}{dt} + \sum_{p\in\mathcal{P}(c)} \sum_{f\in\mathcal{F}(c,p)} S_{pf} P_{cfp} \boldsymbol{n}_{pf} = \mathbf{0}, \\ m_c \frac{dE_c}{dt} + \sum_{p\in\mathcal{P}(c)} \sum_{f\in\mathcal{F}(c,p)} S_{pf} P_{cfp} \mathbf{U}_p \cdot \boldsymbol{n}_{pf} = 0, \end{aligned} \tag{1.55}$$

where the subscript c indicates that the quantity has been mass averaged on the cell. For example, if φ is a physical variable

$$\varphi_c = \frac{1}{m_c} \int_{\omega_c} \rho\varphi \, \mathrm{d}v,$$

denotes its mass averaged value over the cell ω_c. Let us remark that this semi-discrete scheme, in the same form as [118], requires as many pressure flux P_{cfp} than the number of faces f impinging on node p whereas in [48] the pressure flux P_{cp} depends only on the node.

The semi-discrete trajectory equation is written as

$$\frac{d\boldsymbol{X}_p}{dt} = \mathbf{U}_p. \tag{1.56}$$

Finally, the nodal fluxes P_{cfp} and $\mathbf{U}_p$ are the last unknowns to be determined in order to complete this scheme and move the grid.
Let us denote the entropy and the temperature in the cell by η_c and θ_c respectively. The Gibbs relation writes

$$m_c \theta_c \frac{d\eta_c}{dt} = m_c \frac{d\varepsilon_c}{dt} + P_c \frac{dv_c}{dt} = m_c \left[\frac{dE_c}{dt} - \mathbf{U}_c \cdot \frac{d\mathbf{U}_c}{dt} \right] + P_c \frac{dv_c}{dt}$$

Substituting (1.55) in the above equation and following the same steps as in [118] enables to write the semi-discrete entropy equation as

$$m_c \theta_c \frac{d\eta_c}{dt} = \sum_{p\in\mathcal{P}(c)} \sum_{f\in\mathcal{F}(c,p)} S_{pf} \left(P_{cfp} - P_c \right) \left(\mathbf{U}_c - \mathbf{U}_p \right) \cdot \boldsymbol{n}_{pf}.$$

To ensure a positive entropy production, the pressure jump is expressed in terms of the velocity jump as follows

$$P_{cfp} - P_c = Z_c \left(\mathbf{U}_c - \mathbf{U}_p \right) \cdot \boldsymbol{n}_{pf}, \tag{1.57}$$

where $Z_c = (\rho a)_c$ is the acoustic impedance of the cell and $a = \sqrt{(dP/d\rho)_\eta}$ the isentropic speed of sound [113]. This last relation is nothing but the Riemann invariant along direction $\boldsymbol{n}_{pf}$ as used in Section 1.1 for 1D. It remains to compute the nodal velocity by means of a nodal solver. Invoking the total momentum conservation and following the work [118], the nodal velocity $\mathbf{U}_p$ is computed by imposing a momentum balance around the node p. This condition corresponds to balance the pressure fluxes in competition around the node p and writes

$$\sum_{c\in\mathcal{C}(p)} \sum_{f\in\mathcal{F}(c,p)} S_{pf} P_{cfp} \boldsymbol{n}_{pf} = \mathbf{0}.$$

Then, using the relation (1.57), it becomes

$$\mathbb{M}_p \mathbf{U}_p = \boldsymbol{B}, \tag{1.58}$$

where

$$\mathbb{M}_p = \sum_{c \in \mathcal{C}(p)} \sum_{f \in \mathcal{F}(c,p)} S_{pf} Z_c \left(\boldsymbol{n}_{pf} \otimes \boldsymbol{n}_{pf} \right),$$
$$\boldsymbol{B} = \sum_{c \in \mathcal{C}(p)} \sum_{f \in \mathcal{F}(c,p)} S_{pf} \Big[P_c \boldsymbol{n}_{pf} + Z_c \left(\boldsymbol{n}_{pf} \otimes \boldsymbol{n}_{pf} \right) \mathbf{U}_c \Big].$$

The matrix $\mathbb{M}_p$ is positive definite thus invertible and the nodal velocity is given by $\mathbf{U}_p = \mathbb{M}_p^{-1} \boldsymbol{B}$.

Contrary to the formulation derived in [48], one can check that the present nodal solver degenerates exactly onto the acoustic Godunov solver in the case of a 1D flow aligned with a Cartesian grid.

1.5 Second order extension

1.5.1 Second order in space

The second order extension in space of this Godunov-type scheme is performed using a MUSCL method and a piecewise linear representation of the pressure and velocity fields. Let us denote φ a scalar, the linear reconstruction of φ in cell ω_c writes

$$\tilde{\varphi}_c(\boldsymbol{X}) = \bar{\varphi}_c + \nabla \varphi_c . (\boldsymbol{X} - \boldsymbol{X}_c), \quad \boldsymbol{X} \in \omega_c,$$

where $\tilde{\varphi}_c(\boldsymbol{X})$, $\bar{\varphi}_c$ and $\nabla \varphi_c$ are respectively the extrapolated value at point $\boldsymbol{X}$, the mean value and the gradient of variable φ in cell c. Moreover, the cell centroid $\boldsymbol{X}_c$ is defined as

$$\boldsymbol{X}_c = \frac{1}{v_c} \int_{\omega_c} \boldsymbol{X} \, \mathrm{d}v,$$

and numerically evaluated using the method proposed in [122]. These extrapolated values will replace the cell pressure and velocity in the relation (1.57) in order to improve the accuracy of the scheme.

For an arbitrary field, the local extrema around the cell c are defined as

$$\bar{\varphi}_c^{max} = \max \left\{ \max_{c' \in \mathcal{C}_p(c)} (\bar{\varphi}_{c'}), \bar{\varphi}_c \right\} \quad \text{and} \quad \bar{\varphi}_c^{min} = \min \left\{ \min_{c' \in \mathcal{C}_p(c)} (\bar{\varphi}_{c'}), \bar{\varphi}_c \right\},$$

where $\mathcal{C}_p(c)$ is the set of cells c' sharing at least one node with cell c. The monotonicity criterion is then defined as

$$\bar{\varphi}_c^{min} \leq \tilde{\varphi}(\boldsymbol{X}) \leq \bar{\varphi}_c^{max}, \quad \boldsymbol{X} \in \omega_c.$$

Now, since $\tilde{\varphi}$ is a linear field, the monotonicity criterion can be reduced to

$$\bar{\varphi}_c^{min} \leq \tilde{\varphi}(\boldsymbol{X}_p) \leq \bar{\varphi}_c^{max}, \quad p \in \mathcal{P}(c). \tag{1.59}$$

To respect this criterion, the gradient of φ has to be limited. Several slope limiters have been developed in this way [17, 23, 159]. Most of them were developed in the 1D case and are now the subject of major modifications for their extension to the 3D framework [108, 82, 141, 131]. In particular, in the Lagrangian framework, one has to take care that the limiting procedure preserves the symmetries of the flow.

1.5.2 Classic limiters - Barth-Jespersen and Venkatakrishnan

The easiest way to limit a reconstructed field is to apply a scalar $\alpha_c \in [0,1]$ to the cell gradient in order to respect the monotonicity condition (1.59). The limited extrapolated value thus writes

$$\tilde{\varphi}_c^{lim}(\boldsymbol{X}) = \bar{\varphi}_c + \alpha_c \nabla\varphi_c \cdot (\boldsymbol{X} - \boldsymbol{X}_c), \qquad \forall \boldsymbol{X} \in \omega_c.$$

Different limiters can then be constructed depending on the choice made for this scalar α_c. The Barth-Jespersen limiter [17], for example, supposes α_c to be of the form

$$\alpha_c = \min_{p \in \mathcal{P}(c)} (1, \alpha_{c,p}),$$

whereas the Venkatakrishnan limiter [159], used in the work [118], supposes

$$\alpha_c = \min_{p \in \mathcal{P}(c)} \left(\frac{\alpha_{c,p}^2 + 2\alpha_{c,p}}{\alpha_{c,p}^2 + \alpha_{c,p} + 2}\right),$$

where

$$\alpha_{c,p} = \begin{cases} \dfrac{\bar{\varphi}_c^{max} - \bar{\varphi}_c}{\tilde{\varphi}_c(\boldsymbol{X}_p) - \bar{\varphi}_c} & \text{if } \tilde{\varphi}_c(\boldsymbol{X}_p) > \bar{\varphi}_c, \\ \dfrac{\bar{\varphi}_c^{min} - \bar{\varphi}_c}{\tilde{\varphi}_c(\boldsymbol{X}_p) - \bar{\varphi}_c} & \text{if } \tilde{\varphi}_c(\boldsymbol{X}_p) < \bar{\varphi}_c, \\ 1 & \text{if } \tilde{\varphi}_c(\boldsymbol{X}_p) = \bar{\varphi}_c. \end{cases}$$

This last nodal value $\alpha_{c,p}$ is evaluated from scalar values. The velocity norm is used for the velocity limiting in order to deal with a frame independent scalar quantity.

Remark: One can prove that the Barth-Jespersen limiter will replace an overestimated (respectively underestimated) reconstructed value by the local maximum (respectively minimum), and a reconstructed value lying in the monotonicity range will not be modified. However, the Venkatakrishnan limiter will limit the extrapolated value in any case. Indeed, one can easily show that the maximum value of α_c will be $3/4$ for this limiter.

1.5.3 The multi-dimensional minmod limiter for 3D

A classic MUSCL approach consists in computing the cell gradient using a least squares method based on the cells sharing a face with cell ω_c. It is rarely computed on the cells sharing a node with cell ω_c because of symmetrization difficulties at the boundaries. In practice, the limiting is improved by adding an extra limiting factor $\beta \in [0,1]$ to the limited gradient. The drawback of such a factor is that it is user-defined and problem-dependent.
To prevent overshoots and oscillations around strong shocks without resorting to a user-defined limiting factor, it is proposed to build a multi-dimensional extension of the minmod limiter based on nodal gradients and the minmod function. Let us point out that this multi-dimensional limiter degenerates onto the classical minmod limiter in the 1D framework. The interesting behavior of nodal gradients has also been highlighted in [39].

The minmod function is defined as

$$\text{minmod}\{\alpha_1, ..., \alpha_p\} = \begin{cases} 0 \text{ if it exists } i \text{ and } j \text{ such that } \text{sign}(\alpha_i) \neq \text{sign}(\alpha_j), \\ \text{sign}(\alpha_i) \min\limits_{i=1...p} |\alpha_i| \quad \text{otherwise,} \end{cases}$$

where $\{\alpha_1, ..., \alpha_p\}$ is a set of scalar values. In the multi-dimensional frame, the minmod function will be applied to the components of a set of gradients.

Let us consider nodal gradients computed using a least squares method based on the cells $c' \in \mathcal{C}(p)$. The multi-dimensional minmod limiter constructs the cell gradient component by component in an orthonormal reference basis $(\boldsymbol{\xi}_1^c, \boldsymbol{\xi}_2^c, \boldsymbol{\xi}_3^c)$ as detailed in the sequel. This basis is of major importance for preserving the flow symmetries and will represent the pressure and velocity variations as in [111, 104]. In particular:

• For the pressure gradient limiting, $\boldsymbol{\xi}_1^c$ is defined as

$$\begin{cases} \boldsymbol{\xi}_1^c = \dfrac{\nabla P_c}{\|\nabla P_c\|}, & \text{if } \|\nabla P_c\| \neq 0, \\ \boldsymbol{\xi}_1^c = \boldsymbol{e}_x, & \text{otherwise,} \end{cases}$$

where the pressure cell gradient ∇P_c is obtained using a least squares method on the cells c' sharing a face with cell c.

• For the velocity gradient limiting, $\boldsymbol{\xi}_1^c$ is defined as

$$\begin{cases} \boldsymbol{\xi}_1^c = \dfrac{\boldsymbol{U}_c}{\|\boldsymbol{U}_c\|}, & \text{if } \|\boldsymbol{U}_c\| \neq 0, \\ \boldsymbol{\xi}_1^c = \boldsymbol{e}_x, & \text{otherwise.} \end{cases}$$

The remaining basis vectors $\boldsymbol{\xi}_2^c$ and $\boldsymbol{\xi}_3^c$ are then computed arbitrarily in the orthogonal plane.

Let $\mathbb{M}_{\boldsymbol{\xi}}$ be the matrix associated to the change of basis defined as $\mathbb{M}_{\boldsymbol{\xi}} = [\boldsymbol{\xi}_1^c, \boldsymbol{\xi}_2^c, \boldsymbol{\xi}_3^c]$. Let φ be a scalar field and $\boldsymbol{\psi}$ a vectorial field. The nodal gradients of φ and $\boldsymbol{\psi}$ at node p are expressed in the basis $(\boldsymbol{\xi}_1^c, \boldsymbol{\xi}_2^c, \boldsymbol{\xi}_3^c)$ such as

$$\begin{aligned} (\nabla \varphi_p)_{\boldsymbol{\xi}} &= \mathbb{M}_{\boldsymbol{\xi}}^t \nabla \varphi_p, \\ (\nabla \boldsymbol{\psi}_p)_{\boldsymbol{\xi}} &= \mathbb{M}_{\boldsymbol{\xi}}^t \nabla \boldsymbol{\psi}_p \mathbb{M}_{\boldsymbol{\xi}}. \end{aligned}$$

The cell gradient is then constructed component by component as follows

$$\begin{aligned} \left((\nabla \varphi_c)_{\boldsymbol{\xi}}\right)_i &= \underset{p \in \mathcal{P}(c)}{\text{minmod}} \left[\left((\nabla \varphi_p)_{\boldsymbol{\xi}}\right)_i\right], \quad i \in [1,2,3] \\ \left((\nabla \boldsymbol{\psi}_c)_{\boldsymbol{\xi}}\right)_{i,j} &= \underset{p \in \mathcal{P}(c)}{\text{minmod}} \left[\left((\nabla \boldsymbol{\psi}_p)_{\boldsymbol{\xi}}\right)_{i,j}\right], \quad i,j \in [1,2,3] \end{aligned}$$

where i and j are the index of the gradient component. Finally, the cell gradient is expressed in the Cartesian basis as

$$\begin{aligned} \nabla \varphi_c &= \mathbb{M}_{\boldsymbol{\xi}} \left(\nabla \varphi_c\right)_{\boldsymbol{\xi}}, \\ \nabla \boldsymbol{\psi}_c &= \mathbb{M}_{\boldsymbol{\xi}} \left(\nabla \boldsymbol{\psi}_c\right)_{\boldsymbol{\xi}} \mathbb{M}_{\boldsymbol{\xi}}^t. \end{aligned}$$

The monotonicity criterion is then applied to this cell gradient using a Barth-Jespersen limiter which ends the multi-dimensional minmod limiter algorithm.

As a summary, this multi-dimensional minmod limiter constructs a cell gradient by selecting the lowest contributions of nodal gradients, in the sens of the minmod function, in a reference basis $(\boldsymbol{\xi}_1^c, \boldsymbol{\xi}_2^c, \boldsymbol{\xi}_3^c)$. The monotonicity criterion is then ensured by using the Barth-Jespersen limiter.

1.5.4 Second order in time

For the second order extension in time, a Predictor-Corrector scheme is applied [118]. For a numerical scheme written under the general semi-discrete form

$$\frac{d\mathcal{U}}{dt} = \mathcal{F}(t,\mathcal{U}),$$

this time scheme writes

$$\begin{cases} \mathcal{U}_i^{(1)} = \mathcal{U}_i^n + \Delta t \mathcal{F}\left(t^n, \mathcal{U}^n\right), \\ \mathcal{U}_i^{n+1} = \mathcal{U}_i^{(1)} + \dfrac{1}{2}\Delta t \left[\mathcal{F}\left(t^n, \mathcal{U}^n\right) + \mathcal{F}\left(t^{n+1}, \mathcal{U}^{(1)}\right)\right], \\ t^{n+1} = t^n + \Delta t. \end{cases}$$

1.6 Numerical test cases

All the test cases presented in this section are characterized by the gamma gas law which considers a perfect gas ruled by the thermodynamics law

$$P = (\gamma - 1)\rho\varepsilon,$$

where γ is the polytropic index of the gas. One has $\gamma = \frac{5}{3}$ if the gas is monoatomic and $\gamma = \frac{7}{5}$ if the gas is diatomic. The isentropic sound speed in the cell ω_c is defined as

$$a_c = \sqrt{\frac{\gamma_c P_c}{\rho_c}}.$$

The test cases chosen present strong shock waves which lead to important mesh deformations and enable to prove the scheme robustness.

1.6.1 Sod test case

The Sod test case [150] considers the computational domain $x \in [0;1]$. This domain is filled with a diatomic gas such that

$$\begin{cases} (\rho_l, P_l, \boldsymbol{V}_l) &= (1.0, 1.0, \mathbf{0}), & \text{for } x \leq 0.5, \\ (\rho_r, P_r, \boldsymbol{V}_r) &= (0.125, 0.1, \mathbf{0}), & \text{for } x \geq 0.5. \end{cases}$$

This test case highlights the scheme ability to capture shock and rarefaction waves without oscillating. In particular, the second order results with minmod limiter are compared to the Venkatakrishnan limiter used (refer to Fig. 1.8). One can observe that the Venkatakrishnan limiter leads to spurious oscillations around the shock and rarefaction zones. On the contrary, the minmod limiter enables to delete these oscillations without loosing accuracy elsewhere.

1.6.2 Noh test case in 2D and 3D

The Noh problem [128] models the implosion of a monoatomic gas such that $(\rho^0, P^0, \boldsymbol{V}^0) = (1, 10^{-6}, -\boldsymbol{e}_r)$ where $\boldsymbol{e}_r$ is the radial vector. Symmetry conditions are applied on the boundaries holding the origin O whereas the other boundaries are pressure boundary conditions with $P^b = 1.10^{-6}$. This test case can also be found in [114] for 2D results and in [104] for 3D results.

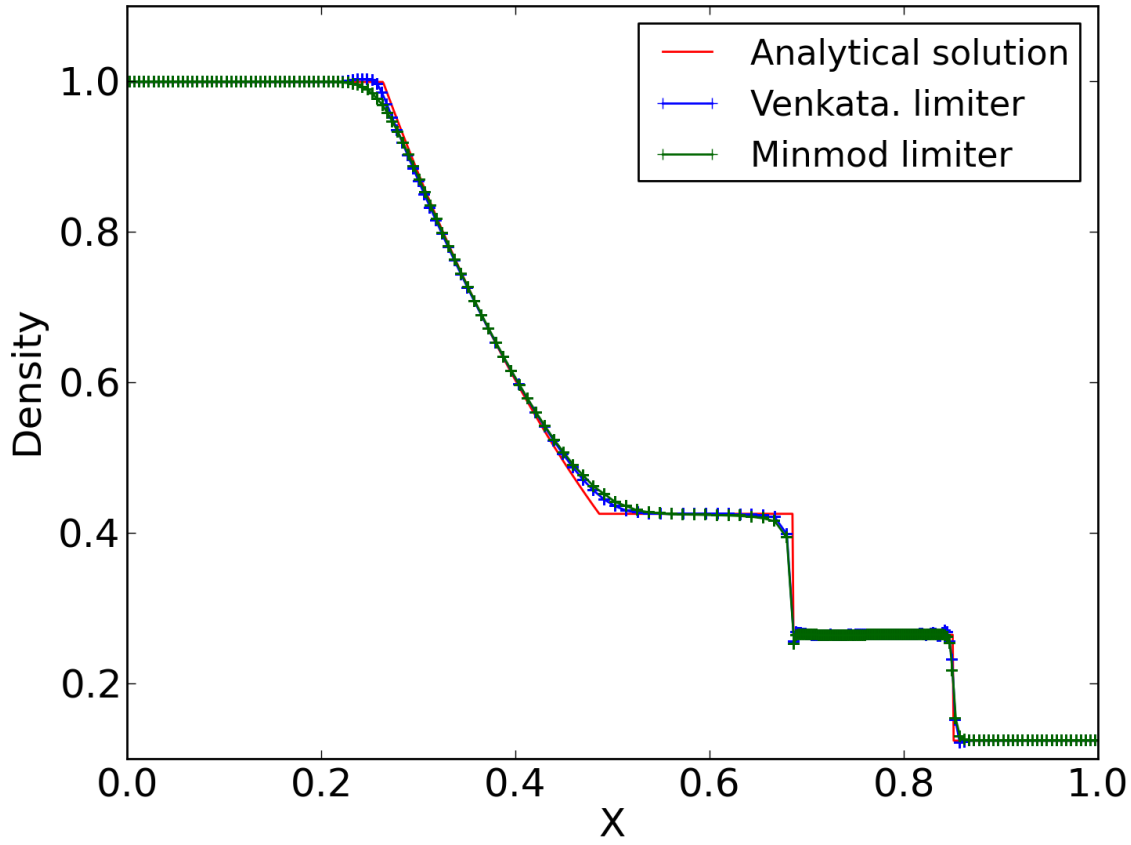

(a)

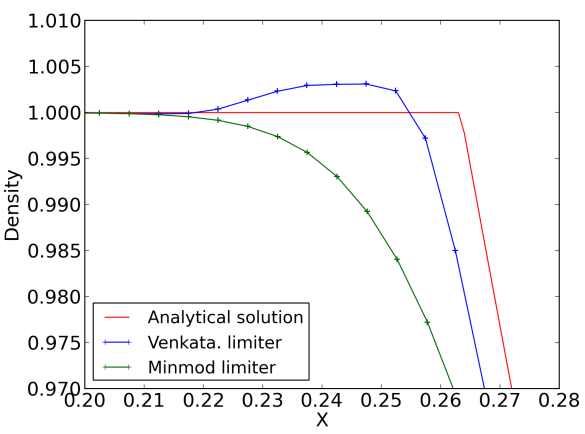

(b)

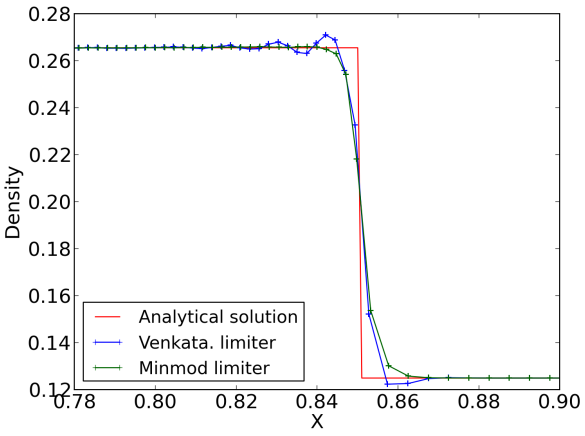

(c)

Figure 1.8: Sod test case - Comparison between the Venkatakrishnan (blue) and the minmod limiter (green). Second-order density at time $t = 0.2$ along the x axis on a 200 cells mesh (1.8a) - Zoom on the beginning of the rarefaction zone (1.8b) - Zoom around the shock zone (1.8c).

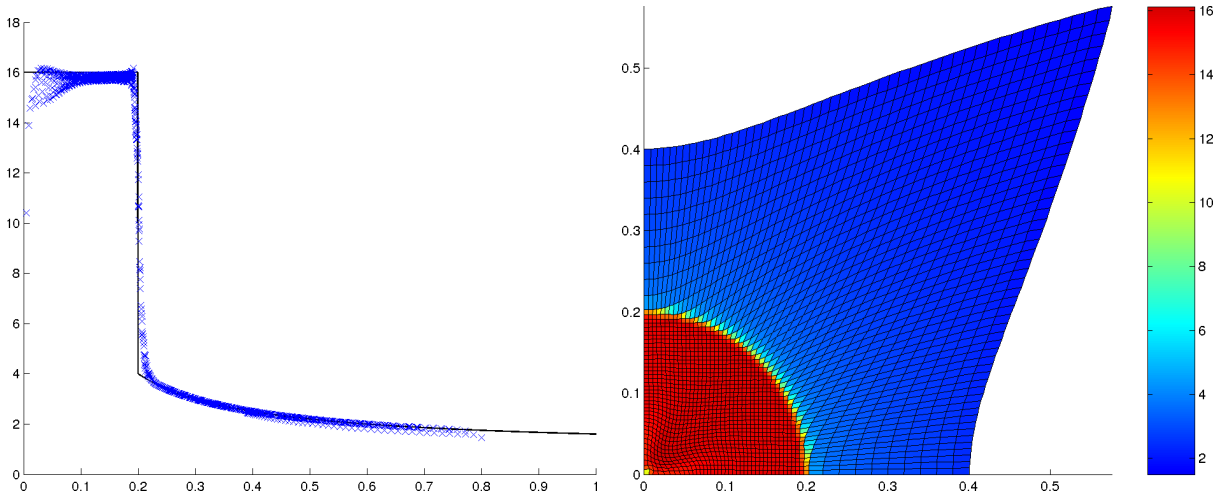

Figure 1.9: 2D planar Noh problem - Barth-Jespersen limiter - Scatter plot of the density in terms of the cell radius (1.9a) and 2D density field (1.9b) at time $t = 0.6$ on a mesh with 50×50 cells.

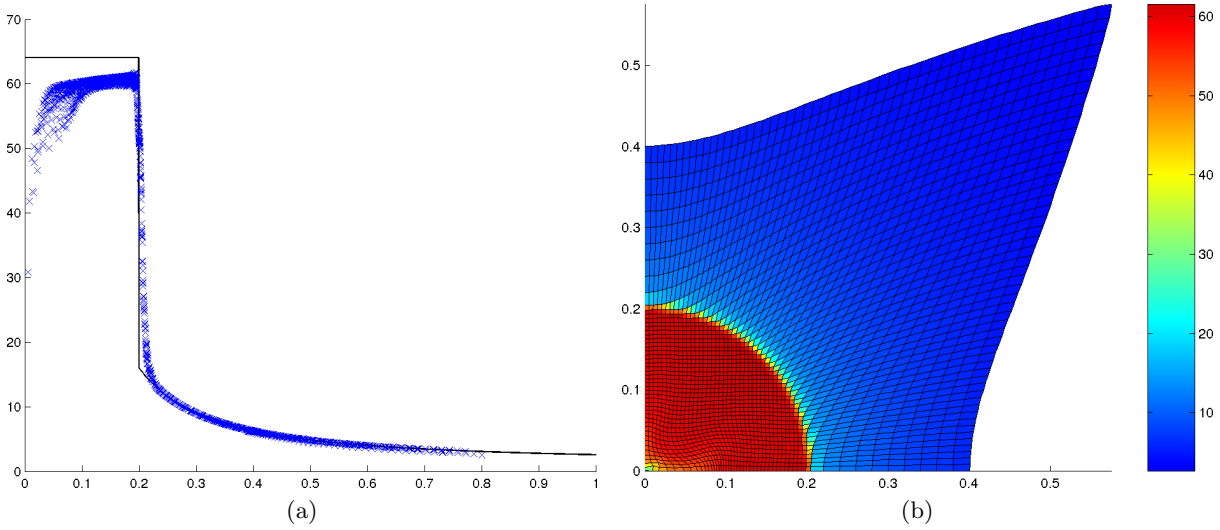

Figure 1.10: 2D axisymmetric Noh problem - Barth-Jespersen limiter - Scatter plot of the density in terms of the cell radius (1.10a) and 2D density field (1.10b) at time $t = 0.6$ on a mesh with 50×50 cells.

This case, defined by Noh in [128], admits a self-similar solution: a shock wave moves inwards at a constant speed. $D = 1/3$. The symmetry of the problem enables to limit the computational domain to an angular sector.
The 2D computation consist in 50×50 quadrangular cells of a square box $(x, y) \in [0; 1]^3$ which enables to test the robustness of the Lagrangian scheme. On FIG. 1.9 and FIG. 1.10 we have respectively represented the results at time $t = 0.6$ for planar and axisymmetric geometry. The timing, the density levels and pressure levels after the shock wave are correct. For planar configuration the maximum density is 16 and it represent a cylindrical implosion whereas for the axisymmetric computation the maximum density is 64 and it represent a spherical implosion. We notice an undershoot for the density that is characteristic of the wall heating phenomena, see [128]. For this computation we use the Barth-Jespersen limiter with an additional limiter coefficient of 0.5 which avoid the overshoot. The use of this coefficient is detailed in [110].

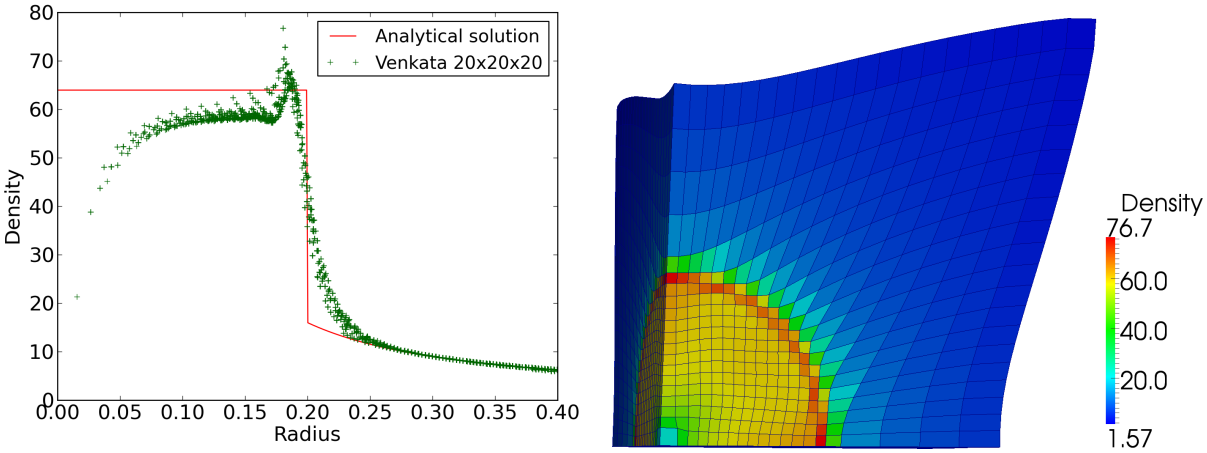

(a) (b)

Figure 1.11: 3D Noh problem - Venkatakrishnan limiter - Scatter plot of the density in terms of the cell radius (1.11a) and 3D density field (1.11b) at time $t = 0.6$ on a mesh with $20 \times 20 \times 20$ cells.

We now present the 3D Noh problem on a cube $(x, y, z) \in [0; 1]^3$. This test case is very sensitive to the limiting procedure. If the shock limiting is not efficient enough, a strong overshoot can be observed as shown in FIG. 1.11 for a second-order solution with the Venkatakrishnan limiter. The minmod limiter enables to remove this overshoot for the same problem (refer to FIG. 1.12a). Moreover, the minmod limited solution presents a good convergence towards the analytical solution with a maximum density of 63.8 (the expected analytical value is 64) for the mesh $80 \times 80 \times 80$ cells (refer to FIG. 1.12).

1.6.3 Saltzman test case in 2D

We consider now the movement of a planar shock wave on a Cartesian grid that has been stretched [59]. This is a well known difficult test case that enables to validate the robustness of our scheme when the mesh is not aligned with the fluid flow. The computational domain is the rectangle $(x, y) \in [0, 1] \times [0, 0.1]$. The initial mesh (shown on FIG. 1.13) is obtained by transforming a uniform 100×10 cells with the mapping

$$\begin{aligned} x_{str} &= x + (0.1 - y)\sin(x\pi), \\ y_{str} &= y. \end{aligned}$$

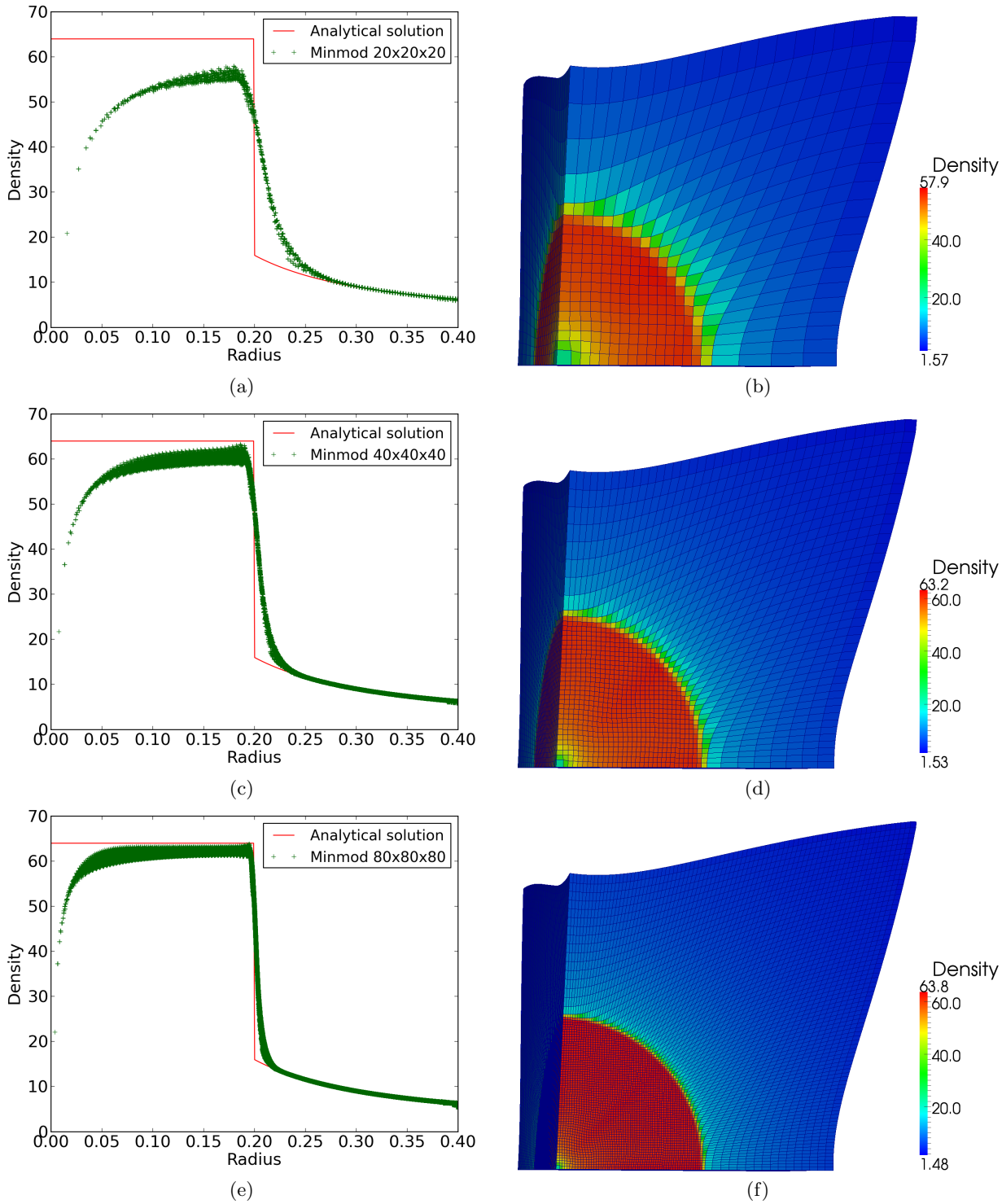

Figure 1.12: Noh problem - Minmod limiter - Scatter plot of the density in terms of the cell radius (1.12a, 1.12c, 1.12e) and 3D density field (1.12b, 1.12d, 1.12f) at time $t = 0.6$ on meshes with $20 \times 20 \times 20$ cells (1.12a, 1.12b), $40 \times 40 \times 40$ cells (1.12c, 1.12d) and $80 \times 80 \times 80$ cells (1.12e, 1.12f).

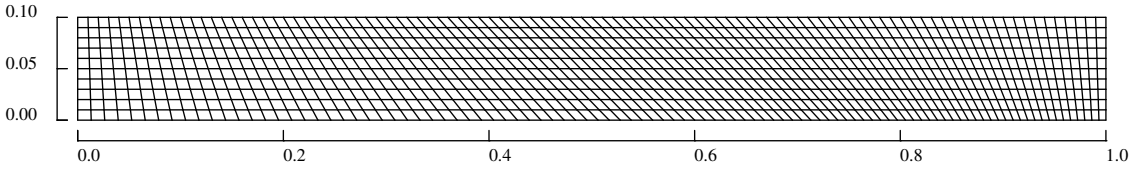

Figure 1.13: Saltzman test case: initial mesh

This domain is filled with a monoatomic gas such that $(\rho^0, P^0, \boldsymbol{U}^0) = (1, 10^{-6}, \mathbf{0})$. The compression is computed by applying the velocity condition $\boldsymbol{U}^b = 1\boldsymbol{e}_x$ on the plane initially at the position $x = 0$. All the other boundaries planes are symmetry boundary conditions.

The exact solution is a planar shock wave that moves at speed $D = 4/3$ from left to right. The propagation of the shock wave at $t = 0.6$ is displayed in FIG. 1.14. The important result is that our 2D scheme preserves one-dimensional solution very well. The FIG. 1.14 shows the mesh at $t = 0.75$ when the shock wave hits the right boundary ($x = 1$).

Behind the shock wave, the initial mesh is distorted, all the horizontal line stays almost parallel with respect to the other ones. The density profile at $t = 0.6$ is displayed on FIG. 1.15a. The shock level is not uniform, but it oscillates around the exact value $\rho = 4$.

The robustness of our scheme is clearly demonstrated by this test case: we are able to reach time $t = 0.96$ which corresponds to two successive rebounds of the shock wave on the vertical boundaries of the domain, see FIG. 1.15b. After this time, the computation stops because the mesh become tangled.

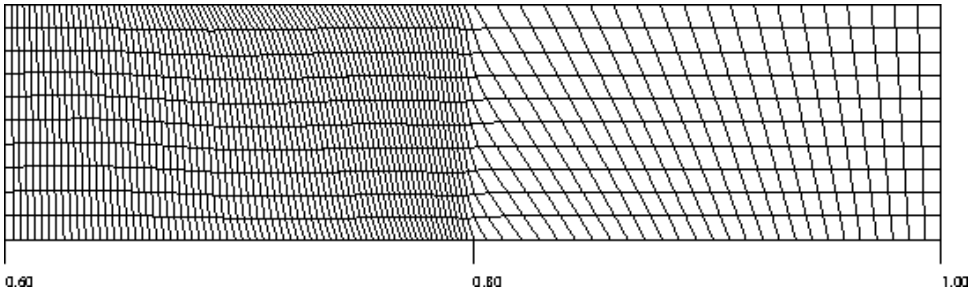

Figure 1.14: Saltzman's test: mesh at $t = 0.6$

1.6.4 Saltzmann test case in 3D

We present here the 3D extension of the Saltzmann test case [46] which simulates the propagation of a piston driven shock wave in the computational domain $(x, y, z) \in [0; 1] \times [0; 0.1] \times [0; 0.1]$. The propagation of the planar shock wave is studied on a distorted mesh such as proposed in [46]

$$\begin{cases} \tilde{x} = x + (0.1 - z)(1 - 20y)\sin(x\pi), & \text{if} \quad 0 \leq y \leq 0.05, \\ \tilde{x} = x + z(20y - 1)\sin(x\pi), & \text{if} \quad 0.05 \leq y \leq 0.1, \\ \tilde{y} = y, \\ \tilde{z} = z. \end{cases}$$

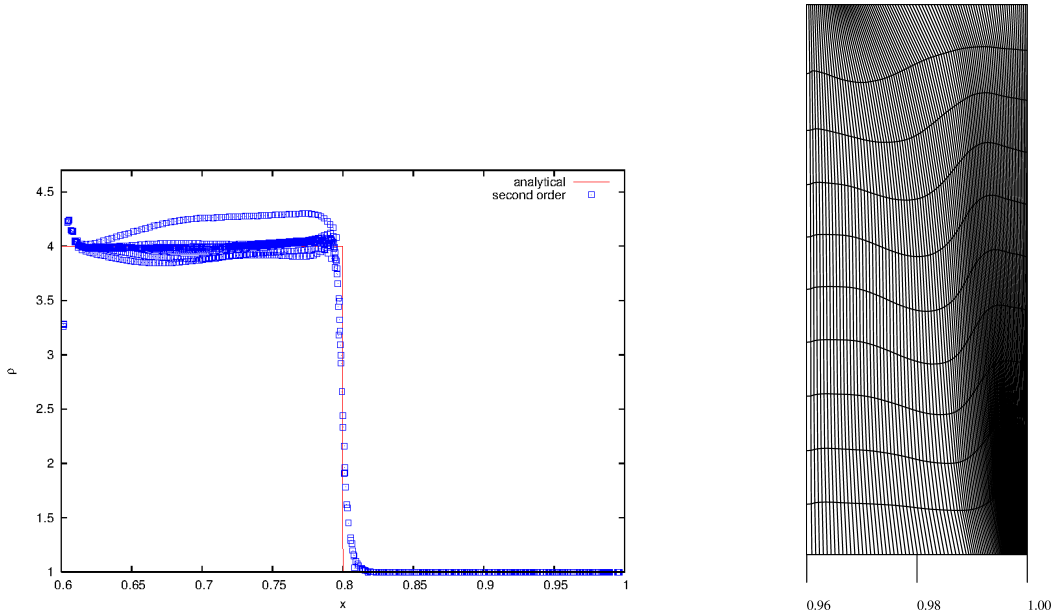

(a) (b)

Figure 1.15: 2D Saltzmann problem - Barth-Jespersen limiter - density profile at $t = 0.6$ (1.15a) and mesh at $t = 0.96$ (1.15b).

The numerical solution obtained at time $t = 0.7$ shows a good accordance with the analytical solution (refer to FIG. 1.16). The density overshoot behind the shock has been reduced with a maximum density of only 4.6 against 5.2 in [118] and 6.2 in [48]. In particular, it is possible to continue the simulation after the shock reaches the wall at time $t = 0.75$. The solution at time $t = 0.9$ is shown in FIG. 1.17. The mesh is still acceptable despite the flattened cells at one corner of the domain. However, these cells prevent to go further in the simulation.

1.6.5 Sedov test case on a cubic grid

The Sedov test case [147] simulates the propagation of a spherical shock wave within the computational domain $(x, y, z) \in [0; 1.2]^3$ filled with diatomic gas such that

$$(\rho^0, P^0, \boldsymbol{U}^0) = (1, 10^{-6}, \mathbf{0}).$$

The shock wave is initialized at the space origin by imposing the pressure $P_o = (\gamma - 1)\varepsilon^0/v^0$ in the cells containing the space origin, where v^0 is the cell volume and $\varepsilon^0 = 0.106384$ is the initial specific internal energy. Symmetry conditions are applied on all boundaries. With this initialization, the diverging spherical shock is characterized by a shock radius $R = 1$ at time $t = 1$ and a maximum density of $\rho^{shock} = 6$ as in [118].

This test case shows the scheme ability to preserve the flow symmetries which is highlighted by the scatter plot of the cell density (refer to FIG. 1.12a, 1.12c, 1.12e). Indeed, one can observe the cell values are close to each other leading to a numerical solution less spread around the analytical solution than in [118]. Moreover, the numerical solution presents a good convergence towards the analytical solution as the mesh is refined.

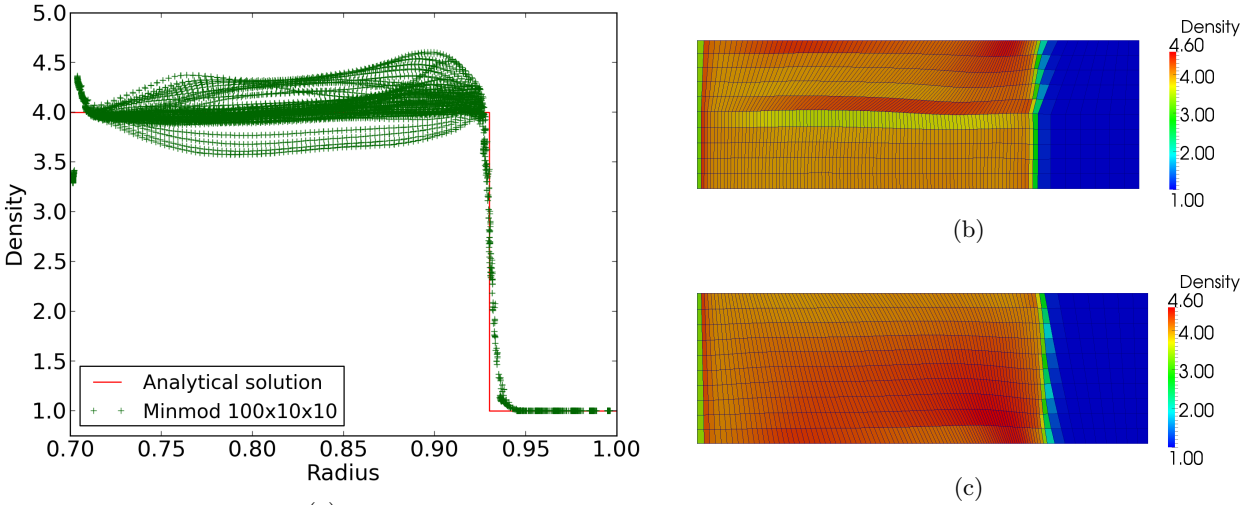

(a) (b) (c)

Figure 1.16: Saltzmann problem - Minmod limiter - Scatter plot of the x-density (1.16a) and 3D density field in the (O,x,y) (1.16b) and the (O,x,z) planes (1.16c) at time $t = 0.7$ on a mesh $100 \times 10 \times 10$.

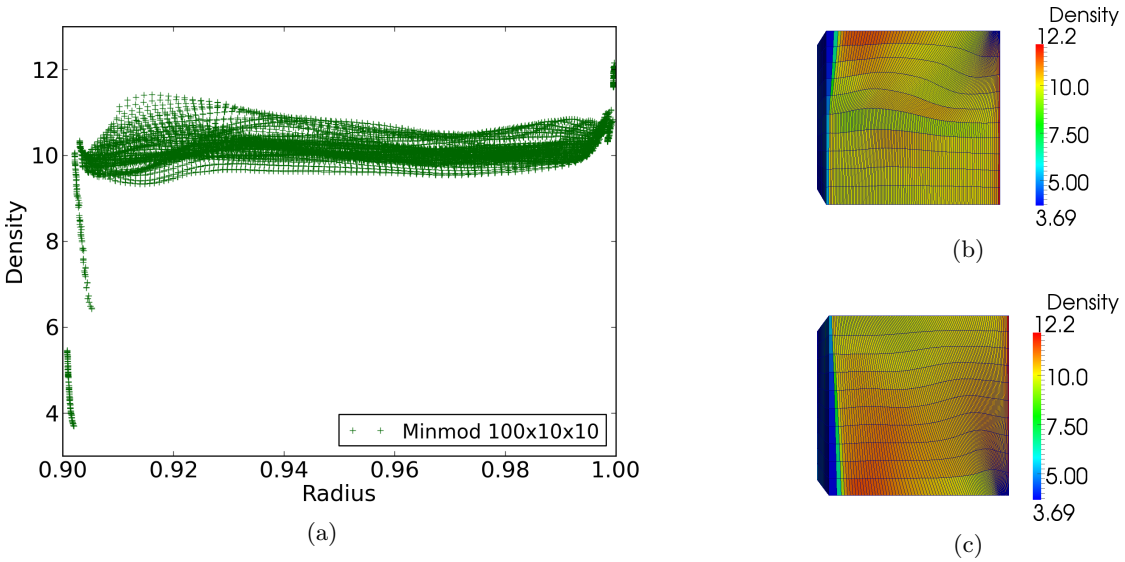

(a) (b) (c)

Figure 1.17: Saltzmann problem - Minmod limiter - Scatter plot of the x-density (1.17a) and 3D density field in the (O,x,y) (1.17b) and the (O,x,z) planes (1.17c) at time $t = 0.9$ on a mesh $100 \times 10 \times 10$.

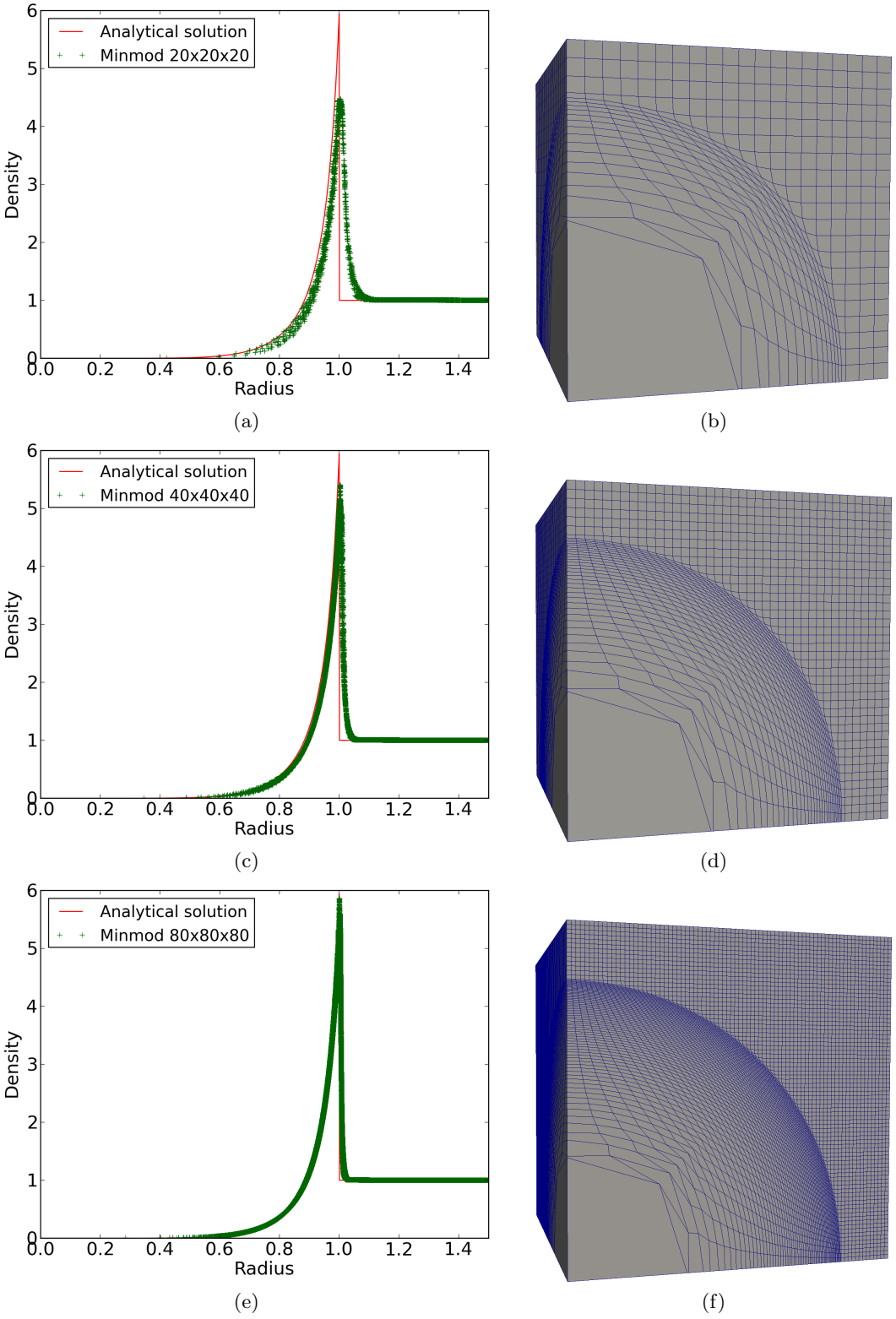

Figure 1.18: Sedov problem - Minmod limiter - Scatter plot of the density in terms of the cell radius (1.12a, 1.12c, 1.12e) and 3D mesh (1.12b, 1.12d, 1.12f) at time $t = 1$ on meshes with $20 \times 20 \times 20$ cells (1.12a, 1.12b), $40 \times 40 \times 40$ cells (1.12c, 1.12d) and $80 \times 80 \times 80$ cells (1.12e, 1.12f).

Chapter 2

Arbitrary-Lagrangian-Eulerian methods for Lagrangian hydrodynamic on unstructured grids

In numerical simulations of multi-material fluid flow, the motion of the fluid can be associated or not to the motion of the grid. One can use a Lagrangian framework or an Eulerian one. The former assumes that the grid moves with the local fluid velocity, the latter deals with a fixed grid. The major advantage of the Lagrangian framework over the Eulerian one is the possibility to track interfaces between different fluid phases. The downside of the Lagrangian framework is that the geometrical quality of the grid elements may degrade significantly. Moreover, the grid can eventually become tangled, causing the simulation to halt. Thus, arbitrary Lagrangian-Eulerian (ALE) methods were introduced in [76] to exploit the advantages of the two previous frameworks, and to optimize accuracy, robustness, and computational efficiency.
In this work, we consider the simulation of multi-material compressible flows on unstructured meshes in planar and cylindrical geometry. For this, we adopt an Arbitrary Lagrangian-Eulerian (ALE) description that has the great advantage to combine the best features of both Eulerian and Lagrangian approaches. Indeed, this choice is not only well adapted to naturally track free surfaces and interfaces between different fluids as purely Lagrangian methods, but also to handle flow distortion as Eulerian methods [15, 22]. Here, a Cell-Centered Arbitrary Lagrangian Eulerian (CCALE) [65, 64] approach is particularly considered.

As depicted on Fig. 2.1, the first step of the algorithm relies on an explicit Lagrangian phase in which the physical variables and grid are updated thanks to the EUCCLHYD scheme described in Chapter 1.
Then, in the context of multi-material computations using ALE method, as grid and fluid move separately, cells containing two or more materials could appear. Multi-material flows treatment is done thanks to specific interface capturing method. This choice allows to track the volume fraction of each material used for the thermodynamical closure relying on the equal strain rates assumption. This approach is quite simple to implement and remains sufficient in most of the cases [65, 148]. This, leads to constant evolution of the volume fraction during the Lagrangian phase. Such an approach allows to reconstruct with accuracy the interface between each material. In this context, many developments have been done for 2D Cartesian geometries. First, a previous version of the CCALE algorithm solving two-material compressible flows using a Volume Of Fluid (VOF) method [165] have been proposed in [32, 65]. To treat interface

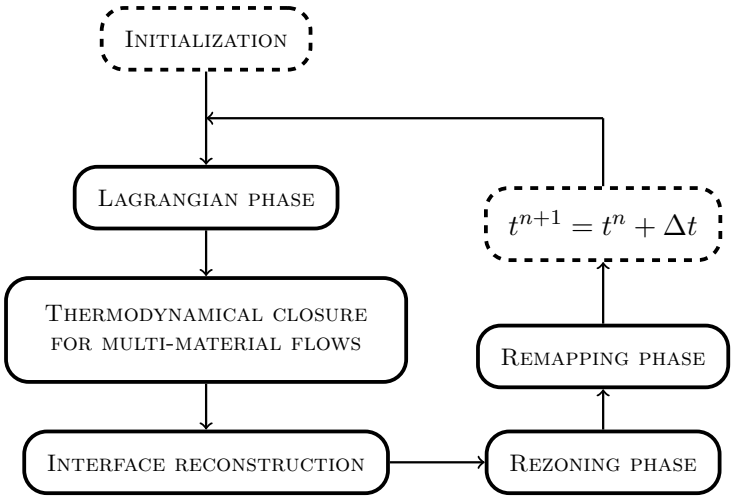

Figure 2.1: Multi-material CCALE-MOF strategy flowchart

flows, Moment Of Fluid (MOF) interface reconstruction method is retained in the sequel. This approach has been considered to enhance multi-material (more than two components) flows as in [5, 61, 64]. Once again, the difficulty here is to propose a natural and consistent adaptation of this approach able to treat axisymmetric and planar interface flows. To this end, formulations of the moments needed to track interface are presented for cylindrical and planar coordinates as in [7]. This leads to an accurate and second order interface reconstruction method that allows to treat multi-material (more than two) interfaces in the lines of [61]. The work introduced here is the result of a fruitful collaboration with M. Shashkov from the Los Alamos National Laboratory (LANL) and it presents the first result coupling of MOF method with ALE and ReALE code to simulate multi-material flows [27, 35].
Subsequently, a rezoning algorithm is used to improve the mesh quality during computation. In standard ALE methods the new mesh from the rezone phase is obtained by moving grid nodes without changing connectivity of the mesh. We are especially interested here in the case of polar meshes. As it is done in [65, 64], mesh rezoning is based on the Condition Number Smoothing (CNS) [90] algorithm on unstructured meshes. Moreover, when used for polar meshes, it is well known that CNS algorithm pushes the nodes toward the origin deteriorating the mesh quality. To avoid this drawback, the main idea developed in this paper is to adapt CNS algorithm to polar grids. Then, extension to unstructured grids (Cartesian-polar) is explored as in [27]. Such rezone strategy has its limitation due to the fixed topology of the mesh especially when strong vorticity appear. An other possible option is called Reconnection Arbitrary Lagrangian Eulerian (ReALE) [103, 102]. This method can be applied to multi-material (more than two) flow problems with material interfaces (immiscible fluids) [35]. In ReALE the main advantage is that the connectivity of the mesh is allowed to change during the rezone phase. As for a standard ALE strategy, the main idea of the rezoning phase is to define a new grid. Here, it is done using specific movement of generators and formalism of Voronoi diagrams [103, 31]. This work has been initiated thanks to a collaboration with M. Shashkov and R. Loubère from CNRS Toulouse. I also had the opportunity to visit M. Owen from the Lawrence Livermore National Laboratory (LLNL) to work on the generation of polygonal grids using the Polytope library developed by LLNL [55].
Finally, the physical variables are conservatively interpolated from the Lagrangian grid onto the new rezoned one during the remapping phase. Here an extension of the hybrid remapping [24] to cylindrical geometries is presented. We want to notice that in ALE framework using cell-centered formulation, this phase is straightforward. In the lines of these works, the CCALE-

MOF algorithm presented here can treat both Cartesian and cylindrical geometry [27]. The main idea is to use an hybrid remapping that combine the main advantages of the swept-face and multi-material cell-intersection remapping as in [24, 65]. The remapping method is also presented for the ReALE method in the case of swept-face and multi-material cell-intersection based method. The last remapping method presented here is a combination of a piecewise quadratic reconstruction and a Flux Corrected Remapping (FCR). This approach provides a bounds preserving method and guarantee the positivity of density and specific internal energy [157].
This chapter, will follow the flowchart presented in Fig. 2.1. First, in Section 2.1 the closure model used to deal with multi-material flow is developed. Then, the MOF method for interface reconstruction method is presented for treating multi-material flows in Section 2.2. In Section 2.3 and 2.4, we introduce two different strategies for the mesh smoothing : rezoning based on mesh regularization and a Voronoi remeshing strategy. Different methods for remapping are given from Section 2.5. Extensive numerical experiments are reported in Section 2.8. They demonstrate not only the robustness and the accuracy of the present methodology but also its ability to handle successfully complex two-dimensional multi-material fluid flows computed on unstructured grids.

2.1 Thermodynamical closure for the multi-material cells

A closure model is required to define how the thermodynamic states of the multi-material cells evolve during the Lagrangian and the Remapping steps. The model we use is based on the reconstruction of the material interface inside a mixed cell, in which, each material evolve separately [65]. The goal here is to compute using the partial quantities the mean pressure and sound speed but also after the Lagrangian step, using mean quantities to update the partial internal energy. Let ϕ_k be the volume fraction defined for the fluid k in the cell c by:

$$\phi_k = \frac{V_k}{V}, \qquad 0 < \phi_k < 1.$$

where V_k is the volume of the cell's part occupied by the fluid k and V the volume of the cell, such that

$$V = \sum_k V_k,$$

and let m_k be the mass of the fluid k and m the mass of a cell c, such that

$$\frac{dm_k}{dt} = 0, \quad \text{and} \quad m = \sum_k m_k.$$

The previous requirements on volume and Mass leads to

$$\sum_k \phi_k = 1, \quad \text{and} \quad \sum_k \phi_k \rho_k = \rho.$$

Where ρ_k and ρ are respectively the partial and mean density. Furthermore, a common velocity field $\boldsymbol{U}$ is used to characterize each material in the mixed cell such that the geometric conservation law equation of each material can be wrote as:

$$\frac{d(\phi_k \rho_k)}{dt} = \phi_k \rho_k \nabla \cdot \boldsymbol{U}. \tag{2.1}$$

The volume fraction evolution is based on an equal strain assumption:

$$\frac{1}{\rho_k}\frac{d\rho_k}{dt} = \frac{1}{\rho}\frac{d\rho}{dt} = -\nabla \cdot \boldsymbol{U}. \tag{2.2}$$

Thus, using Eqs. (2.1) and (2.2), the evolution of volume fraction is modeled by

$$\frac{d\phi_k}{dt} = 0. \tag{2.3}$$

Thermodynamic assumptions are necessary to link effective and partial values of pressure and speed sound. Gibbs relation applied for each material can be written as:

$$m_k\left(\frac{d\varepsilon_k}{dt} - T_k\frac{dS_k}{dt}\right) = -P_k V_k \rho_k \frac{d}{dt}(\frac{1}{\rho_k}).$$

Where P_k, T_k and s_k denote the pressure, temperature and the specific entropy for material k. By summing on all materials, and using equal-strain assumption Eq. (2.1), it leads to

$$m\left(\frac{d\varepsilon}{dt} - T\frac{dS}{dt}\right) = -\sum_k P_k V_k \rho \frac{d}{dt}(\frac{1}{\rho}).$$

Finally, comparing with the Gibbs relation applied to the mean fluid, for pressure we obtain

$$P = \sum_k \phi_k P_k. \tag{2.4}$$

Concerning the sound speed, its definition allows to write:

$$\frac{dP_k}{dt} = c_k^2\frac{d\rho_k}{dt}.$$

Multiplying by ϕ_k, summing on all materials, and using equal strain assumption Eq. (2.1), leads to

$$\frac{dP}{dt} = \sum_k c_k^2 \phi_k \frac{\rho_k}{\rho}\frac{d\rho}{dt}.$$

Finally, comparing with the previous sound speed definition applied to the mean fluid, we obtain

$$c^2 = \sum_k \frac{m_k}{m} c_k^2. \tag{2.5}$$

Contrary to a staggered discretization, in our cell-centered scheme, total energy conservation equation is computed in place of internal energy. It means that, because the pressure is a function of internal energy ($P_k^{n+1} = f(\rho_k^{n+1}, \varepsilon_k^{n+1})$), this quantity must be updated to close the thermodynamic state of each material. This is done, assuming the massic distribution of entropy variation:

$$m_k\frac{d\varepsilon_k}{dt} + P_k\frac{dV_k}{dt} = \phi_k\left(m\frac{d\varepsilon}{dt} + P\frac{dV}{dt}\right). \tag{2.6}$$

2.2 Moment of fluid method for interface reconstruction

The method used in this work to reconstruct interfaces, is the MOF approach well adapted for treating multi-material interface problems [5, 61]. Indeed, such a method enables to capture more accurately interfaces than the classical VOF strategy and allows the treatment of general multi-material flows (more than two materials) [64, 93]. This method has been recently extended in cylindrical geometries, for a single interface problem [7]. We start this section with the planar version of the MOF method and then present the MOF method for cylindrical geometry.

2.2.1 MOF for planar geometry

The main idea of MOF is to track each fluid using its volume fraction and centroid deduced from the zeroth and first moments [61]. Given these two moments, interface is linearly reconstructed insuring volume conservation. To this end, interface update is done minimizing the discrepancy between the given moments and the reconstructed moments of the polygon behind the interface. One should note that no information from neighboring cells is required. This method is exact for linear interfaces and is second order accurate for smoothly curved ones. In the context of multi-material configurations, one has to face to material ordering when reconstructing interface. The method presented here, allows to automatically determine the order of materials by constructing all the possible combination and choosing the sequence that leads to the configuration where the reconstructed moments are the closest to the given ones.

Under volume conservation assumption, the zeroth moment $M^0_{k,c}$ of the k-th fluid in each cell c is given by:

$$M^0_{k,c} = \int_{\Omega_{k,c}} dV, \tag{2.7}$$

from this moment we can deduce the volume fraction which depends on the cell volume V_c

$$\alpha_{k,c} = \frac{M^0_{k,c}}{V_c}, \tag{2.8}$$

The first moment can be defined with:

$$M^1_{k,c} = \int_{\Omega_{k,c}} \mathbf{X} dV, \tag{2.9}$$

From this, we deduce the centroid

$$\mathbf{X}_{k,c} = \frac{M^1_{k,c}}{V_{k,c}}, \text{ with } V_{k,c} = V_c \alpha_{k,c}. \tag{2.10}$$

In the context of multi-material configurations, one has to face to material ordering when reconstructing interface. The method used here, allows to automatically determine the order of materials by constructing all the possible combination and choosing the sequence that leads to the configuration where the reconstructed moments are the closest to the given ones. The two input data (volume fraction and centroid) are supplied by the Lagrangian phase and leads to the definition of the new centroid position which is obtain from a barycentric combination of new positions of grid nodes as done in [64].

2.2.2 Numerical validation

To illustrate multi-material reconstruction, we consider three different cell layouts that are filament (without junction), T-junction and Y-junction on a regular octagon. We can see on Fig. 2.2 that the results reveal the capability of MOF to treat accurately multi-material problem on polygonal cells. More details about implementation considerations can be found in [5, 61].

2.2.3 MOF in axisymmetric geometry

Here, extension to multi-material interface reconstruction phase to cylindrical coordinates is considered.

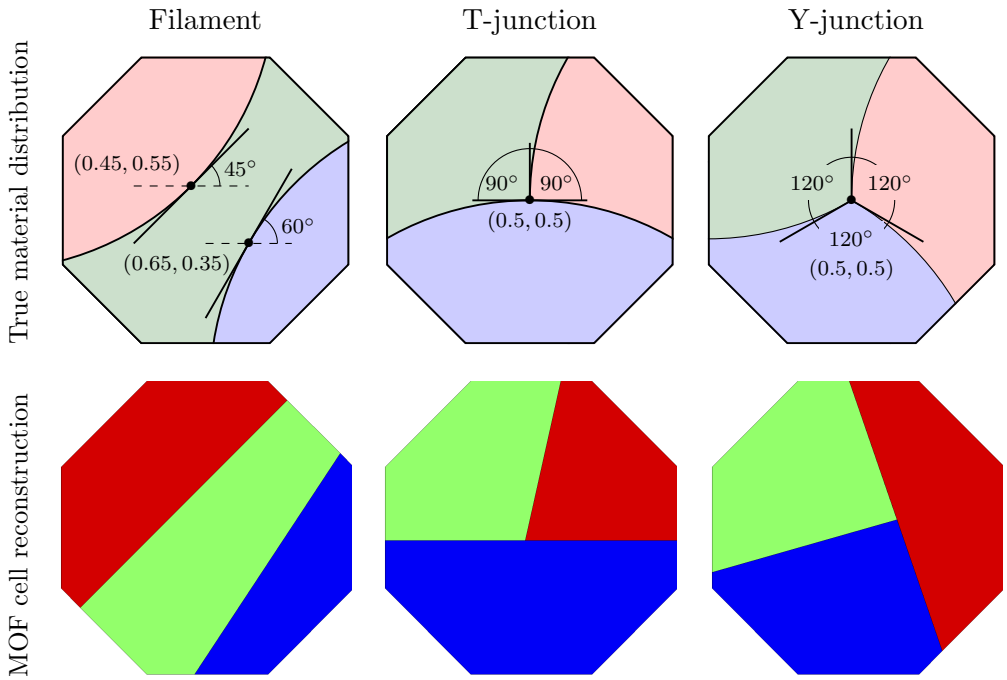

Figure 2.2: MOF interface reconstruction test for three materials. From the top to bottom: true partitions and their MOF reconstructions. From the left to the right: filament, T-junction and Y-junction configurations.

The main difference between cylindrical and planar geometry relies in the definition of the different moments. Since the interface reconstruction is done under volume conservative assumption, the zeroth moment $M^0_{k,c}$ of the k-th fluid in each cell c is obviously given by

$$M^0_{k,c} = \int_{\Omega_{k,c}} \mathcal{R} dA, \tag{2.11}$$

from this moment we can deduce the volume fraction

$$\alpha_{k,c} = \frac{M^0_{k,c}}{V_c}, \tag{2.12}$$

with the cell volume $V_c = \int_{\Omega_c} \mathcal{R} dA$.
Contrary to the zeroth moment, the first moment can be defined without any specific requirement. Thus, it is possible to compute them in the two following different manners. In the one hand we can use the natural extension to axisymmetric geometries

$$M^1_{k,c} = \int_{\Omega_{k,c}} \mathcal{R}\mathbf{X} dA, \tag{2.13}$$

and from this moment we deduce the pseudo-centroid

$$\mathbf{X}_{k,c} = \frac{M^1_{k,c}}{V_{k,c}}, \text{ with } V_{k,c} = V_c \alpha_{k,c}. \tag{2.14}$$

This pseudo-centroid for a matter of simplicity will be called here the axisymmetric centroid. On the other hand it can also be done with a planar definition as follows

$$M^{1,pl}_{k,c} = \int_{\Omega_{k,c}} \mathbf{X} dA, \tag{2.15}$$

and thus planar centroid will be obtain from

$$\mathbf{X}_{k,c}^{pl} = \frac{M_{k,c}^{1,pl}}{A_{k,c}}, \tag{2.16}$$

where $A_{k,c}$ is the area of the k-th fluid in the cell c.
Since this interface reconstruction method is coupled to our Lagrangian hydrodynamics scheme it requires to update the volume fraction and material centroid. Using the equal strain assumption, the volume fraction do not evolve during the Lagrangian step (see [65] for more details). As for planar geometry, the centroid locations are given from the Lagrangian step using a barycentric combination of the new positions of the mesh nodes as done in [64].

2.2.4 Numerical validation

The main goal of this section is to compare, like in Section2.2.2 the results given by both axisymmetric and planar formulations of the centroid on several static test cases in one cell. As in [61], we consider three different mixed-cell layouts that are filament (without junction), T-junction and Y-junction. The first two configurations correspond to $\mathcal{C}^2$-serial partitions whereas the third is not. In the considered test cases, the parameter χ corresponds to the radius of the circles defining the interfaces. Two values are considered with $\chi = 1$ and $\chi = 64$. In addition, the computation domain is reduce to the cell $[0;1] \times [0;1]$ (see FIG. 2.3 and FIG. 2.4).

In the first case, with $\chi = 1$, we notice small differences for the filament case, no notable difference on the T-Junction but the Y-junction results for axisymmetric and planar formulations present distinct interface positions due to a different ordering of the materials. For a large radius $\chi = 64$, the curves are reduced to piecewise linear interfaces. Then, the result using both formulations are very close to each other. For the two first cases filament and T-junction, the results are exact. Regarding the Y-junction, it remains a good approximation. These results illustrate the capability of both planar and axisymmetric centroid formulation for MOF to treat accurately multi-material problem. Nevertheless, for consistency with the global cylindrical coordinate formulation, the axisymmetric formulation for the centroid is retained in the sequel.

2.3 Rezoning phase improvement for polar meshes

The rezoning phase introduced in [65, 64] consists in moving the Lagrangian grid to improve its geometric quality. The objective of this part is to extend this approach to polar meshes. To this end, the proposed procedure relies on two main steps. The first phase is dedicated to compute the smoothed grid from the Lagrangian one through CNS method. Then the final mesh is deduced from the smoothed one by a relaxation procedure to keep the rezoned grid as close as possible to the Lagrangian grid in order to insure computation accuracy and avoid unphysical mesh rezoning. In the sequel one should note that rezoning is formulated only for planar geometry in the frame $\{0, X, Y\}$.

For the sake of readability, in the rest of the paper the quantities without any accent ϕ are associated to Lagrangian mesh. After the rezoning step we use ϕ^{rez}, and finally after relaxation the quantities related to the rezoned mesh are noted with the tilde accent $\tilde{\phi}$.

2.3.1 General condition number smoothing (GCNS)

As it is pointed out in the introduction, CNS approach is well adapted to rezone Cartesian meshes but it still suffers from drawbacks for polar ones. Indeed, in this case the mesh seems

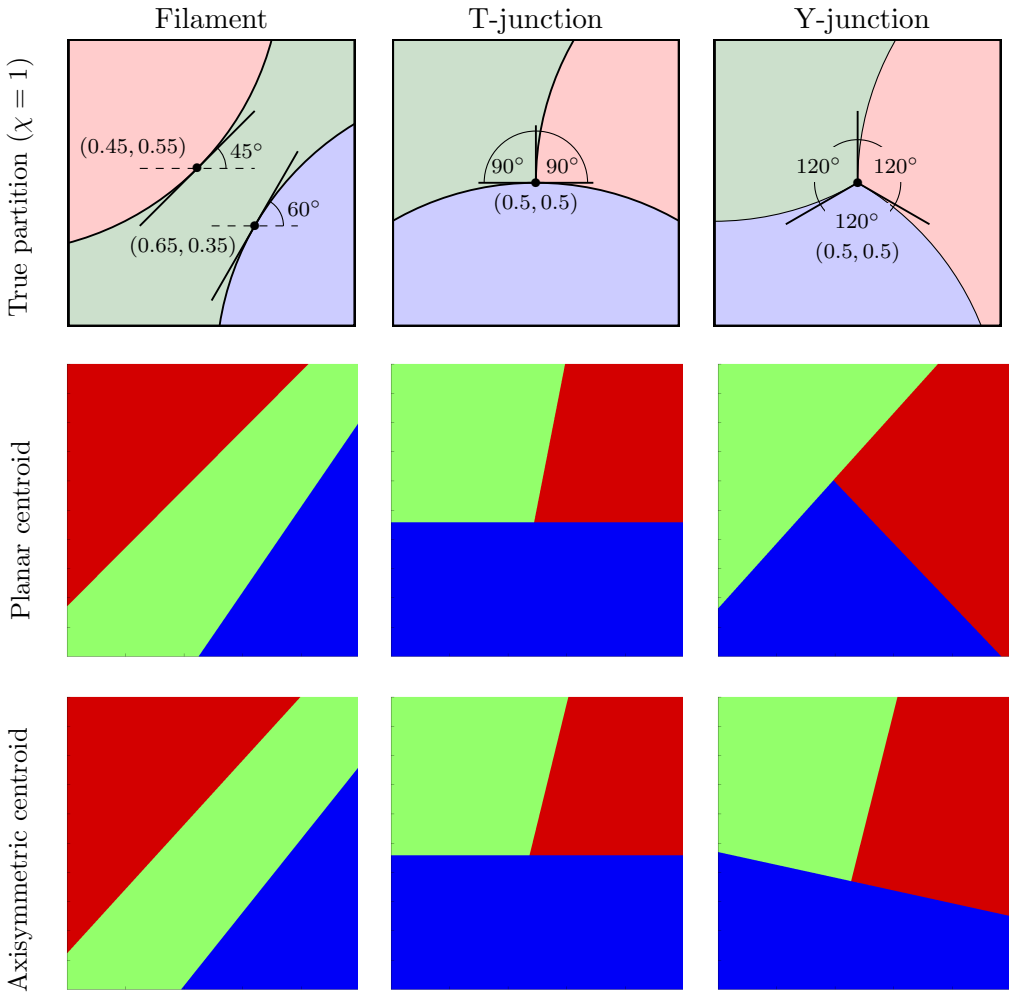

Figure 2.3: MOF interface reconstruction test for three materials. From the top to the bottom: the true partitions for $\chi = 1$ and their MOF reconstructions obtained with planar and axisymmetric centroid. From the left to the right: filament, T-junction and Y-junction configurations.

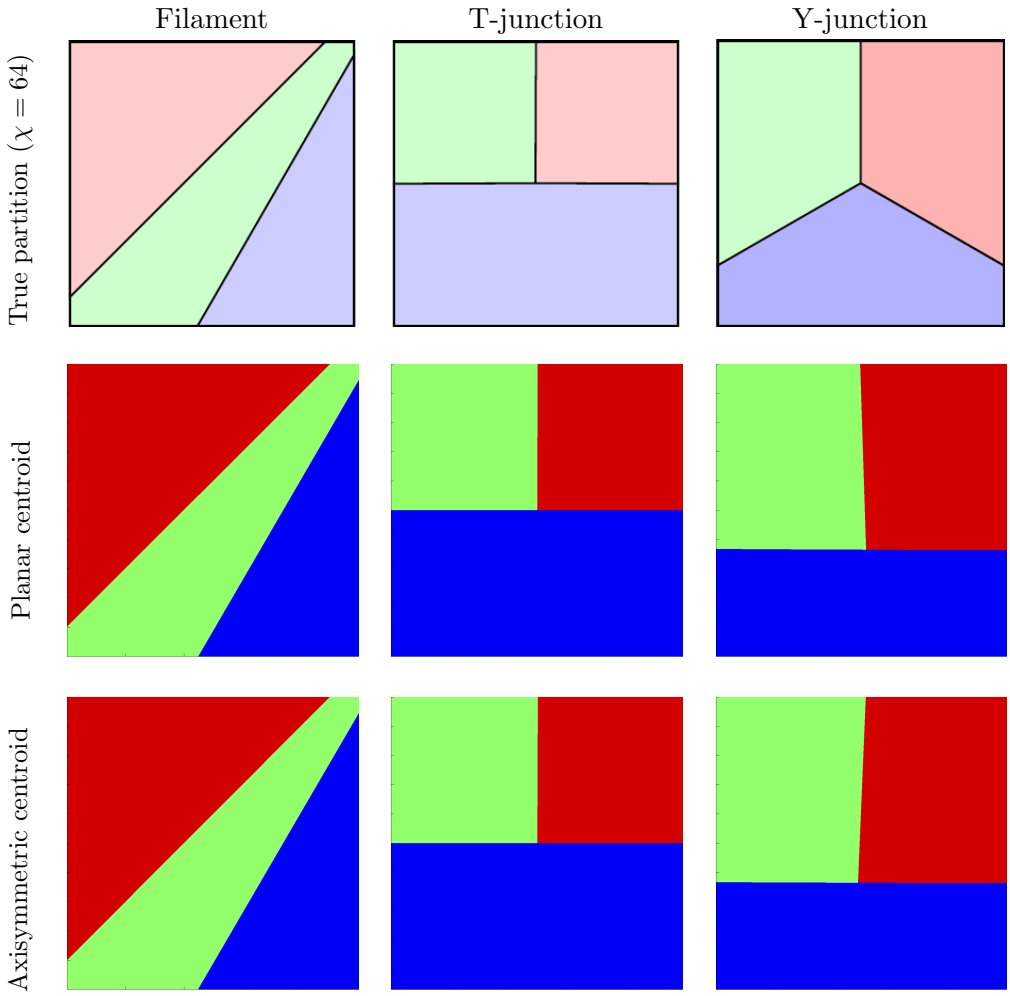

Figure 2.4: MOF interface reconstruction test for three materials. From the top to the bottom: the true partitions for $\chi = 64$ and their MOF reconstructions obtained with planar and axisymmetric centroid. From the left to the right: filament, T-junction and Y-junction configurations.

to collapse (like an implosion) to the origin. To circumvent this difficulty, it has been proposed to modify the CNS algorithm using specific weight associated to the mesh geometry [156] that controls mesh rezoning with regards to the radius for example. Nevertheless, this approach is not completely satisfactory. First, it strongly depends on the choice of the weight, that may affect the quality of the mesh which can be shifted in the opposite direction to the origin for example. Furthermore, there is still a residual compression near the origin due to singularity at this point. In conclusion, it does not preserve a uniform polar mesh. For this reason, a different strategy is presented here. The main idea developed here is to apply the CNS rezoning algorithm in (r, θ)-coordinate system to polar block. In fact, a polar block mesh initially expressed using a Cartesian coordinates (X, Y) leads to a structured Cartesian mesh in (r, θ)-coordinates. Here, a general presentation of the algorithm is made for a classical type of unstructured meshes that are made of different blocks which can be either Cartesian or polar.

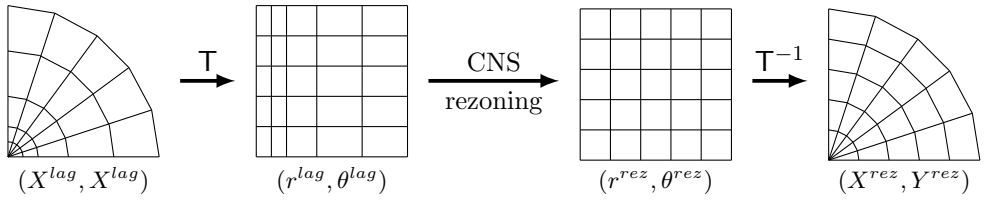

Figure 2.5: Rule representation for GCNS algorithm for a polar mesh.

Assuming that the resulting mesh from the Lagrangian phase is unfolded (otherwise untangling procedure is used to correct invalid cells [154]) . Thus, the proposed algorithm consists for polar meshes in three different steps as depicted on FIG. 2.5. For the sake of simplicity, we consider in the sequel only the case of Cartesian and polar structured meshes.

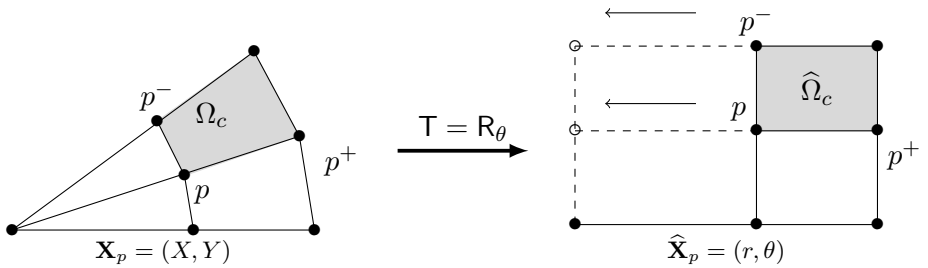

Figure 2.6: Notations and mapping between cartesian and polar coordinates.

The first step, is dedicated to the mapping between Cartesian and polar coordinates. To this end, consider c a given cell of the Lagrangian grid for (X, Y)-coordinates, $p \in \mathcal{P}(c)$ a node of this cell. Notation used in the sequel are depicted on FIG. 2.6. The mapping between a point $p \in c$ of Cartesian coordinates $\mathbf{X}_p = (X, Y)^t$ to $\widehat{\mathbf{X}}_p = (r_p, \theta_p)^t$ in polar ones is done using the definition $\theta_p = \arctan\left(\dfrac{Y_p}{X_p}\right)$ and $r_p = \sqrt{X_p^2 + Y_p^2}$. When mapping (X, Y) to (r, θ), the origin node has to be specifically treated. Indeed the transformation is not defined for this point. Then as it is needed in the rezoning algorithm in the (r, θ) frame, the origin node is defined by a mapping of the first row on $r = 0$ axis (see FIG. 2.6). Note that these nodes are not used for the final backward mapping.
The second step is the GCNS algorithm. It is based on a minimization problem of a local functional that controls the quality of the mesh. As done in [65, 64], one has to distinguish

boundary nodes and internal node for which the smoothing procedure is different.
For internal nodes, let us introduce as in [90] the condition number for (r, θ)-coordinates that writes

$$\kappa(\widehat{\mathsf{J}}_{cp}) = \frac{||\widehat{\mathbf{X}}_{pp^+}||^2 + ||\widehat{\mathbf{X}}_{pp^-}||^2}{\widehat{A}_{cp}}, \tag{2.17}$$

where $\widehat{\mathbf{X}}_{pp^\pm} = \widehat{\mathbf{X}}_p - \widehat{\mathbf{X}}_{p^\pm}$, and $\widehat{A}_{cp} = \det(\widehat{\mathsf{J}}_{cp})$ is the area of the triangle delimited by $\{p, p^+, p^-\}$ in the rezoned grid and $\widehat{\mathsf{J}}_{cp} = [\widehat{\mathbf{X}}_{pp^+}, -\widehat{\mathbf{X}}_{pp^-}]$ the 2×2 Jacobian matrix associated to each corner at vertex p of cell c. Thanks to this condition number we define the local function associated to the node p

$$F_p(\widehat{\mathbf{X}}_p) = \sum_{c\in\mathcal{C}(p)} \kappa(\widehat{\mathsf{J}}_{cp}), \tag{2.18}$$

Finally, the new position $\widehat{\mathbf{X}}_p^{rez}$ is obtained by the minimization of the local function F_p using the first step of a Newton algorithm. This leads to the formula

$$\widehat{\mathbf{X}}_p^{rez} = \widehat{\mathbf{X}}_p - \mathsf{H}_{cp}^{-1}(\widehat{\mathbf{X}}_p)\nabla F_p(\widehat{\mathbf{X}}_p), \tag{2.19}$$

where H_{cp}^{-1} and ∇F_p are respectively the Cartesian 2×2 Hessian matrix and gradient related to the local functional F_p.
For boundary nodes, the rezoned position $\widehat{\mathbf{X}}_p^{rez}$ of p is computed in consistent way with the GCNS algorithm. To this end, $\widehat{\mathbf{X}}_p^{rez}$ is given thanks to a second-order interpolation Bézier curve [65] leading to

$$\widehat{\mathbf{X}}_p^{rez} = \widehat{\mathcal{X}}_p(s^{rez}) = (1-(s^{rez})^2)\widehat{\mathbf{X}}_{p^-} + 2(1-s^{rez})s^{rez}\widehat{\mathbf{X}}_i + (s^{rez})^2\widehat{\mathbf{X}}_{p^+}, \tag{2.20}$$

where $s^{rez} \in [0,1]$ and $\widehat{\mathbf{X}}_i$ such that $\widehat{\mathcal{X}}_p(1/2) = \widehat{\mathbf{X}}_p$. Furthermore, the parameter s^{rez} is computed to minimize $F_p(\widehat{\mathcal{X}}_p(s))$ (for more details on this procedure see [65]).

Finally, the third step consists in backward mapping between $\widehat{\mathbf{X}}_p^{rez}$ and $\mathbf{X}_p^{rez}$ using $X_p = r_p cos(\theta_p)$ and $Y_p = r_p sin(\theta_p)$.

2.3.2 Relaxation algorithm

The relaxation algorithm consists in making a convex combination between rezoned grid obtained from GCNS step and its location after Lagrangian step. This reads for each mesh node p by:

$$\widetilde{\mathbf{X}}_p = \mathbf{X}_p + \omega_p(\mathbf{X}_p^{rez} - \mathbf{X}_p), \text{ with } \omega_p \in [0,1],$$

where $\widetilde{\mathbf{X}}_p$ is the new mesh node position after the complete rezoning phase. The coefficient ω_p is computed as a function of the right Cauchy-Green tensor associated to the Lagrange grid deformation over a time step (for details see [65, 103]).

2.3.3 Numerical validation

In this section, we compare results obtained by the GCNS algorithm to those obtained for classical CNS for the rezoning of uniform polar and unstructured meshes.

Uniform mesh First, we consider an uniform polar mesh made of 20×10 elements see FIG. 2.7-(a). Results obtained after 100 iterations for the classical and general smoothing are presented on FIG. 2.7. For each method the relaxation coefficient ω_p is taken equal to 1. As already mentioned, the classical smoothing does not converge on polar mesh and implies the collapse of cell layers to the origins (see FIG. 2.7-(b)). However, for the GCNS, the result obtained (see FIG. 2.7-(c)) is converged. The mesh initially uniform, is not modified at the end of the computation. This clearly illustrates the good behavior of our smoothing algorithm.

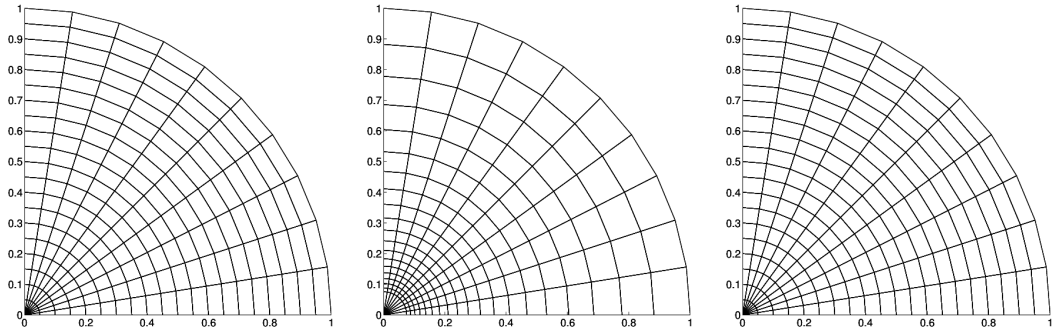

(a) (b) (c)

Figure 2.7: Smoothing of a static polar grid 16×10: (a) initial grid; Smoothed grids after 100 iterations: (b) CNS, (c) GCNS.

Unstructured mesh Now, rezoning for an unstructured mesh is studied. Let us consider a mesh made of 175 quadrangular cells as depicted on FIG. 2.8-(a). When applying the full Cartesian rezoning to the mesh, similar observations as previously can be made. It suffers from an implosion of central cells to the origin and does not converge (see FIG.2.8-(b)). For the full GCNS algorithm, one can see after convergence, the formation of mesh distortion on the square region and a polar mesh far from the center (see FIG.2.8-(c)). Nevertheless, it is possible

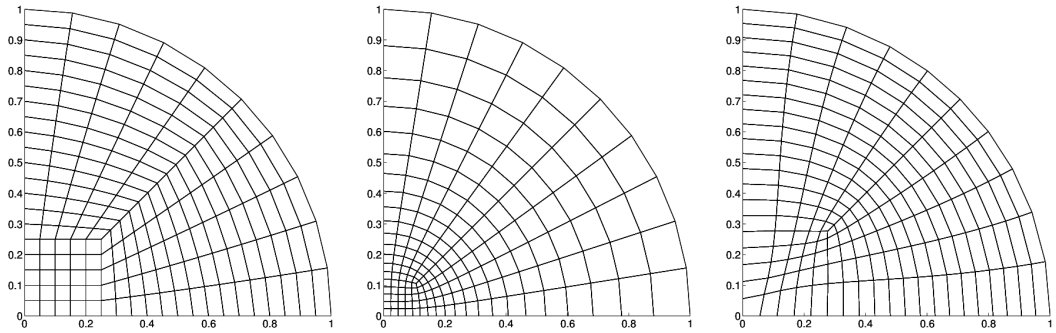

(a) (b) (c)

Figure 2.8: Smoothing of a static unstructured grid: (a) initial grid; Smoothed grids after 100 iterations: (b) CNS, (c) GCNS.

to improve this rezoning. Thus, the main idea developed in the sequel is to apply the GCNS rezoning algorithm differently for a node belonging initially to a Cartesian or polar region of the mesh. These regions are represented thanks to red and blue color (see FIG. 2.9-(a)) for the considered mesh. Nodes localized at the frontier between the polar and Cartesian meshes (black nodes on FIG. 2.9-(a)) can be considered either polar, or Cartesian. As represented on

FIG. 2.9-(b,c), both possibilities are tested. The obtained results illustrate that the Cartesian choice remains better contrary to the polar one that introduce mesh distortion.

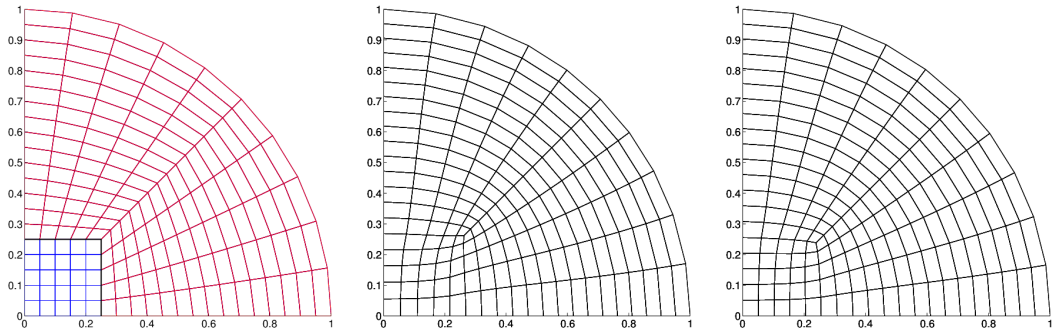

(a) (b) (c)

Figure 2.9: Smoothing of a static unstructured grid: (a) initial grid with Cartesian (blue) and polar (red) rezoning regions; Smoothed grids after 100 iterations (b) GCNS with interfacial polar rezoning, (c) GCNS with interfacial Cartesian rezoning.

2.4 Rezoning phase with reconnection

We consider now the simulation of multi-material compressible flows on unstructured meshes. The ReALE strategy used is an adaption of the ALE description. ReALE differs from ALE as connectivity between cells of the mesh can change during the reconnection phase in order to create a polygonal mesh which is able to follow material evolution efficiently.

2.4.1 Reconnection algorithm

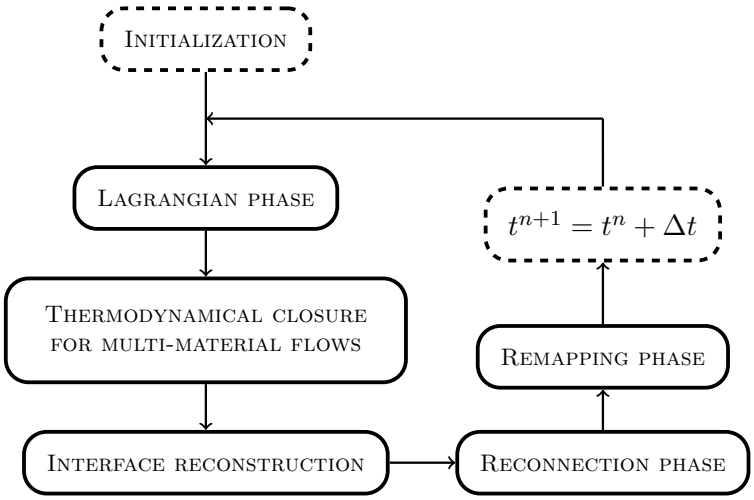

Figure 2.10: Multi-material ReALE strategy flowchart

The ReALE-MOF strategy, described in the flowchart on FIG. 2.10, is used to relax the constraints on mesh topology and allow change in connection between cells.
In this work, we keep the number of cells unchanged, but the number of vertices of each cell can change due to the connectivity evolution. The reconnection phase of ReALE includes both mesh

movement and reconnection procedure using a Voronoi tessellation based on a set of discrete mesh-generating points also called generators $\mathbf{G}_c$ (Fig. 2.11).
The rezoning step of classical ALE method correspond to the reconnection step of ReALE. Rezoning is usually based on geometric consideration and the aim of this step is to improve the quality of the mesh. In ALE the main drawback is due to the fixed topology whereas in ReALE method we allow change in the topology. This leads for ReALE to a polygonal mesh which follow more efficiently the flow and recover the Lagrangian features which is lost using ALE with fixed topology. The reconnection capability allows to deal with complex geometries and high vorticity problems contrary to ALE method. Here, the number of cells remains constant whereas number of vertices of each cell can be modified during the computation. A complete description of ReALE method is available in [103].

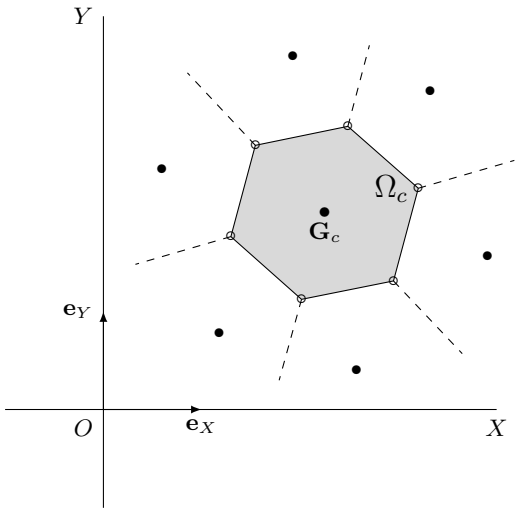

Figure 2.11: Voronoi Tesselation configuration

2.4.2 Generator displacement

In order to obtain regular polygons like with the Lloyd's algorithm, we move the generators thanks to centroids motion. An example of Lloyd's smoothing is presented in Fig. 2.12.

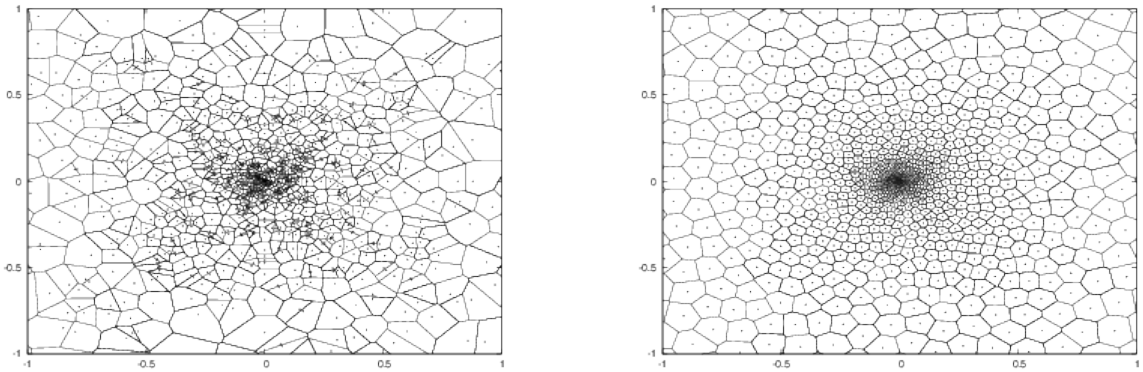

(a) Mesh before Lloyd's smoothing

(b) Mesh after Lloyd's smoothing

Figure 2.12: Mesh smoothing using Lloyd's algorithm

In the method [103] we use a convex combination between the Lagrangian displacement and motion of centroids.

$$\mathbf{G}_c^{n+1} = \mathbf{G}_c^{n+1,lag} + \omega_c(\mathbf{X}_c^{n+1} - \mathbf{G}_c^{n+1,lag}),$$

where $\mathbf{X}_c = \frac{1}{V_c}\int_c X dX$ denotes the centroid of the cell c, $\omega_c \in [0,1]$ is constructed using invariants of the right Cauchy Green strain tensor associated to the Lagrangian cell c between times t_n ant t_{n+1}. For this work, we still use also the Lagrangian displacement :

$$\mathbf{G}_c^{n+1,lag} - \mathbf{G}_c^n = \alpha_c^{lag}\mathbf{N}_c^{lag},$$

where $\mathbf{N}_c^{lag}$ is the unit vector in the direction of $(\mathbf{G}_c^{n+1,lag} - \mathbf{G}_c^n)$ and α_c^{lag} is the norm of this vector. We define $\mathbf{T}_c^{lag}$ as the perpendicular at the displacement.

We use the motion of centroids like Lloyd's algorithm to regularize the polygons

$$(\mathbf{X}_c^{n+1} - \mathbf{G}_c^n) = \alpha^{reg}\mathbf{N}_c^{reg},$$

where $\mathbf{N}_c^{reg}$ is the unit vector and α^{reg} is the norm of ($\mathbf{X}_c^{n+1} - \mathbf{G}_c^n$). In order to have the same order of magnitude as in the Lagrangian displacement, we limit this regularization by $\alpha^{limit} = min(\alpha^{lag}, \alpha^{reg})$. This limitation avoid the too large change into the mesh that caused the loss the Lagrangian features.

To preserve the Lagrangian displacement, we allow only a tangential regularization :

$$\alpha^{proj} = (\mathbf{X}_c^{n+1} - \mathbf{G}_c^n).\mathbf{T}_c^{lag}.$$

We obtain the new displacement for the generators thanks to

$$\mathbf{G}_c^{n+1} = \mathbf{G}_c^n + \alpha_c^{lag}\mathbf{N}_c^{lag} + \alpha^{proj}\mathbf{T}_c^{lag}.$$

This method presented in [31] leads to a regular polygonal mesh and allows to keep Lagrangian features better than for the convex combination methods used in [103].

2.5 Hybrid remapping

During the remapping phase, the physical unknowns (density, velocity, total energy) computed thanks to the Lagrangian step are conservatively remapped from the Lagrangian mesh to the rezoned one. To this end, an extension of the *Hybrid Remapping Algorithm* for multi-material flows [64, 92, 24] to cylindrical geometry is presented here as in [27]. This strategy consists in the following two steps. First a *swept-faced remapping* is used to treat cells and nodes localized far from the interface. Then, a *cell-intersection-based* method [65] is applied to the cells and nodes in the neighborhood of the interface. In this way, this approach combines the ability of the cell-intersection method to remap the interface and the efficiency of the swept flux approach for the other cells that significantly reduce the global computing cost of the method. As done previously, in the perspective of general use of the method, a global formulation including both Cartesian and axisymmetric framework is presented.

We assume in the sequel, that there is no topology change of the mesh, the cells of the Lagrangian and rezoned grids are respectively designed by Ω_c and $\widetilde{\Omega}_c$.

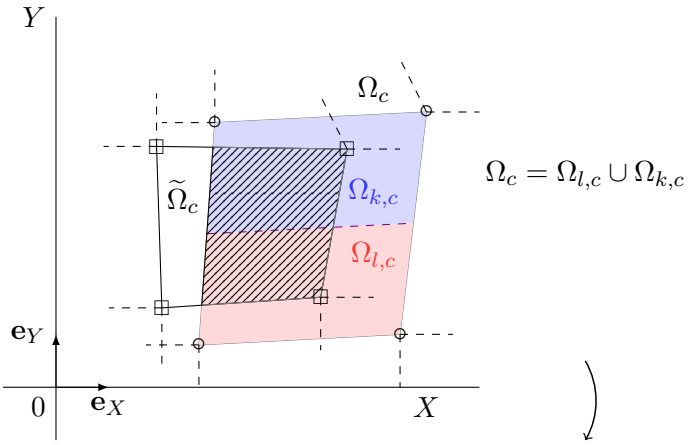

Figure 2.13: Notations for MCIB method.

2.5.1 Multi-material cell-intersection-based (MCIB) remapping

The main goal of remapping is to compute the exact intersection between the Lagrangian grid and the rezoned one in order to remap the Lagrangian physical quantities onto the rezoned mesh as shown in Fig. 2.13. Given the piecewise constant representation of the physical variables per unit of volume $(\rho, \rho\mathbf{U}, \rho E)$ noted $\psi_c = \rho_c \phi_c$ in each cell of the Lagrangian grid, we want to compute its equivalent $\widetilde{\psi}_c$ in each cell of the rezoned grid given as

$$\widetilde{\psi}_c = \frac{1}{\widetilde{V}_c} \int_{\widetilde{\Omega}_c} \widetilde{\rho\phi} \mathcal{R} dA, \tag{2.21}$$

with $\widetilde{V}_c$ the volume of the cell $\widetilde{\Omega}_c$. Contrary to single fluid approach, here the rezoned values $\widetilde{\psi}_c$ cannot be computed directly in each cell c. In fact, one has to take into account multi-material aspects.

First of all, let us introduce some notations. Each material of the flow noted k occupies the polygon $\Omega_{k,c} \subset \Omega_c$, within the MOF framework, such that $\Omega_c = \bigcup_k \Omega_{k,c}$ and is characterized by its partial mass, density, pressure, internal energy and variables per unit of volume (total energy, momentum) whose averaged values in each sub-cell are respectively $m_{k,c}, \rho_{k,c}, P_{k,c}, \varepsilon_{k,c}$ and $\psi_{k,c} = \rho_{k,c}\phi_{k,c}$ with $\phi_{k,c}$ the partial velocity or energy per unit of mass.

Thus, for multi-material flow, the main idea of remapping is not to directly compute the global rezoned quantities $\widetilde{\psi}_c$ but the partial rezoned ones noted $\widetilde{\psi}_{k,c}$. This is particularly true for the MCIB method that is dedicated to treat cell in the interface neighborhood. To this end, we first propose a second order reconstruction $\Psi_{k,c}(\mathbf{X})$ of $\psi_{k,c}$ over each Lagrangian cell c through the piecewise linear function

$$\Psi_{k,c}(\mathbf{X}) = \psi_{k,c} + (\nabla \Psi_k)_c (\mathbf{X} - \mathbf{X}_{k,c}), \tag{2.22}$$

where $(\nabla \Psi_k)_c$ denotes the constant gradient of $\Psi_{k,c}$ within cell c computed thanks to a least-squares approach. A Barth-Jespersen limiter is used to ensure monotonicity [17]. Finally $\mathbf{X}_{k,c}$ is the centroid related to the k-th fluid in the cell c given by

$$\mathbf{X}_{k,c} = \frac{1}{V_{k,c}} \int_{\Omega_{k,c}} \mathcal{R}\mathbf{X} dA. \tag{2.23}$$

Thanks to these notations, the remapped value for MCIB is given by

$$\widetilde{\psi}_{k,c} = \frac{1}{\widetilde{V}_{k,c}} \sum_{d \in \mathcal{C}(c)} \int_{\Omega_{k,d} \cap \widetilde{\Omega}_c} \mathcal{R}\Psi_{k,c}(\mathbf{X}) dA, \tag{2.24}$$

where the intersection polygons $\Omega_{k,d} \cap \widetilde{\Omega}_c$ are computed thanks to a specific triangulation of the mesh. The procedure is detailed in [65]. The set $\mathcal{C}(c)$ contains the cells including c that share at least one node with the cell c. At last, the partial volume defined on the rezoned cell is $\widetilde{V}_{k,c} = \sum_{d \in \mathcal{C}(c)} \int_{\Omega_{k,d} \cap \widetilde{\Omega}_c} \mathcal{R} dA$.

In the context of MOF reconstruction, one has to define additional quantities as the partial remapped mass corresponding to material k. It is computed as $\widetilde{m}_{k,c} = \widetilde{\rho}_{k,c} \widetilde{\alpha}_{k,c} \widetilde{V}_{k,c}$ with the volume fraction

$$\widetilde{\alpha}_{k,c} = \frac{1}{\widetilde{V}_c} \sum_{d \in \mathcal{C}(c)} \int_{\Omega_{k,d} \cap \widetilde{\Omega}_c} \mathcal{R} dA, \tag{2.25}$$

thus the partial volume can be also expressed as $\widetilde{V}_{k,c} = \widetilde{V}_c \widetilde{\alpha}_{k,c}$. In addition, each material centroid position is defined thanks to

$$\widetilde{\mathbf{X}}_{k,c} = \frac{1}{\widetilde{V}_{k,c}} \sum_{d \in \mathcal{C}(c)} \int_{\Omega_{k,d} \cap \widetilde{\Omega}_c} \mathcal{R}\mathbf{X} dA. \tag{2.26}$$

2.5.2 Pure cell swept-face (PCSF) remapping

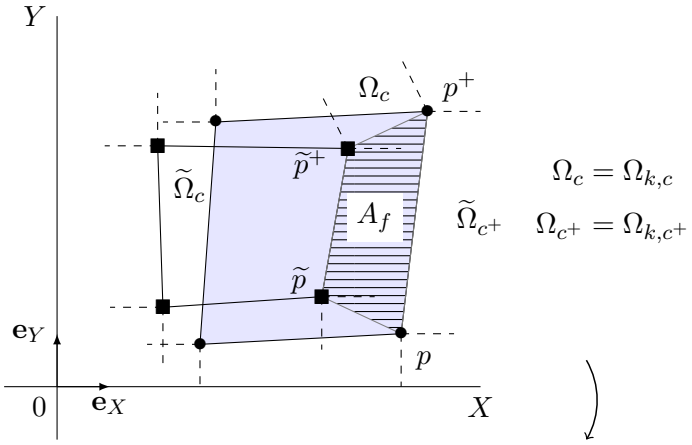

Figure 2.14: Notations for swept face-based method.

As explained before, the PCSF remapping is used only to treat single fluid cells. In this context, one should remark that $\Omega_c = \Omega_{k,c}$, thus the mean value $\widetilde{\psi}_{c,k}$ is given through

$$\widetilde{\psi}_{k,c} = \psi_{k,c} + \sum_{f \in \mathcal{F}(c)} \int_{A_f} \mathcal{R}\Psi_{k,f} dA, \tag{2.27}$$

with A_f the quadrangular signed area swept by the face f of a cell c between the Lagrangian grid and the rezoned grid delimited by the ordered nodes $\{\mathbf{X}_p, \mathbf{X}_{\widetilde{p}}, \mathbf{X}_{\widetilde{p}^+}, \mathbf{X}_{p^+}\}$ (refer to FIG. 2.14). We note $\mathcal{F}(c)$ the set of the faces f of a cell c. In addition, $\Psi_{k,f}$ is the upwind value given by

$$\Psi_{k,f} = \begin{cases} \Psi_{k,c^+}(\mathbf{X}) & \text{if } A_f > 0 \\ \Psi_{k,c}(\mathbf{X}) & \text{otherwise.} \end{cases} \tag{2.28}$$

with c^+ the neighbor cell of c through the face f. During this step the volume fractions $\widetilde{\alpha}_{k,c} = \alpha_{k,c}$ do not change as we consider single fluid cells and the material centroid can be updated directly from the geometry $\widetilde{\mathbf{X}}_{k,c} = \widetilde{\mathbf{X}}_c$ where $\widetilde{\mathbf{X}}_c$ is the centroid of the cell $\widetilde{\Omega}_c$.

2.5.3 Integration strategy

For both PCSF and MCIB remapping, one has to compute several surface integrals, on polygons where the integrand is a polynomial function of (X, Y). This can be done using a triangulation of these areas. Nevertheless, this is expensive. Here, we rather adopt a more efficient method as in [121]. In this context, integrals are simplified using Taylor decomposition of the polynomial integrand and Green's formula [122] leading to compute circular integrals over the edges of the polygons defining the integration areas. For further details on integral computations see [121].

2.5.4 Hybrid remapping algorithm

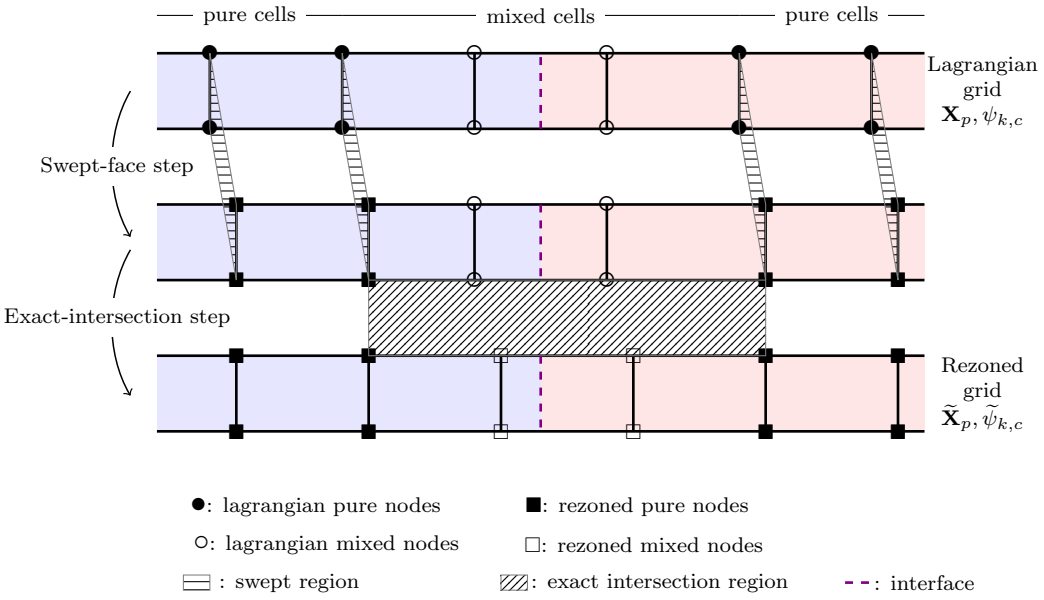

Figure 2.15: Hybrid remapping principle in one-dimension case.

In this part, we detail the hybrid remapping algorithm that is summarized on Fig. 2.15. To this end, let us introduce $\mathcal{N}^P$ and $\mathcal{N}^M$ the sets of nodes and in the same manner $\mathcal{C}^P$ and $\mathcal{C}^M$ the sets of cells respectively used for PCSF and MCIB remapping. Here $\mathcal{N}^M$ collects mixed nodes belonging to cells that contain the interface or are on this interface (white nodes on Fig. 2.15) despite $\mathcal{N}^P$ contains the pure ones (black nodes on Fig. 2.15). In addition, $\mathcal{C}^M$ is the set of mixed cell that include cells intersected by the interfaces and their neighbors by nodes. Finally, $\mathcal{C}^P$ contains the cells that have at least one node in $\mathcal{N}^P$.
The hybrid remapping procedure consists in performing the following steps.

1. **PCSF step.** In this step we first move the pure nodes included in $\mathcal{N}^P$ and we remap the quantities in cell c belonging to $\mathcal{C}^P$. Thus, we have $\widetilde{\psi}_{k,c} = (\widetilde{\rho}_{k,c}, \widetilde{\rho E}_{k,c}, \widetilde{\rho \mathbf{U}}_{k,c})$ using relation (2.27) and $\widetilde{m}_{k,c}, \widetilde{\alpha}_{k,c}, \widetilde{\mathbf{X}}_{k,c}$ for each cell $c \in \mathcal{C}^p$.

2. **MCIB step.** Now, the mixed nodes in $\mathcal{N}^M$ are moved and the $\widetilde{\psi}_{k,c} = (\widetilde{\rho}_{k,c}, \widetilde{\rho E}_{k,c}, \widetilde{\rho \mathbf{U}}_{k,c})$ are remapped thanks to (2.24) and $\widetilde{m}_{k,c}, \widetilde{\alpha}_{k,c}, \widetilde{\mathbf{X}}_{k,c}$ are computed for cells $c \in \mathcal{C}^M$.

Since $\mathcal{C}^M \cap \mathcal{C}^P \neq \{\emptyset\}$, one should note that cells included in this intersection are remapped at each step of the algorithm.

At the end of remapping, only the partial values of the physical variables per unit of volume are known. At this step, a first point is to compute the physical variables per unit of mass. The remapped partial total energy is given using $\widetilde{E}_{k,c} = \widetilde{(\rho E)}_{k,c}/\widetilde{\rho}_{k,c}$. However, this is different for the remapped partial velocity $\widetilde{\mathbf{U}}_{k,c}$. Indeed, as explained in the second part of this paper, the Lagrangian computation of the velocity is done in Cartesian geometry. For this reason, the remapped velocity is deduced from the $\widetilde{(\rho\mathbf{U})}_{k,c}$ through $\widetilde{\mathbf{U}}_{k,c} = \widetilde{(\rho\mathbf{U})}^{pl}_{k,c}/\widetilde{\rho}^{pl}_{k,c}$ using the *planar* remapped density and momentum given through (2.24) and (2.27) with $\mathcal{R} = 1$. The second point is dedicated to the reconstruction of the global values required for the next Lagrangian step. To this end, a classical procedure is to use specific averages

$$\widetilde{\phi}_c = \frac{1}{\widetilde{m}_c} \sum_k \widetilde{m}_{k,c} \widetilde{\phi}_{k,c}, \tag{2.29}$$

with the global mass and density deduced from

$$\widetilde{m}_c = \sum_k \widetilde{m}_{k,c} \widetilde{\alpha}_{k,c} \text{ and } \widetilde{\rho}_c = \sum_k \widetilde{\rho}_{k,c} \widetilde{\alpha}_{k,c}. \tag{2.30}$$

At last, thermodynamical variables as pressure P and internal energy ε are obtained thanks to specific thermodynamical closures as done in [65].

2.6 Remapping for ReALE

2.6.1 PCSF remapping for ReALE

In this step we remap the physical variables from the Lagrangian grid onto the reconnected grid. Both grid have the same number of cells but they may have a different number of vertices due to reconnection. To perform the remapping step one can perform an exact intersection between the grids [103, 65]. The main drawback of such method is the computational time. A new method has been developed in [75] based on a swept-intersection as in [31]. We present here the axisymmetric extension of this method. The physical variables that we want to remap are ρ, ρU, and ρE. In the sequel Ψ_c represent the mean value on the cell c of one of these physical variable. The goal of the remapping step is to compute the new value of Ψ over the new reconnected mesh. We use a MUSCL approach to represent the variable Ψ on the Lagrangian grid which correspond to the piecewise linear function $\Psi_c(X)$ as in (2.22). During the reconnection process three types of configurations (Fig. 2.16) allow us to use the classical flux swept approach [121] for the remapping.
The goal of the flux swept approach is to compute the mean value of Ψ over the cell $\widetilde{c}$ using

$$\Psi_{\widetilde{c}} = \frac{1}{V_{\widetilde{c}}} \left(\int_c \mathcal{R}\Psi d\mathbf{X} + \sum_{f,p} \int_{Q^s} \mathcal{R}\Psi d\mathbf{X} \right) \tag{2.31}$$

where $V_{\widetilde{c}} = V_c + \sum_{f,p} \int_{Q^s} \mathcal{R} d\mathbf{X}$ is the volume of the new cell $\widetilde{c}$ and Q^s is one of the swept region $\{Q^s_{f\widetilde{f}}, Q^s_{f\widetilde{p}}, Q^s_{p\widetilde{f}}\}$ of the Fig. 2.16. The sign of $\int_{Q^s} \mathcal{R} d\mathbf{X}$ depends on the counter-clockwise orientation according to the cell c considered.

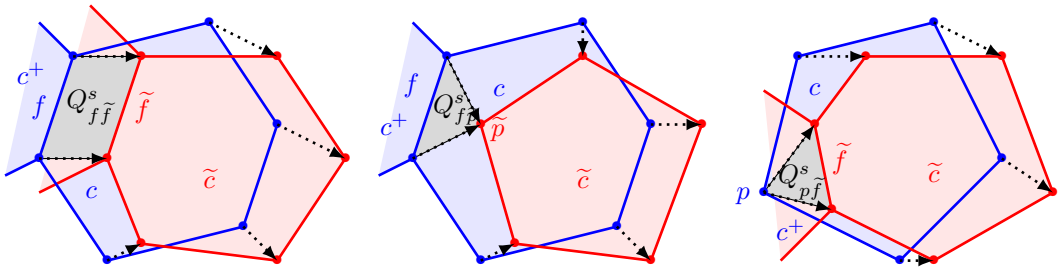

Figure 2.16: three types of configurations using flux swept approach for the projection in ReALE

The integral of $\int_{Q^s} \mathcal{R}\Psi d\mathbf{X}$ is computed using an upwind approximation

$$\int_{Q^s} \mathcal{R}\Psi d\mathbf{X} = \begin{cases} \int_{Q^s} \mathcal{R}\Psi_{c^+}(\mathbf{X}) d\mathbf{X} & \text{if } Q^s \geq 0 \\ \int_{Q^s} \mathcal{R}\Psi_{c}(\mathbf{X}) d\mathbf{X} & \text{otherwise} \end{cases} \tag{2.32}$$

where $\Psi_c(\mathbf{X})$ and $\Psi_{c^+}(\mathbf{X})$ are the piecewise linear reconstruction of the function Ψ over the Lagrangian cells c and c^+. Here, for $Q^s_{f\widetilde{f}}$ and , $Q^s_{f\widetilde{p}}$ the cell c^+ is the neighbor of the cell c through the face f. In the case of $Q^s_{p\widetilde{f}}$ the cell c^+ is the neighbor of the cell c through the face $\widetilde{f}$. At the end we need to compute surface integrals of polynomial function on polygons. The method used a Taylor decomposition and Green's formula. For further details see [121].

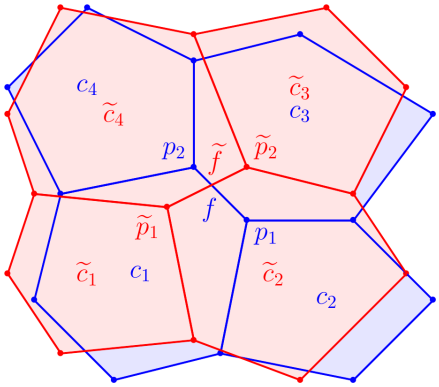

Figure 2.17: Example of Voronoi-like reconnection

During the ReALE computation drastic change in the connectivity between the cell may occur. In the voronoi-like reconnection (FIG. 2.17) cell neighborhood changes on both side of a face need to be treated. In this case, c_1 is neighbor of c_3 on the Lagrangian mesh but during the reconnection their common face is removed and a new face has appeared between $\widetilde{c}_2$ and $\widetilde{c}_4$.

To deal with such reconnection we use a reference cell c_{ref} on the Lagrangian mesh to perform the reconstruction. This cell can be one of the two neighbors cells of the Lagrangian face f, that is $c_{ref} = c_1$ or $c_{ref} = c_3$ (FIG. 2.18). The choice of the reference cell is based on the volume of the swept region $Q^s_{f\widetilde{p}_1}$ and $Q^s_{f\widetilde{p}_2}$. If $\int_{Q^s_{f\widetilde{p}_1}} \mathcal{R}d\mathbf{X} > \int_{Q^s_{f\widetilde{p}_2}} \mathcal{R}d\mathbf{X}$ then $c_{ref} = c_1$, else $c_{ref} = c_3$. Using the previous method we can now compute the new mean value of the reconnected cells using:

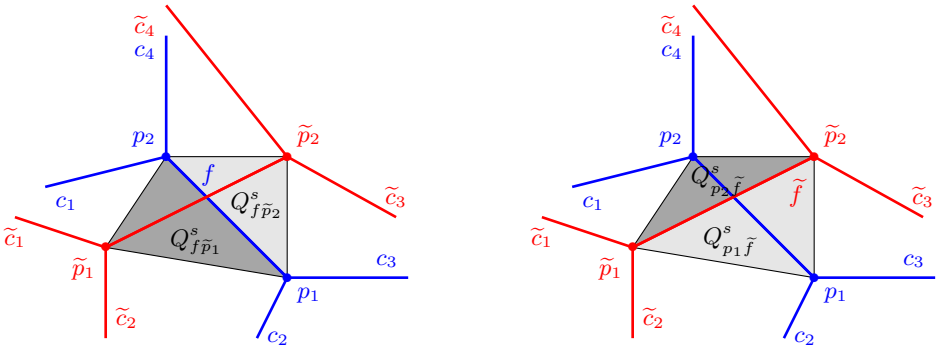

(a) Shrinking of face f over $\widetilde{p}_1$ and $\widetilde{p}_2$

(b) Projections of p_1 and p_2 on $\widetilde{f}$

Figure 2.18: Reconnection zone used for swept-intersection-based method

$$\Psi_{\widetilde{c_1}} = \frac{1}{V_{\widetilde{c_1}}}\left(\int_{c_1}\mathcal{R}\Psi_{c_1}d\mathbf{X} + \int_{Q^s_{f\widetilde{p}_1}}\mathcal{R}\Psi_{c_{ref}}(\mathbf{X})d\mathbf{X} + \sum_{f,p}\int_{Q^s}\mathcal{R}\Psi d\mathbf{X}\right) \tag{2.33}$$

$$\Psi_{\widetilde{c_2}} = \frac{1}{V_{\widetilde{c_2}}}\left(\int_{c_2}\mathcal{R}\Psi_{c_2}d\mathbf{X} - \int_{Q^s_{p_1\widetilde{f}}}\mathcal{R}\Psi_{c_{ref}}(\mathbf{X})d\mathbf{X} + \sum_{f,p}\int_{Q^s}\mathcal{R}\Psi d\mathbf{X}\right) \tag{2.34}$$

$$\Psi_{\widetilde{c_3}} = \frac{1}{V_{\widetilde{c_3}}}\left(\int_{c_3}\mathcal{R}\Psi_{c_3}d\mathbf{X} - \int_{Q^s_{f\widetilde{p}_2}}\mathcal{R}\Psi_{c_{ref}}(\mathbf{X})d\mathbf{X} + \sum_{f,p}\int_{Q^s}\mathcal{R}\Psi d\mathbf{X}\right) \tag{2.35}$$

$$\Psi_{\widetilde{c_4}} = \frac{1}{V_{\widetilde{c_4}}}\left(\int_{c_4}\mathcal{R}\Psi_{c_4}d\mathbf{X} + \int_{Q^s_{p_2\widetilde{f}}}\mathcal{R}\Psi_{c_{ref}}(\mathbf{X})d\mathbf{X} + \sum_{f,p}\int_{Q^s}\mathcal{R}\Psi d\mathbf{X}\right) \tag{2.36}$$

If during the computation more than two Voronoi-like reconnection appear at the same face, then the time step is reduced such that only one reconnection of this type occur.

2.6.2 MCIB Remapping for ReALE

As shown in Fig. 2.10, the Lagrangian mesh, which also include the reconstructed interface, is remapped onto the new mesh. In the case of ReALE, the new mesh is the Voronoi mesh corresponding to the positions of generator created by the reconnection phase. As the old (Lagrangian) and new polygonal meshes may not have the same connectivity, the remapping phase in the case of ReALE computation for several materials is based on a multi-material cell-intersection-based (MCIB) exact intersection as depicted in Fig. 2.19.
Each material of the flow noted k occupies the polygon $\Omega_{k,c} \subset \Omega_c$, within the MOF framework, such that $\Omega_c = \bigcup_k \Omega_{k,c}$ and is characterized by its partial mass, density, pressure, internal energy and variables per unit of volume (total energy, momentum) whose averaged values in each sub-cell are respectively $m_{k,c}, \rho_{k,c}, P_{k,c}, \varepsilon_{k,c}$ and $\psi_{k,c} = \rho_{k,c}\phi_{k,c}$ with $\phi_{k,c}$ the partial velocity or energy per unit of mass.

Here, the main idea of remapping is not to directly compute the global rezoned quantities $\widetilde{\psi}_c$ but the partial rezoned ones noted $\widetilde{\psi}_{k,c}$. This is particularly true for the MCIB method that is dedicated to treat cell in the interface neighborhood. To this end, we use the second order

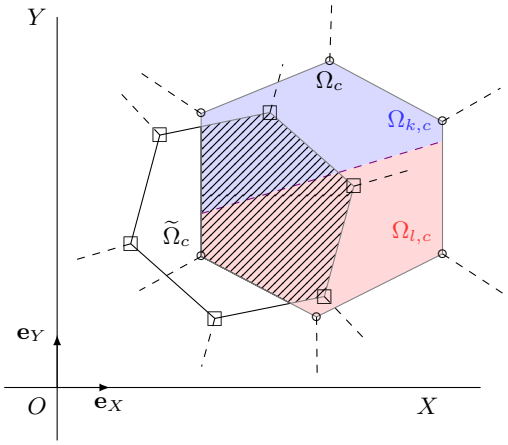

Figure 2.19: Notations for MCIB method used for multi-material ReALE.

reconstruction $\Psi_{k,c}(\mathbf{X})$ of $\psi_{k,c}$ over each Lagrangian cell c through the piecewise linear function $\Psi_c(\mathbf{X})$ as in (2.22). The main difference with the MCIB method presented in section 2.5.1 is the topology change that may occur during the reconnection phase.

2.7 Flux Corrected Remapping

Here we present the Flux Corrected Remapping (FCR) [101] to avoid non-physical oscillations. The core of the method is the convex combination of a low-order bound-preserving numerical fluxes of the conservative quantities with high-order fluxes. Using this method, the remapped quantities preserve local bounds directly by construction. As in the MOOD method [49], a variety of the constraints can be selected, e.g. here we employ the bounds on density, velocity and specific internal energy. Here, FCR is a priori method while MOOD is an iterative a posteriori method. The preservation of the bounds is not affected by the choice of a swept flux-based integration [94]. We avoid also the non-physical repair techniques [149, 106] and construct a simple bounds-preserving remapping method. When the Lagrangian method preserves positive specific internal energy, then its lower bound guarantees its positivity after the remap.

The core feature of the interpolation of the fluid quantities from the Lagrangian grid to the re-zoned one is the conservation of appropriate quantities. For the Euler hydrodynamic equations, these quantities are total mass $\sum_i \mathcal{M}_i$, total momentum components $\sum_i \mathcal{P}_i^x$, $\sum_i \mathcal{P}_i^y$ and total energy $\sum_i \mathcal{E}_i$. The summation goes over all cells i of the computational grid. For the considered case where the old and new cells are close to each other (for details of this analog of the CFL condition see [158]), the conservation is achieved by the flux form of remapped values

$$\tilde{\mathcal{U}}_i = \overline{\mathcal{U}}_i + \sum_{k \in \mathcal{C}_i} F_{ik}^{\mathcal{U}} \,. \tag{2.37}$$

Here $\overline{\mathcal{U}}_i \in \{\mathcal{M}_i, \mathcal{P}_i^x, \mathcal{P}_i^y, \mathcal{E}_i\}$ stands for the old mean cell conservative quantity and $F_{ik}^{\mathcal{U}}$ for its numerical flux through the face (i,k). The set of all edge-neighboring cells to the cell i is denoted by $\mathcal{C}_i$. The other remapped variables (lower-case) are then defined as a combination of the conservative ones, that is mean cell density $\tilde{\rho}_i$, velocity $\tilde{\boldsymbol{U}}_i$, momentum $\tilde{\boldsymbol{\mu}}_i$, total energy $\tilde{e}_i$

and specific internal energy $\tilde{\varepsilon}_i$

$$\tilde{\rho}_i = \tilde{\mathcal{M}}_i / \tilde{V}_i \tag{2.38}$$

$$\tilde{\boldsymbol{U}}_i = \tilde{\boldsymbol{\mu}}_i / \tilde{\rho}_i = \tilde{\boldsymbol{\mathcal{P}}}_i / \tilde{\mathcal{M}}_i \tag{2.39}$$

$$\tilde{\varepsilon}_i = \tilde{e}_i / \tilde{\rho}_i - \tilde{\boldsymbol{U}}_i^2 / 2 = \tilde{\mathcal{E}}_i / \tilde{\mathcal{M}}_i - \tilde{\boldsymbol{\mathcal{P}}}_i^2 / 2\tilde{\mathcal{M}}_i^2 \,. \tag{2.40}$$

To be conservative, the reconstruction inside each cell is performed for the conservative quantities $\overline{u}_i \in \{\rho_i, \boldsymbol{\mu}_i, e_i\}$. The employed FCR method is however able to preserve bounds on different quantities.

The application of the Flux Corrected Transport method during the remapping step of the ALE algorithm is reviewed in [100]. The basic idea of the method is to provide a convex combination of the bound-preserving low-order numerical flux and the precise high-order one, which satisfy the given bounds. The remapped conservative quantity in the cell i has the form

$$\tilde{\mathcal{U}}_i = V_i \overline{u}_i + \sum_{k \in \mathcal{C}_i} F_{ik} = \overline{\mathcal{U}}_i + \sum_{k \in \mathcal{C}_i} \left[F_{ik}^L + C_{ik} \underbrace{(F_{ik}^H - F_{ik}^L)}_{dF_{ik}} \right] = \tilde{\mathcal{U}}_i^L + \sum_{k \in \mathcal{C}_i} C_{ik} dF_{ik} \,. \tag{2.41}$$

The summation goes over the set of all edge neighbors $\mathcal{C}_i$, V_i represents the old cell volume, $\tilde{U}_i^L$ the quantity remapped by the low-order method and dF_{ik} the difference between the high- and low-order numerical fluxes, i.e. so called anti-diffusive flux. The task is how to compute the edge-based correction factors $C_{ik} \in < 0, 1 >$ for the mass, momentum and total energy remap.

In the 1D sequential FCR idea [155], the correction factor for the momentum remap C_{ik}^{μ} is expressed as $C_{ik}^{\mu} = C_{ik}^m C_{ik} < C_{ik}^m$ (where C_{ik}^m is the correction factor for the mass remap) and similarly $C_{ik}^{\mathcal{E}} = C_{ik}^{\mu} C_{ik}^m C_{ik}$ for the energy remap. More recently, Synchronized FCR (SFCR) [101] method uses a local optimization procedure with one constrained minimization problem for each interface (i, k) to get the optimal values of the independent correction factors $(C_{ik}^m, C_{ik}^{\mu}, C_{ik}^{\mathcal{E}})$ for mass, momentum and energy.

On the contrary, the same value of the correction factors $C_{ik}^m = C_{ik}^{\mu} = C_{ik}^{\mathcal{E}} = C_{ik}$ is assumed in the presented method. This allows to resolve all constraints in a simple and more efficient way. Expected increase of numerical diffusion near shocks caused by the same correction factors for all conservative quantities is compensated by the use of the described third-order piecewise quadratic (instead of the standard piecewise linear) reconstruction for the high-order fluxes (see Appendix A). All conservative quantities are discontinuous on the shock and thus all these quantities need to be limited. Our choice of the same value of the correction factors means that we limit all the quantities in the same manner.

The method is constructed to preserve the bounds on the remapped density, the components of velocity projected in the local flow direction (ξ, η) and the specific internal energy

$$\rho_i^{\min} \le \tilde{\rho}_i \le \rho_i^{\max}, \qquad \rho_i^{\min\,/\,\max} = \min_{k \in \{i, \mathcal{C}_i\}} / \max_{k \in \{i, \mathcal{C}_i\}} (\rho_k) \tag{2.42}$$

$$w_i^{\xi,\min} \le \tilde{\boldsymbol{U}}_i^{\xi} \le w_i^{\xi,\max}, \qquad w_i^{\xi,\min\,/\,\max} = \min_{k \in \{i, \mathcal{C}_i\}} / \max_{k \in \{i, \mathcal{C}_i\}} \left(\left(\mathbb{R}_i \mathbf{U}_k \right)^{\xi} \right) \tag{2.43}$$

$$w_i^{\eta,\min} \le \tilde{\boldsymbol{U}}_i^{\eta} \le w_i^{\eta,\max}, \qquad w_i^{\eta,\min\,/\,\max} = \min_{k \in \{i, \mathcal{C}_i\}} / \max_{k \in \{i, \mathcal{C}_i\}} \left(\left(\mathbb{R}_i \mathbf{U}_k \right)^{\eta} \right) \tag{2.44}$$

$$\varepsilon_i^{\min} \le \tilde{\varepsilon}_i \le \varepsilon_i^{\max *}, \qquad \varepsilon_i^{\min} = \min_{k \in \{i, \mathcal{C}_i\}} (\varepsilon_k) \tag{2.45}$$

$$\mathbb{R}_i = \frac{1}{|\mathbf{U}_i|} \begin{pmatrix} (\mathbf{U}_i)^x & (\mathbf{U}_i)^y \\ -(\mathbf{U}_i)^y & (\mathbf{U}_i)^x \end{pmatrix}, \qquad \varepsilon_i^{\max *} = \max \left(\tilde{\varepsilon}_i^L, \max_{k \in \{i, \mathcal{C}_i\}} (\varepsilon_k) \right) . \tag{2.46}$$

The classical velocity bounds in the Cartesian x and y directions do not preserve symmetry for remap of a polar velocity field from one polar mesh to another[158]. To achieve the symmetry, we apply the bounds in the direction of the local velocity and the direction orthogonal to it by multiplying the velocity by the rotation matrix $\mathbb{R}_i$, see [158] inspired by [112]. Because of the form (2.40), even the remapped internal energy $\tilde{\varepsilon}_i^L$ by the low-order method can exceed its maximum bound. Therefore, the maximum of this remapped value $\tilde{\varepsilon}_i^L$ and the maximum over the neighboring cells is included in (2.46). We know all the low-order remapped values of mass $\tilde{\mathcal{M}}_i^L$, local flow direction momentum components $\tilde{\mathcal{P}}_i^{\xi,L}$, $\tilde{\mathcal{P}}_i^{\eta,L}$ (radial and polar for radial flow) and total energy $\tilde{\mathcal{E}}_i^L$; as well as corresponding anti-diffusive fluxes $dF_{ik}^{\mathcal{M}}$, $dF_{ik}^{\mathcal{P}^\xi}$, $dF_{ik}^{\mathcal{P}^\eta}$, $dF_{ik}^{\mathcal{E}}$. The standard FCR machinery substitutes (2.41) into both sides of inequalities (2.42,2.43,2.44,2.45) and with respect to (2.38,2.39,2.40) provides a set of cell-based constraints

$$C_{ik} \le D_i^1 = \frac{\rho_i^{\min}\tilde{V}_i - \tilde{\mathcal{M}}_i^L}{\sum\limits_{k\in\mathcal{C}_i} \min\left(0, dF_{ik}^{\mathcal{M}}\right)} \tag{2.47}$$

$$C_{ik} \le D_i^2 = \frac{\rho_i^{\max}\tilde{V}_i - \tilde{\mathcal{M}}_i^L}{\sum\limits_{k\in\mathcal{C}_i} \max\left(0, dF_{ik}^{\mathcal{M}}\right)} \tag{2.48}$$

$$C_{ik} \le D_i^3 = \frac{w_i^{\xi,\min}\tilde{\mathcal{M}}_i^L - \tilde{\mathcal{P}}_i^{\xi,L}}{\sum\limits_{k\in\mathcal{C}_i} \min\left(0, dF_{ik}^{\mathcal{P}^\xi} - w_i^{\xi,\min} dF_{ik}^{\mathcal{M}}\right)} \tag{2.49}$$

$$C_{ik} \le D_i^4 = \frac{w_i^{\xi,\max}\tilde{\mathcal{M}}_i^L - \tilde{\mathcal{P}}_i^{\xi,L}}{\sum\limits_{k\in\mathcal{C}_i} \max\left(0, dF_{ik}^{\mathcal{P}^\xi} - w_i^{\xi,\max} dF_{ik}^{\mathcal{M}}\right)} \tag{2.50}$$

$$C_{ik} \le D_i^5 = \frac{w_i^{\eta,\min}\tilde{\mathcal{M}}_i^L - \tilde{\mathcal{P}}_i^{\eta,L}}{\sum\limits_{k\in\mathcal{C}_i} \min\left(0, dF_{ik}^{\mathcal{P}^\eta} - w_i^{\eta,\min} dF_{ik}^{\mathcal{M}}\right)} \tag{2.51}$$

$$C_{ik} \le D_i^6 = \frac{w_i^{\eta,\max}\tilde{\mathcal{M}}_i^L - \tilde{\mathcal{P}}_i^{\eta,L}}{\sum\limits_{k\in\mathcal{C}_i} \max\left(0, dF_{ik}^{\mathcal{P}^\eta} - w_i^{\eta,\max} dF_{ik}^{\mathcal{M}}\right)} \tag{2.52}$$

$$C_{ik} \le D_i^7 = \frac{\varepsilon_i^{\min}(\tilde{\mathcal{M}}_i^L)^2 - \tilde{\mathcal{E}}_i^L\tilde{\mathcal{M}}_i^L + \frac{1}{2}\left[\left(\tilde{\mathcal{P}}_i^{\xi,L}\right)^2 + \left(\tilde{\mathcal{P}}_i^{\eta,L}\right)^2\right]}{\sum\limits_{k\in\mathcal{C}_i} \min\left(0, dF_{ik}^{de,\min} + \sum\limits_{l\in\mathcal{C}_i} \min\left(0, dF_{ikl}^{ds,\min}\right)\right)} \tag{2.53}$$

$$C_{ik} \le D_i^8 = \frac{\varepsilon_i^{\max *}(\tilde{\mathcal{M}}_i^L)^2 - \tilde{\mathcal{E}}_i^L\tilde{\mathcal{M}}_i^L + \frac{1}{2}\left[\left(\tilde{\mathcal{P}}_i^{\xi,L}\right)^2 + \left(\tilde{\mathcal{P}}_i^{\eta,L}\right)^2\right]}{\sum\limits_{k\in\mathcal{C}_i} \max\left(0, dF_{ik}^{de,\max} + \sum\limits_{l\in\mathcal{C}_i} \max\left(0, dF_{ikl}^{ds,\max}\right)\right)}\,. \tag{2.54}$$

The demonstrative derivation of one inequality and the definition of $dF_{ik}^{de,\min\,/\,\max}$, $dF_{ikl}^{ds,\min\,/\,\max}$ is provided in the Appendix. Note that all quantities on the right-hand side are known, so the computation of the cell-based D_i's consists only from summation of known quantities according to their signs. For the edge (i,k) between cells i and k, the final correction factor is

$$C_{ik} = \min_{j\in\{1,\dots,8\}} (D_i^j, D_k^j)\,. \tag{2.55}$$

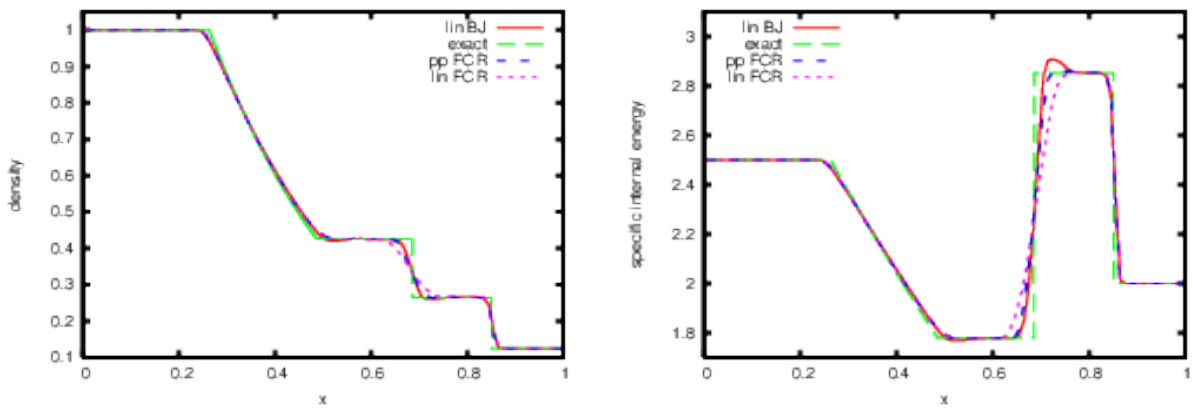

(a) (b)

Figure 2.20: 1D Sod shock tube at time $t = 0.2$, Eulerian mode, 3×100 cells. Density (a) and specific internal energy (b).

2.8 Numerical results

We present in this section several numerical test cases performed using the various development proposed in this chapter. In the sequel, all the materials are governed by perfect gas equation of state $p = \rho\varepsilon(\gamma - 1)$, where ε stands for the internal energy and γ for the polytropic index of gas.

2.8.1 Eulerian Sod shock tube and Noh problem

To demonstrate the bounds preservation using FCR method presented in Section 2.7, we start with the standard Sod shock tube test [150]. The Eulerian mode, i.e. remapping in every time step to the initial grid, was used to emphasize the properties of the remap. Final density Fig. 2.20(a) and internal energy Fig. 2.20(b) are shown in Fig. 2.20. For the piecewise linear reconstruction, the FCR method is more diffusive on the contact discontinuity than the BJ-limited method. This is probably due to the application of the same correction factors to the numerical fluxes of all conservative quantities. The piecewise quadratic reconstruction compensates this penalty. Both piecewise linear and piecewise quadratic FCR methods preserve the bounds on density, velocity and specific internal energy during the remapping stage of the calculation, whereas the standard BJ limiter does not remove all numerical oscillations in the internal energy.
The same can be observed from the results of the Noh implosion test case [128] in Fig. 2.21 at the final time 0.6 of the Eulerian computation with the constant initial density 1 and the radial velocity -1 on the square grid with 100×100 cells. The initial and boundary pressure was set to 1E-6. We want to notice that the BJ-limited remapping method fails to pass these complex tests with negative internal energy.

2.8.2 Axisymmetric Sedov problem using ALE

We present now the Sedov problem for a point blast in a uniform medium with spherical symmetry [147, 88]. We use this test case to compare our new formulation with the original EUCCLHYD scheme in pure Lagrangian and coupled to the CCALE-MOF procedure. Both formulation are based on the high-order extension of the Lagrangian scheme as it is presented in [109]. The initial conditions are given by $(\rho^0, P^0, \mathbf{U}^0) = (1, 10^{-6}, \mathbf{0})$ in a spherical domain of

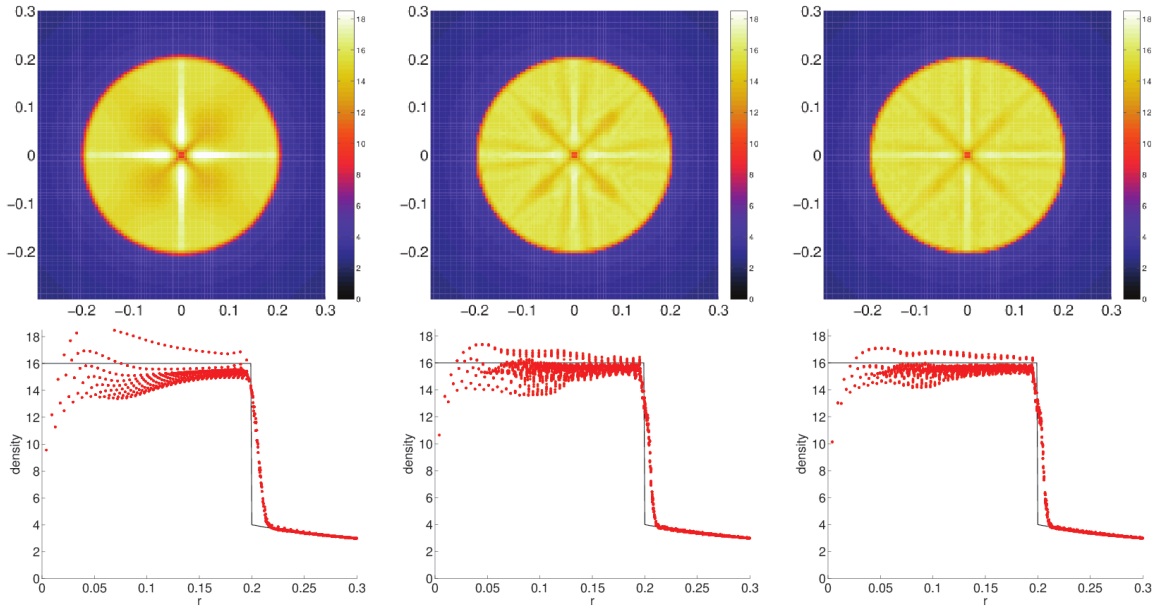

(a) (b) (c)

Figure 2.21: Density for the Noh test case at time $t = 0.6$, FCR with a piecewise constant- (a), linear- (b), resp. parabolic (c) high-order reconstruction. Eulerian mode.

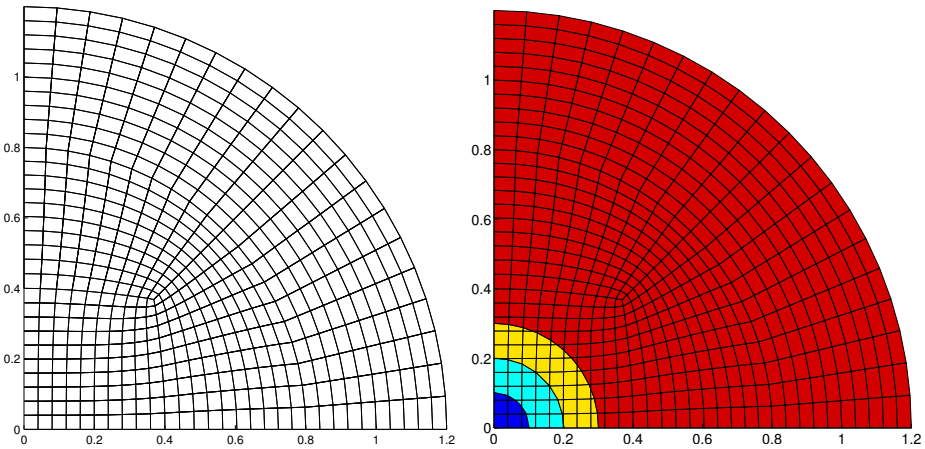

Figure 2.22: Initial grid and material positions for the Sedov problem.

radius 1.2 except in the cell at the origin $(0,0)$ where an initial delta-function energy source is set through the pressure

$$P_{or} = (\gamma - 1)\rho_{or}\frac{\mathcal{E}_0}{V_{or}},$$

with V_{or} the volume of the origin cell and $\mathcal{E}_0 = 0.851072$ is the total amount of released energy. The fluid has its polytropic index γ equal to $\frac{7}{5}$. Contrary to the original single material test case, we add here three artificial interfaces, to test our multi-material CCALE-MOF algorithm. These interfaces are initially located for a radius equal to 0.1, 0.2 and 0.3 (see FIG. 2.22).
Here we consider both Lagrangian and ALE computations for an initial unstructured mesh depicted on FIG. 2.22. This grid is obtained after one rezoning step, with $\omega_p = 1$ of an unstructured mesh initially paved with 500 quadrangular cells. Numerical results are depicted on FIG. 2.23 for a final time of $t_{end} = 1$ and compared to the analytical solution computed using self-similar arguments as done in [27]. It consists of a diverging shock wave whose front is exactly localized at radius $R = 1$. As it is illustrated on FIG. 2.23, the pure Lagrangian solutions are in good agreement with the analytical one. Indeed for the Lagrangian method as for the CCALE-MOF one the shock location is well resolved without any spurious oscillation (FIG. 2.23). In addition, this simple problem underlines the robustness (better mesh quality near the origin) and accuracy (shock location) of the axisymmetric CCALE-MOF approach especially when considering multi-material flows whose interfaces are well captured thanks to the MOF reconstruction (see FIG. 2.25).
We point out that during the Lagrangian computation, non-convex cells appeared. This may lead to interface reconstruction failure when considering multi-material flows. As illustrated by the previous numerical results, the proposed CCALE-MOF algorithm remains adapted to treat such configuration without any difficulty demonstrating once again its robustness.

2.8.3 Planar Sedov problem using ReALE

The initial conditions are given by $(\rho^0, P^0, \mathbf{U}^0) = (1, 10^{-6}, \mathbf{0})$ in a square domain $[0, 1.2] \times [0, 1.2]$ except in the cell at the origin $(0,0)$ where an initial delta-function energy source is set through the pressure

$$P_{or} = (\gamma - 1)\rho_{or}\frac{\mathcal{E}_0}{V_{or}},$$

with V_{or} the volume of the origin cell and $\mathcal{E}_0 = 0.244816$ is the total amount of released energy. The fluid has its polytropic index γ equal to $\frac{7}{5}$. The solution to this problem consists of a diverging shock whose front is located at radius $\mathcal{R} = 1$ at the final time $t = 1$ and peak density reaches the value 6. Contrary to the original single material test case, we add here three artificial interfaces, to test our multi-material ReALE-MOF algorithm. These interfaces are initially located for a radius equal to 0.1, 0.2 and 0.3 (see FIG. 2.24).
Here we consider both Lagrangian and ReALE computations for an initial unstructured mesh paved with 625 cells depicted on FIG. 2.24. This mesh has initially mainly quadrangular cells. The generators used to create this mesh are in the center of the cells except for generators at the corners. As shown in FIG. 2.25, this problem does not require the ReALE technique as it runs pure Lagrangian up to final time.
This problem is presented here as a sanity check test case to assess the ability of our Lagrangian phase and ReALE scheme to handle multi-interface problems. Numerical results are depicted in FIG. 2.25 for a final time of $t_{end} = 1$ and compared to the analytical solution computed using self-similar arguments as done in [65]. It consists of a diverging shock wave whose front is exactly localized at radius $R = 1$ at the final time. As illustrated in FIG. 2.25, the computed solutions are in good agreement with the analytical one for both approaches. As a matter of fact, shock

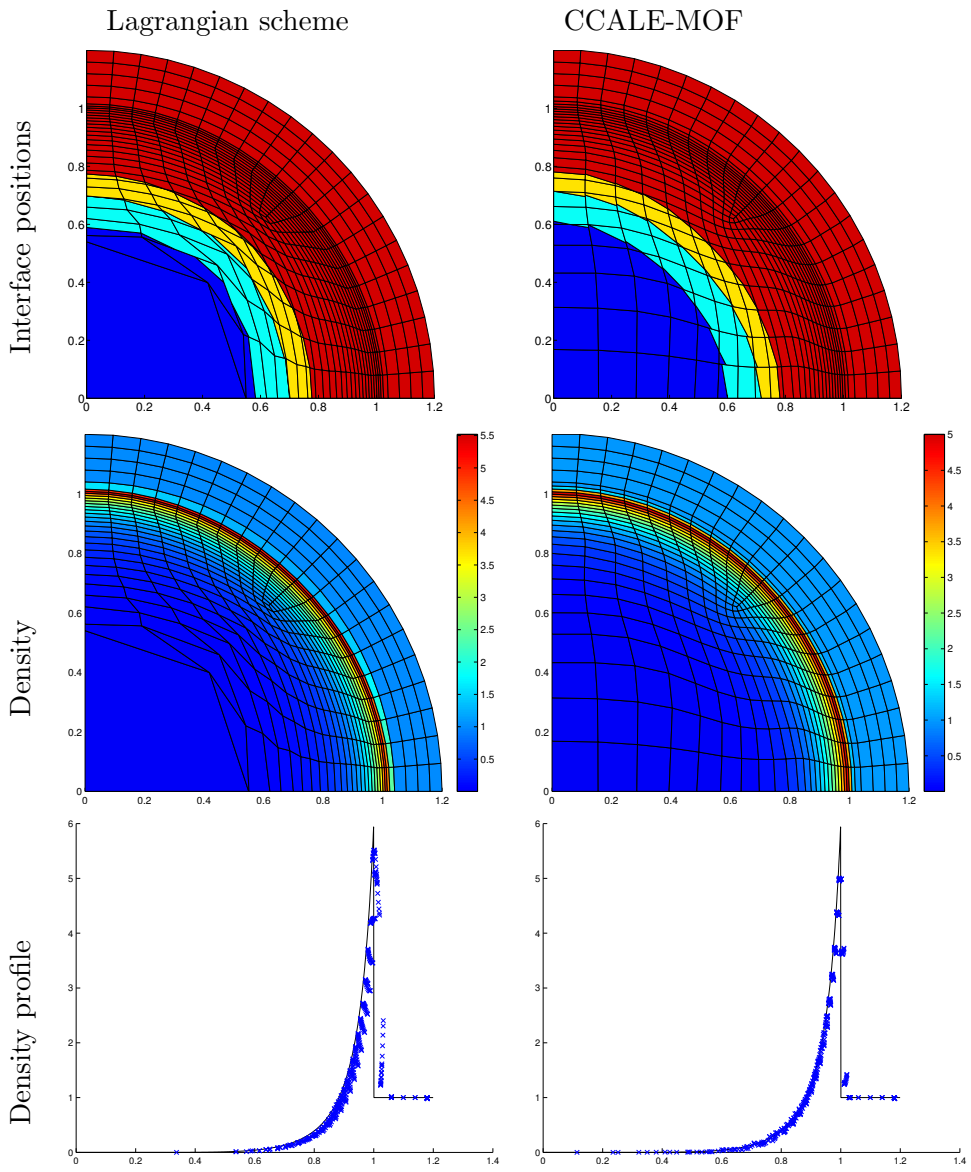

Figure 2.23: Sedov problem. From the top to the bottom: Interface positions, density maps, density profiles defined as a function of the cell center radius compared to the analytical solution at final time step for the pure Lagrangian computation AW scheme (left) and the CCALE-MOF procedure (right).

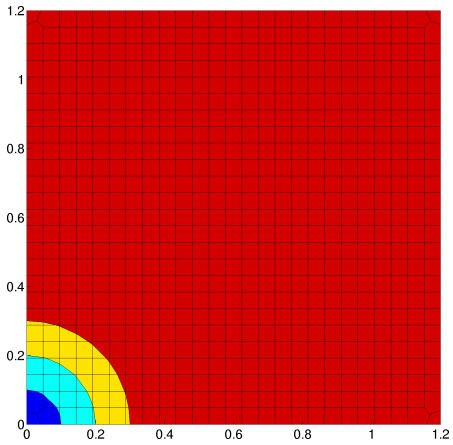

Figure 2.24: Initial grid and material positions for the Sedov problem.

and interface locations are well resolved for the Lagrangian method. For the ReALE-MOF method we have some diffusion due to the reconnection-remap algorithm but we have a good symmetry preservation on the density profiles. This simple problem underlines the robustness and accuracy of the ReALE-MOF approach especially when considering multi-material flows whose interfaces are well captured thanks to the MOF interface reconstruction (see FIG. 2.25).

2.8.4 Axisymmetric triple point problem using ALE

We consider in this part a three-material problem that corresponds to a three-state Riemann problem in an axisymmetric geometry also called the triple point problem. This problem has been wisely studied in Cartesian geometry [65, 93] and here we propose new results for cylindrical geometry. The computational domain is rectangular and composed of three regions (blue, green, red) whose dimensions are depicted on FIG.2.26. The top, left and right boundaries are closed thanks to walls. A symmetry condition is applied to the bottom boundary corresponding to the X-axis. Initially, the blue region contains a fluid with high pressure and density taken equal to $(\rho_1, p_1) = (1, 1)$. The green region contains a low density and pressure fluid whose initial state is $(\rho_2, p_2) = (0.125, 0.1)$. The third fluid in the red region, initially has a low pressure and an high density equal to $(\rho_3, p_3) = (1, 0.1)$. At the beginning of the computation, all fluids are supposed to be at rest then $\mathbf{U}_1 = \mathbf{U}_2 = \mathbf{U}_3 = \mathbf{0}$. The blue and green material have the same polytropic index $\gamma_1 = \gamma_2 = 1.5$, despite the red one has $\gamma_3 = 1.4$.

The computation using the presented axisymmetric extension of the CCALE-MOF algorithm is made on a grid initially paved with 140×60 square cells until a final time $t_f = 5$. For this simulation, comparison with a full Lagrangian computation can not be performed since its suffers from important mesh tangling as shown in [103]. However comparison to full Eulerian simulations is done. In this case, nodes are moved to their initial positions during the rezoning step. Numerical results for both ALE and Eulerian methods representing interfaces and meshes are depicted on FIG.2.27-2.28. As expected, since there is a shock wave with high speed that propagates from the heavy material (blue) to the light one (red), the interface is sheared at the triple point producing a Kelvin-Helmholtz like instability. Here, comparison to planar 2D computations [65] demonstrates that axisymmetric geometry particularly affects the vortex shape that is 3D. Although the global behavior of the solutions is very similar comparing ALE approach to the Eulerian one.

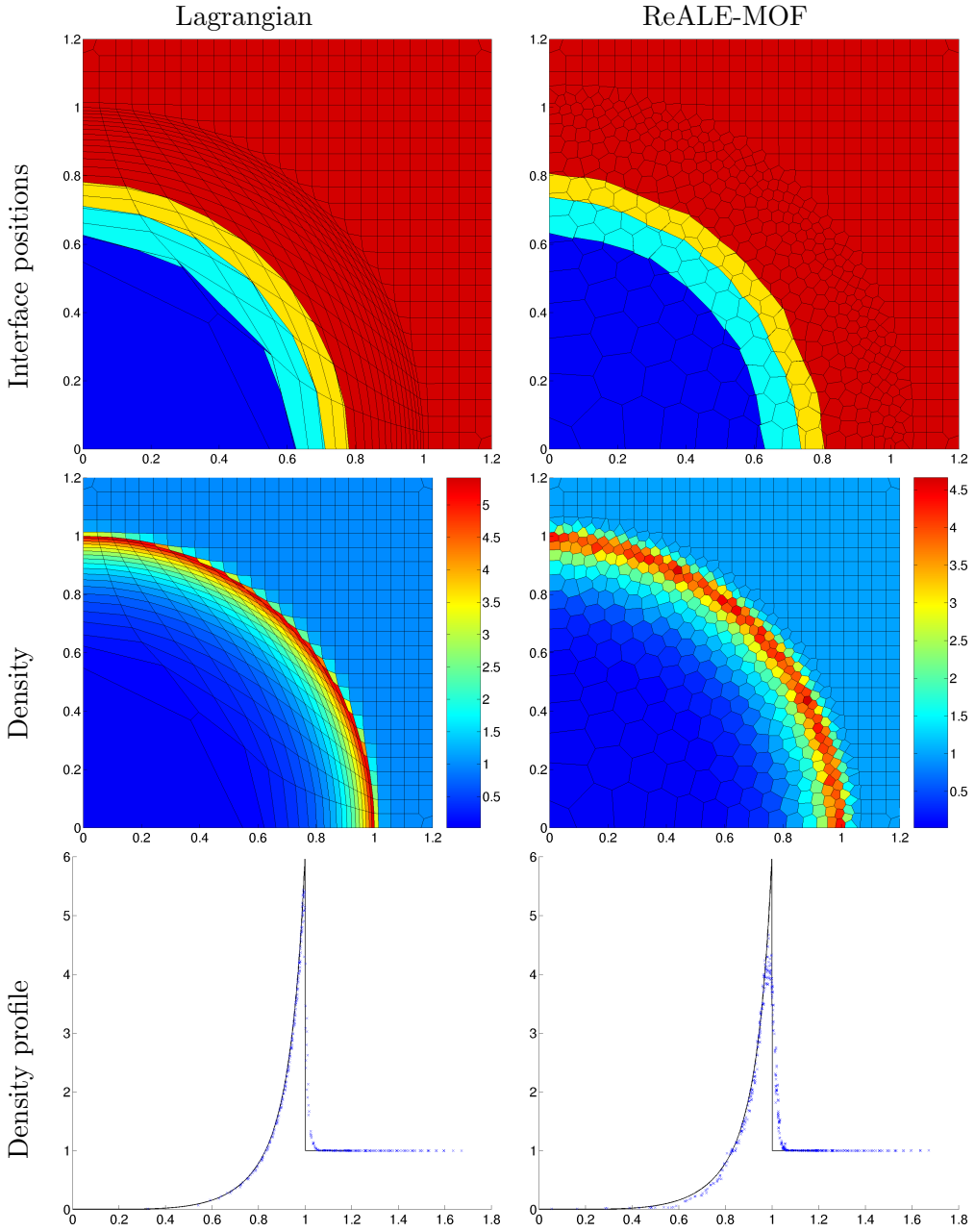

Figure 2.25: Sedov problem. From the top to the bottom: Interface positions, density maps, density profiles defined as a function of the cell center radius compared to the analytical solution at final time for the pure Lagrangian procedure (left) and the ReALE-MOF procedure (right).

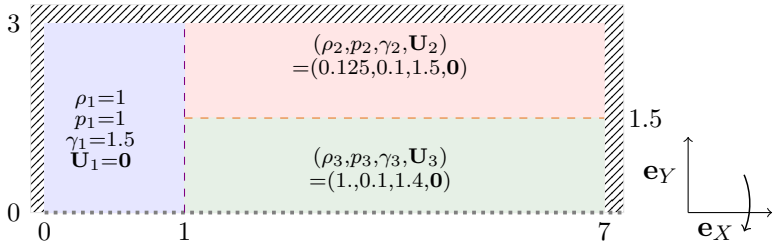

Figure 2.26: Axi-symmetric triple point problem : geometry and initial data.

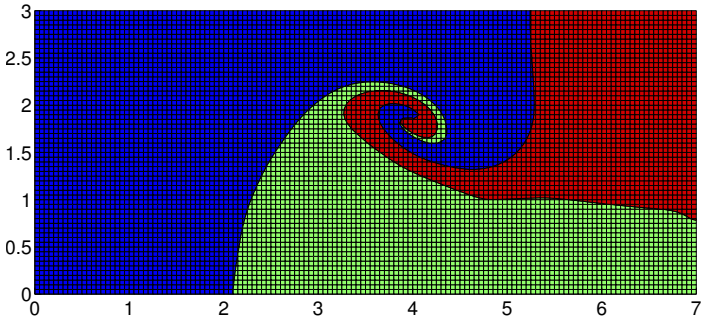

Figure 2.27: Axisymmetric triple point problem. Mesh and material positions at $t = 5$ for Eulerian computation.

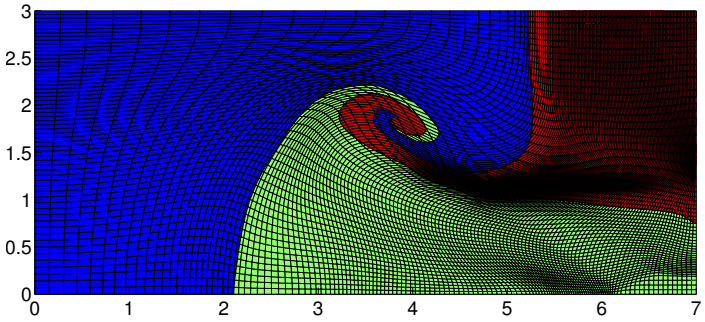

Figure 2.28: Axisymmetric triple point problem. Mesh and material positions at $t = 5$ for ALE computation.

2.8.5 Planar triple point problem using ReALE

We consider now the triple point problem in planar geometry with ReALE strategy as in [93, 134]. The computational domain is rectangular and composed of three regions (blue, green, red) whose dimensions are depicted on Fig. 2.29. All the boundary conditions are set to wall. The computation using the ReALE-MOF algorithm is made on a grid initially paved with 8400 cells until a final time $t_{end} = 5$. For this simulation, comparison with a full Lagrangian computation can not be performed since its suffers from severe mesh tangling as shown in [103]. However comparison to ALE simulations is done using CCALE-MOF method on a 140×60 grid. Numerical results for both CCALE-MOF and ReALE-MOF methods representing interfaces and meshes are depicted on top of Fig. 2.30-2.31. Additionally, we present at the bottom the material initially present in that cell. As expected, since there is a shock wave with high speed that propagates from the heavy material (blue) to the light one (red), the interface is sheared at the triple point producing a Kelvin-Helmholtz like-instability. Here, comparison between CCALE-MOF and ReALE-MOF shows that the ReALE formulation keeps the Lagrangian

property of the mesh to follow the material whereas the ALE computation clearly shows a mesh stagnation. One should note a notable difference in the shape vortex. Indeed, like in the previous test case, the vortex produced using ReALE is more rolled up than with ALE. In both ALE and ReALE computations MOF interface reconstruction succeed to track a filament of green fluid of a cell size in the vortex.

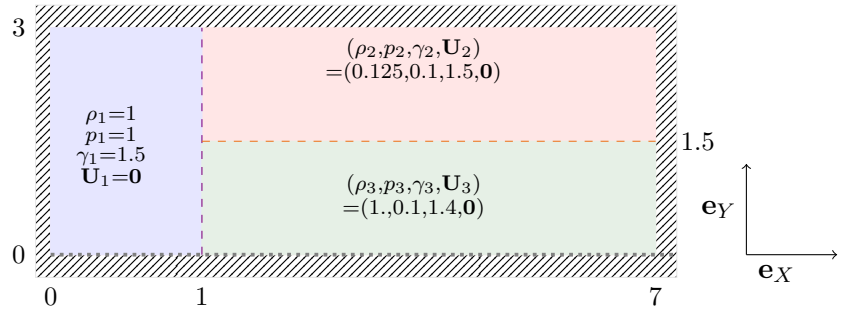

Figure 2.29: Triple point problem : geometry and initial data.

2.8.6 Rayleigh-Taylor instability using ReALE

This test case deals with the well-known Rayleigh-Taylor instability.
The computational domain is the rectangular box $[0, \frac{1}{3}] \times [0, 1]$. The initial set up consists of two immiscible fluids which are separated by a perturbed interface, whose equation writes $y_{\rm i}(x) = \frac{1}{2} + a_0 \cos(6\pi x)$. The interface amplitude a_0 is set to the value $a_0 = 10^{-2}$. The heavy fluid is located above the light one. The densities of the two fluids are $\rho_{\rm h} = 2$ and $\rho_{\rm l} = 1$. The same polytropic index $\gamma_{\rm h} = \gamma_{\rm l} = 1.4$ is shared by the two fluids. A downward gravity field is applied, $\boldsymbol{g} = (g_x, g_y)^t = (0, -0.1)^t$. Initially both fluids are at rest and the initial pressure distribution is deduced by setting hydrostatic equilibrium as

$$
\begin{aligned}
P_{\rm h}(x,y) &= 1 + \rho_{\rm h} g_y (y-1), \quad \text{if} \quad y > y_{\rm i}(x), \\
P_{\rm l}(x,y) &= 1 + \rho_{\rm h} g_y [y_{\rm i}(x) - 1] + \rho_{\rm l} g_y [y - y_{\rm i}(x)], \quad \text{if} \quad y \leq y_{\rm i}(x).
\end{aligned}
$$

In this problem a heavy fluid drop while a light fluid rise. Due to a sinusoidal initialization of the interface and to gravity, vortices develop in the vicinity of the interface and lead at later time to an interface which has a mushroom-like shape. Although this problem is incompressible and does not involve any shock wave, we run it using our multi-material CCALE-MOF [64] and ReALE-MOF algorithms. The computation is run until the final time $t_{end} = 9$ first using the CCALE-MOF algorithm on a polygonal grid of 1717 cells. Then, we use a grid made of 1818 generators to run it using ReALE-MOF method.
In Fig. 2.32(a)-(b) we present the material interface on the left and the material initially in this cell on the right respectively for CCALE-MOF and ReALE-MOF computations. We clearly see that the generators in the ReALE computation follow material interface whereas the rezoned mesh in the ALE simulation stagnates. At that point the ALE computation is mostly Eulerian. We have also superimposed the interface obtained using the front tracking code FronTier [68, 67]. The results of this code are used by the courtesy of J.W. Grove of the Los Alamos National Laboratory. We point out that FronTier is run with a very fine resolution characterized by 106×320 cells. We note that we have a rather good agreement between our ReALE results and Frontier interface compare to the ALE results which present a more stretched mesh. This test case clearly illustrate the limitation of the fixed topology of the ALE computation.

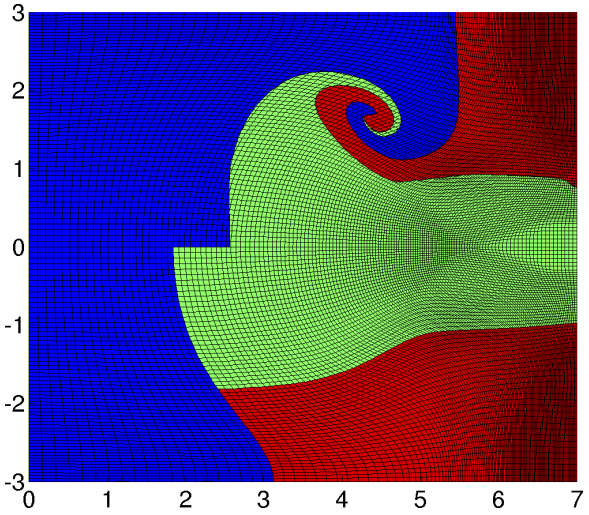

Figure 2.30: Triple point problem. Material positions (top) and initial material in a cell (bottom) at $t = 5$ for ALE computation.

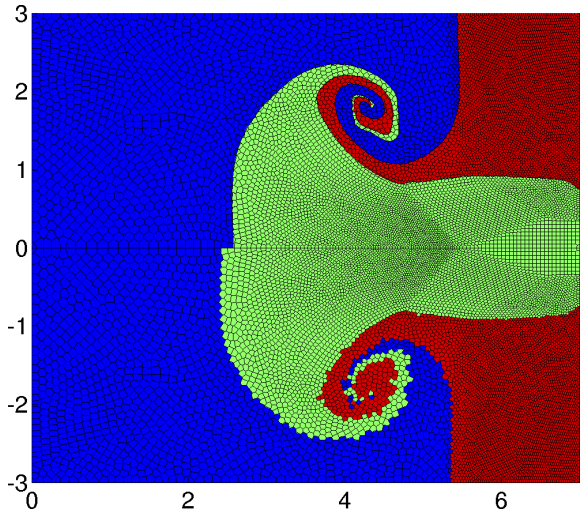

Figure 2.31: Triple point problem. Material positions (top) and initial material in a cell (bottom) at $t = 5$ for ReALE computation.

2.8.7 Kelvin-Helmholtz instability

This test case deals with another instability, the Kelvin-Helmholtz one [151]. The initial domain is a rectangular domain displayed in FIG. 2.33. All quantities are initialized as shown in FIG. 2.33, and we set for all zones the same adiabatic constant $\gamma = 5/3$. A single mode is excited with a wave-length equal to half the box size by perturbing the velocity field $\boldsymbol{U} = (u, v)$, according to:

$$v(x, y) = \omega_0 \sin(4\pi x) \left(\exp\left(\frac{(y - 0.25)^2}{2\sigma^2} \right) + \exp\left(\frac{(y - 0.75)^2}{2\sigma^2} \right) \right),$$

where $\omega_0 = 0.1$ and $\sigma = 0.05/\sqrt{2}$.
The computational domain is a square box $[0, 1] \times [0, 1]$ with periodic boundary conditions. The computation is run until the final time $t_{end} = 2$. First, an Eulerian computation is performed on a grid paved with 100×100 square cells. Eulerian computation is performed using 'Lagrange plus remap' technique. For this case, periodic boundary conditions are computed by adding

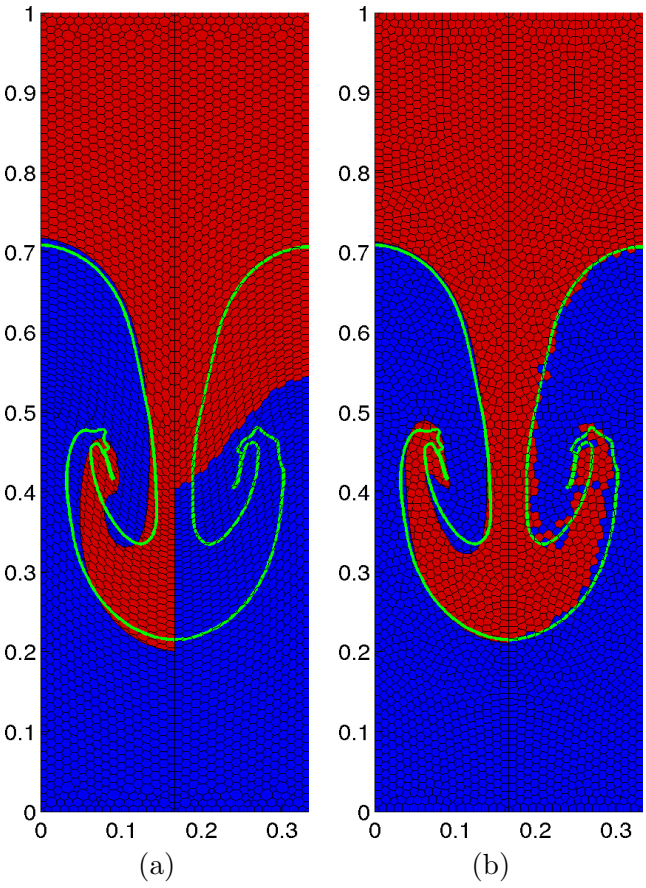

Figure 2.32: Incompressible Rayleigh-Taylor instability. Comparison versus FronTier interface (green curve). (a) CCALE-MOF snapshots of the grid and interface at final time (left) and cells initially filled of heavy fluid (right). (b) ReALE-MOF snapshots of the grid and interface at final time (left) and cells initially filled of heavy fluid (right).

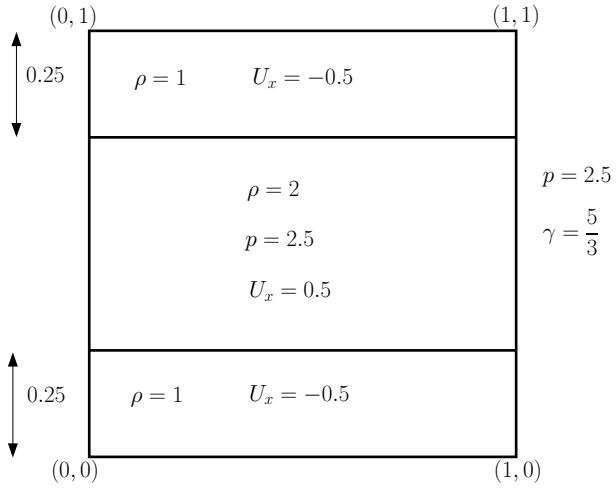

Figure 2.33: Initial conditions of the Kelvin-Helmholtz instability.

ghost cells on the left and right sides of the domain. In these ghost cells we impose the value of the corresponding cells from the computational domain. Then, a ReALE computation is performed using the same initial grid. In that case, periodic boundary conditions are computed

by moving generators that go out of the domain on the opposite side. As shown in Fig. 2.34 ReALE produce a stronger roll up than the Eulerian computation.

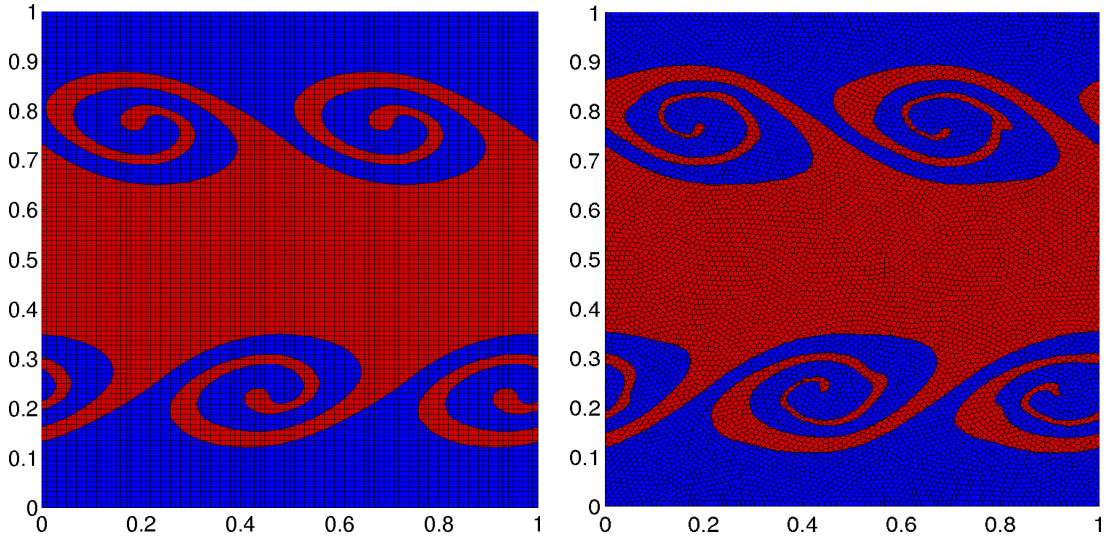

Figure 2.34: Kelvin-Helmholtz instability. Eulerian (left) and ReALE (right) computation.

2.8.8 Spherical implosion

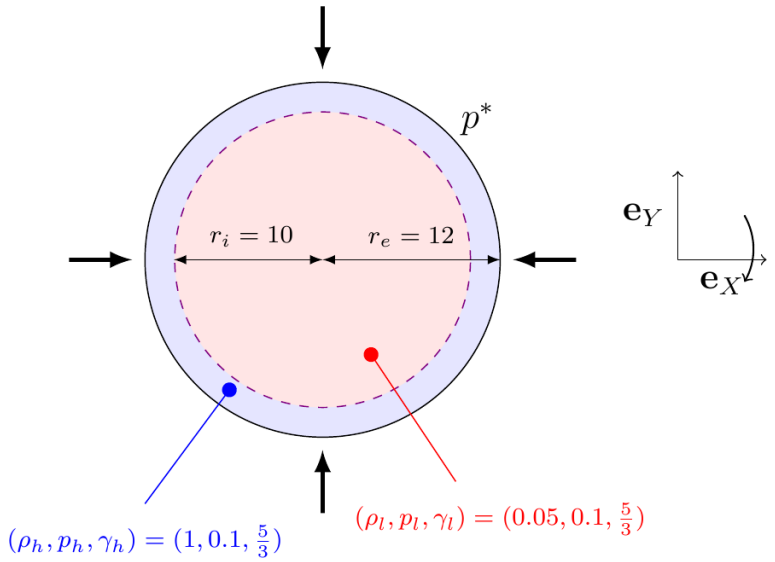

Figure 2.35: Multi-mode implosion in spherical geometry. Initial geometry and data.

The last test-case of this chapter deals with the numerical computation of a spherical implosion as initially treated in [166]. The interest of this simulation is twofold. First, this is a realistic problem quite close to those encountered in Ignition Confinement Fusion (ICF) simulation. Then, it allows to test the capability of the multi-material CCALE-MOF algorithm with hybrid rezoning.
Here we focus on the treatment of perturbed interfaces where compressible Rayleigh-Taylor instabilities occur.

Let us consider a spherical ball of light fluid ($r \in [0, 10]$) initially surrounded by a shell of heavy fluid ($R \in [10, 12]$) as depicted on FIG. 2.35. For both fluid the polytropic index is the same $\gamma_l = \gamma_h = \dfrac{5}{3}$. The initial pressures and densities are $(\rho_l, p_l) = (0.05, 0.1)$ and $(\rho_h, p_h) = (1, 0.1)$. The implosion is driven by imposing the following pressure law on the dense shell boundary

$$p^*(t) = \begin{cases} 10 & \text{if } t \in [0, 0.5], \\ 12 - 4t & \text{if } t \in [0.5, 3]. \end{cases}$$

Finally, the interface between the light and the heavy fluids is initially perturbed according to the law

$$r_p^{per} = r_p(1 + a_0 \mathcal{D}(r_p) P_l(\cos(\theta_p))$$

with the damping factor

$$\mathcal{D}(r_p) = \begin{cases} 1 - \dfrac{r_p - r_i}{r_e - r_i} & \text{if } r_p \in [r_i, r_e], \\ 1 - \dfrac{r_i - r_p}{r_i} & \text{if } r_p \in [0, r_i]. \end{cases}$$

where r_i^{per} denotes the perturbed radius and a_0 is the amplitude of the perturbation. Finally, P_l is the l^{th} Legendre polynomial. In the sequel $l = 10$ and several values of a_0 are considered from the non-perturbed case $a_0 = 0$, to weakly and strongly perturbed one with respectively $a_0 = 2 \times 10^{-4}$ and $a_0 = 1 \times 10^{-3}$.

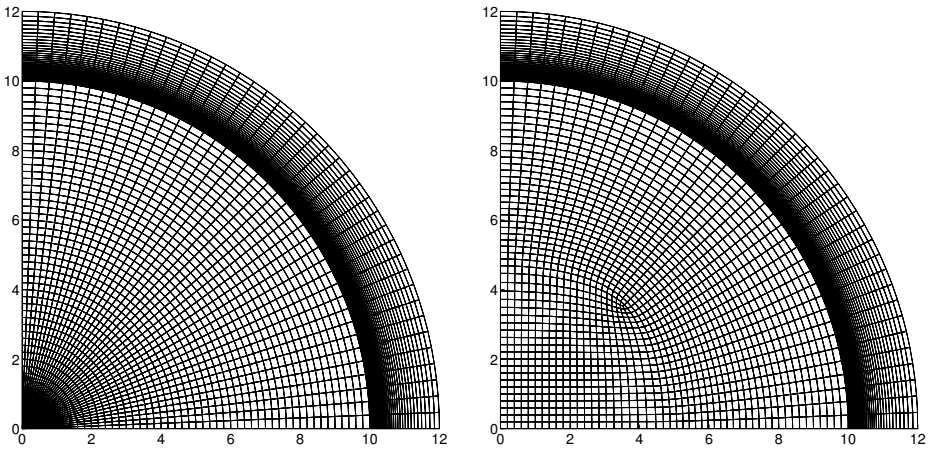

Figure 2.36: Spherical implosion. Initial polar (left) and unstructured (right) grids.

Computations are made for two different meshes until the final time $t_f = 3$. The first one is a polar grid displayed on FIG. 2.36-(left) composed of 90×40 cells. Size of cells in the radial direction have been chosen respecting a mass radial spacing deduced from the equivalent one-dimensional test case. The other grid, is obtained after an hybrid regularization for $\omega_p = 1$ of an unstructured mesh initially paved with 3200 quadrangular cells respecting the mass radial spacing (see FIG. 2.36-(right)).

Non-perturbed case with $a_0 = 0$. As a first study, we test the behavior of our algorithm in axisymmetric geometries in pure Lagrange computation for both meshes. One advantage of the unstructured mesh is to not impose a drastic time step for computation due to triangular cells with high aspect ratio in the polar mesh as shown in FIG. 2.37-(right).

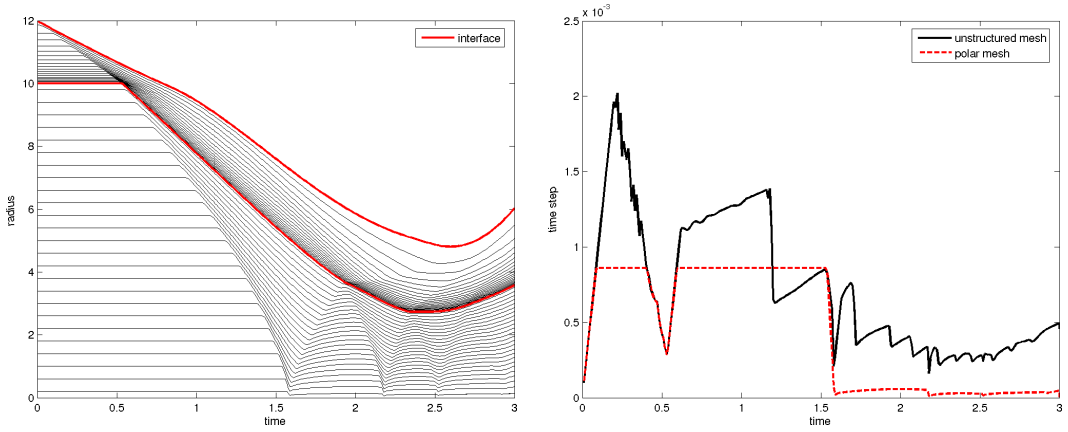

Figure 2.37: Spherical implosion without deformation. $t - R$ diagram constructed using polar grid (left). Time step history using two-dimensional grids (right).

The $t - R$ diagram is plotted in FIG. 2.37-(left) and represents the radius of each point on the symmetry axis $Y = 0$ of the polar grid as function of time. The red thick curves outline the inner and outer radii. This diagram allows to follow the waves that propagate in the shell. After time $t = 1.5$, the shock waves bounce between the center and the inner interface of the shell and decelerate the implosion of the shell. This phase is called the stagnation phase and finish when the inner interface radius reaches its minimum value. After this phase the light fluid present in the center of the shell is pushing the heavy fluid that surround it. This type of flow is unstable in the sense of the Rayleigh-Taylor instability. It leads to a phase wherein perturbation at the inner interface grow exponentially as a function of time.

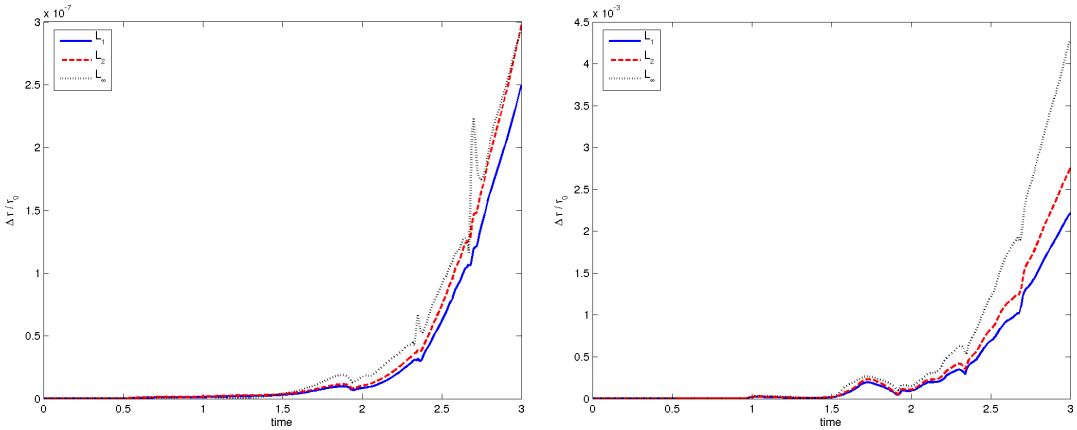

Figure 2.38: Spherical implosion without deformation. L_1, L_2 and L_∞ norms for symmetry preservation on polar grid (left) and unstructured grid (right).

To study the symmetry preservation of the non-perturbed case we define the following norms

$$L_\infty(t) = \max_{i=1,\dots,N_p} \frac{\mid r_i(t) - \bar{r}(t) \mid}{\bar{r}(t)},$$

$$L_1(t) = \frac{1}{N_p} \sum_{i=1}^{N_p} \frac{\mid r_i(t) - \bar{r}(t) \mid}{\bar{r}(t)},$$

$$L_2(t) = \frac{\sqrt{\frac{1}{N_p} \sum_{i=1}^{N_p} [r_i(t) - \bar{r}(t)]^2}}{\bar{r}(t)}.$$

Where $r_i(t)$ is the radius of a vertex at the inner interface and $\bar{r}(t)$ is the mean radius computed as

$$\bar{r}(t) = \frac{1}{N_p} \sum_{i=1}^{N_p} r_i(t),$$

with $N_p = 41$. Those norms are displayed for both grids in FIG. 2.38. The polar grid leads to the best symmetry preservation as the maximum deviation is around 3×10^{-7} whereas the unstructured grid deviation reaches 4.5×10^{-3}. This is due to the triple point present in the unstructured grid at the intersection of the different blocks of mesh. The unstructured grid is less stable than the polar mesh but as we can see on FIG. 2.39 the growth of the perturbations during the Rayleigh-Taylor phase is still not visible.

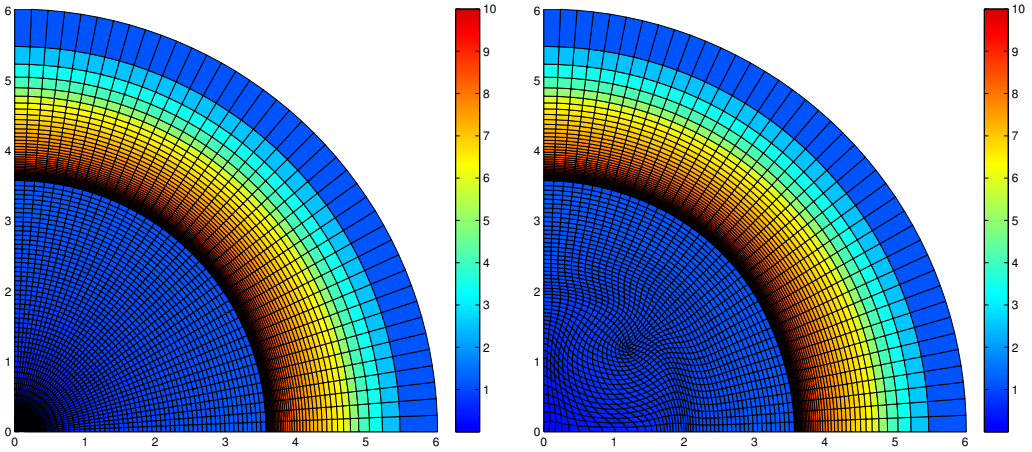

Figure 2.39: Spherical implosion without deformation. Mesh and density for polar (left) and unstructured (right) grids at final time $t_f = 3$.

Weakly perturbed case with $a_0 = 2 \times 10^{-4}$. Now, we investigate the capability of our CCALE-MOF algorithm to treat perturbed interfaces on both non-structured and polar meshes. To this end, comparisons with pure Lagrangian results are first achieved for weakly perturbed interfaces imposing $a_0 = 2 \times 10^{-4}$. Here for both polar and hybrid meshes, the GCNS is used. As demonstrated on FIG. 2.40, for the polar mesh as well as for the non-structured mesh, ALE results, especially concerning the interface deformation, are in very good agreement to those obtained thanks to pure Lagrangian computations. Furthermore, one should note that for the ALE computation on polar grid the quality of the mesh is improved near the origin. Indeed, the central cells are not systematically shifted to the origin contrary to computations achieved using CNS rezoning.

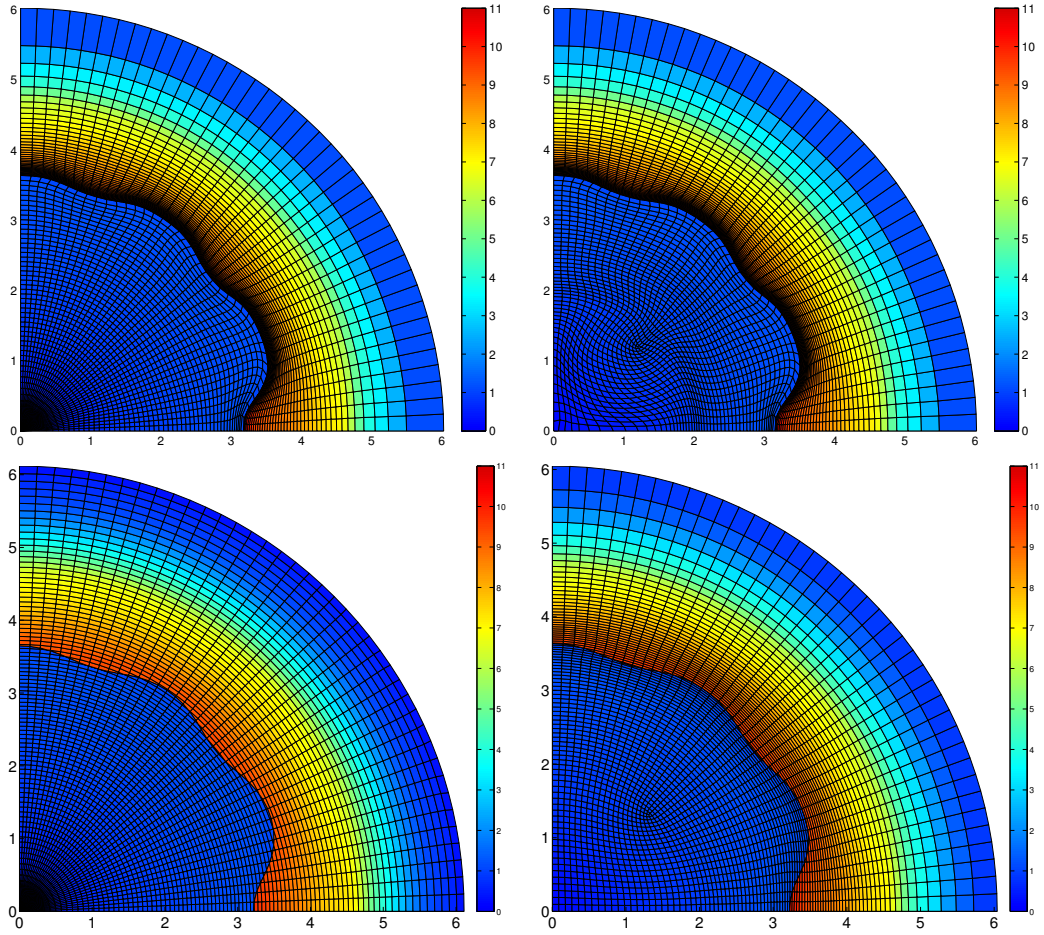

Figure 2.40: Spherical implosion with small deformation. Mesh and density for Lagrangian (top) and ALE (bottom) computations at final time $t_f = 3$ for both polar (left) and unstructured (right) grids.

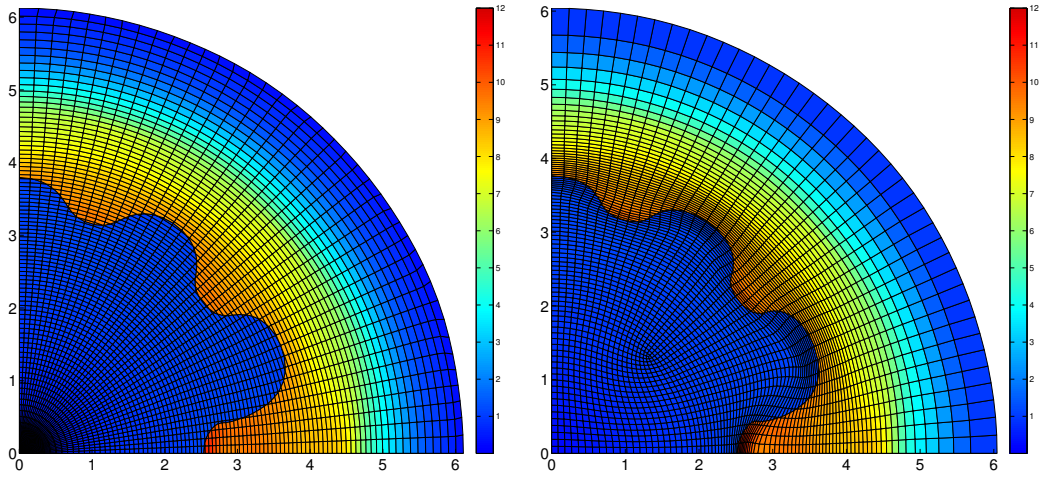

Figure 2.41: Spherical implosion with important deformation. Mesh and density for ALE computation for both polar (left) and unstructured (right) grids at final time $t_f = 3$.

Strongly perturbed case with $a_0 = 1 \times 10^{-3}$. Finally, we perform a computation of this implosion for a more pertubated interface choosing a_0 five times greater than previously with $a_0 = 1 \times 10^{-3}$. Due to mesh tangling, this is not possible to purchase such a test case using only Lagrangian method whose computation fails for $t > t_{fail} = 2.6$. Here, only results obtained thanks to our axisymmetric multi-material CCALE-MOF are presented. Contrary, to Lagrangian computations, the multi-material ALE simulations run without any difficulties thanks to specific rezoning. For both grids, final results (see FIG. 2.41) are very close. In particular we note the Rayleigh-Taylor instability has grown in a same way leading to similar interface shape deformation at final time.

Chapter 3

A multi-dimensional cell-centered finite volume scheme for solving anisotropic diffusion on unstructured grids

In this chapter we are interested in the resolution of anisotropic diffusion on non-conformal non-orthogonal 2D and 3D meshes. Simulation in the context of High Energy Density Physics (HEDP) and more precisely in the field of laser plasma interaction requires usually Lagrangian schemes for the hydrodynamics part. Therefore, the modelization of electron transport, which requires the resolution of anisotropic diffusion equation in the presence of magnetic field, should be done on distorted grids with a strong coupling between gas dynamics and diffusion [33]. Moreover, the lack of robustness of Lagrangian methods due to strong grid deformations requires usually to regularize the mesh through the use of Arbitrary Lagrangian Eulerian (ALE) methods [65]. Theses methods usually add some diffusion and a loss of precision is observed. In this paper we propose to use Adaptive Mesh Refinement (AMR) techniques to reduce this loss of accuracy. This work focus on the resolution of the anisotropic diffusion operator on ALE-AMR grids. AMR approach is a good candidate to capture fine physical details without using too many degrees of freedom, especially for 3D. AMR grids are usually based on quadrangular cells in 2D and hexahedral cells in 3D but they will present hanging-node between two level of refinement when two cells share a face with one cell. While classical AMR schemes deal with orthogonal meshes [81, 133, 167] we will use non-orthogonal grids as we want to couple our diffusion scheme with a Lagrangian or ALE hydrodynamics code in which the grid is moving and is thus deformed [9].
The Support Operator Method (SOM) also called Mimetic Finite Difference (MFD) method has been already used to solve diffusion equation on AMR like grids [98]. MFD method used in [98] is characterized by unknowns located at both cell-centers and face centers.
The resolution of anisotropic diffusion problems on unstructured distorted grids has motivated the development of the multi-point flux approximations (MPFA) scheme [1, 2, 62]. In this method, a multi-point expression is used to approximate the flux through transmissibility coefficients. These coefficients are computed using the point-wise continuity of the normal flux and the temperature across cell interfaces. There are many variants of the MPFA methods and the most popular for heterogeneous anisotropic diffusion problems is the MPFA O-scheme which is based on cell-centered unknowns and a local stencil. The global matrix obtained from this type of scheme is generally non-symmetric. However, the resolution of anisotropic diffusion problems on AMR grid with cellwise discontinuous diffusion coefficients can not be handled by

the O-scheme. A more recent MPFA method, the L-scheme, based on a more compact stencil is able to solve this drawback [3].

The numerical scheme we present here is an extension of the Cell-Centered Lagrangian Diffusion (CCLAD or CCLADS) scheme first presented in [36] in 2D and then extended in 3D in [86]. We will focus here on the Non-Symmetric version of this scheme (CCLADNS) described in [115]. This scheme has similarity with the MPFA scheme as it is based on piecewise linear reconstruction and continuity conditions on mesh edges. This scheme is a cell-centered finite volume scheme that solves the anisotropic heat conduction equation and we will extend it here for d-dimensional AMR grids.

Let us first introduce the governing equations for the present work. The domain $\Omega(t) \in \mathfrak{R}^d$ is an open set of the d-dimensional space and $\Sigma(t)$ its boundary. The position vector of an arbitrary point inside the domain is denoted by $\boldsymbol{x}$. The goal is to construct a numerical scheme which solves the following initial-boundary-value problem for the temperature $T = T(\boldsymbol{x}, t)$

$$\rho C_v \frac{\partial T}{\partial t} + \nabla \cdot \boldsymbol{q} = \rho r, \qquad (\boldsymbol{x}, t) \in \Omega(t) \tag{3.1a}$$

$$T(\boldsymbol{x}, 0) = T^0(\boldsymbol{x}), \qquad \boldsymbol{x} \in \Omega(t) \tag{3.1b}$$

$$T(\boldsymbol{x}, t) = T^*(\boldsymbol{x}, t), \qquad \boldsymbol{x} \in \Sigma(t)_D \tag{3.1c}$$

$$\boldsymbol{q}(\boldsymbol{x}, t) \cdot \boldsymbol{n} = q_N^*(\boldsymbol{x}, t), \qquad \boldsymbol{x} \in \Sigma(t)_N \tag{3.1d}$$

Here, ρ, C_v and r denote respectively the density of the material, the heat capacity at constant volume and a source term. The initial condition is given by the initial temperature field T^0. Two types of boundary conditions are considered here: Dirichlet and Neumann boundary conditions. They consist in specifying respectively the temperature and the flux. We introduce the partition $\Sigma(t) = \Sigma(t)_D \cup \Sigma(t)_N$ of the boundary domain. Here, T^* and q_N^* denote respectively the prescribed temperature and flux for the Dirichlet and Neumann boundary conditions. The vector $\boldsymbol{q}$ denotes the heat flux and $\boldsymbol{n}$ is the outward unit normal to the boundary of the domain $\Omega(t)$.

Equation (3.1a) is a parabolic partial differential equation for the temperature T, where the conductive flux, $\boldsymbol{q}$, is defined according to the Fourier law

$$\boldsymbol{q} = -\mathbb{K}\nabla T. \tag{3.2}$$

Where the second-order tensor $\mathbb{K}$, is the conductivity tensor which is an intrinsic property of the material under consideration. In the next section we present the three-dimensional extension of the CCLADNS scheme, originally described in 2D by Maire and Breil in [115], following the approach presented in 3D in [86]. Then we will discuss the two-dimensional extension to AMR meshes before introducing the three-dimensional extension of the 3D AMR version of the CCLADNS scheme. Finally, we will present some numerical results which illustrate the accuracy of the CCLADNS scheme.

3.1 Space discretization of the CCLADNS scheme in three dimensions

We now present the space discretization of the CCLADNS scheme in three-dimensional geometries. We first recall the notations needed to describe the three-dimensional scheme [86] and we use them along with the CCLADNS approach described in [115].

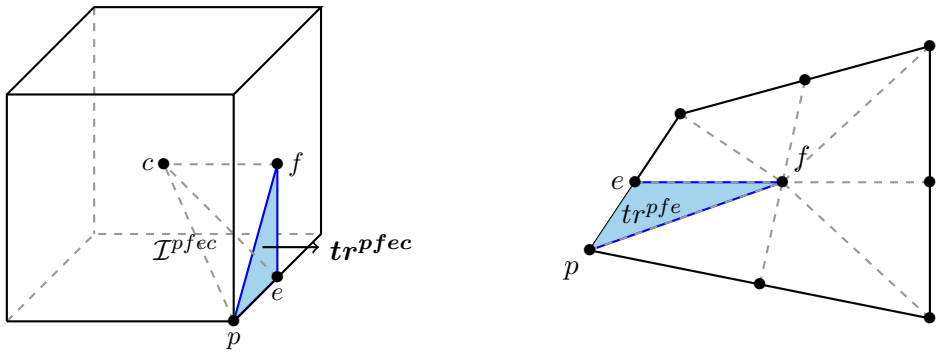

Figure 3.1: Representation of the iota $\mathcal{I}^{pfec}$ and the outward normal vector $\boldsymbol{tr}^{pfec}$ related to point p, face f and edge e in the hexahedral cell c (left). Quadrilateral face, f, related to the hexahedral cell ω_c. The sub-face, S_p^f, related to point p and face f is obtained by gathering the triangular faces corresponding to the triangles tr^{pfe} (right).

3.1.1 Geometrical notations

Let us dicretize the spatial domain $\Omega(t)$ in N_c non-overlapping polyhedrons denoted ω_c such that $\Omega(t) = \bigcup_c \omega_c$. The list of vertices (points) of cell c is denoted by $\mathcal{P}(c)$. In addition, p being a generic point, we denote by $\boldsymbol{x}_p$ its position vector and by $\mathcal{C}(p)$ the set of all the cells surrounding point p. To complete the cell geometry description, we introduce the set $\mathcal{F}(c)$ as being the list of the faces of cell c. A face can be denoted either by the index f or by $\partial\omega_c^f$. Here, the mesh is composed of polyhedral cells, which is a volume enclosed by an arbitrary number of faces. Each face is determined by an arbitrary number (3 or more) of vertices. In 3D, a face which have four or more vertices, can be non-coplanar, thus the face is not a plane and it is difficult to define its unit outward normal. To overcome this problem, we use the decomposition of a polyhedral cell into elementary tetrahedrons, as introduced by Burton in [38]. Using the same terminology, these elementary tetrahedrons are called iotas, since ι is the smallest letter in the Greek alphabet. Being given the polyhedral cell c, we consider the vertex $p \in \mathcal{P}(c)$ which belongs to the face $f \in \mathcal{F}(c)$ and the edge e. The iota, denoted $\mathcal{I}^{pfec}$, related to point p, face f and edge e of cell c, is constructed by connecting point p, the centroid of cell c, the centroid of face f and the midpoint of edge e as displayed in FIG. 3.1. Furthermore, we denote by $\boldsymbol{tr}^{\boldsymbol{pfec}}$, the outward normal vector of the triangular face obtained by connecting the point p to the midpoint of edge e and the centroid of face f related to cell c. Let us point out that $tr^{pfe} = |\, \boldsymbol{tr}^{\boldsymbol{pfec}} \,|$ is the area of the triangular face (FIG. 3.1).

The set of sub-faces, $\{\partial\omega_{pc}^f, \quad p \in \mathcal{P}(c,f)\}$, where $\mathcal{P}(c,f)$ is the set of points of cell c lying on face f, is a partition of the face f. From this decomposition we can define the set $\mathcal{F}(p,c)$, which is the list of sub-faces related to the faces f of cell c impinging at point p. We observe that the former set is linked to the latter by $\mathcal{F}(c) = \cup_{p\in\mathcal{P}(c)}\mathcal{F}(p,c)$. We can also define the decomposition of the polyhedral cell ω_c into sub-cells ω_{pc} as shown in FIG. 3.2. The sub-cell ω_{pc} related to point p is obtained by gathering the iotas attached to point p as follows

$$\omega_{pc} = \bigcup_{f\in\mathcal{F}(p,c)} \quad \bigcup_{e\in\mathcal{E}(p,f)} \mathcal{I}^{pfec},$$

where $\mathcal{E}(p,f)$ is the set of the edges of face f holding point p. For the hexahedral cell displayed in FIG. 3.2, the sub-cell ω_{pc} is made of 6 iotas since there are 3 faces impinging at point p and

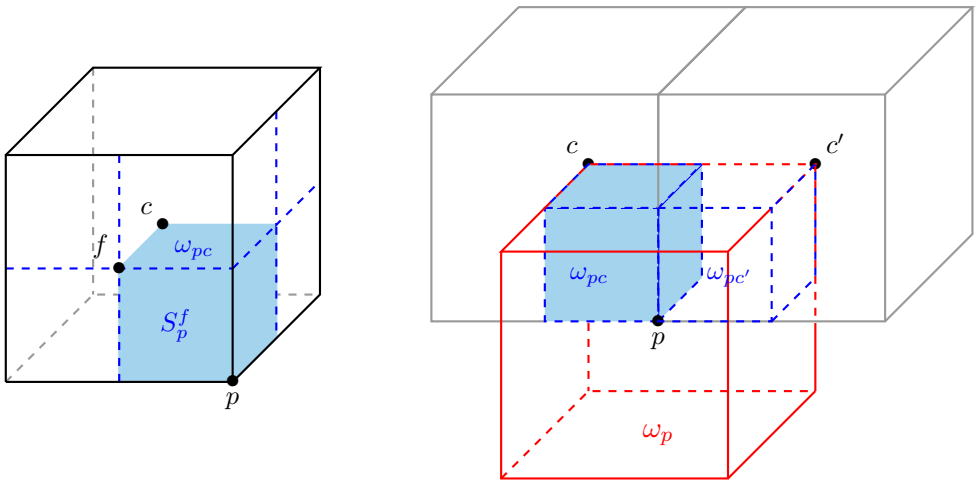

Figure 3.2: Representation of the sub-cell ω_{pc}, the sub-face S_p^f (left) and the dual-cell ω_p (right) in the simple case of hexahedral cells with square faces.

two edges connected to point p (cf. FIG. 3.1). The volume of the sub-cell ω_{pc} is then given by

$$| \omega_{pc} | = \sum_{f \in \mathcal{F}(p,c)} \sum_{e \in \mathcal{E}(p,f)} | \mathcal{I}^{pfec} | .$$

The polyhedral cell c can be reconstructed using the set of sub-cells, $\{\omega_{pc}, \ p \in \mathcal{P}(c)\}$, and thus the cell volume is defined by

$$| \omega_c | = \sum_{p \in \mathcal{P}(c)} | \omega_{pc} | .$$

We can finally define the dual cell ω_p related to node p, by gathering all the sub-cells ω_{pc} around this node as

$$\omega_p = \bigcup_{c \in \mathcal{C}(p)} \omega_{pc},$$

where $\mathcal{C}(p)$ is the set of all the cells sharing node p. The dual cell ω_p is displayed in FIG. 3.2 in the simple case of an hexahedral cell.

The sub-face related to point p and face f is denoted by $\partial\omega_{pc}^f$ and defined as $\partial\omega_{pc}^f = \omega_{pc} \cap \partial\omega_c^f$. It consists of the union of the two outer triangular faces attached to the two iotas related to point p and face f, refer to FIG. 3.2. The area and the unit outward normal of the sub-face $\partial\omega_{pc}^f$ are respectively given by

$$S_p^f = \sum_{e \in \mathcal{E}(p,f)} tr^{pfe} \quad \text{and} \quad \boldsymbol{n}_{pc}^f = \frac{1}{S_p^f} \sum_{e \in \mathcal{E}(p,f)} \boldsymbol{tr}^{pfec}.$$

3.1.2 Scheme construction

To proceed with the construction of the numerical scheme, let us integrate (3.1) over ω_c and make use of the divergence formula

$$m_c C_{vc} \frac{d}{dt} T_c + \int_{\partial\omega_c} \boldsymbol{q} \cdot \boldsymbol{n} \, \mathrm{d}s = m_c r_c, \tag{3.3}$$

Here, m_c denotes the mass of the cell such that, $m_c = \rho_c \mid \omega_c \mid$ where $\boldsymbol{n}$ denotes the unit outward normal of the cell boundary $\partial\omega_c$. Let us point out that $T_c = T_c(t)$ is nothing but the mean value of the temperature over ω_c such that

$$T_c(t) = \frac{1}{\mid \omega_c \mid} \int_{\omega_c} T(\boldsymbol{x}, t)\, \mathsf{d}v.$$

To finish the space discretization of (3.3), it remains to discretize the surface integral of the heat flux. Knowing that $\partial\omega_c = \cup_{f\in\mathcal{F}(c)}\partial\omega_c^f$ the surface integral of the heat flux reads

$$\int_{\partial\omega_c} \boldsymbol{q}\cdot\boldsymbol{n}\, \mathsf{d}s = \sum_{f\in\mathcal{F}(c)} \int_{\partial\omega_c^f} \boldsymbol{q}\cdot\boldsymbol{n}\, \mathsf{d}s.$$

Now, recalling the partition of face f into sub-faces, *i.e.*, $\partial\omega_c^f = \cup_{p\in\mathcal{P}(c,f)}\partial\omega_{pc}^f$, leads to

$$\begin{aligned}\int_{\partial\omega_c} \boldsymbol{q}\cdot\boldsymbol{n}\, \mathsf{d}s &= \sum_{f\in\mathcal{F}(c)} \sum_{p\in\mathcal{P}(c,f)} \int_{\partial\omega_{pc}^f} \boldsymbol{q}\cdot\boldsymbol{n}\, \mathsf{d}s \\ &= \sum_{p\in\mathcal{P}(c)} \sum_{f\in\mathcal{F}(p,c)} \int_{\partial\omega_{pc}^f} \boldsymbol{q}\cdot\boldsymbol{n}\, \mathsf{d}s.\end{aligned}$$

Let us denote by q_{pc}^f the piecewise constant representation of the normal component of the heat flux over sub-face $\partial\omega_{pc}^f$ such that

$$q_{pc}^f = \frac{1}{S_p^f} \int_{\partial\omega_{pc}^f} \boldsymbol{q}\cdot\boldsymbol{n}\, \mathsf{d}s. \tag{3.4}$$

Gathering the above results, Equation (3.3) turns into

$$m_c C_{vc} \frac{\mathsf{d}}{\mathsf{d}t} T_c + \sum_{p\in\mathcal{P}(c)} \sum_{f\in\mathcal{F}(p,c)} S_p^f q_{pc}^f = m_c r_c. \tag{3.5}$$

Moreover, we introduce the sub-face temperature T_{pc}^f, which is useful in the description of our scheme as an auxiliary unknown and is defined as

$$T_{pc}^f = \frac{1}{S_p^f} \int_{\partial\omega_{pc}^f} T(\boldsymbol{x}, t)\, \mathsf{d}s. \tag{3.6}$$

Writing this equation, we also assumed a piecewise constant approximation of the temperature field over each sub-face.

Let consider two neighboring cells denoted by c and c' sharing a face and a point. The sub-cells ω_{pc} and $\omega_{pc'}$ are sharing the sub-face $\partial\omega_{pc}^f \equiv \partial\omega_{pc'}^f$, as displayed in FIG. 3.2. We can now use the continuity conditions, in terms of sub-face fluxes and sub-face temperatures. From the sub-cell ω_{pc} the sub-face temperature and the sub-face flux are denoted by T_{pc}^f and q_{pc}^f, whereas from the sub-cell $\omega_{pc'}$ they are denoted respectively by $T_{pc'}^f$ and $q_{pc'}^f$. As the unit outward normal satisfy $\boldsymbol{n}_{pc}^f = -\boldsymbol{n}_{pc'}^f$ leads to write the continuity conditions for the temperatures and the heat flux as

$$S_p^f q_{pc}^f + S_p^f q_{pc'}^f = 0, \tag{3.7a}$$

$$T_{pc}^f = T_{pc'}^f = T_p^f. \tag{3.7b}$$

Using these continuity conditions we can define T_p^f as the sub-face temperature. To achieve the space discretization of (3.5), it remains to construct an approximation of the sub-face normal flux, that is to say to define a numeric sub-face flux function h_{pc}^f such that:

$$q_{pc}^f = h_{pc}^f(T_p^1 - T_c, \ldots, T_p^k - T_c, \ldots, T_p^{\mathfrak{F}_{pc}} - T_c), \quad \forall f \in \mathcal{F}(p,c), \tag{3.8}$$

where $\mathfrak{F}_{pc}$ denotes the number of faces of cell c impinging at point p, and is defined as $\mathfrak{F}_{pc} = |\mathcal{F}(p,c)|$.

To write the scheme we are going to define an approximation of the sub-face numerical fluxes in terms of sub-face temperatures and cell-centered temperatures. We shall then eliminate the sub-face temperatures using the continuity conditions (3.7) across the sub-faces interfaces.

3.1.3 Expression of a vector in terms of its normal components

Here, we describe the methodology to reconstruct a three-dimensional vector at a vertex of a polyhedron from the normal components related to the sub-faces impinging at this vertex. Let $\boldsymbol{\phi}$ be an arbitrary vector of the three-dimensional space $\mathfrak{R}^3$ and $\boldsymbol{\phi}_{pc}$ its piecewise constant approximation over the sub-cell ω_{pc}. Let ϕ_{pc}^f be the sub-face normal component of $\boldsymbol{\phi}_{pc}$ defined by

$$\boldsymbol{\phi}_{pc} \cdot \boldsymbol{n}_{pc}^f = \phi_{pc}^f, \quad \forall f \in \mathcal{F}(p,c),$$

This relation leads to a 3×3 linear system, where the unknowns are the Cartesian components of the vector $\boldsymbol{\phi}_{pc}$. This system is properly defined provided that $\mathfrak{F}_{pc} = 3$ which implies that the number of faces of cell c impinging at point p must be strictly equal to 3. We assume here that the polyhedral cells we are using are characterized by $\mathfrak{F}_{pc} = 3$. Let us remark that this restriction allows us to cope with tetrahedrons, hexahedrons and prisms. The extension to the case $\mathfrak{F}_{pc} > 3$ will be investigated in the case of AMR cells.

Introducing the corner matrix $\mathbb{J}_{pc} = [\boldsymbol{n}_{pc}^1, \boldsymbol{n}_{pc}^2, \boldsymbol{n}_{pc}^3]$ enables to rewrite the above linear system as

$$\mathbb{J}_{pc}^t \boldsymbol{\phi}_{pc} = \begin{pmatrix} \phi_{pc}^1 \\ \phi_{pc}^2 \\ \phi_{pc}^3 \end{pmatrix},$$

where the superscript t denotes the transpose matrix. Granted that the vectors $\boldsymbol{n}_{pc}^f$, for $f = 1 \ldots 3$, are not colinear, the above linear system has always a unique solution which reads

$$\boldsymbol{\phi}_{pc} = \mathbb{J}_{pc}^{-t} \begin{pmatrix} \phi_{pc}^1 \\ \phi_{pc}^2 \\ \phi_{pc}^3 \end{pmatrix}. \tag{3.9}$$

3.1.4 Sub-cell linear approximation

In this section we want to find a way to express the numerical flux q_{pc}^f. Different methods can be used. For instance we can build a sub-cell-based variational formulation of the Fourier Law which lead us to the construction the CCLADS scheme described in its three-dimensional version in [86]. In this paper, we extend the CCLADNS [115] scheme which rely on a piecewise linear approximation of the temperatures in the sub-cell.

Let us write T_h the piecewise linear approximation of the temperature over the cell ω_c as

$$T_h(\boldsymbol{x}) = T_c - \mathbb{K}_c^{-1} \boldsymbol{q}_c \cdot (\boldsymbol{x} - \boldsymbol{x}_c), \tag{3.10}$$

where $\boldsymbol{x}_c$ is the centroid of the cell, defined as $\boldsymbol{x}_c = \frac{1}{|\omega_c|}\int_{\omega_c} \boldsymbol{x}\,\mathrm{d}v$ and $\boldsymbol{q}_c = -\mathbb{K}_c(\boldsymbol{\nabla}T)_c$ is the piecewise approximation of the heat flux. We want to compute the temperatures in the sub-cell ω_{pc} at the sub-faces S_p^f, so we can write

$$\overline{T}_p^f - T_c = -\mathbb{K}_c^{-1}\boldsymbol{q}_c \cdot (\overline{\boldsymbol{x}}_p^f - \boldsymbol{x}_c). \tag{3.11}$$

The bar notation help us to make the difference between the cell centered unknown and the sub-face unknown. Let us note $\boldsymbol{x}_{pc}^f = \overline{\boldsymbol{x}}_p^f - \boldsymbol{x}_c$. Where $\overline{\boldsymbol{x}}_p^f$ denote the vector position of the sub-face centroid. This sub-face centroid can be obtain from the centroid of the two triangles of the sub-face S_p^f.
Using the normal vector decomposition and introducing $\boldsymbol{q}_{pc}$ as the heat flux in the sub-cell ω_{pc} we obtain

$$\overline{T}_p^f - T_c = -\mathbb{K}_c^{-1}\boldsymbol{q}_{pc} \cdot \boldsymbol{x}_{pc}^f. \tag{3.12}$$

Using the normal vector decomposition methodology (3.9)

$$\overline{T}_p^f - T_c = -\mathbb{K}_c^{-1}\mathbb{J}_{pc}^{-t}\begin{pmatrix} q_{pc}^1 \\ q_{pc}^2 \\ q_{pc}^3 \end{pmatrix} \cdot \boldsymbol{x}_{pc}^f. \tag{3.13}$$

Now, noticing that

$$\boldsymbol{x}_{pc}^f = \mathbb{J}_{pc}^{-t}\mathbb{J}_{pc}^t\boldsymbol{x}_{pc}^f = \mathbb{J}_{pc}^{-t}\begin{pmatrix} \boldsymbol{x}_{pc}^f \cdot \boldsymbol{n}_{pc}^1 \\ \boldsymbol{x}_{pc}^f \cdot \boldsymbol{n}_{pc}^2 \\ \boldsymbol{x}_{pc}^f \cdot \boldsymbol{n}_{pc}^3 \end{pmatrix}, \tag{3.14}$$

and introducing the matrix $\mathbb{X}_{pc}^{i,j} = \boldsymbol{x}_{pc}^i \cdot \boldsymbol{n}^j$ enables to write

$$\overline{T}_p^f - T_c = -\mathbb{J}_{pc}^{-1}\mathbb{K}_c^{-1}\mathbb{J}_{pc}^{-t}\begin{pmatrix} q_{pc}^1 \\ q_{pc}^2 \\ q_{pc}^3 \end{pmatrix} \cdot \begin{pmatrix} \mathbb{x}_{pc}^{f,1} \\ \mathbb{x}_{pc}^{f,2} \\ \mathbb{x}_{pc}^{f,3} \end{pmatrix}. \tag{3.15}$$

We introduce the sub-cell conductivity tensor

$$\mathbb{K}_{pc} = \mathbb{J}_{pc}^t\mathbb{K}_c\mathbb{J}_{pc}. \tag{3.16}$$

Using the previous relations we can write for the three sub-faces impinging at node p

$$\begin{pmatrix} \overline{T}_p^1 - T_c \\ \overline{T}_p^2 - T_c \\ \overline{T}_p^3 - T_c \end{pmatrix} = -\mathbb{X}_{pc}\mathbb{K}_{pc}^{-1}\begin{pmatrix} q_{pc}^1 \\ q_{pc}^2 \\ q_{pc}^3 \end{pmatrix}, \tag{3.17}$$

which rewrites

$$\begin{pmatrix} q_{pc}^1 \\ q_{pc}^2 \\ q_{pc}^3 \end{pmatrix} = -\mathbb{K}_{pc}\mathbb{X}_{pc}^{-1}\begin{pmatrix} \overline{T}_p^1 - T_c \\ \overline{T}_p^2 - T_c \\ \overline{T}_p^3 - T_c \end{pmatrix}. \tag{3.18}$$

Since the sub-face normal fluxes are deduce from a piecewise linear approximation of the temperature field, Equation (3.18) can be seen as a finite difference approximation of q_{pc}^f. The main drawback of this procedure is that the matrix defined by the normal components of $\mathbb{X}_{pc}$ is not a symmetric positive definite in general. However, we will show that using this approximation of the flux q_{pc}^f enables to preserves linear solution regardless the shape of the cells.

3.1.5 Elimination of the sub-face temperatures

Having defined the flux approximation in the sub-cell ω_{pc} in term of the difference between the sub-face and the cell temperatures, we shall express the sub-face temperatures in terms of the cell temperatures which are surrounding a specific point p of the dual cell ω_p (see FIG. 3.2). In order to have a simpler expression of the equations we are going to introduce some new local notations. First of all, in this section we are dealing with quantities located around a point p, so in all the notations we will omit to specify the subscript p. With this notation a sub-face temperature $\overline{T}_p^f$ is denoted by $\bar{T}^f$. For each face f in the list $\mathcal{F}(p)$ of the faces impinging at the node p we associate two tuples (c,i) and (c',j) which identify the neighboring cells c and c' of the face f and their local numbering i (resp. j) in the subset $\mathcal{F}(p,c)$ (resp. $\mathcal{F}(p,c')$) of $\mathcal{F}(p)$. With this notation a sub-face temperature $\overline{T}_{pc}^i$ is denoted by $\bar{T}_c^i$ and using the continuity condition on the temperature is equal to $\overline{T}_{pc'}^j$ which is denoted $\bar{T}_{c'}^j$ and can also be simply denoted by $\bar{T}^f$. The bar notation help us to make the difference between the cell centered unknown and the sub-face unknown. Similarly the area of the sub-face f can be indifferently noted S_c^i, $S_{c'}^j$ or S^f. We also introduce $\mathbb{L}_{pc} = \mathbb{K}_{pc}\mathbb{X}_{pc}^{-1}$ which will be denoted by $\mathbb{L}^c$ so its components $(\mathbb{L}_{pc})_{ij}$ can be written $\mathbb{L}_{ij}^c$.

Using this notation Equation (3.18), which defines the heat flux approximation, rewrites

$$q_c^i = -\sum_{k=1}^{3} \mathbb{L}_{ik}^c (\bar{T}_c^k - T_c). \tag{3.19}$$

The continuity condition (3.7a) of the sub-face fluxes across the face $f \equiv (c,i) \equiv (c',j)$ reads

$$S_c^i q_c^i + S_{c'}^j q_{c'}^j = 0.$$

Replacing the sub-face fluxes by their approximation (3.19) into the above equation yields to

$$-S_c^i \sum_{k=1}^{3} \mathbb{L}_{ik}^c (\bar{T}_c^k - T_c) - S_{c'}^j \sum_{k=1}^{3} \mathbb{L}_{jk}^{c'} (\bar{T}_{c'}^k - T_{c'}) = 0.$$

Let us point out that this equation holds for all the faces f impinging at node p, *i.e.* for all $f \in \mathcal{F}(p)$. Denoting by $\mathfrak{F}_p = |\mathcal{F}(p)|$ the number of faces impinging at node p, the set of all the above equations forms a $\mathfrak{F}_p \times \mathfrak{F}_p$ linear system, which can be written under the compact form

$$\mathbb{M}\bar{\boldsymbol{T}} = \mathbb{N}\boldsymbol{T}. \tag{3.20}$$

Here, the matrix $\mathbb{M}$ is a $\mathfrak{F}_p \times \mathfrak{F}_p$ square matrix and $\bar{\boldsymbol{T}} \in \mathfrak{R}^{\mathfrak{F}_p}$ is the vector of sub-face temperatures. Denoting by $\mathfrak{C}_p = |\mathcal{C}(p)|$ the number of cells surrounding node p, the matrix $\mathbb{N}$ is a $\mathfrak{F}_p \times \mathfrak{C}_p$ rectangular matrix and $\boldsymbol{T} \in \mathfrak{R}^{\mathfrak{C}_p}$ is the vector of cell temperatures. The matrix $\mathbb{M}$ has five non-zero terms on each lines, its diagonal element writes

$$\mathbb{M}_{ff} = S_c^i \mathbb{L}_{ii}^c + S_{c'}^j \mathbb{L}_{jj}^{c'}.$$

Regarding its extra-diagonal parts, two terms come from the contribution of the sub-cell ω_{pc}. Let g be a generic face of cell c impinging at point p characterized by the index k in the local numbering , *i.e.*, $g \equiv (c,k)$, then the extra-diagonal entries related to cell c and faces i and k write

$$\mathbb{M}_{fg} = S_c^i \mathbb{L}_{ik}^c, \quad \text{for} \quad k \in [1,3] \quad \text{and} \quad k \neq i.$$

The two remaining terms come from the sub-cell $\omega_{pc'}$. Let g be a generic face of cell c' impinging at point p characterized by the index k in the local numbering , *i.e.*, $g \equiv (c', k)$, then the extra-diagonal entries related to cell c' and faces j and k write

$$\mathbb{M}_{fg} = S^j_{c'} \mathbb{L}^{c'}_{jk}, \quad \text{for} \quad k \in [1,3] \quad \text{and} \quad k \neq j$$

Let us remark that in general the matrix $\mathbb{M}$ is not symmetric positive definite as it has been noticed for the 2D version of the CCLADNS scheme [115] and it will lead to a non-symmetric diffusion matrix.

Finally, the matrix $\mathbb{N}$ has two non-zero terms on each row, one term for each neighboring cell c and c' of the face f

$$\mathbb{N}_{fc} = \sum_{k=1}^{3} S^i_c \mathbb{L}^c_{ik} \quad \text{and} \quad \mathbb{N}_{fc'} = \sum_{k=1}^{3} S^j_{c'} \mathbb{L}^{c'}_{jk}.$$

3.1.6 Construction of the global diffusion matrix

In this section, we gather the results obtained in the previous sections to achieve the space discretization of the diffusion Equation (3.5).

$$m_c C_{vc} \frac{\mathsf{d}}{\mathsf{d}t} T_c + \sum_{p \in \mathcal{P}(c)} \sum_{f \in \mathcal{F}(p,c)} S^f_p q^f_{pc} = m_c r_c.$$

We define the contribution of the sub-cell ω_{pc} to the diffusion flux as

$$Q_{pc} = \sum_{f \in \mathcal{F}(p,c)} S^f_p q^f_{pc}.$$

Using the local numbering of the sub-faces surrounding point p yields to rewrite the above expression as

$$Q_{pc} = \sum_{k=1}^{3} S^k_c q^k_c.$$

Now, we replace the normal flux by its corresponding expression (3.19) leading to

$$Q_{pc} = -\sum_{k=1}^{3} S^k_c \sum_{i=1}^{3} \mathbb{L}^c_{ki} (\bar{T}^i_c - T_c)$$

, Then switching the order of the summations yields to

$$Q_{pc} = -\sum_{i=1}^{3} \sum_{k=1}^{3} (S^k_c \mathbb{L}^c_{ki}) (\bar{T}^i_c - T_c).$$

To obtain a more compact form of Q_{pc}, we define the matrix $\widetilde{\mathbb{N}}$ whose elements write

$$\widetilde{\mathbb{N}}_{fc} = \sum_{k=1}^{3} (S^k_c \mathbb{L}^c_{ki}), \tag{3.21}$$

where $f \equiv (c, i)$. Employing this notation, the sub-cell contribution to the diffusion flux reads

$$Q_{pc} = -\sum_{f \in \mathcal{F}(p)} \widetilde{\mathbb{N}}^t_{cf} (\bar{T}^f - T_c).$$

Eliminating the sub-face temperatures by means of (3.20) leads to

$$Q_{pc} = -\sum_{d\in\mathcal{C}(p)} \mathbb{G}^p_{cc'}(T_{c'} - T_c), \tag{3.22}$$

where $\mathbb{G}^p$ is a $\mathfrak{C}_p \times \mathfrak{C}_p$ matrix defined at point p by $\mathbb{G}^p = \widetilde{\mathbb{N}}^t\mathbb{M}^{-1}\mathbb{N}$. Let us point out that the entries of $\mathbb{G}^p$ have the physical dimension of a conductivity. Thus, it can be viewed as the effective conductivity tensor at point p in the dual cell ω_p. More precisely, it follows from (3.22) that the entry $\mathbb{G}^p_{cc'}$ stands for the effective conductivity between cells c and c' through the point p. This node-based effective conductivity tensor will be the cornerstone to assemble the global diffusion matrix over the computational grid. We can now write the semi-discrete scheme as

$$m_c C_{vc}\frac{\mathsf{d}}{\mathsf{d}t}T_c - \sum_{p\in\mathcal{P}(c)}\sum_{c'\in\mathcal{C}(p)} \mathbb{G}^p_{cc'}(T'_c - T_c) = m_c r_c, \tag{3.23}$$

This equation allows to construct the generic entries of the global diffusion matrix $\mathbb{D}$ as follows

$$\mathbb{D}_{cc} = \sum_{p\in\mathcal{P}(c)}\sum_{c'\in\mathcal{C}(p)} \mathbb{G}^p_{cc'} \text{ and } \mathbb{D}_{cc'} = -\sum_{p\in\mathcal{P}(c)} \mathbb{G}^p_{cc'}, c \neq c'.$$

If $\mathfrak{C}_\mathcal{D}$ denotes the total number of cells composing the computational grid, then matrix $\mathbb{D}$ is a $\mathfrak{C}_\mathcal{D} \times \mathfrak{C}_\mathcal{D}$ square matrix. The vector of cell-centered temperatures $\boldsymbol{\mathcal{T}} \in \mathfrak{R}^{\mathfrak{C}_\mathcal{D}}$ is the solution of the system of differential equations

$$\mathbb{W}\mathbb{C}_v\frac{\mathsf{d}}{\mathsf{d}t}\boldsymbol{\mathcal{T}} + \mathbb{D}\boldsymbol{\mathcal{T}} = \mathbb{W}\boldsymbol{\mathcal{R}}. \tag{3.24}$$

Here, $\boldsymbol{\mathcal{R}} \in \mathfrak{R}^{\mathfrak{C}_\mathcal{D}}$ is the source term vector, $\mathbb{W}$ is the weight matrix and $\mathbb{C}_v$ the heat capacity matrix. Those matrices are diagonal and their entries are respectively the cell mass m_c and the cell heat capacity C_{vc}. Time discretization can be performed using a first-order implicit discrete scheme as in [86].

3.2 CCLADNS for Adaptive Mesh Refinement

As it has been already shown in [115] the CCLADNS scheme can achieve second order convergence rate on different mesh types, even on polygonal cells. We will see here that while an AMR cell can be viewed as a polygonal cell, the CCLADNS scheme exhibits a singularity around the AMR nodes (also called hanging nodes). Before describing this issue, we recall the CCLADNS scheme on two dimensional geometries.

3.2.1 CCLADNS scheme in the case of non-conformal cell in two-dimensional geometries

Let us first introduce some notations needed to develop the discretization scheme in two dimensions of space. Being given $p \in \mathcal{P}(c)$, a node belonging to cell c, we note p^- and p^+ the previous and the following points with respect to p in the ordered list of vertices of cell c. Let ω_c be a generic polygonal cell, for each vertex $p \in \mathcal{P}(c)$, we define the sub-cell ω_{pc} which connects the centroid of ω_c to the midpoints of edges $e^- = [p^-, p]$ and $e^+ = [p, p^+]$ impinging at node p, refer to Fig. 3.3. In two dimensions, the sub-cell we defined, is always a quadrilateral. We can see in Fig. 3.3 that in the case of an AMR cell, the sub-cell ω_{pc} degenerates into a triangle.

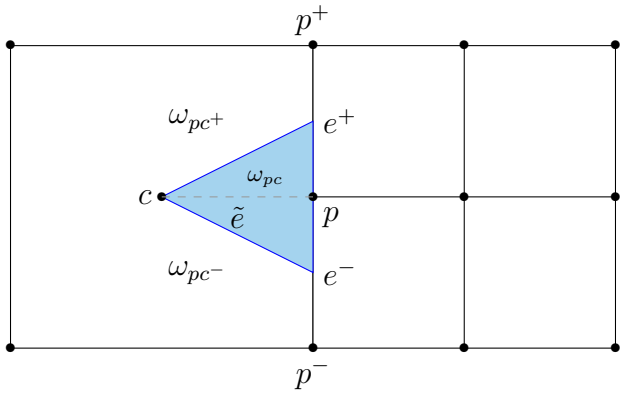

Figure 3.3: Notation related to polygonal cell ω_c with a sub-cell ω_{pc} in the case of a non-conformal cell.

The main matter of the CCLADNS scheme is to define an approximation of the fluxes over each half-edges of the mesh. To do so, we define a finite difference approximation of the temperature in each cells, which writes over ω_c as

$$T_h(\boldsymbol{x}) = T_c - \mathbb{K}_c^{-1}\boldsymbol{q}_c \cdot (\boldsymbol{x} - \boldsymbol{x}_c), \quad \forall \boldsymbol{x} \in \omega_c. \tag{3.25}$$

Here $\boldsymbol{x}_c$ is the centroid of the cell and T_c is the cell averaged temperature. Using $\boldsymbol{x}_p^{\pm}$ as the position vector of the midpoint segment $e^{\pm}$ and defining the half-edge temperature $\bar{T}_p^{\pm}$ given by $\bar{T}_p^{\pm} = T_h(\boldsymbol{x}_p^{\pm})$ we have

$$\begin{aligned} \bar{T}_p^- - T_c &= -\mathbb{K}_c^{-1}\boldsymbol{q}_{pc} \cdot (\boldsymbol{x}_p^- - \boldsymbol{x}_c), \\ \bar{T}_p^+ - T_c &= -\mathbb{K}_c^{-1}\boldsymbol{q}_{pc} \cdot (\boldsymbol{x}_p^+ - \boldsymbol{x}_c). \end{aligned} \tag{3.26}$$

Defining $\boldsymbol{x}_{pc}^{\pm}$ as $\boldsymbol{x}_{pc}^{\pm} = \boldsymbol{x}_p^{\pm} - \boldsymbol{x}_c$, we transform (3.26) by expressing the vectors $\boldsymbol{q}_{pc}$ and $\boldsymbol{x}_{pc}^{\pm}$ in terms of their normal components

$$\begin{aligned} \bar{T}_p^- - T_c &= -\mathbb{K}_c^{-1}\mathbb{J}_{pc}^{-t}\begin{pmatrix} q_{pc}^- \\ q_{pc}^+ \end{pmatrix} \cdot \mathbb{J}_{pc}^{-t}\begin{pmatrix} \boldsymbol{x}_{pc}^- \cdot \boldsymbol{n}_{pc}^- \\ \boldsymbol{x}_{pc}^- \cdot \boldsymbol{n}_{pc}^+ \end{pmatrix}, \\ \bar{T}_p^+ - T_c &= -\mathbb{K}_c^{-1}\mathbb{J}_{pc}^{-t}\begin{pmatrix} q_{pc}^- \\ q_{pc}^+ \end{pmatrix} \cdot \mathbb{J}_{pc}^{-t}\begin{pmatrix} \boldsymbol{x}_{pc}^+ \cdot \boldsymbol{n}_{pc}^- \\ \boldsymbol{x}_{pc}^+ \cdot \boldsymbol{n}_{pc}^+ \end{pmatrix}. \end{aligned}$$

Introducing the sub-cell conductivity tensor $\mathbb{K}_{pc}$ defined by (3.16) in the sub-cell ω_{pc} and after some manipulations, the above equations rewrite as

$$\begin{pmatrix} \bar{T}_p^- - T_c \\ \bar{T}_p^+ - T_c \end{pmatrix} = -\begin{pmatrix} \boldsymbol{x}_{pc}^- \cdot \boldsymbol{n}_{pc}^- & \boldsymbol{x}_{pc}^- \cdot \boldsymbol{n}_{pc}^+ \\ \boldsymbol{x}_{pc}^+ \cdot \boldsymbol{n}_{pc}^- & \boldsymbol{x}_{pc}^+ \cdot \boldsymbol{n}_{pc}^+ \end{pmatrix} \mathbb{K}_{pc}^{-1} \begin{pmatrix} q_{pc}^- \\ q_{pc}^+ \end{pmatrix}.$$

which rewrites using the previous notations as

$$\begin{pmatrix} \bar{T}_p^- - T_c \\ \bar{T}_p^+ - T_c \end{pmatrix} = -\mathbb{X}_{pc}\mathbb{K}_{pc}^{-1} \begin{pmatrix} q_{pc}^- \\ q_{pc}^+ \end{pmatrix}. \tag{3.27}$$

Assuming we can compute the inverse matrix of $\mathbb{X}_{pc}$ and solving the above linear system leads to the final expression of the half-edge normal fluxes

$$\begin{pmatrix} q_{pc}^- \\ q_{pc}^+ \end{pmatrix} = -\mathbb{K}_{pc}\mathbb{X}_{pc}^{-1} \begin{pmatrix} \bar{T}_p^- - T_c \\ \bar{T}_p^+ - T_c \end{pmatrix}. \tag{3.28}$$

We can actually compute it under the form

$$\begin{pmatrix} q_{pc}^- \\ q_{pc}^+ \end{pmatrix} = -\frac{1}{\Delta_{pc}} \mathbb{K}_{pc} \begin{pmatrix} \boldsymbol{x}_{pc}^+ \cdot \boldsymbol{n}_{pc}^+ & -\boldsymbol{x}_{pc}^- \cdot \boldsymbol{n}_{pc}^+ \\ -\boldsymbol{x}_{pc}^+ \cdot \boldsymbol{n}_{pc}^- & \boldsymbol{x}_{pc}^- \cdot \boldsymbol{n}_{pc}^- \end{pmatrix} \begin{pmatrix} \bar{T}_p^- - T_c \\ \bar{T}_p^+ - T_c \end{pmatrix}, \tag{3.29}$$

where $\Delta_{pc} = (\boldsymbol{x}_{pc}^- \cdot \boldsymbol{n}_{pc}^-)(\boldsymbol{x}_{pc}^+ \cdot \boldsymbol{n}_{pc}^+) - (\boldsymbol{x}_{pc}^- \cdot \boldsymbol{n}_{pc}^+)(\boldsymbol{x}_{pc}^+ \cdot \boldsymbol{n}_{pc}^-)$ is the determinant of the matrix $\mathbb{X}_{pc}$.

In the special case of the AMR cell, as shown in FIG. 3.3, we have $\boldsymbol{n}_{pc}^- = \boldsymbol{n}_{pc}^+$ so $\Delta_{pc} = 0$. This means that we can not write (3.29) in an AMR cell. The CCLADNS scheme can not be used on this kind of grids. We will present in the next section an extension of the scheme that allows us to write the CCLADNS scheme on this kind of non-conformal cell.

3.2.2 CCLADNS for AMR in two-dimensional geometries

We use here the fact that we can detect a non-conformal cell by computing the scalar product of $\boldsymbol{n}_{pc}^-$ and $\boldsymbol{n}_{pc}^+$ which will be equal to zero when these two vectors are colinear. In this case we use a partition of the sub-cell as presented in FIG. 3.3. We introduce now two sub-cell $\omega_{pc^\pm}$ which are respectively the two triangles based on the node $(\boldsymbol{x}_c, \boldsymbol{x}_p, \boldsymbol{x}_p^\pm)$. Using $\tilde{\boldsymbol{x}}_p^\pm$ as the position vector of the midpoint segment $\tilde{e}$ respectively for the two sub-cells $\omega_{pc^\pm}$ and defining the half-edge temperature $\tilde{T}_p^\pm$ given by $\tilde{T}_p^\pm = T_h(\tilde{\boldsymbol{x}}_p^\pm)$ we have in the sub-cell ω_{pc^-}

$$\begin{aligned} \bar{T}_p^- - T_c &= -\mathbb{K}_c^{-1} \boldsymbol{q}_c \cdot (\boldsymbol{x}_p^- - \boldsymbol{x}_c), \\ \tilde{T}_p^- - T_c &= -\mathbb{K}_c^{-1} \boldsymbol{q}_c \cdot (\tilde{\boldsymbol{x}}_p^- - \boldsymbol{x}_c). \end{aligned} \tag{3.30}$$

and in the sub-cell ω_{pc^+}

$$\begin{aligned} \tilde{T}_p^+ - T_c &= -\mathbb{K}_c^{-1} \boldsymbol{q}_c \cdot (\tilde{\boldsymbol{x}}_p^+ - \boldsymbol{x}_c), \\ \bar{T}_p^+ - T_c &= -\mathbb{K}_c^{-1} \boldsymbol{q}_c \cdot (\boldsymbol{x}_p^+ - \boldsymbol{x}_c). \end{aligned} \tag{3.31}$$

we can then define the matrix $\mathbb{X}_{pc}^-$ for the sub-cell ω_{pc^-}

$$\mathbb{X}_{pc}^- = \begin{pmatrix} \boldsymbol{x}_{pc}^- \cdot \boldsymbol{n}_{pc}^- & \boldsymbol{x}_{pc}^- \cdot \tilde{\boldsymbol{n}}^- \\ \tilde{\boldsymbol{x}}_{pc} \cdot \boldsymbol{n}_{pc}^- & \tilde{\boldsymbol{x}}_{pc} \cdot \tilde{\boldsymbol{n}}^- \end{pmatrix}, \tag{3.32}$$

where $\tilde{\boldsymbol{n}}^-$ is the normal to the edge $\tilde{e}$ from ω_{pc^-}. In the same way, we have for the sub-cell ω_{pc^+}

$$\mathbb{X}_{pc}^+ = \begin{pmatrix} \tilde{\boldsymbol{x}}_{pc} \cdot \tilde{\boldsymbol{n}}^+ & \tilde{\boldsymbol{x}}_{pc} \cdot \boldsymbol{n}_{pc}^+ \\ \boldsymbol{x}_{pc}^+ \cdot \tilde{\boldsymbol{n}}^+ & \boldsymbol{x}_{pc}^+ \cdot \boldsymbol{n}_{pc}^+ \end{pmatrix}, \tag{3.33}$$

where $\tilde{\boldsymbol{n}}^+$ is the normal to the edge $\tilde{e}$ from ω_{pc^+} and $\tilde{\boldsymbol{n}}^- = -\tilde{\boldsymbol{n}}^+$. Using these matrices we can define, as in section 3.1.5 two matrices $\mathbb{L}_{pc}^\pm = \mathbb{K}_{pc}(\mathbb{X}_{pc}^\pm)^{-1}$ such that for ω_{pc^-}

$$\begin{pmatrix} q_{pc}^- \\ \tilde{q_{pc}}^- \end{pmatrix} = \mathbb{L}_{pc}^- \begin{pmatrix} \bar{T}_p^- - T_c \\ \tilde{T}_p^- - T_c \end{pmatrix}, \tag{3.34}$$

and for ω_{pc^+}

$$\begin{pmatrix} \tilde{q_{pc}}^+ \\ q_{pc}^+ \end{pmatrix} = \mathbb{L}_{pc}^+ \begin{pmatrix} \tilde{T}_p^+ - T_c \\ \bar{T}_p^+ - T_c \end{pmatrix}, \tag{3.35}$$

using the fact that $\tilde{q_{pc}}^+ + \tilde{q_{pc}}^- = 0$ and since $\tilde{T}_p^- = \tilde{T}_p^+ = \tilde{T}_p$, we can demonstrate that

$$\begin{pmatrix} q_{pc}^- \\ {q_{pc}}^+ \end{pmatrix} = \begin{pmatrix} (\mathbb{L}_{pc}^-)_{11} - \frac{(\mathbb{L}_{pc}^-)_{12}(\mathbb{L}_{pc}^-)_{21}}{(\mathbb{L}_{pc}^+)_{11} + (\mathbb{L}_{pc}^-)_{22}} & -\frac{(\mathbb{L}_{pc}^-)_{12}(\mathbb{L}_{pc}^+)_{12}}{(\mathbb{L}_{pc}^+)_{11} + (\mathbb{L}_{pc}^-)_{22}} \\ -\frac{(\mathbb{L}_{pc}^-)_{21}(\mathbb{L}_{pc}^+)_{21}}{(\mathbb{L}_{pc}^+)_{11} + (\mathbb{L}_{pc}^-)_{22}} & (\mathbb{L}_{pc}^+)_{22} - \frac{(\mathbb{L}_{pc}^+)_{12}(\mathbb{L}_{pc}^+)_{21}}{(\mathbb{L}_{pc}^+)_{11} + (\mathbb{L}_{pc}^-)_{22}} \end{pmatrix} \begin{pmatrix} \bar{T}_p^- - T_c \\ \bar{T}_p^+ - T_c \end{pmatrix}. \tag{3.36}$$

We have now an expression of the fluxes in term of difference of temperature and introducing the matrix $\tilde{\mathbb{L}}_{pc}$ we can write

$$\begin{pmatrix} q_{pc}^{-} \\ {q_{pc}}^{+} \end{pmatrix} = \tilde{\mathbb{L}}_{pc} \begin{pmatrix} \bar{T}_p^{-} - T_c \\ \bar{T}_p^{+} - T_c \end{pmatrix}. \tag{3.37}$$

This matrix $\tilde{\mathbb{L}}_{pc}$ is then used instead of the matrix $\mathbb{L}_{pc}$ in the computation of the heat fluxes in Equation (3.19). The construction of the nodal matrices $\mathbb{M}$ and $\mathbb{N}$ (see Section 3.1.5) is straightforward. Using this modification of the CCLADNS scheme the size of the nodal system is not modified and leads to an invertible matrix $\mathbb{M}$, which allows us to build the global system. We could have added in the system (3.20) the additional temperature $\tilde{T}_p$ but this would have changed the size of the nodal system. We now present the space discretization on AMR meshes in a three dimensional space.

3.2.3 CCLADNS for AMR in three-dimensional geometries

The method presented in the previous section is easy and straightforward to implement in two dimensional geometries. Moreover there exists only one type of AMR node in two-dimensional geometries, so we only had to compute one specific modified matrix $\tilde{\mathbb{L}}_{pc}$. However three dimensional geometries are much more complex, and there appears to be a lot of different kind of AMR nodes. We would need to compute a specific matrix for each one of these different kinds of node. Of course this is not practical, so we need to find a generic way to compute these matrices.
Around an AMR node the two normal vectors are colinear, we overcome that problem in Section 3.2 by dividing this peculiar sub-cell in two fictitious sub-cells. In each sub-cell we can then define a basis and write the scheme. In 3D, The sub-cell decomposition is done by introducing fictitious sub-cells made of a iota. As we will show later in this section, this elemental subdivision, allows us to avoid the non-invertibility problem, because the iotas always allow us to define a local basis based on their normals. We will show that the CCLADNS scheme can be written on these iotas sub-cells. Of course, one of the drawbacks of the method is that the size of these new local matrices increases compared to the classical scheme. This method is a generalization of the method presented in [86] for the CCLAD schemes with hybrid 3D meshes and pyramid elements.

Remark 1: *For the sake of simplicity we do not try to compute the optimal decomposition in terms of fictitious sub-cells. By optimal we mean here the smallest subset that allow us to compute the local fluxes. We compute the simplest valid subset, which is also the largest in terms of fictitious sub-cells. Some of these fictitious or iota sub-cells could be merged and still lead to valid invertible matrices. The determination of the smallest subset of fictitious sub-cells should be performed in order to improve the computational cost of the scheme on AMR grids but it is out of the scope of this article.*

In the following we consider that p is what we call an AMR node. Those nodes are detected while reading the initial mesh, or after a refinement step. For instance, an AMR node can be located in the middle of an edge or in the middle of a face as presented in Fig. 3.4. When we encounter such a node we know we might have some issues with the decomposition in terms of normal components. To overcome this difficulty, we subdivide all the surrounding sub-cells ω_{pc} into $2 \times \mathfrak{F}_{pc}$ iota sub-cells $\mathcal{I}^{pfec}$. We observe that there is always two iota sub-cell per face impinging at vertex p. Each iota sub-cell $\mathcal{I}^{pfec}$ has 3 faces impinging at node p: one is part of the outer sub-face $\partial\omega_{pc}^{f}$ and two inner sub-faces which result from the subdivision. Bearing this

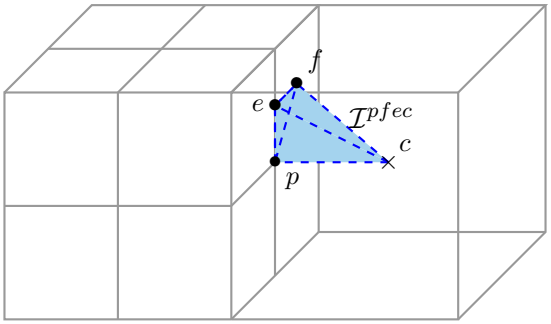

Figure 3.4: A iota sub-cell $\mathcal{I}^{pfec}$ in a 3D AMR cell.

in mind, we can use (3.19) to write the flux approximation within each iota sub-cell $\mathcal{I}^{pfec}$. It writes

$$q^i_{\mathcal{I}} = -\sum_{k=1}^{3} \mathbb{L}^c_{ik}(\bar{T}^k_{\mathcal{I}} - T^{\mathcal{I}}), \tag{3.38}$$

here the index $\mathcal{I}$ represents one of the iota sub-cell $\mathcal{I}^{pfec}$ and $T^{\mathcal{I}}$ is the cell-centered temperature of this iota sub-cell, $\bar{T}^k_{\mathcal{I}}$ represents the iota sub-face temperatures. We write the continuity conditions on the iota sub-faces and obtain a modified version of the system (3.20), namely it now writes

$$\mathbb{M}^{\mathcal{I}}\bar{\boldsymbol{T}}^{\mathcal{I}} = \mathbb{N}^{\mathcal{I}}\boldsymbol{T}^{\mathcal{I}},$$

where $\bar{\boldsymbol{T}}^{\mathcal{I}}$ is the vector of iota sub-face temperatures around node p, and $\boldsymbol{T}^{\mathcal{I}}$ is the vector of iota sub-cell temperatures. The vector $\bar{\boldsymbol{T}}^{\mathcal{I}}$ is of size $\mathfrak{F}^{\mathcal{I}}_p$, the number of iota sub-faces and the vector $\boldsymbol{T}^{\mathcal{I}}$, is of size $\mathfrak{C}^{\mathcal{I}}_p$ the number of iota sub-cells around node p. The matrices $\mathbb{M}^{\mathcal{I}}$ and $\mathbb{N}^{\mathcal{I}}$ are respectively of size $\mathfrak{F}^{\mathcal{I}}_p \times \mathfrak{F}^{\mathcal{I}}_p$ and $\mathfrak{F}^{\mathcal{I}}_p \times \mathfrak{C}^{\mathcal{I}}_p$ and are constructed in the same way than in Section 3.1.5. The matrix $\mathbb{M}^{\mathcal{I}}$ is invertible, and the solution of the above linear system writes

$$\bar{\boldsymbol{T}}^{\mathcal{I}} = \left(\mathbb{M}^{\mathcal{I}}\right)^{-1}\mathbb{N}^{\mathcal{I}}\boldsymbol{T}^{\mathcal{I}}.$$

This formula allows to express the iota sub-face temperatures around node p in terms of the iota sub-cell temperatures surrounding vertex p. Finally, using the procedure described in Section 3.1.6, the contribution of a iota sub-cell $\mathcal{I}$ to the diffusion flux at vertex p writes

$$Q_{p\mathcal{I}} = -\sum_{\mathcal{I}' \in \mathfrak{C}^{\mathcal{I}}_p} \mathbb{G}^{p,\mathcal{I}}_{\mathcal{I}\mathcal{I}'}(T^{\mathcal{I}'} - T^{\mathcal{I}}), \tag{3.39}$$

where $\mathfrak{C}^{\mathcal{I}}_p$ is the set of the iota sub-cells $\mathcal{I}$ surrounding vertex p.

The $\mathfrak{C}^{\mathcal{I}}_p \times \mathfrak{C}^{\mathcal{I}}_p$ matrix $\mathbb{G}^{p,\mathcal{I}}$ is given by

$$\mathbb{G}^{p,\mathcal{I}} = \left(\widetilde{\mathbb{N}}^{\mathcal{I}}\right)^t \left(\mathbb{M}^{\mathcal{I}}\right)^{-1}\mathbb{N}^{\mathcal{I}}, \tag{3.40}$$

where $\mathbb{N}^{\mathcal{I}}$ is defined by Eq (3.21) using the iota sub-cells notations. We point out that the cell index, $\mathcal{I}'$, employed in (3.39), refer to a iota sub-cell. More precisely, $Q_{p\mathcal{I}}$ contains contributions coming from temperatures attached to the iota sub-cells. These additional degrees of freedom can be eliminated by equating them to the cell temperature T_c. This is equivalent to express the vector of iota sub-cell temperatures, $\boldsymbol{T}^{\mathcal{I}} \in \mathfrak{R}^{\mathfrak{C}^{\mathcal{I}}_p}$, in terms of the vector of the cell-centered temperatures $\boldsymbol{T} \in \mathfrak{R}^{\mathfrak{C}_p}$ as follows

$$\boldsymbol{T}^{\mathcal{I}} = \mathbb{P}\boldsymbol{T}. \tag{3.41}$$

Here, $\mathbb{P}$ is a rectangular matrix of size $\mathfrak{C}_p^{\mathcal{I}} \times \mathfrak{C}_p$. Let i (resp. j) be the generic index of a cell in the local numbering of the cells belonging to $\mathfrak{C}_p^{\mathcal{I}}$ (resp. $\mathfrak{C}_p$), then according to (3.41), temperature $T_i^{\mathcal{I}}$ writes

$$T_i^{\mathcal{I}} = \sum_{j=1}^{\mathfrak{C}_p} \mathbb{P}_{ij} T_j.$$

For $i = 1 \dots \mathfrak{C}_p^{\mathcal{I}}$ and $j = 1 \dots \mathfrak{C}_p$, the generic entry of $\mathbb{P}$ writes

$$\mathbb{P}_{ij} = \begin{cases} 1 & \text{if } i \text{ corresponds to a fictive sub-cell included inside } c \text{ and } j \text{ corresponds to cell } c, \\ 0 & \text{elsewhere.} \end{cases}$$

Finally, substituting (3.41) into (3.39) leads to the expression of Q_{pc} in terms of cell-centered temperatures

$$Q_{pc} = - \sum_{c' \in \mathcal{C}(p)} \mathbb{G}_{cc'}^p (T_{c'} - T_c), \tag{3.42}$$

where $\mathbb{G}_{cc'}^p = \mathbb{P}^t \mathbb{G}^{p,\mathcal{I}} \mathbb{P}$. This means that we have a definition of the fluxes (3.42) that writes under the form of (3.22). The construction of the global diffusion matrix remains unchanged.

3.3 Numerical results

Let us recall that we are solving the generic diffusion equation

$$\rho C_v \frac{\partial T}{\partial t} - \nabla \cdot (\mathbb{K} \nabla T) = \rho r, \qquad (\boldsymbol{x}, t) \in \mathcal{D} \times [0, \mathcal{T}], \tag{3.43a}$$

$$T(\boldsymbol{x}, 0) = T^0(\boldsymbol{x}), \qquad \boldsymbol{x} \in \mathcal{D}, \tag{3.43b}$$

where $r = r(\boldsymbol{x})$ is a source term. The density and the specific heat capacity are fixed at the values $\rho = 1$ and $C_v = 1$. The boundary conditions, the source term and the heat conductivity tensor $\mathbb{K}$ will be specified for each test case.
The analytical solutions of all the problems studied are stationary, thus, we start the computations with the initial condition $T^0(\boldsymbol{x}) = 0$ and run the simulation until the steady state is reached. For all the test cases, the numerical solutions are obtained by solving linear systems using the localized ILU(0) Preconditioned BiCGStab algorithm [161, 125]. The relative error tolerance to achieve the convergence is set to 10^{-16}. The procedure employed to perform the convergence analysis is the same as in [86]. We will deduce an estimation of the order of the truncation error q_α, where $\alpha = 2,\ \infty$, is based on the discrete L^2 and L^∞ norms respectively.

3.3.1 Numerical results of the 3D extension of CCLADNS on isotropic diffusion problem

The aim of this section is to assess the robustness and the accuracy of the CCLADNS scheme against analytical test cases using various types of grids. This problem consists in finding the steady solution of (3.43) with $r = 0$ and an isotropic conductivity tensor defined by $\mathbb{K} = \kappa \mathbb{I}$, where $\mathbb{I}$ is the unit tensor of $\mathfrak{R}^3$ and the scalar conductivity is given by $\kappa = 1$. The computational domain is $\mathcal{D} = [0, 1]^3$ and we apply the following boundary conditions on the boundaries of $\mathcal{D}$

- Dirichlet boundary conditions such that $T(\boldsymbol{x}) = 0$, for $x = 0$ and $T(\boldsymbol{x}) = 1$, for $x = 1$.

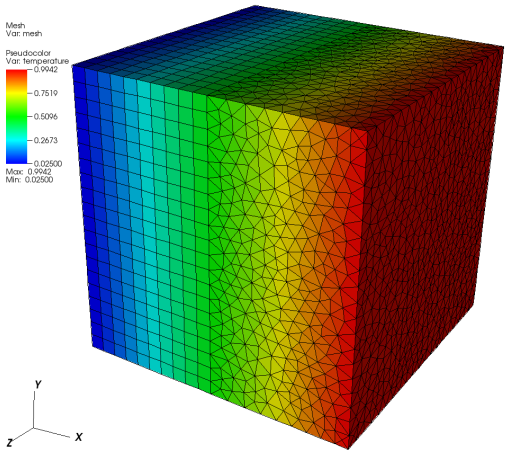

Figure 3.5: Linear solution using CCLADNS on a 3D hybrid mesh made of 21 806 tetrahedrons, 4 000 hexahedrons and 400 pyramids.

Table 3.1: Isotropic diffusion problem, asymptotic errors in both L_∞ and L_2 norms and corresponding truncation errors using the CCLADS scheme on a series of hybrid 3D grids.

# Cells	h	E_∞^h	L_∞^h	E_2^h	L_2^h
3 615	6.52D-02	1.28D-02	**1.05**	4.48D-03	**1.04**
26 206	3.36D-02	6.40D-03	**0.99**	2.26D-03	**0.98**
195 836	1.72D-02	3.32D-03	**0.96**	1.16D-03	**1.01**
1 473 418	8.79D-03	1.74D-03	**1.06**	5.88D-04	**1.00**
11 735 235	4.40D-03	8.41D-04	-	2.93D-04	-

- Neumann boundary conditions such that $\boldsymbol{q}(x) \cdot \boldsymbol{n} = 0$, for all the other boundaries of the domain.

The steady analytical solution is $\hat{T}(\boldsymbol{x}) = x$. The aim of this simple test case is to assess the ability of the CCLADNS scheme to preserve linear fields on various meshes. We have computed the steady numerical solution on different kinds of grids, including Cartesian hexahedron, randomly perturbed hexahedron, Kershaw-like and tetrahedral grids. The corresponding asymptotic errors are equal to zero up to machine precision. As expected, our finite volume scheme preserves linear solutions on theses meshes. Let us point that this result confirms the conclusion already drawn for this type of numerical methods, in the context of two-dimensional geometries, refer to [115].

We also performed a convergence analysis for the hybrid grids using the 3D CCLADS scheme of [86], refer to Fig. 3.5. For this kind of grids we use the special subcell decomposition using iota as presented in the section 3.2.3, in order to cope with the number of faces impinging on the head of pyramids. In Table 3.1 we present the truncation errors obtained with the CCLADS scheme on these grids. This shows that the CCLADS scheme exhibits a rate of convergence of first-order only. Let us point out that the maximal error is always located at the layer of pyramids which allows to link the tetrahedral and the hexahedral regions of the grid. Using the same subcell decomposition on the pyramids with the CCLADNS scheme we are now able to reach asymptotic errors equal to zero up to machine precision.

3.3.2 Isotropic diffusion problem on AMR meshes

Here, we run the same test case as in section 3.3.1 but now using AMR meshes. The aim of this simple test case is to assess the ability of our scheme to preserve linear fields on AMR meshes.

An example of the solution obtained on a randomly perturbed AMR mesh is pictured in Fig. 3.6(a) in 2D and Fig. 3.6(b) in 3D. As already shown in [115] for the CCLADNS scheme in 2D, the modified AMR version of CCLADNS still captures linear solutions up to machine precision. This result is also confirmed in 3D.

Figure 3.6: Solution of linear diffusion problem on AMR meshes

(a) Isotropic linear solution on a randomly perturbed 2D AMR grid. Machine precision reached with CCLADNS scheme.

(b) Isotropic linear solution on a randomly perturbed 3D AMR grid. Machine precision reached with CCLADNS scheme.

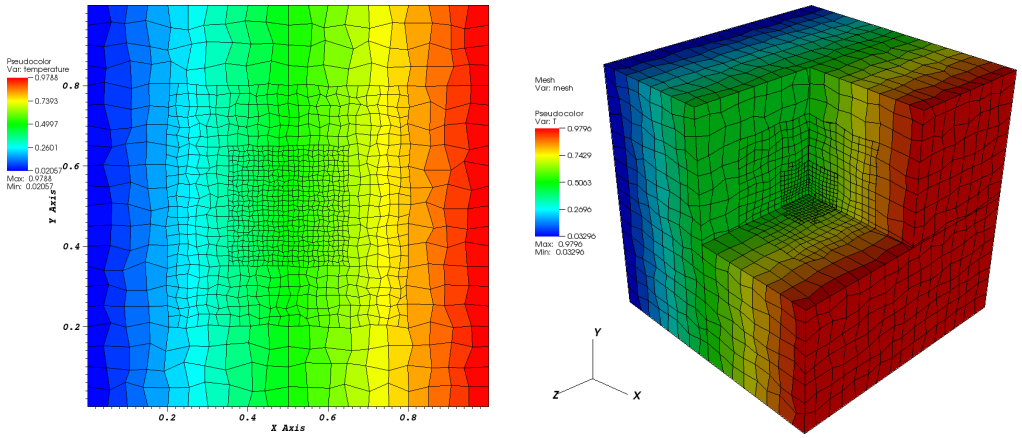

3.3.3 Anisotropic non-linear 2D problem with a non-symmetric conductivity tensor

This test case is taken from [98]. In this test case we compute a source term such that the solution is defined as

$$T(x,y) = 1 - \tanh\left(\frac{(x-0.5)^2 + (y-0.5)^2}{0.01}\right). \tag{3.44}$$

This solution is defined on $[0,1]^2$, where we impose Dirichlet conditions using the analytic solution on the boundaries and we use an anisotropic tensor defined as

$$\mathbb{K} = \begin{pmatrix} 4 & 2 \\ -1 & 3 \end{pmatrix}$$

As we can see in Fig. 3.7, the solution present a strong peak in the middle of the domain while it quickly reaches values near zero when going away from the middle. Therefore we need a lot of precision in the middle of the domain while the boundaries can remains coarsely meshed. This kind of test case is interesting to assess the precision of an AMR capable scheme.

We ran this test on non-conformal Cartesian meshes as pictured in Fig. 3.7(a) and randomly perturbed non-conformal meshes as shown in Fig. 3.7(b). Because of the nature of the AMR meshes we cannot compute the order of the method. Indeed, the mesh size is not uniform so we

Table 3.2: Anisotropic non-linear problem, asymptotic errors in both L_∞ and L_2 norms and corresponding truncation errors using the CCLADNS scheme on a series of uniform and AMR Cartesian 2D grids.

Uniform mesh						AMR mesh			
# Cells	h	E_∞^h	L_∞^h	E_2^h	L_2^h	# Cells	ratio	E_∞^h	E_2^h
256	6.52D-02	1.10D-01	**2.17**	2.98D-02	**3.28**	256	1.00	1.10D-01	2.98D-02
1 024	3.12D-02	2.44D-02	**2.00**	3.05D-03	**2.04**	556	1.84	2.44D-02	3.05D-03
4 096	1.56D-02	6.09D-03	**2.00**	7.43D-04	**2.01**	988	4.14	7.50D-03	1.02D-03
16 384	7.81D-03	1.52D-03	**1.99**	1.84D-04	**2.00**	3 952	4.14	1.90D-03	2.64D-04
65 536	3.90D-03	3.81D-04	-	4.60D-05	-	15 808	4.14	4.79D-04	6.65D-05

Table 3.3: Anisotropic non-linear problem, asymptotic errors in both L_∞ and L_2 norms and corresponding truncation errors using the CCLADNS scheme on a series of uniform and AMR randomly deformed 2D grids.

Uniform mesh						AMR mesh			
# Cells	h	E_∞^h	L_∞^h	E_2^h	L_2^h	# Cells	ratio	E_∞^h	E_2^h
256	6.52D-02	1.16D-01	**2.03**	3.67D-02	**3.11**	256	1.00	1.16D-01	3.67D-02
1 024	3.12D-02	3.93D-02	**1.85**	4.25D-03	**1.99**	556	1.84	2.42D-02	3.26D-03
4 096	1.56D-02	1.08D-02	**1.99**	1.06D-03	**2.37**	988	4.14	9.94D-03	1.05D-03
16 384	7.81D-03	2.72D-03	**1.92**	2.06D-04	**2.00**	3 952	4.14	3.50D-03	2.80D-04
65 536	3.90D-03	7.14D-04	-	5.13D-05	-	15 808	4.14	8.25D-04	7.18D-05

cannot compute a meaningfull cell size. However, we can compute the order of the method on uniform grids and then compare the error level obtained on an equivalently refined AMR grid. On a well adapted AMR grid we expect to obtain a similar precision while using less cells than an uniform grid.
We can see in Table 3.2 and Table 3.3 that we reach second order accuracy on Cartesian and randomly perturbed grids. We also obtain the same level of precision on the AMR grids while using 4.14 time less cells.

Figure 3.7: Solution of an anisotropic non-linear solution in 2D on a Cartesian AMR mesh

(a) Anisotropic non-linear solution in 2D on a Cartesian AMR mesh made of 988 cells.

(b) Anisotropic non-linear solution in 2D and randomly deformed AMR mesh made of 3 952 cells.

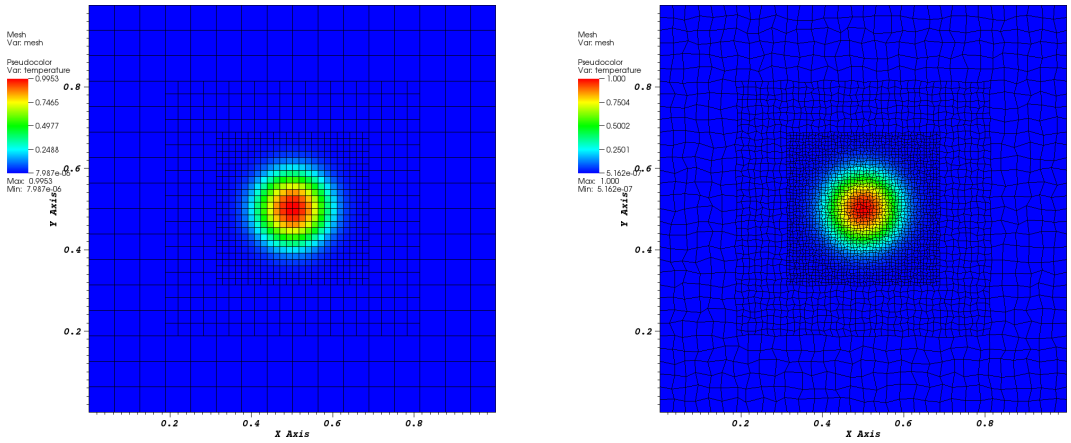

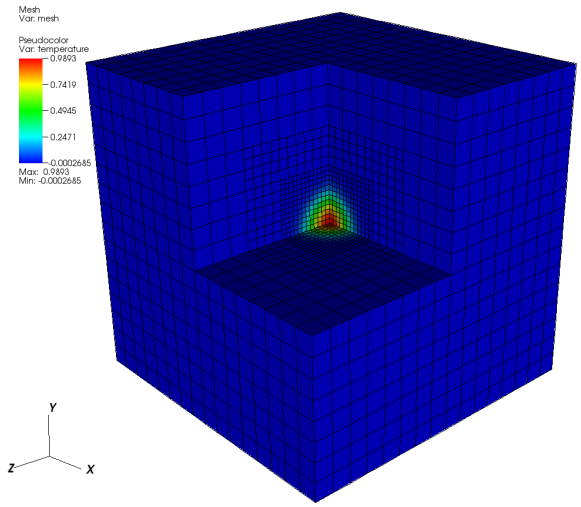

Figure 3.8: Anisotropic non-linear solution in 3D on 30 304 cells.

3.3.4 Anisotropic non-linear 3D problem with a non-symmetric conductivity tensor

This test case is the 3D extension of the previous test case. In this test case we compute a source term such that the solution is defined as

$$T(x,y,z) = 1 - \tanh\left(\frac{(x-0.5)^2 + (y-0.5)^2 + (z-0.5)^2}{0.01}\right). \tag{3.45}$$

This solution is defined on the domain $[0,1]^3$, where we impose Dirichlet conditions on the boundaries and we use an anisotropic tensor defined as

$$\mathbb{K} = \begin{pmatrix} 5 & 2 & -1 \\ 3 & 4 & 2 \\ -3 & 0.5 & 6 \end{pmatrix}$$

We run the calculations on different grids that are refined in order to compute the order of our method. We first run the computations on uniform grids. Then we run the computations on Cartesian AMR grids. The procedure used to obtain the AMR meshes starts from an uniform grid and we proceed in two steps. For each cell c of the mesh we compute the radius $r_c = \max(|x_c - \frac{1}{2}|, |y_c - \frac{1}{2}|, |z_c - \frac{1}{2}|)$ where (x_c, y_c, z_c) are the coordinates of the centroid of cell c. On the first step if $r_c < \frac{5}{16}$ we refine cell c by dividing it in 8 subcells. Cell c is replaced in the new mesh by these 8 subcells. If this criteria is not fullfilled, cell c is kept in the mesh without any modifications. On the second pass the refinement criterion is set to $rc < \frac{5}{32}$, and we compute this refinement process on the mesh obtained after the first pass. The mesh obtained after this refinement process is shown in Fig. 3.8. The results are given in Table 3.4. On the uniform meshes we observe a second order convergence rate of the CCLADNS scheme for the Cartesian grids. Once again we cannot compute an order of convergence on the AMR meshes due to non-uniform grid sizes, but we observe that the errors obtained on the AMR grids are really close to the one obtained on the uniform grids. We are able, on this specific test case, to obtain the same error using 8.65 times less computational power.

Table 3.4: Anisotropic non-linear problem, asymptotic errors in both L_∞ and L_2 norms and corresponding truncation errors using the CCLADNS scheme on a series of uniform and AMR Cartesian 3D grids.

Uniform mesh						AMR mesh			
# Cells	h	E_∞^h	L_∞^h	E_2^h	L_2^h	# Cells	ratio	E_∞^h	E_2^h
4 096	6.25D-2	1.03D-01	**1.82**	6.68D-03	**2.54**	4 096	1.00	1.03D-01	6.68D-03
32 768	3.12D-2	2.91D-02	**1.99**	1.14D-03	**2.04**	11 096	2.95	2.91D-02	1.14D-03
262 144	1.56D-2	7.32D-03	**1.99**	2.78D-04	**2.00**	30 304	8.65	7.33D-03	2.78D-04
2 097 152	7.81D-3	1.83D-03	**1.99**	6.91D-05	**2.00**	242 432	8.65	1.83D-03	6.91D-05
16 777 216	3.90D-3	4.56D-04	-	1.72D-05	-	1 939 456	8.65	4.57D-04	1.72D-05

Chapter 4

Multi-material ALE computation using the radiation hydrodynamic code CHIC

In ICF a high power laser compress a spherical capsule to a high density and temperature hot spot in order to ignite a thermonuclear burn. During this compression process we have to deal with large displacements and strong shocks. Spherical capsule used in ICF are usually the assembly of multi-material layers. For numerical purpose and with regards to the large volume change, Lagrange formulation is well adapted to compute such problems. As the mesh moves with the fluid it handles naturally the interface between different materials and the large displacement during the compression of the target. One of the critical issue in direct drive ICF is the sensibility to hydrodynamics instabilities especially to Rayleigh-Taylor instability at the interface between the different materials during stagnation phase [97]. To deal with such problems pure Lagrange frame suffers from a lack of robustness. When such instabilities occur large distortions of the mesh can lead to tangled cells. A commonly used alternative is to consider an Arbitrary Lagrangian Eulerian (ALE) formulation [76]. A pure Lagrangian phase is followed by a two-step process: the rezoning of the Lagrangian mesh followed by a remapping step.
In this context of multi-material computation using the Full-ALE method as interface is modified by the rezoning, mixed cells containing several materials may appear. These mixed cells contain material interfaces, which need special treatment to be taken into account. In our strategy, this is done using the MOF method presented in section 2.2. Furthermore, a closure model is applied in the way to determinate the evolution of the volume fraction and the thermodynamic state of each material using real equations of state (EOS) during the Lagrangian steps. We have developed such a strategy in the 2D CHIC (Code d'Hydrodynamique d'Implosion du CELIA) code [33] which is based on a cell-centered discretization of Lagrangian hydrodynamic to simulate ICF and plasma physics experiment created by laser interaction with target.
This Chapter is organized as follows. We first briefly describe the coupling of the numerical methods. Then, theoretical and experimental studies from [37, 115, 74, 129, 19] are given to highlight the robustness and accuracy of the CHIC code.

4.1 Physical model of CHIC code

CHIC is a 2D ALE integrated ICF code developed at CELIA. This code is currently used to simulate ICF studies [146, 136, 74, 129, 126]. The code includes two-dimensional Lagrangian hydrodynamics in planar and cylindrical geometry, ion and classical or non-local electron heat

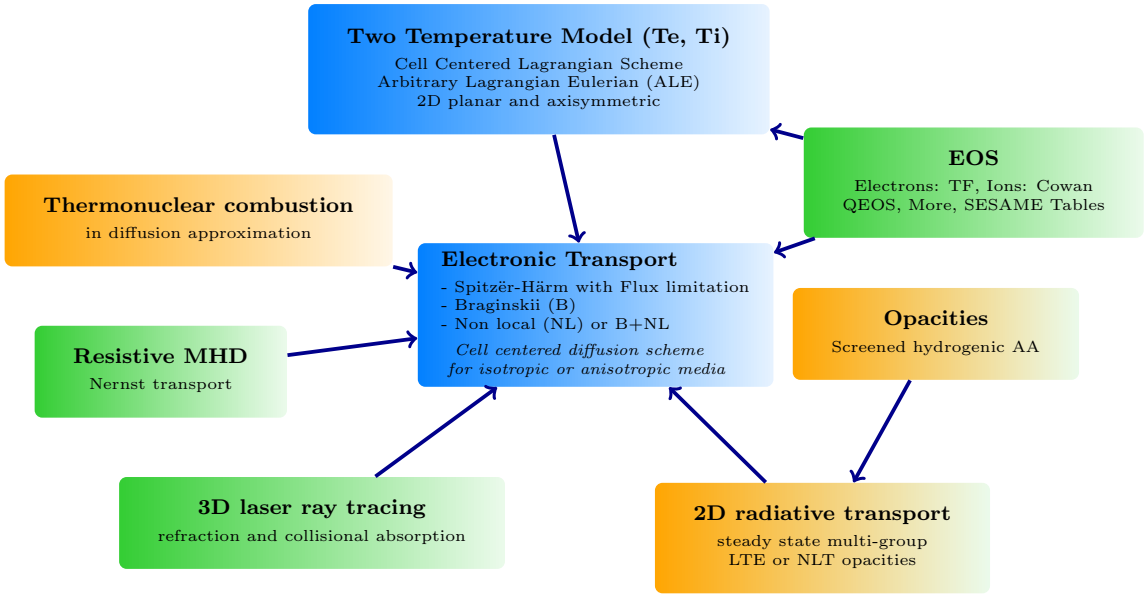

Figure 4.1: CHIC main packages

conduction, thermal coupling of electrons and ions and a detailed radiation transport. The ALE method is implemented to improve the geometrical quality of the grid elements and to optimize accuracy, robustness and computational efficiency [32, 65]. The ionization and the opacity data are tabulated, assuming a local thermodynamic equilibrium (LTE) or a non-LTE depending on the plasma parameters. The radiative transport is computed assuming that the radiation field is quasistationary and weakly anisotropic with regards to angular dependency (multigroup diffusion). The equations of state implemented in the code are QEOS and SESAME. The laser propagation, refraction and collisional absorption are treated by a ray tracing algorithm. A resistive Magnetohydrodynamics (MHD) package accounting for the azimuthal magnetic fields generated by the thermal sources (crossed gradients of the density and the electron temperature) is also included. As we can see on FIG. 4.1 all the different physical model are strongly coupled to the hydrodynamics model. The plasma fluid model in Lagrangian formalism writes as

$$
\begin{aligned}
&\rho\frac{d\tau}{dt} - \nabla\cdot\boldsymbol{U} = 0,\\
&\rho\frac{d\boldsymbol{U}}{dt} + \boldsymbol{\nabla}(P_\mathrm{i}+P_\mathrm{e}) = \boldsymbol{0},\\
&\rho\left(\frac{d\varepsilon_\mathrm{e}}{dt} + P_\mathrm{e}\frac{d\tau}{dt}\right) - \nabla\cdot(\lambda_\mathrm{e}\boldsymbol{\nabla}T_\mathrm{e}) = \Omega_\mathrm{ei}(T_\mathrm{i}-T_\mathrm{e}) + W_\mathrm{las} + W_\mathrm{rad} + W_\mathrm{fus},\\
&\rho\left(\frac{d\varepsilon_\mathrm{i}}{dt} + P_\mathrm{i}\frac{d\tau}{dt}\right) = \Omega_\mathrm{ei}(T_\mathrm{e}-T_\mathrm{i}).
\end{aligned}
$$

Here ρ denotes the density, $\tau = \frac{1}{\rho}$, $\boldsymbol{U}$ the velocity, P_i and P_e are the ion and electron pressures, ε_i and ε_e are the specific internal energies for ion and electron and T_i and T_e are the ion and electron temperatures. We introduce Ω_ei which is an exchange energy term between ion and electron and λ_e is the conductivity coefficient for electron transport. W_las, W_rad and W_fus are respectively the source term for laser, radiative transport and nuclear fusion.

The thermodynamic closure of this system is given by the equation of state (EOS), $P_\mathrm{e} \equiv \mathcal{P}_\mathrm{e}(\rho, T_\mathrm{e})$, $P_\mathrm{i} \equiv \mathcal{P}_\mathrm{i}(\rho, T_\mathrm{i})$, $\varepsilon_\mathrm{e} \equiv \epsilon_\mathrm{e}(\rho, T_\mathrm{e})$ and $\varepsilon_\mathrm{i} \equiv \epsilon_\mathrm{i}(\rho, T_\mathrm{i})$.

4.1.1 Numerical methods

In the context of multi-material ALE computation, as grid and fluid move separately mixed cells containing material interface appear. A number of numerical methods exist for taking into account such interface. Here we use the MOF method presented in section 2.2. A closure model is also required to define how the thermodynamic states of the multi-material cells evolve during the Lagrangian and the remapping phases [22]. In this work, we will use an homogeneous model for the temperature and we will set only one temperature for the ion and electron such that each material will have the same ion and electron temperature in a mixed cell. Finally, we will need closure model for all the different physical quantities that are usually material dependent.

4.1.2 Lagrangian phase

In Lagrangian hydrodynamics methods, a computational cell moves with the flow velocity its mass being time-invariant. Thus, Lagrangian methods can capture contact discontinuity sharply in multi-material fluid flows. Here the Lagrangian scheme is based on a cell-centered discretization of Lagrangian hydrodynamics equations [113]. This scheme is written in total energy form.

$$\begin{aligned}
&\rho \frac{d\tau}{dt} - \nabla \cdot \boldsymbol{U} = 0, \\
&\rho \frac{d\boldsymbol{U}}{dt} + \boldsymbol{\nabla} P = \boldsymbol{0}, \\
&\rho \frac{dE}{dt} + \nabla \cdot \boldsymbol{P}\, \boldsymbol{U} = 0.
\end{aligned}$$

Where $P = P_{\mathrm{i}} + P_{\mathrm{e}}$ is the total pressure and E the total energy. The accuracy in space is improved thanks to a second-order extension which uses the piecewise linear monotone reconstruction of the pressure and velocity. The piecewise linear monotone reconstruction is achieved using a least squares procedure followed by a slope limitation procedure. The time discretization is a one step high order extension based on the acoustic generalized Riemann problem. This high-order Lagrangian scheme is precisely described in [114].

4.1.3 Two-temperature model

Based on total energy conservation, the Lagrangian scheme must deal with the exchange between the kinetic energy and the internal energy of ion and electron. The system we want to solve for the internal energy of ion and electron is

$$\begin{aligned}
&\rho \left(\frac{d\varepsilon_{\mathrm{e}}}{dt} + P_{\mathrm{e}} \frac{d\tau}{dt} \right) - \nabla \cdot (\lambda_{\mathrm{e}} \boldsymbol{\nabla} T_{\mathrm{e}}) = \Omega_{\mathrm{ei}} (T_{\mathrm{i}} - T_{\mathrm{e}}), \\
&\rho \left(\frac{d\varepsilon_{\mathrm{i}}}{dt} + P_{\mathrm{i}} \frac{d\tau}{dt} \right) = \Omega_{\mathrm{ei}} (T_{\mathrm{e}} - T_{\mathrm{i}}).
\end{aligned}$$

We will compute the new ion and electron internal energy in two steps. First, after the Lagrangian step we have a new internal energy which is the sum of ion and electron internal energy. To compute the electron internal energy we make the assumption that the entropy deposition is done on the ion internal energy [168]. Thus, electrons follow the isentropic evolution

$$m \frac{d\, \varepsilon_{\mathrm{e}}}{dt} + P_{\mathrm{e}} \frac{d\, V}{dt} = 0.$$

Where $m = \rho\, V$ is the mass and V the volume. We can deduce ion internal energy from

$$\varepsilon_{\mathrm{i}} = \varepsilon - \varepsilon_{\mathrm{e}}$$

Where $\varepsilon = E - \frac{1}{2}\boldsymbol{U}^2$ is the mean internal energy. Then, to solve the non linear conduction and the energy transfer between ion and electron we use a Newton algorithm. The system we solve in this step is equivalent to

$$\rho\frac{d\varepsilon_{\mathrm{e}}}{dt} - \nabla\cdot(\lambda_{\mathrm{e}}\boldsymbol{\nabla}T_{\mathrm{e}}) = \Omega_{\mathrm{ei}}(T_{\mathrm{i}} - T_{\mathrm{e}}),$$
$$\rho\frac{d\varepsilon_{\mathrm{i}}}{dt} = \Omega_{\mathrm{ei}}(T_{\mathrm{e}} - T_{\mathrm{i}}).$$

Here λ_{e} is the Spitzer-Härm thermal conductivity which is proportional to $\approx T_{\mathrm{e}}^{\frac{5}{2}}$. The diffusion operator is discretized using a numerical scheme [36, 115] which is a second order cell centered finite volume scheme that can be applied to unstructured mesh. It is a robust and accurate scheme well adapted to distorted mesh.
At that time we need to update pressure using EOS as temperature field has been modified. Due to the electron transport modelized by the diffusion term we also need to update the mean internal energy and total energy

$$\varepsilon = \varepsilon_{\mathrm{i}} + \varepsilon_{\mathrm{e}},$$
$$E = \varepsilon + \frac{1}{2}\boldsymbol{U}^2.$$

4.1.4 Thermodynamical closure for the multi-material cells

A closure model is required to define how the thermodynamic states of the multi-material cells evolve during the Lagrangian and the remapping steps. The model we use is based on the reconstruction of the material interface inside a mixed cell, in which, each material evolves separately. The goal here is to compute, using the partial quantities, the mean pressure and sound speed using the quantities of every material. Let ϕ_k be the volume fraction defined for the fluid k in a cell by $\phi_k = \frac{V_k}{V}$, where V_k is the volume of the cell's part occupied by the fluid k and V the volume of the cell. Using Gibbs relation applied to the mean fluid, the pressure of the mean fluid is obtained

$$P = \sum_k \phi_k P_k.$$

Concerning the sound speed, we obtain

$$c^2 = \sum_k \frac{m_k}{m} c_k^2.$$

We make now the assumption that we have only one electron and one ion temperature for each material per mixed cells. We define the mean conductivity, using harmonic mean

$$\lambda_{\mathrm{e}} = \frac{\sum_k \phi_k}{\sum_k \frac{\phi_k}{\lambda_{\mathrm{e},k}}}.$$

Harmonic mean is usually used when a mean conductivity is required for example at the interface between two materials. For the exchange energy term between ion and electron we use arithmetic mean

$$\Omega_{\mathrm{ei}} = \sum_k \phi_k \Omega_{\mathrm{ei,k}}.$$

4.2 Modelling of the magnetic field effects using tensorial diffusion

This work is part of a collaboration we had with the Institute of Laser Engineering (ILE) at Osaka University where I was invited to work on the coupling of such magnetic field with the plasma [124]. In laser generated plasmas, magnetic fields are created whenever density and temperature gradients are not colinear. Dedicated experiments and numerical computations evidenced fields in the 100 kG-1MG range in plasmas typical of laser driven ICF [146, 126, 6]. As the corresponding magnetic pressure stays far below the kinetic pressure, the hydrodynamic flow is not directly altered by such fields. Conversely, the electron gyrofrequency is comparable to the electron-ion collision frequency in the vicinity of the critical density region, which may affect dramatically the electron heat flow. Key issues of ICF are laser matter coupling, mass ablation, hydrodynamic instabilities and hot spot dynamics. Because all of these phenomena are highly sensitive to electron heat transport, accurate modelling of the electron conduction is an essential ingredient of numerical simulations. However, the electron conduction model implemented in the majority of hydrodynamic codes is based upon the flux limited Spitzer-Härm theory and does not account for magnetic fields. The classical formulas by Braginskii predict that magnetic fields provide a reduction of the magnitude of the heat flux and its rotation through the Righi-Leduc effect. Splitting the Righi-Leduc term or approximating it as an advection term or an effective conductivity often leads to mathematical and physical anomalies. Alternatively, a direct space differencing of the full conduction operator raises accuracy and consistency issues. We developed in CELIA a new, fully tensorial approach which overcomes these difficulties. We propose a new second order tensorial diffusion method which is based on a cell-centered diffusion scheme [115]. We present the main idea of the space differencing scheme and some numerical results that illustrate the efficiency of the method compared to standard approaches. The packages describing the magnetic field generation and the anisotropic electron heat transport have been incorporated in the hydrodynamic code CHIC.

4.2.1 Underlying physical models

In deriving a numerical method to solve the heat conduction equation (3.1), we aim at developing numerical modeling of physical phenomena encountered in plasma physics. More precisely, we are concerned by heat transfer within laser-heated plasma flows such as those obtained in the domain of direct drive Inertial Confinement Fusion, refer to [13]. In this context, the energy released by the laser is transferred throughout the plasma flows by means of electron heat conduction. Omitting the pressure work term, which results from coupling to hydrodynamics, the electron temperature, T_e, is governed by a heat conduction equation similar to (3.1). In the classical regime, the electron heat flux, $\boldsymbol{q}_e$ is given by the Spitzer-Härm law: $\boldsymbol{q}_e = -\kappa_e \boldsymbol{\nabla} T_e$, where the electron thermal conductivity, κ_e, depends on the electron temperature as a power law, *i.e.*, $\kappa_e(T_e) \sim T_e^{\frac{5}{2}}$, refer to [51, 168]. This corresponds to an isotropic nonlinear heat conduction equation. However, in presence of magnetic fields, this isotropic model for heat conduction is not valid anymore. Such a situation occurs frequently for laser driven plasma wherein the density and pressure gradients are not colinear. In this particular case, a self-generated magnetic field, $\boldsymbol{B}$, is created by the rotational component of the ambipolar electric field, $\boldsymbol{E} = -\frac{1}{eN_e}\boldsymbol{\nabla} P_e$, where e is the electron charge, N_e is the electron density per unit volume and P_e is the electron pressure, refer to [51]. Knowing that the magnetic field is governed by the Faraday law, *i.e.*, $\frac{\partial \boldsymbol{B}}{\partial t} + \boldsymbol{\nabla} \times \boldsymbol{E} = \boldsymbol{0}$, we deduce that the time evolution of the magnetic field

is governed by the following equation

$$\frac{\partial \boldsymbol{B}}{\partial t} = \frac{1}{e}\boldsymbol{\nabla}(\frac{1}{N_e}) \times \boldsymbol{\nabla} P_e. \tag{4.1}$$

The magnetic field dramatically modifies electron heat transport leading to a anisotropic electron conductivity. It implies not only a reduction of the magnitude of the heat flux but also its rotation. Using plasma kinetic theory, Braginskii [30] has obtained the following expression of the electron heat flux with magnetic field

$$\boldsymbol{q}_e = -\kappa_{\parallel}(\boldsymbol{\nabla} T_e \cdot \boldsymbol{b})\boldsymbol{b} - \kappa_{\perp}[\boldsymbol{\nabla} T_e - (\boldsymbol{\nabla} T_e \cdot \boldsymbol{b})\boldsymbol{b}] - \kappa_{\wedge}\boldsymbol{b} \times \boldsymbol{\nabla} T_e, \tag{4.2}$$

where $\boldsymbol{b} = \frac{\boldsymbol{B}}{|\boldsymbol{B}|}$ is unit vector corresponding to the direction of the magnetic field and $\kappa_{\parallel}$, $\kappa_{\perp}$ and $\kappa_{\wedge}$ are scalar conductivities given in [30]. Let us consider a two-dimensional plasma flow in planar geometry. Let $(\boldsymbol{e}_x, \boldsymbol{e}_y, \boldsymbol{e}_z)$ be the orthonormal basis of $\mathfrak{R}^3$ and suppose that the two-dimensional flow is contained in the frame (x, y) equipped with the orthonormal basis $(\boldsymbol{e}_x, \boldsymbol{e}_y)$. By virtue of (4.1), it is obvious that the self-generated magnetic field is transverse to the two-dimensional flow, that is, $\boldsymbol{B} = B\boldsymbol{e}_z$. Setting $b = \frac{B}{|B|}$, we have $\boldsymbol{b} = b\boldsymbol{e}_z$, where $b^2 = 1$. Bearing this in mind, the electron heat flux expression (4.2) collapses to

$$\boldsymbol{q}_e = -\kappa_{\perp}\boldsymbol{\nabla} T_e - \kappa_{\wedge}\boldsymbol{b} \times \boldsymbol{\nabla} T_e. \tag{4.3}$$

Developing the above equation over the Cartesian frame (x, y) allows to write the electronic heat flux

$$\boldsymbol{q}_e = -\mathbb{K}_e \boldsymbol{\nabla} T_e, \tag{4.4}$$

where the second-order tensor $\mathbb{K}_e$ corresponds to the electronic conductivity defined by

$$\mathbb{K}_e = \begin{pmatrix} \kappa_{\perp} & -b\kappa_{\wedge} \\ b\kappa_{\wedge} & \kappa_{\perp} \end{pmatrix}. \tag{4.5}$$

The Braginskii transport coefficients $\kappa_{\parallel}$, $\kappa_{\perp}$ and $\kappa_{\wedge}$ can be expressed in terms of the Spitzer-Härm conductivity, κ_e, as

$$\kappa_{\parallel} = \kappa_e, \quad \kappa_{\perp} = \kappa_e f_{\perp}(\Omega_e \tau_{ei}), \quad \kappa_{\wedge} = \kappa_e f_{\wedge}(\Omega_e \tau_{ei}),$$

where $f_{\perp}$, $f_{\wedge}$ are the functions describing the magnetization of the heat flux. In addition, $\Omega_e \sim \mid \boldsymbol{B} \mid$, is the electron cyclotron frequency and τ_{ei} the electron-ion collision frequency. Note that Ω_e has the dimension of the reciprocal of time, thus parameter $\Omega_e \tau_{ei}$ is dimensionless; it describes the effect of the magnetic field on the electron heat conductivity as a ratio between the electron gyration time in the magnetic field and the electron collision time. Bearing this in mind we have displayed in FIG. 4.2 the normalized Braginskii transport coefficients with respect to the normalized parameter $\Omega_e \tau_{ei}$ knowing that $f_{\perp}(x) = \frac{1}{1+x^2}$, $f_{\wedge}(x) = \frac{x}{1+x^2}$. For a weak magnetic field, that is, $\Omega_e \tau_{ei} \in [0, 1]$, we have $\kappa_{\perp} > \kappa_{\wedge}$, whereas for a strong magnetic filed $\kappa_{\perp} < \kappa_{\wedge}$. In the limit $\mid \boldsymbol{B} \mid \to 0$, the normalized parameter $\Omega_e \tau_{ei}$ also tends to zero and the Braginskii coefficients behave as follows: $\kappa_{\perp} \to \kappa_e$ and $\kappa_{\wedge} \to 0$. In this regime, the anisotropic conductivity tensor $\mathbb{K}_e$ recovers the isotropic Spitzer-Härm conductivity, *i.e.*, $\mathbb{K}_e \to \kappa_e \mathbb{I}_2$.
We conclude this section by remarking that $\mathbb{K}_e$ is not symmetric and transforms as $\mathbb{K}_e(-b) = \mathbb{K}_e^t(b)$. This non-symmetry of the conductivity tensor is a consequence of the presence of the magnetic field, this behavior is known as the Righi-Leduc effect, refer to [71] chapter XI. It rotates the heat flux vector without changing its absolute value. This property corresponds to the following result: for all arbitrary vector $\boldsymbol{\phi}$

$$\mathbb{K}_e \boldsymbol{\phi} \cdot \boldsymbol{\phi} = \kappa_{\perp} \mid \boldsymbol{\phi} \mid^2 .$$

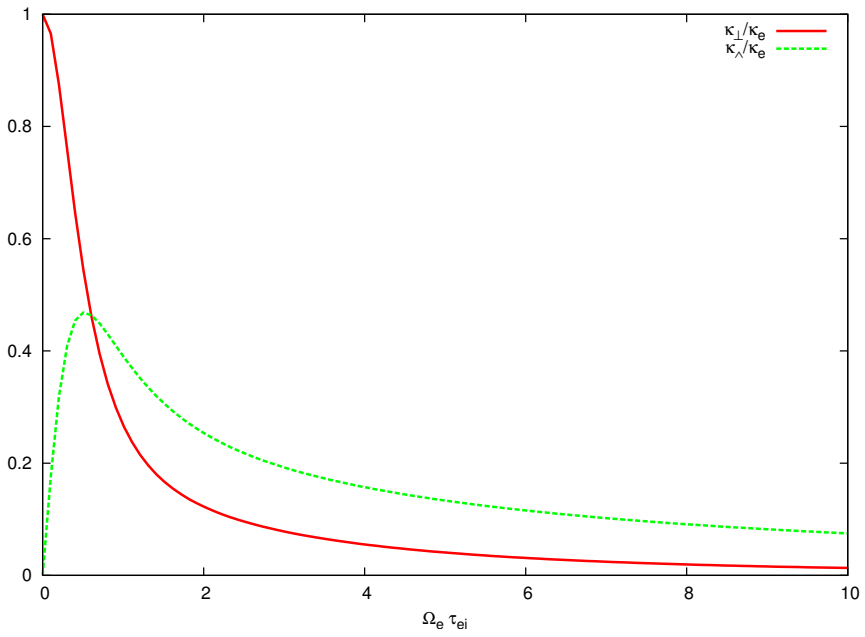

Figure 4.2: Normalized Braginskii transport coefficients $\kappa_\perp$ and $\kappa_\wedge$ versus normalized parameter $\Omega_e \tau_{ei}$.

Since $\kappa_\perp$ is positive, the above result shows that $\mathbb{K}_e$ is a positive definite tensor which satisfies the thermodynamic requirement. It is interesting to note that for an arbitrary vector $\boldsymbol{\phi}$, $\mathbb{K}_e\boldsymbol{\phi}$ can be decomposed as follows

$$\mathbb{K}_e\boldsymbol{\phi} = \kappa_\perp\boldsymbol{\phi} + b\kappa_\wedge \mathcal{R}_{\frac{\pi}{2}}\boldsymbol{\phi}, \tag{4.6}$$

where $\mathcal{R}_{\frac{\pi}{2}}$ denotes the counterclockwise rotation through the angle $\frac{\pi}{2}$. The above equation states that the anisotropic conductivity tensor acts as an isotropic conductivity tensor supplemented by a rotation tensor which follows directly from the magnetic field. Finally, computing the divergence of the anisotropic heat flux (4.3) yields

$$\nabla \cdot \boldsymbol{q}_e = -\nabla \cdot (\kappa_\perp \boldsymbol{\nabla} T_e) + \boldsymbol{A} \cdot \boldsymbol{\nabla} T_e, \tag{4.7}$$

where $\boldsymbol{A} = [-\frac{\partial}{\partial y}(b\kappa_\wedge), \frac{\partial}{\partial x}(b\kappa_\wedge)]^t$. Under this form the anisotropic diffusion operator appears as the sum of an isotropic diffusion operator plus an advection operator characterized by the velocity-like vector $\boldsymbol{A}$. This decomposition suggests to solve the anisotropic heat conduction equation discretizing separately the isotropic diffusion operator and the advection operator. However, such a splitting strategy may suffer from a lack of robustness in case of strong magnetic fields. That is why, the numerical scheme used in the sequel is based on an anisotropic heat conduction [115].

4.2.2 Magnetic field effects in a 2D configuration

We first test our method on a 2D problem without hydro and a constant and imposed magnetic field :

$B(x,y) = B_0 \exp^{-\left(\frac{\sqrt{(x-x_0/2)^2+(y-(1+x_0/2))^2}}{x_0/4}\right)^4}$ with $x_0 = 20.10^{-4}$ and $B_0 = -1.10^7 G$.

Our domain is a square of $20 \times 20 \mu m$ with a mesh of 50×50 cells. It is field of Hydrogen $Z = 1$ with a constant initial density of $0.025 g/cm^3$. Initial temperature is $T_1 = 1.10^3 K$

for $0. < x < 18.\mu m$ and $T_1 = 3.10^7 K$ for $18.\mu m < x < 20.\mu m$. We run three different types of computation first is Braginskii without Righi-Leduc effect then we have an effective conductivity which is used usually in 2D code then our tensorial formulation (see FIG. 4.3). On the 2D isoline of temperature we can observe a limitation of the heat flux on all the results due to the magnetic field. Then if we take into account of the Righi-Leduc effect with tensorial formulation the rotation of the heat flux is enhanced and no oscillation is observed (FIG. 4.4).

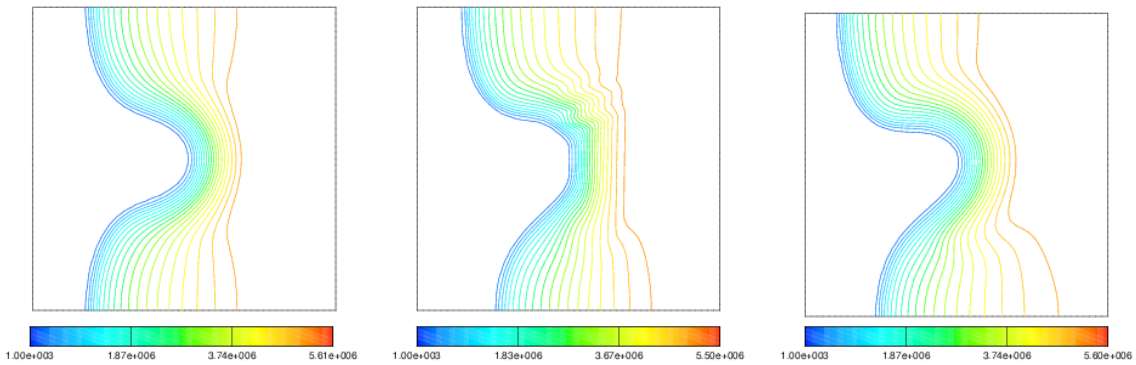

Figure 4.3: Braginskii without Righi-Leduc effect (left), effective conductivity treatment (center), tensorial formulation (right) at $t = 25ps$.

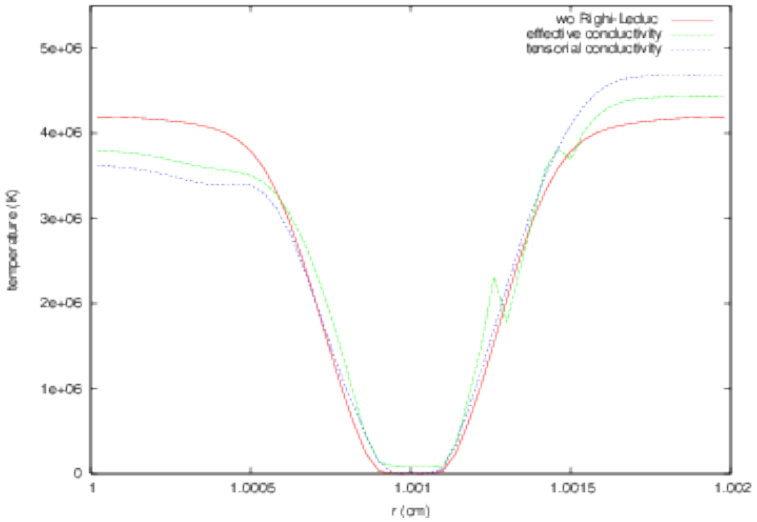

Figure 4.4: Temperature profile at $x = 10\mu m$ and $t = 25ps$.

4.2.3 Plastic target irradiated with a Laser

In this case we study a plastic target (CH) of 100 μm thickness and 1000 μm height irradiated by a laser beam : $\lambda = 0.35$ μm, maximal intensity 1. 10^{15}W cm^{-2}.
This tensorial method leads to a better computation of the Braginskii fluxes. Contrary to the effective method in which the Righi-Leduc effect is partially truncated this tensorial scheme correctly rotates heat fluxes. Comparison between Spitzer and Braginskii show that magnetic field play an important role in the case of laser ablation physics. We can see that magnetic field appear in the zone where density and temperature gradients are not colinear. The magnitude of

the self-generated magnetic field is also more intense using the tensorial method (see FIG. 4.5). The effect of self-generated magnetic field in the case of a laser ablation case totally changes the heat transport process. The tensorial method in this case also presents result free of numerical oscillation.

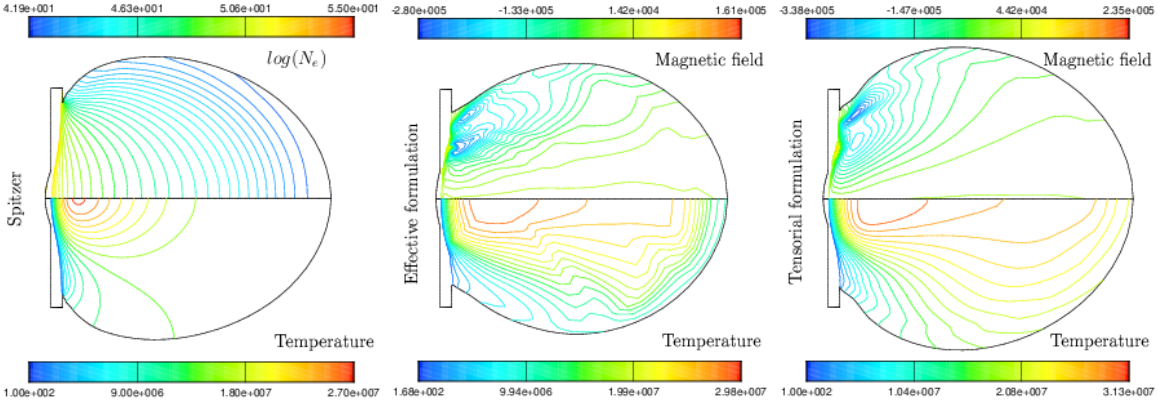

Figure 4.5: temperature and $log(N_e)$ Spitzer (left), temperature and magnetic field effective conductivity (center), temperature and magnetic field tensorial conductivity (right) at $t = 1.25ns$.

4.3 Hydrodynamic implosion symmetry of HiPER's targets

In ICF, within the Fast-Ignition strategy (FI), the use of Petawatt class lasers allows to directly deliver ignition energy to the target. A much less energy is then required by the main laser pulse; ignition being achieved by ultra-fast and ultra-intense ignition laser. First designs show that corresponding implosion velocity is reduced, suggesting that hydrodynamic instabilities could be reduced. Three targets are studied and compared with help of 2D hydrodynamic simulations and instability modeling. First we recall the main features of the laser nonuniformities optimization, within HiPER constraints. Then 2D perturbed simulations as well as a hydrodynamic perturbation modeling sequence are presented.

4.3.1 Irradiation nonuniformities study

Irradiation nonuniformities are directly connected to the laser device. Such nonuniformities produce low mode perturbation which needs to be accurately known in order to investigate the consequence on hydrodynamic target stability. For this purpose a specific illumination 3D code, the CECLAD code, has been developed [63]. It calculates target irradiation by multi-laser beams and enables to optimize illumination of complex geometries in terms of energy distribution in the focal spot or beams number. To improve confidence in CECLAD, the code has been validated against published results [42], with analytical solutions [164] giving perfect uniform irradiation and with existing results of known facilities (Omega). Published results are reproduced. The CECLAD code has been used to define the baseline specifications of the HiPER project (see Appendix C and [60]).

Optimization procedure

Several configurations of laser beams (size, energy balance, pointing, centering) and target (shape, position, size) can be tested with this tool (see Appendix C). The irradiation uniformity

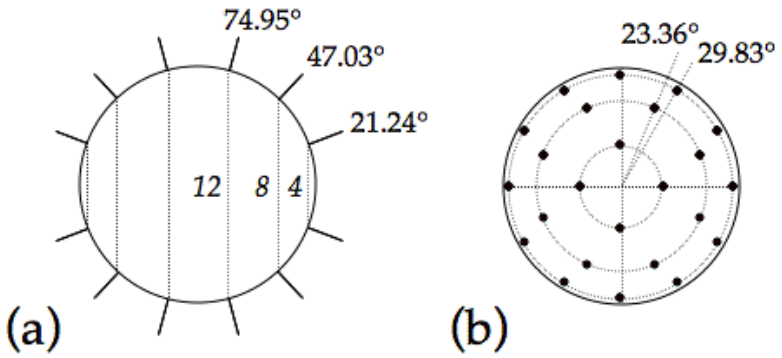

Figure 4.6: The polar (a) and azimuth angles of the 48 illumination scheme.

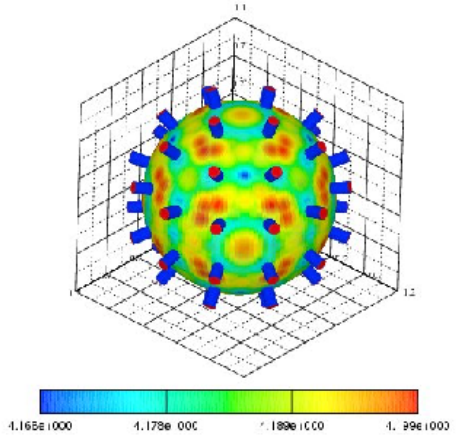

Figure 4.7: Nominal irradiation of the 48 illumination scheme.

can be optimized through various criteria. The first one is the quadratic mean of deviation of the intensity (σ_{rms}) which is a function of parameters featuring beams and targets. The second one is the energy balance η_B which is the ratio between the energy on the target and the laser beam energy. A Legendre polynomial expansion of the illumination gives amplitudes of the main modes. These criteria determine a robustness analysis by varying control parameters of the beams. Statistical variations according to a normal distribution around the nominal configuration can be performed to test the robustness of the chosen pattern.

A 48 beams HiPER illumination scheme

Initial HiPER specifications are 50 beams with 15 kJ per beams at 1 ω (6 kJ at 3 ω) [60]. From these technical constraints one can carry out a σ_{rms} and an energy balance η_B analysis. Obviously the σ_{rms} decreases with the number of laser beams. Meantime the energy balance reaches a value close to 97 % for a 60 laser beams configuration (OMEGA). If one describes the energy distribution in the focal spot by two parameters a, where a is radius at 1/e intensity, and by m, the order of the supergaussian,

$$I(r) = \exp\left[-\left(\frac{r}{a}\right)^{2m}\right],$$

a 48 laser beams scheme described in Fig. 4.6 gives σ_{rms}=0.15 % and $\eta_B = 94\%$ for parameters $a = 0.61$ and $m = 1.02$. On Fig. 4.7 we show a 3D representation of the target with all the

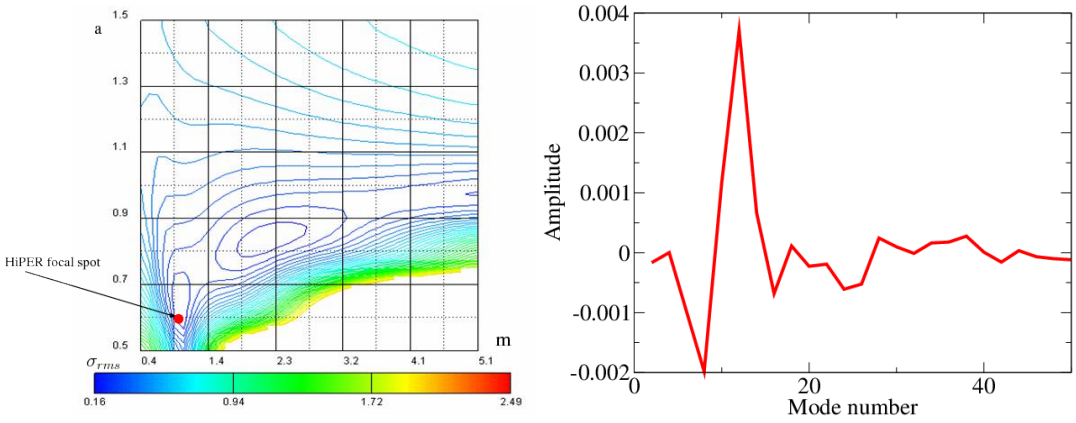

Figure 4.8: On the left σ_{rms} contours in a a, m diagram for the 48 beams HiPER illumination scheme, on the right calculated illumination spectrum (relative amplitude on mode number) for the 48 beams HiPER illumination scheme.

beams impinging on it. The field represented on the target is the intensity. This 48 beams illumination scheme yields small σ_{rms} during the whole target implosion (i.e., a increasing) as it can be seen in FIG. 4.8 which shows σ_{rms} contours in a a, m diagram.
The robustness of this scheme has been tested over 100 000 realizations. A normal repartition of the beam to beam imbalance (10%), of the beam pointing (5%), and of the beam centering 2% have confirmed previous values and given a validity σ_{rms} range. Within the frame of the FI, cone presence can strongly damage illumination uniformities. This 48 beams pattern yields also a low intensity on cone surface and reduces undesired effects like preheating of the cone surface. A Legendre polynomial expansion has been carried out which shows modes related to main illumination nonuniformities are l=12, 8 and 10, with a maximum relative nonuniformity of 0.5 % for mode l=12 (FIG. 4.8 on the right).

4.3.2 Perturbed hydrodynamics simulations and modelings

We want here to show the validity of a linear approximation in the hydrodynamic perturbation growth, and to justify a monomode, half a wavelength, perturbation on a sector type mesh. Two sets of simulations have been carried out on the Atzeni's design [11] which is considered here as the reference test case for the hydrodynamic perturbation modeling sequence.
The full spectrum of the laser irradiation has been introduced in the 2D CHIC [33] simulations on a 90 degrees mesh grid. Strictly speaking only even modes can be dealed with because of the mesh symmetry. The mesh includes 256 grid points in the radial direction, with a refinement in the absorption region, and 56 grid points, regularly spaced, in the transverse direction. The mode number l=20 will be described by 6 grid points for half a wavelength which limits our multimode analysis to mode numbers lower than 20. For simplicity reasons, laser power has been calculated from 1D total absorption at the critical density and modulated by a Legendre expansion, constant in time, taken from FIG. 4.8 (on the left). The resulting illumination versus angle is presented in FIG. 4.9.
Multimode CHIC (FIG. 4.10) simulation indicates that the mode number l=12 remains dominant up to the time of maximum areal density, i.e., the stagnation time. The maximum deformation achieved at internal interface is about 10 μm from peak to valley. This deformation is the consequence of the illumination nonuniformities which have seeded perturbations at the ablation surface. Then these perturbations have been transmitted to internal interface during shock wave transit and amplified by Bell-Plesset mechanism. Fourier analysis, i.e., modal anal-

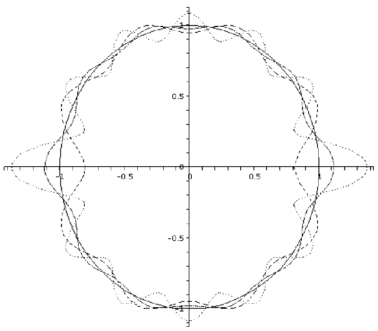

Figure 4.9: Illumination spectrum versus angle applied in 2D multimode CHIC simulations. The mode number l=12 is the dominant mode number.

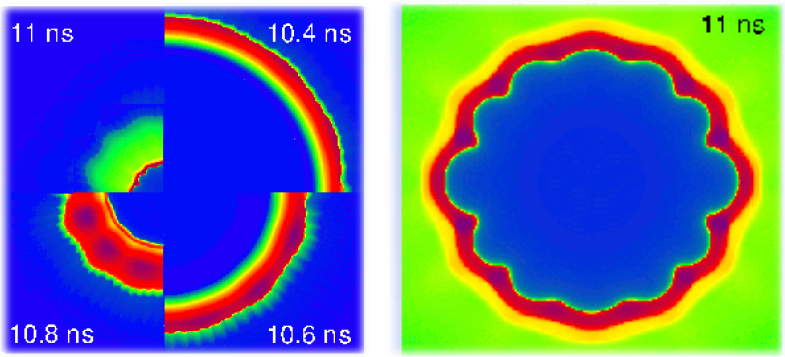

Figure 4.10: Multimode, 90 degrees, CHIC simulation of Atzeni's reference design. Four density contours at time t=10.4 ns, t=10.6 ns, t=10.8 ns and t=11 ns are presented on the left panel. A magnified view of density contours is presented on the right panel at time t=11 ns, i.e., just before time of maximum areal density ($\approx$ 11.17 ns).

ysis, of the internal interface deformation at stagnation is presented in Fig. 4.11. It confirms that dominant mode number is the l=12 and it shows that lower mode numbers have considerably decreased. Nonlinear mode coupling does not really take place, although contribution of l=16 mode number slightly increases. This result is confirmed by an evaluation of the ratio perturbation amplitude on inflight radius ($a/\Delta R$) which is lower than 1 (not shown here). These results show that deformation of the internal interface can be obtained with monomode simulations, the whole spectrum being obtained by reconstruction of each modal contribution. Moreover, previous studies [80] have shown that monomode simulations by using sector grid meshes covering half a wavelength gave results similar to that obtained on a 90 degrees mesh.

4.4 Non-linear amplification of high mode perturbations at ablation front in HiPER targets

A safety factor discussion for low modes perturbations ($l \leq 50$), related to laser irradiation non uniformities, is addressed in Ref. [74]. It is shown that a self-consistent numerical method provides accurate estimates for the perturbation growth at the ablation front and at Deuterium Tritium (DT) interfaces. Also some analytical estimates could be obtained by coupling the perturbed shock waves with the ablation front in a high aspect ratio target. Thus, the perturbation growth can be understood by combining direct numerical simulations with a model post-treatment for low mode numbers corresponding to large wavelength perturbations. These

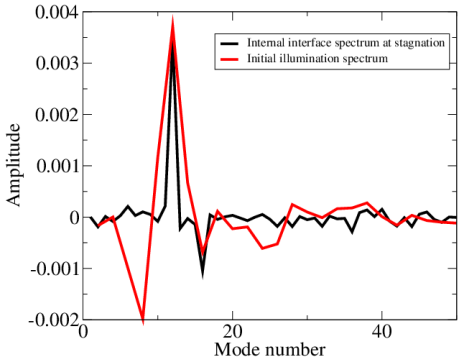

Figure 4.11: Fourier analysis, i.e., modal analysis, of the internal interface deformation at stagnation. The mode number l=12 remains the dominant mode number which justifies linear monomode simulations in order to study the deformations up to the stagnation phase.

perturbations can be initiated, for example, by laser irradiation non uniformities. A tolerance guideline on the laser irradiation was suggested and dominant mode numbers were identified.

Pursuing hydrodynamic stability studies for the HiPER baseline target, we address here the problem of high mode perturbations ($l \geq 20$) induced by shell roughness.

Here, contrary to the low wave numbers case, non-linear behaviour has to be accounted for during the shell acceleration. Finally, it is shown that, for high modes, the ablative Rayleigh-Taylor (ART) instability behaves apart from the spatial perturbation seeded during the shock transit time. It depends only on the amplitude achieved at the beginning of the acceleration. Numerical simulations with 2D code CHIC [33] provide an accurate estimate of the linear perturbation growth and give an assessment of the non linear stage. It is also shown that stabilizing schemes based on adiabat shaping [8] reduce the perturbation growth and delay the beginning of the non-linear phase. This allows to discuss the problem of determining the admissible initial roughness spectrum for the baseline HiPER target. A good agreement is found between simulations and self-consistent theories up to the end of the weakly non-linear phase.

4.4.1 Non-linear ART simulation with the ALE CHIC code

To study the perturbation evolution at the ablation front we impose a Legendre single-mode perturbation at the external surface. This perturbation is radial and, because of the relatively small range of the spatial perturbation dependency, a linear decay inside the shell is used. This approximation preserves the ART seeding and growth. A purely Lagrangian computation may stop before end of acceleration, during the non-linear stage due to tangled mesh. The ALE method allows to improve the geometrical quality of the grid elements and to optimize accuracy, robustness, and computational efficiency. A special rezoning procedure is implemented in the ablation zone. A traditional mesh smoothing is not sufficient in our case as it could decrease the accuracy of the Lagrangian computation with the consequence to loose the spatial resolution. It is necessary to preserve the Lagrangian displacement at the ablation front. In the rezoning procedure implemented in CHIC, the Lagrangian characteristic of the mainstream flow and especially the perturbation at the ablation front are preserved using an orthoradial projection. In this rezoning procedure we keep the radial Lagrangian displacement of the nodes during all the computation and we orthogonally project the orthoradial displacement onto this radius. The rezoning phase is followed by a second order remapping phase where all the conservative quantities are conservatively remapped from the Lagrangian mesh onto this rezoned mesh. Once the non-linear perturbation growth has started, we add to this rezoning an additional

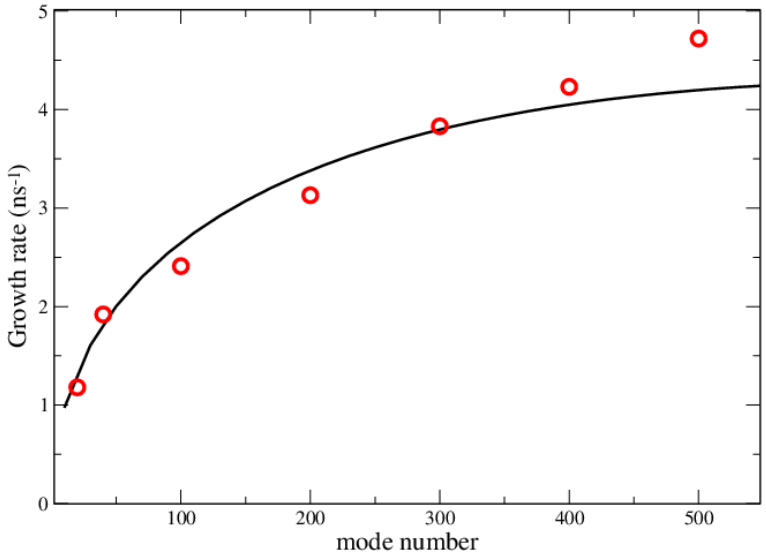

Figure 4.12: Linear growth rate at short times (7.5 - 8 ns) versus mode number obtained from the CHIC simulations (dots) compared to theoretical model (solid line) [25].

mesh smoothing to avoid mesh tangling. By using such rezoning, a non-linear evolution of mode numbers up to $l = 800$ can be studied by using 35 grid points per wavelength.

4.4.2 2D high mode simulations of perturbed flow

Fig. 4.12 presents a cross-check validation of high mode instantaneous linear growth rates obtained in CHIC simulations and from theory [25]. This comparison is made for short times up to 8 ns, because of the early non-linear stage, which occurs for modes higher than l=100 including small initial perturbation amplitudes. Indeed for $l = 100$ and a 0.1 cm radius, the non-linear threshold $ak \sim 0.1$ [96] is expected to be reached, for amplitudes larger than 1 μm, in the nanosecond time scale. Note that at the beginning of acceleration, most unstable modes are in the range [500-600] as the maximum growth factor are obtained for modes in the range [200-300]. It shows an important time dependency in the perturbations development for the linear and non-linear regimes, including the contribution of at least the second harmonic.
In Fig. 4.13(a) we show the perturbation amplitude at ablation front versus time for different initial amplitudes with initial single-mode perturbation $l = 200$. The transition to the non-linear stage is indicated by the slope modification in the amplitude evolution. The perturbation evolves in the linear regime (see Fig. 4.13(b)) and then reaches the weakly non-linear regime (Fig. 4.13(c)). At that moment, the particular shape of density contours are characteristic of the ART instability behaviour. Here at least a double frequency structure is present. The effect of ablation on the perturbation shape during the weakly non-linear regime is clearly seen. This shape is described and explained in [144, 143]. The spikes may flatten and enlarge due to the dynamical ablation overpressure. In this regime, the perturbation shape is the result of early seeding of harmonics and their feedback to the fundamental mode. These harmonics can appear with the same or opposite phase relatively to the fundamental mode [144]. Fig. 4.14 (a) shows the amplitudes (absolute values) of the first and second harmonics as a function of time. Fig. 4.14 (b) shows a Fourier analysis of the modal spectrum during the main acceleration, at time t=9.2 ns, up to fifth harmonic. The density contours shape (wide and flattened) in Fig. 4.13(c) is due to the phase inversion of the second harmonic (Fig. 4.14 (b)).
The different shapes of the density contours for $l = 200$ are shown at different times in Fig. 4.15

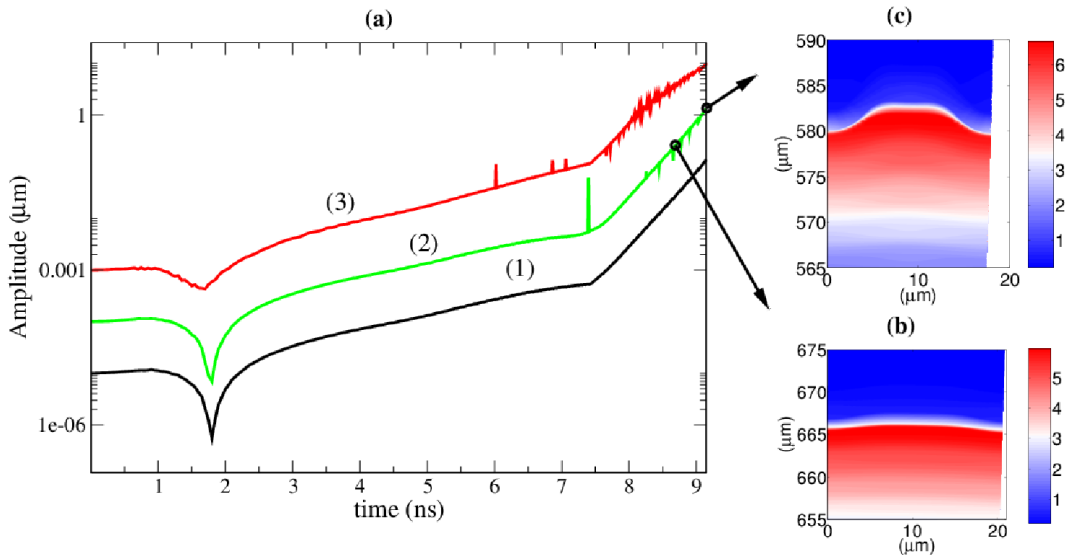

Figure 4.13: a) Ablation front perturbation versus time for $l = 200$ mode with three different initial amplitudes and density contour shapes (g/cm^3) of curve (2) at times b) 8.7 ns and c) 9.2 ns. On density contours, the blue zone on the top is the external vacuum, the red zone is the compressed DT and the blue zone on the bottom is the vapor-pressure DT gas in the center.

excited by the initial roughness of about 1 nm (Fig. 4.15a-b-c). A peak-and-valley shape can be seen up to the fully non-linear regime at the time t > 9 ns. The non-linear shape consists in spikes and bubbles structures. At the end of the simulation, multi-frequency structures appear. For a few nm initial amplitude, the non-linear evolution lasts most of the acceleration phase and non-linear couplings may be very strong. For a higher initial amplitude around 10 nm and more, characteristic structures appears with very singular shape (see Fig. 4.15 (e)), previously observed in planar simulations in [144]. At large time, an asymptotic case is achieved, where the shell is completely decompressed (Fig. 4.15 (f)). These initial conditions lead to exhibit very complex multimode structures of the non-linear regime, where ablation plays an important role. Namely the shape of the perturbation differs from the classical case where thin spikes and thick bubbles are expected [144]. This new repartition is clearly observed for higher modes in our simulations. In Fig. 4.16, for mode $l = 300$, one can see the clear inversion of the shape perturbation (thin bubbles, thick spikes) from the weakly non-linear stage (Fig. 4.16(a)). This behaviour has been observed for all higher modes. Theory exhibits a threshold wave number for this feedback. Our simulations, initiated by a single-mode perturbation ($l = 300, 500, 800$), reproduce the inversion of spikes and bubbles thickness, contrary to a classical Rayleigh-Taylor (RT) weakly non-linear perturbation shape, i.e., without ablation. Simulations results are consistent with the existence of this threshold and all unsteady effects. For example, the dominant mode in the linear regime differs at the beginning of the main acceleration and subsequent times. For this reason, the non-steady effects act on the growth of both fundamental and harmonics of the initial perturbation. The initial amplitude may also change the contribution of the behaviour corresponding to each mode perturbation. At later times, the perturbation evolves in the non-linear regime with a multimode bubble-spike structure (Fig. 4.16(b)). Non-linear effects at the ablation front produce very elongated bubbles which extend from the ablation front into the expanding low density plasma (Fig. 4.16(c)).

Figure 4.17 shows the temporal evolution of the perturbation amplitude at the ablation front for the mode $l = 300$ and for three initial amplitudes. The behaviour is the same before the main acceleration phase as long as the perturbation remains in the linear stage. The slope

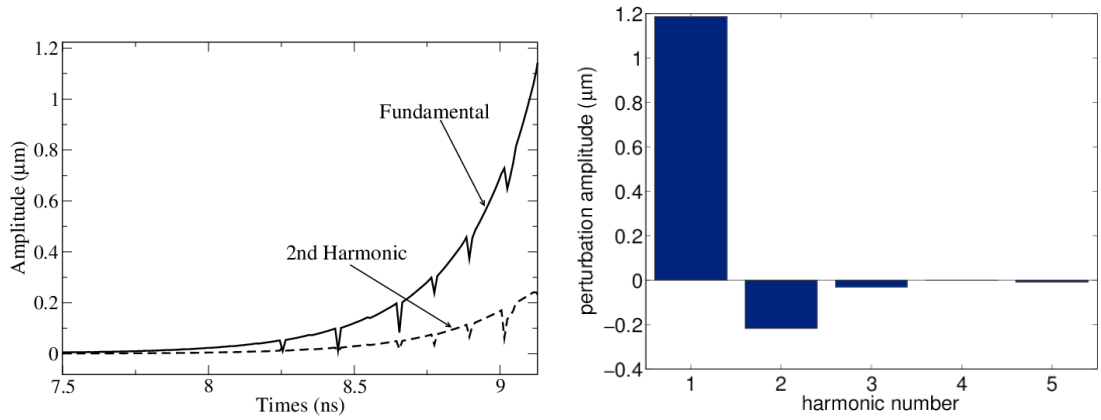

(a) (b)

Figure 4.14: For mode $l = 200$: a) Amplitude of the first and second harmonics versus the time during the acceleration phase; b) Fourier analysis of ablation front perturbation at time 9.2 ns acceleration, up to fifth harmonic. The second harmonic appears with opposite phase.

variation indicating the non-linear perturbation behaviour occurs for the same amplitudes. The Y curves indicate fraction levels of the perturbation wavelength λ. In particular, $Y = 0.1\lambda$ corresponds to the classical weakly non-linear saturation criteria [96]. For the mode $l = 300$, we checked that the radiation transport has weak influence on the instability growth. At the end of acceleration, the radiation changes the amplitude less than 10%. For modes greater than 300, the shape inversion was observed, with thicker spikes. Additionally, for these modes, the perturbation may reverse phase during the weakly non-linear stage. A multimode computation has been also performed Fig. 4.18 based on a initial $l = 300$ and with 10% of $l = 100$. It exhibit bubble competition and indicate that a study should be performed using real initial spectrum for the baseline HiPER target, has performed in the work of [130]. Experimental study has also been realized to study the ART instability growth [52], on the OMEGA laser facility and the radiation hydrodynamic CHIC code has been used for the design and the interpretation of the results.

4.5 Study on shock propagation in the context of polar direct drive shock ignition

In the Direct-Drive Inertial Confinement Fusion (ICF) scheme, the classical process leading to DT ignition is the conversion of the shell kinetic energy into internal energy of a central hot spot, which further acts as an ignition spark [13]. To achieve central ignition, the shock ignition (SI) scheme has been extensively studied theoretically and experimentally [97, 26, 43, 138]. Shock ignition was first proposed by Betti et al. [10], it consist to ignite the target by means of a strong convergent shock launched in the target at the end of the compression phase and prior to the final stagnation of fuel at target center. This new concept has been experimentally studied in planar [138, 20, 10] or in spherical geometry [18, 137, 153]. It was demonstrated that a properly timed final shock significantly enhances the neutron yield [12] and that the coupling of high-intensity spike beam energy into the imploding capsule was studied, which suggests that the yield increase was partially due to hot electrons coupled into the compressing target. [79]. Recently, encouraged results obtained from strong spherical shock [152] demonstrate the capability to generate high shock pressure 300 Mbar at laser intensities in the range of 1015 to

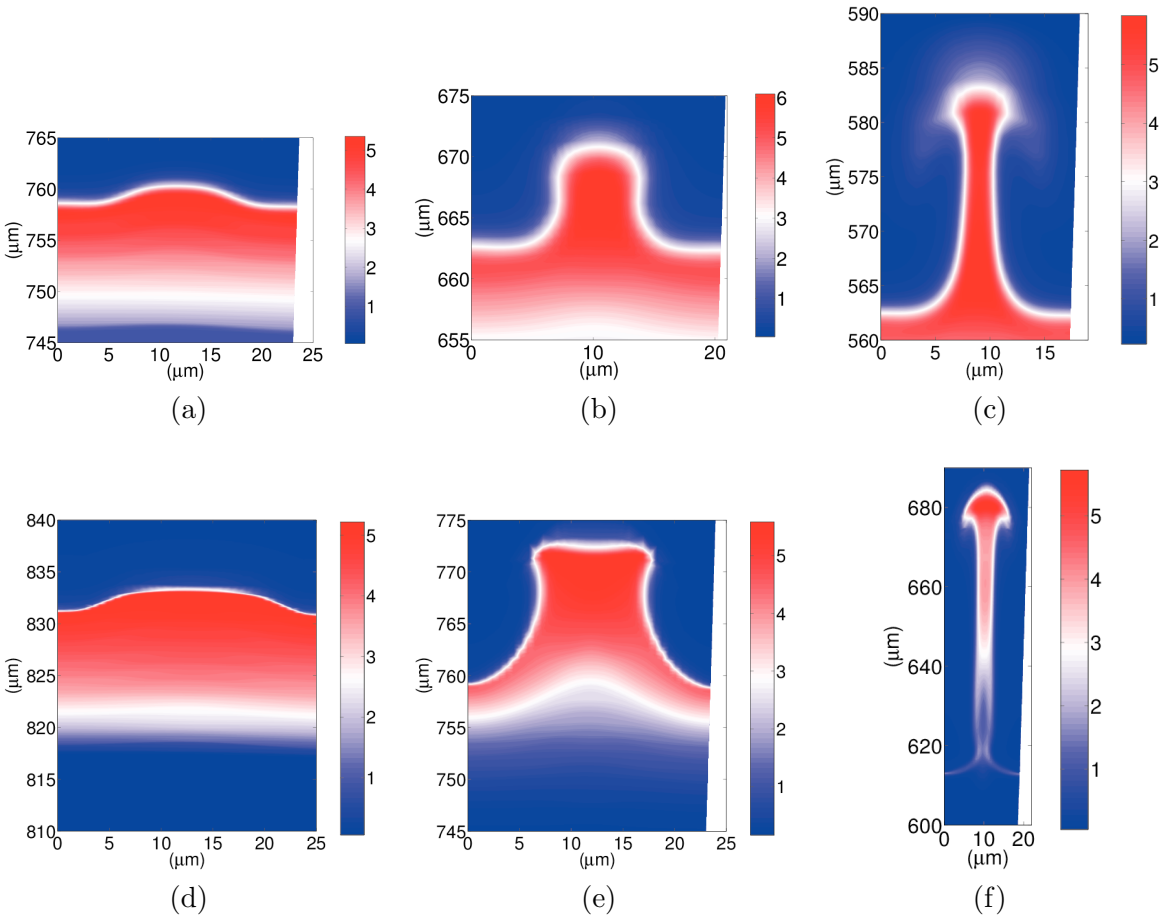

Figure 4.15: Evolution of the perturbation shape on density contours for $l = 200$ mode: with initial amplitude $a_0 \sim 1$ nm at times a) 8 ns, b) 8.7 ns, c) 9.2 ns; with initial amplitude $a_0 \sim 10$ nm at times d) 7.3 ns, e) 8 ns, f) 8.7 ns. On density contours, the blue zone on the top is the external vacuum, the red zone is the compressed DT and the blue zone on the bottom is the vapor-pressure DT gas in the center.

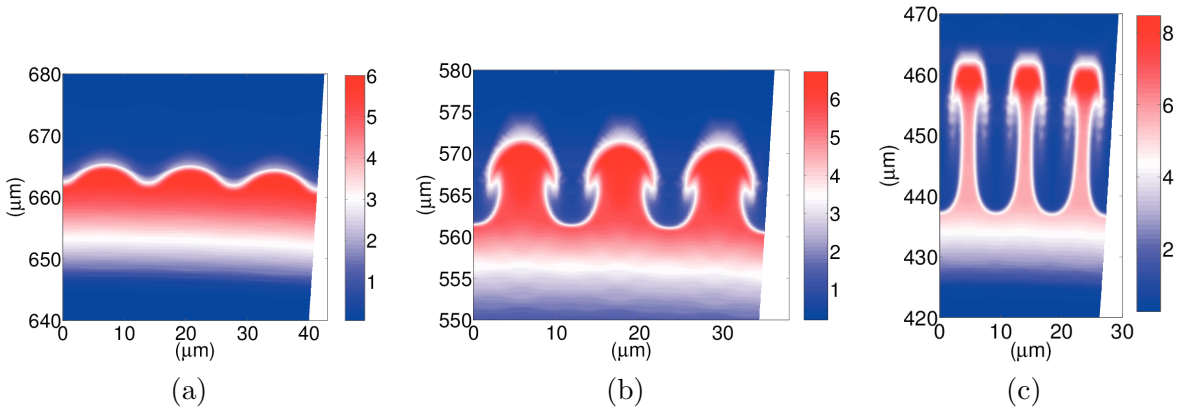

Figure 4.16: Evolution of the density contours of mode $l = 300$ at times a) 8.7 ns, b) 9.2 ns, c) 9.7 ns. An inversion of the bubble-spike symmetry is observed.

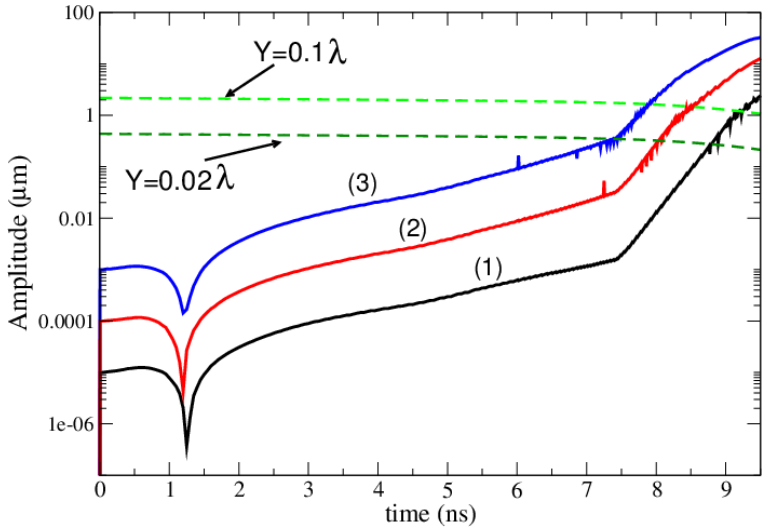

Figure 4.17: Ablation front perturbation amplitude versus time for $l = 300$ mode, with standard pulse and three different initial amplitudes.

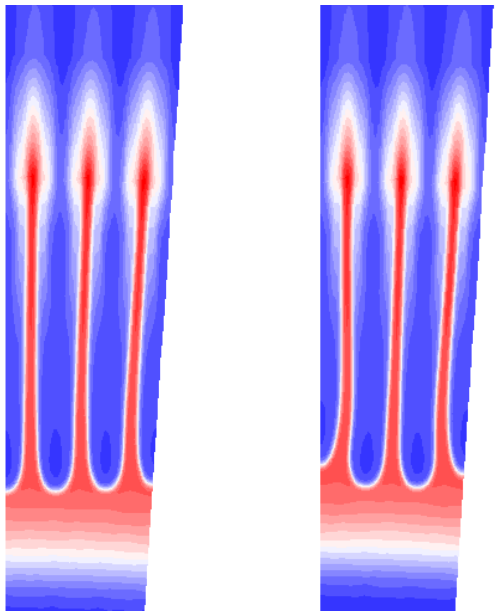

(a) (b)

Figure 4.18: a) Monomode calculation $l = 300$; b) multimode for $l = 300$ and 10% of $l = 100$ both at time t=10.2 ns.

1016 $W/cm2$. This physical issue is crucial for the credibility of SI [152].
In this section, we study the possibility to ignite the hot spot with a strong no-uniform irradiation for the ignitor shock. The shock ignition is a two step process, first a uniform illumination compressed the target at low velocity, then a strong shock converge to ignite the hot spot. Although the compression require a uniform irradiation, for the ignitor shock it is not mandatory require. This possibility studied in [153] shows that because the critical radius target is reduced at the shock launching time, the focal spot needed for the ignitor could be smaller than the compression beam. This allow a better absorption and demonstrated the high flexibility and robustness of this concept [153], i.e. even in bipolar irradiation the ignition occurs. In this configuration the hydrodynamic simulations show that two planar shocks propagate inside the hot spot and collide to ignite the target. To study the bipolar ignition scheme, an experiment on the LIL facility was proposed to experimentally reproduce the formation of a convergent planar shock by a spike laser pulse in presence of a SI relevant plasma. In this experiment, the LIL quad Gaussian beam is focused on hemispherical target and compare to the planar one. In the two configurations VISAR an SOP diagnostics allowed to give to the inferred shock pressures and shapes.
Here we report the results obtained on the hemispherical target. Due to the complex geometry this experiment was the first which use the multi-material Eulerian version of CHIC at CELIA. This version uses the last development of the CHIC code for the multi-material treatment based on the MOF method for the interface reconstruction. As it is shown in Fig. 4.19 and Fig. 4.20 the CHIC code enables to recover all the shock timing at ± 100 ps visible on the VISAR diagnostic.

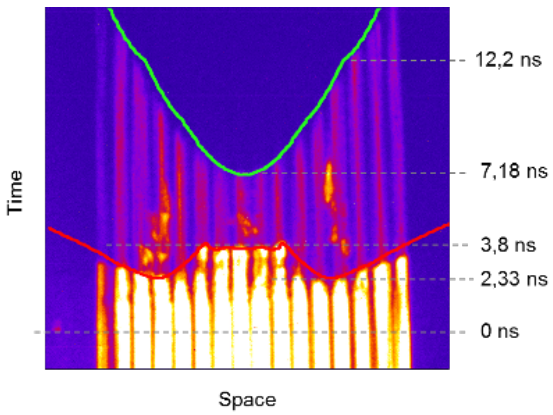

Figure 4.19: VISAR experimental results compared to the simulated VISAR using the CHIC code (red and green curve).

The initial configuration is shown in Fig. 4.20(a) on the left and right very light density material also called pseudo material are initialized. Then from the left to the right we have a thick slice of quartz of $250\mu m$, then $30\mu m$ of Molybdenum (Mo) and finally the CH part of the target which include the hemisphere. At $t = 2.4ns$, Fig. 4.20(b), the shock as penetrated the Mo and it is the first signal visible on the VISAR Fig. 4.19. At this time the pseudo material on the right has been totally replaced by the CH plasma due to the ablation of the CH target. At $t = 3.7ns$, Fig. 4.20(c), a planar shock reach the left interface of the Mo and it corresponds to the plateau of Fig. 4.19. At that time we can see the thin Mo slice has been compressed by the shock. At $t = 7.1ns$, Fig. 4.20(d), a shock reach the left interface of the quartz which is visible on Fig. 4.19. Here the Mo is much deformed by the shock interaction. At $t = 12.25ns$, Fig. 4.20(e), two shock converge on the left interface of the quartz and change the slope of the VISAR results, green curve on Fig. 4.19. As the laser has been turned off at $t = 4ns$ the

Mo expand and some droplet of material are visible on Fig. 4.20(e) and Fig. 4.20(f). The quartz penetrate the pseudo vacuum on the left. Due to the very strong deformation of the Mo material on Fig. 4.20(f) we can see that some cells contain three different materials quartz-Mo-CH which is one of capability of the MOF method to track multi-material cell with more than two materials.

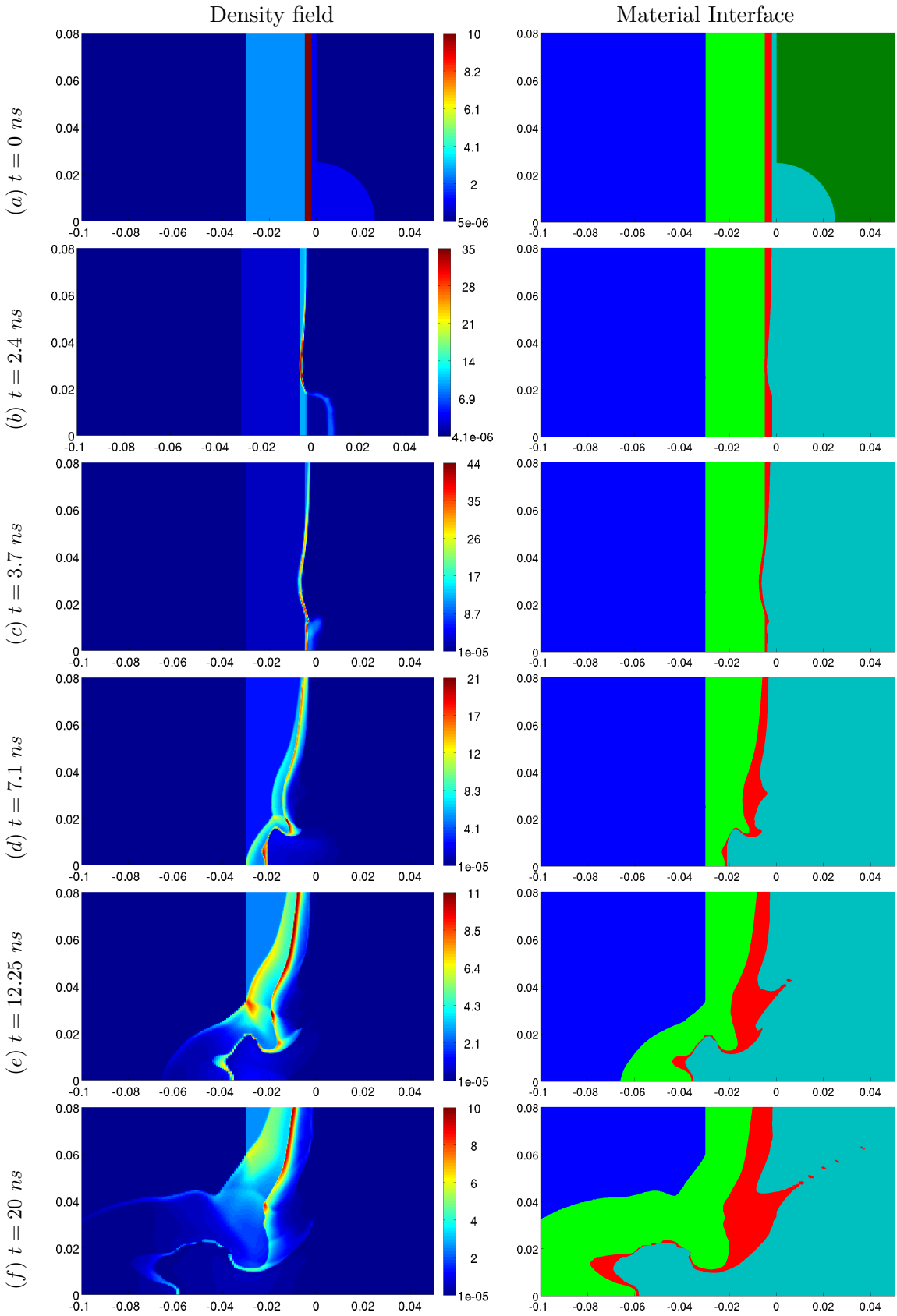

Figure 4.20: Density fields (left) and material interface (right) at different time.

Conclusion and perspectives

In this document a part of the works done for the last ten years has been presented. This work has initiated numerous international collaborations with American national Laboratories (LANL, LLNL) for the numerical part and with ILE in Japan for MHD applications. I personally had the opportunity to be invited at LLNL in US and ILE in Japan to work closely with local teams. This work also gave me the opportunity to mentor a number of internships student, thesis and postdoc. This research work has been presented in numerous seminar, workshop and international conference, some as invited speaker. Most of the numerical schemes presented here, have been published in original research peer-reviewed articles. The CCALE-MOF strategy based on the EUCCLHYD Lagrangian scheme coupled to the CCLADNS scheme which solve anisotropic diffusion equation has been presented here. These numerical schemes are the numerical bricks of the CHIC code that has been developed at CELIA. Some applications using the CHIC code have been also presented to highlight the capability concerning the HEDP domain and more precisely ICF for FI and SI.

In this document, extension of the scheme to the case of hypo-elastic constitutive laws material has not been presented [119] but it is now being implemented in the CHIC code. Concerning the EUCCLHYD scheme we have proposed a 3D extension which is based on a symmetric and systematic geometric decomposition of the polyhedral cells using the faces barycenter [66]. Using the assumption of a linear velocity field on the cell faces, this decomposition enables to define a discrete divergence operator and to respect the GCL on any unstructured polyhedral mesh. Moreover, a new multi-dimensional minmod limiter is constructed from nodal gradients and the minmod function. This method enables to drastically reduce overshoots around strong shocks while preserving the flow symmetries. These two methods are applied to a second-order cell-centered Lagrangian scheme based on the work [118]. This scheme satisfies an entropy inequality and conserves globally the momentum and total energy.

For the ALE formulation, we have introduced a simple and unified formulation of the Lagrangian scheme relying on an area-weighted formulation, a multi-material MOF interface reconstruction, a new formulation of rezoning for polar, Cartesian and unstructured grids and finally a general hybrid remap procedure for both axisymmetric and Cartesian geometry. As demonstrated on several academical as well as ICF-like test cases, the proposed method remains accurate and robust. Additional validation results can be found in Appendix B where we propose comparisons with experimental results. A possible extension for the ALE method could be an ALE-AMR method which could couple the ALE strategy to an Adaptive Mesh Refinement (AMR) method [123]. This could improve the interface tracking in the ALE framework.
As a future work, the implementation of an Arbitrary Lagrangian-Eulerian (ALE) method in 3D could improve the scheme ability to treat flows with strong vorticity and shearing in 3D. In particular, such a method coupled to a 3D interface reconstruction, would enable the modeling of multi-material compressible flows with propagation of a perturbation such as the Kelvin-Helmholtz instability or the triple point problem [32].

We have shown that our cell-centered ALE with MOF interface reconstruction algorithm gives accurate and efficient results on problems that use real EOS. Furthermore, our method improves the robustness of ALE calculations on ICF implosion problems. Pressure relaxation closure model should be implemented [14, 148] to overcome the problem of overshoot in Lagrangian computation with mixed cells.

Comparison between ALE and ReALE has shown that the ReALE formulation succeeds in keeping the Lagrangian property whereas the ALE computation presents some limitation. Indeed, using this multi-material ReALE strategy coupled to the Moment of Fluid (MOF) interface reconstruction method we recover the Lagrangian features of following material interface that we lose using standard ALE methods with fixed connectivity. In all computations, MOF interface reconstruction demonstrate its ability to follow the material interface and even succeeds in tracking thin filaments of material. As future work, we could improve the remapping phase as exact intersection is quite expensive and apply the hybrid remapping method [24] to multi-material ReALE. We also plan to study adaptation using the possibility to add and remove generator dynamically during the ReALE simulation as in [28]. As future work, we would like to incorporate the ReALE method in the multi-physics code CHIC dedicated to the simulation of ICF experiment. The main goal is to treat eventually more general configurations notably coupling realistic EOS, laser energy deposition, with multi-material hydrodynamics in the lines of [33].

Finally, we have described the cell-centered finite volume CCLADNS scheme which aims at solving anisotropic diffusion problems on two and three-dimensional unstructured ALE-AMR grids. This scheme is characterized by cell-centered unknowns and a local stencil like the CCLAD scheme [36] which is also used in the CHIC code. The partition of grid cells (resp. faces) into sub-cells (resp. sub-faces) allows to construct a sub-face flux approximation by means of a sub-cell-based variational formulation. The sub-face fluxes are expressed locally to the node in terms of the surrounding cell-centered temperatures invoking continuity conditions of the temperature and normal heat flux at the cell interface.
We have described a modification of the scheme, which enables to compute solutions on 2D and 3D AMR grids. For these specific grids we have introduced a modification of the underlying sub-cell decomposition in order to obtain, in each sub-cells, a basis constructed upon their normal vectors. With this modification, only local linear systems are modified, and the construction of the global system remains unchanged.
Regarding its accuracy, the CCLADNS scheme preserves linear fields with respect to the space variable over polygonal and polyhedral grids and exhibits a second-order rate of convergence on these grids for analytic solutions.

In a future work we plan to investigate the mathematical properties of the CCLADNS scheme. For now, we successfully validated the scheme on numerous test cases, but we are still missing the mathematical evidence of its properties. Moreover, we ran tests on static AMR grids only. In the future we plan to develop a dynamic AMR method, using a posteriory error estimates to dynamically refine or coarsen the mesh. This is a really challenging problem from a mathematical point of view and from a computer science point of view. From a mathematical point of view we need to find estimators that are well suited to handle the different physics at hand. All the details of the different physics need to be taken into account. From a computer science point of view, this is also a really challenging task. When we refine the mesh, we need to keep a balanced load between the parallel processes in order to keep also a good computational efficiency. For this specific task we plan to use the Scotch library [132] that allows efficient repartitioning techniques. In future, we would like also to study the coupling between diffusion

and 3D Lagrangian hydrodynamics [66] on AMR grid, like in [50], which is based on orthogonal grid in presence of multi-material interfaces. The treatment of such multi-material flows on distorted grid should be done in the same manner as in [35].

Appendix A

Piecewise quadratic reconstruction for FCR remap

To get the high-order numerical fluxes for the FCR method, the piecewise quadratic reconstruction [49] is used. In this section, we repeat the procedure to provide necessary formulas to compute the quadratic reconstruction in the selected cell (we omit here the index i of the cell for simplicity). The quadratic reconstruction of an unknown function in one cell has the form

$$u^H(x,y) = \overline{u} - \lambda_0 + \lambda_1(x - x_c) + \lambda_2(y - y_c) + \lambda_3(x - x_c)^2 + \lambda_4(x - x_c)(y - y_c) + \lambda_5(y - y_c)^2\,,$$

where $\overline{u}$ represents the cell mean value of the conservative quantity (density, momentum or total energy); x_c, respectively y_c the coordinates of the cell centroid and $\{\lambda_0, \ldots, \lambda_5\}$ a set of the unknown coefficients of the reconstruction. To preserve a mean value of the conservative quantity, the first coefficient has the form (the meaning of "generalized centroids" x_s, y_s, z_c is described later)

$$\lambda_0 = \lambda_3(x_s - x_c^2) + \lambda_4(z_c - x_c y_c) + \lambda_5(y_s - y_c^2)\,. \tag{A.1}$$

The remaining coefficients $\Lambda = (\lambda_1, \ldots, \lambda_5)^T$ are calculated by the minimization of the reconstruction error in the neighboring cells

$$\sum_{k \in \mathcal{N}} \left(\overline{u}_k - \frac{1}{V_k} \int_{\Omega_k} u^H(x,y)\,\mathrm{d}V \right)^2 . \tag{A.2}$$

Here Ω_k stands for the area of the cell with the volume V_k and $\mathcal{N}$ represents the set of n neighboring cells to the given cell. To get a unique solution for Λ, at least 5 neighboring cells are required. We choose the corner neighbors for the quadrilateral mesh and the edge neighbors for the other polygonal meshes. Ghost cells are attached to the boundary with conservative quantities filled by given boundary conditions, so that each internal cell has the full stencil $\mathcal{N}$. The minimization is equivalent to the solution of the following over determined linear system in the least square sense

$$\mathbb{A}\Lambda = \boldsymbol{B} \qquad \boldsymbol{B} = (\beta_1, \ldots, \beta_n)^T \qquad \mathbb{A} = \begin{pmatrix} \alpha_{1,1} & \cdots & \alpha_{1,5} \\ \vdots & \ddots & \\ \alpha_{n,1} & & \alpha_{n,k} \end{pmatrix} \tag{A.3}$$

with

$$\begin{aligned}
\beta_k &= \overline{u}_k - \overline{u} \\
\alpha_{k,1} &= x_{c_k} - x_c \\
\alpha_{k,2} &= y_{c_k} - y_c \\
\alpha_{k,3} &= x_{s_k} - x_s + 2(x_c^2 - x_c x_{c_k}) \\
\alpha_{k,4} &= z_{c_k} - z_c + 2x_c y_c - x_{c_k} y_c - y_{c_k} x_c \\
\alpha_{k,5} &= y_{s_k} - y_s + 2(y_c^2 - y_c y_{c_k}) \,.
\end{aligned}$$

The centroid coordinates x_c, y_c of the cell and x_{c_k}, y_{c_k} of the adjacent cell k and similar quantities x_s, y_s, z_c are defined as

$$\begin{aligned}
x_c = \frac{1}{V}\int_\Omega x \,\mathrm{d}V &= \frac{1}{6V}\sum_{q\in\mathcal{P}}(x_q^2 + x_q x_{q-1} + x_{q-1}^2)(y_q - y_{q-1}) \\
y_c = \frac{1}{V}\int_\Omega y \,\mathrm{d}V &= -\frac{1}{6V}\sum_{q\in\mathcal{P}}(y_q^2 + y_q y_{q-1} + y_{q-1}^2)(x_q - x_{q-1}) \\
x_s = \frac{1}{V}\int_\Omega x^2 \,\mathrm{d}V &= \frac{1}{12V}\sum_{q\in\mathcal{P}}(x_q + x_{q-1})(x_q^2 + x_{q-1}^2)(y_q - y_{q-1}) \\
y_s = \frac{1}{V}\int_\Omega y^2 \,\mathrm{d}V &= -\frac{1}{12V}\sum_{q\in\mathcal{P}}(y_q + y_{q-1})(y_q^2 + y_{q-1}^2)(x_q - x_{q-1}) \\
z_c = \frac{1}{V}\int_\Omega xy \,\mathrm{d}V &= \frac{1}{24V}\sum_{q\in\mathcal{P}}\big[x_{q-1}^2(3y_{q-1} + y_q) + 2x_{q-1}x_q(y_{q-1} + y_{q-1}) + \\
&\qquad + x_q^2(y_{q-1} + 3y_q)\big](y_q - y_{q-1}) \\
V = \int_\Omega \mathrm{d}V &= \frac{1}{2}\sum_{q\in\mathcal{P}}(x_q + x_{q-1})(y_q - y_{q-1}) \,.
\end{aligned}$$

Here $\mathcal{P}$ is a set of all nodes of the selected cell and we assume (without the loss of generality) an ordering which allows us to select the previous $(q-1)$ and the next $(q+1)$ point in this set in the counter-clockwise order.

Neglecting the parabolic terms (the last three columns of the matrix $\mathbb{A}$ (A.3)) in (A.2) leads to the standard piecewise linear reconstruction. In the piecewise linear case, the minimization problem has an easy solution given by a system of two linear algebraic equations. In the piecewise quadratic case, we use the singular value decomposition method to solve the least-square system (A.3).

This reconstruction is used to compute the high-order numerical fluxes through the mesh edges. For the piecewise linear reconstruction, the integration over swept regions is described in [95]. This method does not require the costly computation of the cells intersections. In the numerical results section, we show that accuracy of this method, for the considered problems, is comparable to the intersection based method. Here we present the final formula for one particular numerical flux

$$\begin{aligned}
F_{\mathcal{S}}^H = \int_{\mathcal{S}} u^H \,\mathrm{d}V = \big[&(\overline{u} - \lambda_0) + \lambda_1(x_c^{\mathcal{S}} - x_c) + \lambda_2(y_c^{\mathcal{S}} - y_c) + \\
&+ \lambda_3(x_s^{\mathcal{S}} - 2x_c^{\mathcal{S}}x_c + x_c^2) + \lambda_4(z_c^{\mathcal{S}} - y_c^{\mathcal{S}}x_c - x_c^{\mathcal{S}}y_c + x_c y_c) + \lambda_5(y_s^{\mathcal{S}} - 2y_c^{\mathcal{S}}y_c + y_c^2)\big]\, V^{\mathcal{S}} \,,
\end{aligned}$$

where the x_c, y_c are coordinates of the cell centroid and all other terms are given by the integral formulas above over the swept region $\mathcal{S}$, e.g. $x_s^{\mathcal{S}} = \frac{1}{V^{\mathcal{S}}} \int_{\mathcal{S}} x^2 \, \mathrm{d}V$. The low-order piecewise constant reconstruction is simply given by the mean value in the cell $u^L(x, y) = \overline{u}$ and therefore $F_{\mathcal{S}}^L = \int_{\mathcal{S}} u^L \, \mathrm{d}V = \overline{u} V^{\mathcal{S}}$.

Appendix B

Validation of ALE and ReALE based on experimental results

Validation presented in the document for the ALE and ReALE methods are mainly based on analytical solutions we propose here some comparisons with experimental results.

B.1 ALE simulation of a spherical Air-Helium shock/bubble interaction test

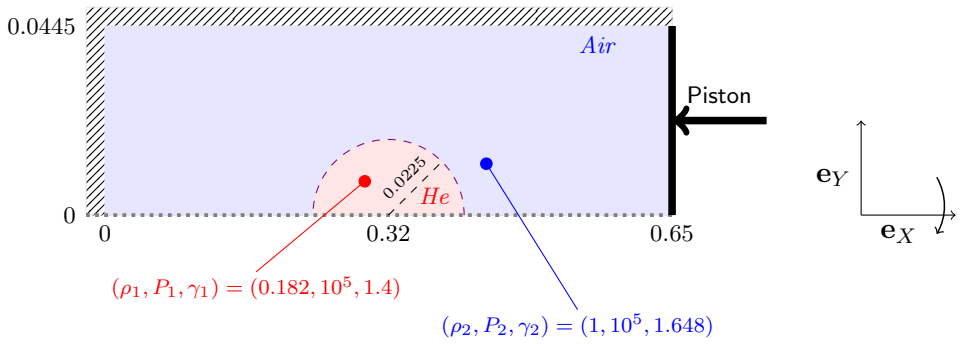

Figure B.1: Spherical Air-Helium shock/bubble interaction. Initial geometry and data.

We deal in this part with the numerical simulation of the experiment presented in [72]. We study here, the interaction of a Mach 1.25 shock travelling through the air with a spherical bubble of Helium. To this goal, let us consider a rectangular domain of dimensions $[0, 0.65] \times [0, 0.0445]$ initially full of Air characterized by $(\rho_1, P_1, \gamma_1) = (0.182, 10^5, 1.4)$. This domain contains a spherical bubble of Helium $(\rho_2, P_2, \gamma_2) = (1, 10^5, 1.648)$ in an half disc centered in $(0, 0.32)$ of radius 0.0225 as depicted on FIG. B.1. Here, spherical geometry of the bubble is obtained thanks to axisymmetric geometry. Wall boundary and symmetry conditions are respectively chosen for the left and top boundaries. Despite, a piston-like condition is imposed to the right one for an incoming velocity equal to $\mathbf{U}^* = (u^*, 0)$. Here, the horizontal velocity u^* is computed thanks to Rankine-Hugoniot conditions and is given by $u^* = -140.312$ corresponding to an incident shock moving at the velocity $D_c = -467.707$.

The domain is initially paved with a structured Cartesian grid composed of 520×72 cells. Here, the bubble is directly initialized through the volume fraction on this mesh. Computations are done for the multi-material axisymmetric CCALE-MOF for a final time chosen equal to

$t_f = t_i + 600 \times 10^{-6}$ where $t_i = 657.463 \times 10^{-6}$ corresponds to the time of the shock/bubble interaction. Here once again, simulations can not be achieved using pure Lagrangian framework due to the apparition of important mesh distortion. Numerical results associated to the Schlieren density profiles [73] are depicted on FIG. B.2.

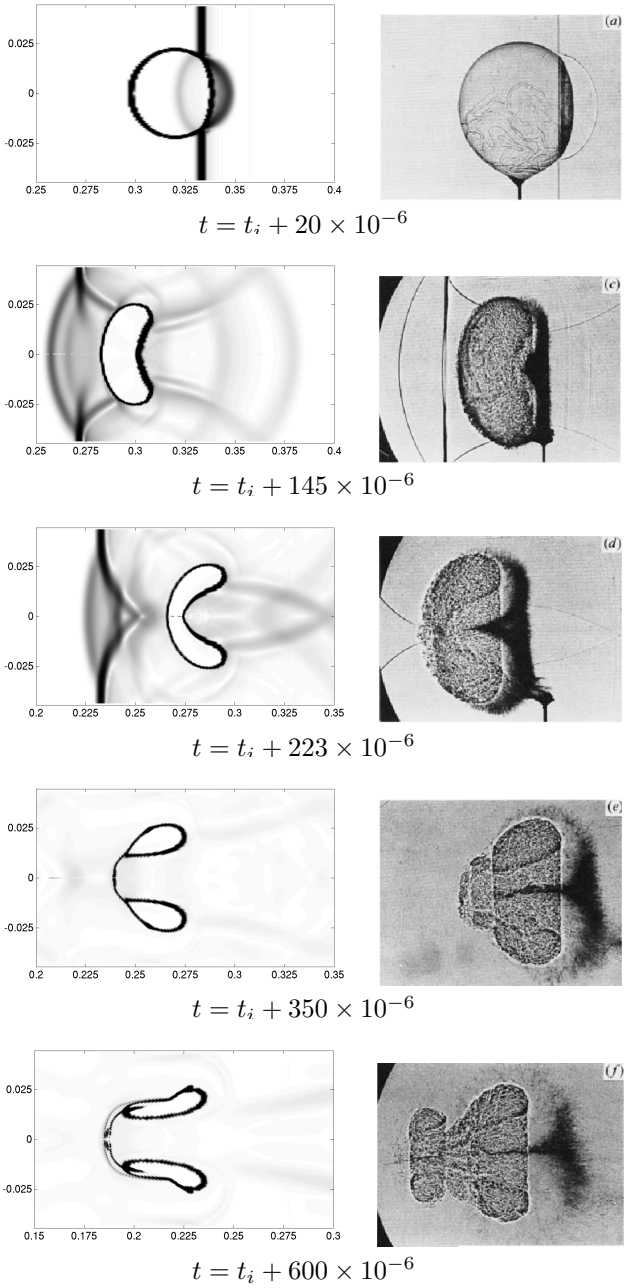

Figure B.2: Spherical Air-Helium shock/bubble interaction. Schlieren diagram of density. Axisymmetric CCALE-MOF results (on the left) compared to experimental results (on the right) [72] after the shock hits the bubble at time $t_i = 657.463 \times 10^{-6}$.

Let us note that each pictures are obtained thanks to an axial symmetry with respect to the X-axis. Comparisons between the Schlieren density profiles and the shadow-graphs of the experiment show a good agreement, especially when observing the bubble shape deformations. Moreover, waves generated by the initial shock are well localized and illustrate multiple reflec-

tions and refractions especially on the bubble and the domain boundaries. These main points clearly demonstrate the accuracy and the robustness of the method and validate the axisymmetric CCALE-MOF approach when computing spherical test-cases coming from experiment.

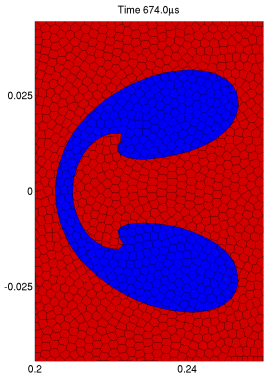

Figure B.3: Zoom on Interface and mesh for the Cylindrical Air-Helium bubble test at time $t_f = 674 \times 10^{-6}$ after shock/bubble interaction.

B.2 ReALE simulation of a cylindrical Air-Helium shock/bubble interaction test

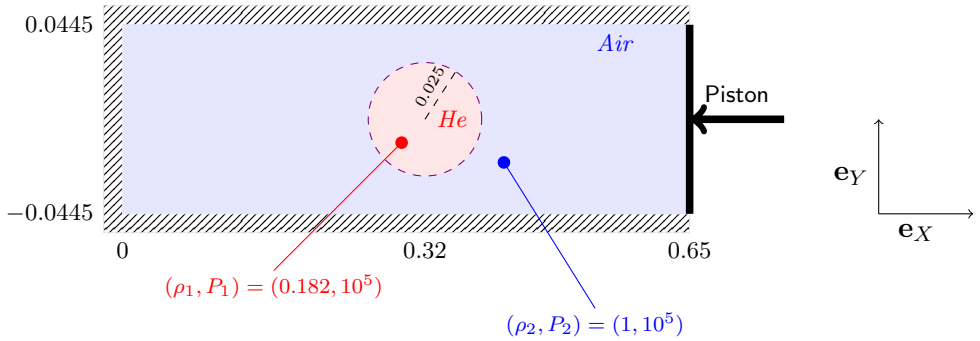

Figure B.4: Air-Helium shock/bubble interaction. Initial geometry and data.

In this part, we focus on the numerical simulation of the experiment of [72] concerning the impact of a Mach 1.22 shock traveling through the air onto a cylindrical bubble of Helium. Let us consider a rectangular domain of dimensions $[0, 0.65] \times [-0.0445, 0.0445]$ initially full of Air of data $(\rho_1, P_1, \gamma_1) = (0.182, 10^5, 1.4)$ except in a disc centered in $(0, 0.32)$ of radius 0.025 that contains Helium characterized by $(\rho_2, P_2, \gamma_2) = (1, 10^5, 1.648)$ as depicted on Fig. B.4. Wall boundary conditions are respectively chosen for the left, bottom and top boundaries. Whereas, a piston-like condition is imposed to the right one for an incoming velocity equal to $\mathbf{U}^* = (u^*, 0)$. Here, the horizontal velocity u^* is computed thanks to Rankine-Hugoniot conditions and is given by $u^* = -124.824$. The domain is initially paved with a grid composed of 38033 cells. Here, the bubble is directly initialized through the volume fraction on the mesh.
Computation is done using the multi-material ReALE-MOF for a final time chosen equal to $t_f = t_i + 674 \times 10^{-6}$ where $t_i = 668.153 \times 10^{-6}$ corresponds to the time of the shock/bubble interaction. Numerical results associated to the Schlieren density profiles [73] are depicted on

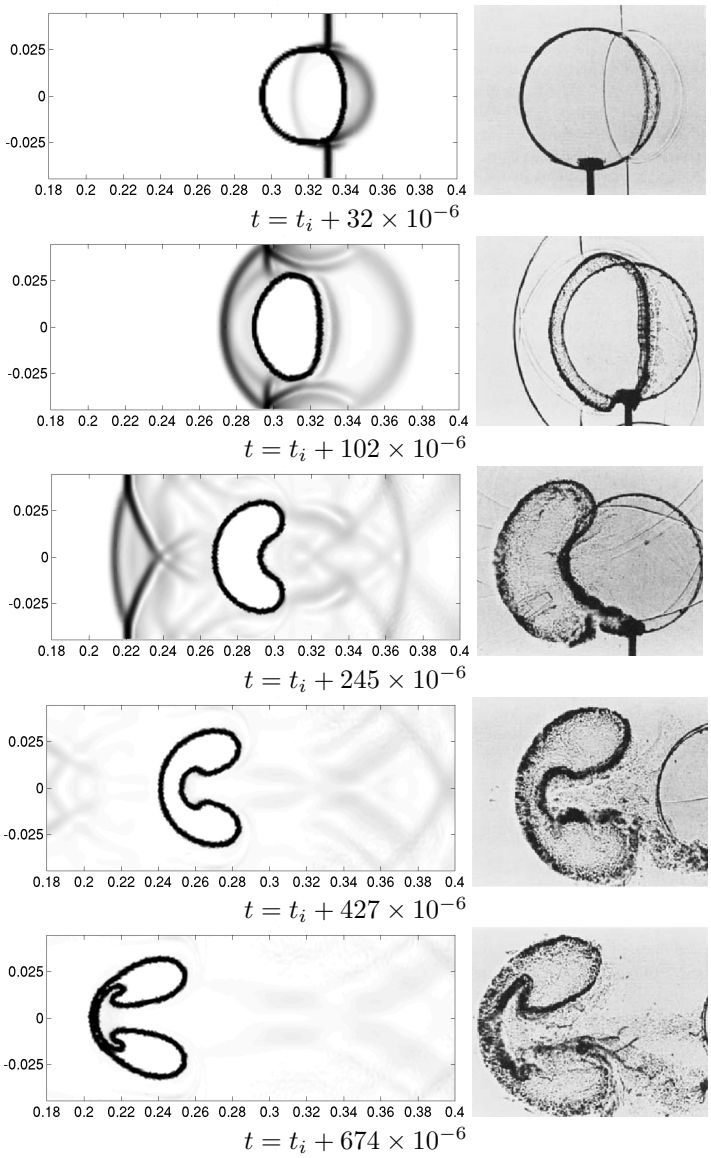

Figure B.5: Cylindrical Air-Helium shock/bubble interaction. Schlieren diagram of density. ReALE results (on the left) compared to experimental results [72] (on the right).

FIG. B.5. Comparisons between the Schlieren density profiles and the shadow-graphs of the experiment show a good agreement, especially when observing the bubble shape deformations. Moreover, waves generated by the initial shock present multiple reflections and refractions especially on the bubble and the domain boundaries. In These main points clearly demonstrate the accuracy and the robustness of the method and validate the ReALE-MOF approach when computing test-case coming from experiment. In FIG. B.3 we show the material interface on the polygonal grid for a coarse mesh.

B.3 Schardin's problem

This test case, also known as Schardin's problem [145], concerns shock wave diffraction on a triangular body. In this problem, a planar shock impinges on a finite-length wedge and generates curved reflected and diffracted waves. In agreement with experimental data, we use an isosceles triangle that has a front vertex angle of $\theta = 55°$ and a base length of 20 mm (FIG. B.6). The Mach number of the incident shock wave is $M_s = 1.3$ which is the same value as the experiments of Schardin [145]. We initialize the pressure in the shock tube with $P_0 = 0.05\ MPa$ and we use $\rho_0 = 1.2\ kg.m^{-3}$ as initial density.

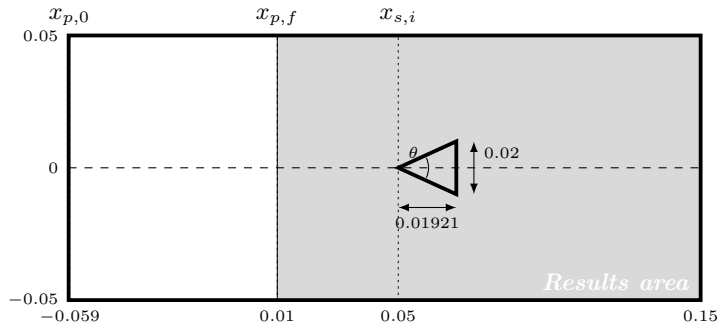

Figure B.6: Schardin's problem configuration with $x_{p,0} = -0.059$ the initial lagrangian position of the piston, $x_{p,f} = 0.01$ the final position of the piston and $x_{s,i} = 0.49$ the position of the incident shock at the beginning of the interaction time.

For this configuration, a piston-like condition is imposed to the left boundary condition with a prescribed velocity equal to $\mathbf{U}^* = (u^*, 0)$. Here, the horizontal velocity u^* is computed thanks to Rankine-Hugoniot conditions and is given by $u^* = -106.83\ m.s^{-1}$. This corresponds to an incident shock moving at the velocity $Dc = 314\ m.s^{-1}$. Computation is done using ReALE and the final time is equal to $t_f = t_i + t_s$ where $t_i = 342.98 \times 10^{-6}\ s$ corresponds to the time of the displacement of the shock wave to the position $x_{s,i}$, and $t_s = 307 \times 10^{-6}\ s$ is the time of the shock/triangle interaction. The domain is initially paved with a grid composed of 23892 square cells. During calculation, ReALE strategy leads progressively to a polygonal mesh as depicted on FIG. B.7.
In FIG. B.8, we compare experimental shadowgraphs extracted from [145] to computed isopycnic at different times. We choose to represent 50 isopycnic from the lowest to the highest density value for each representation. We observe that the flow structure includes Mach reflections and several interactions between the diffracted waves. Further, the flow separates on the wedge trailing edge, and the developing slip line rolls up into a spiral vortex. The Kelvin-Helmholtz instability of the slip lines leads to the emergence of small secondary vortices. The investigation of Schardin's problem based on visualizations comparison reveals that the numerical ReALE simulation faithfully reproduces the main flow structure.

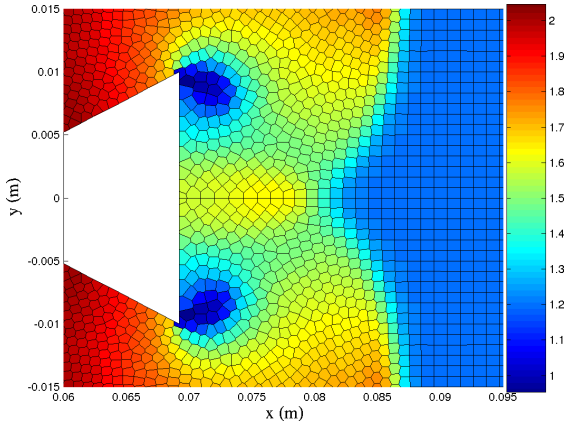

Figure B.7: Density field in $kg.m^{-3}$ and mesh topology at $t = 115\mu s$ for Shardin's problem

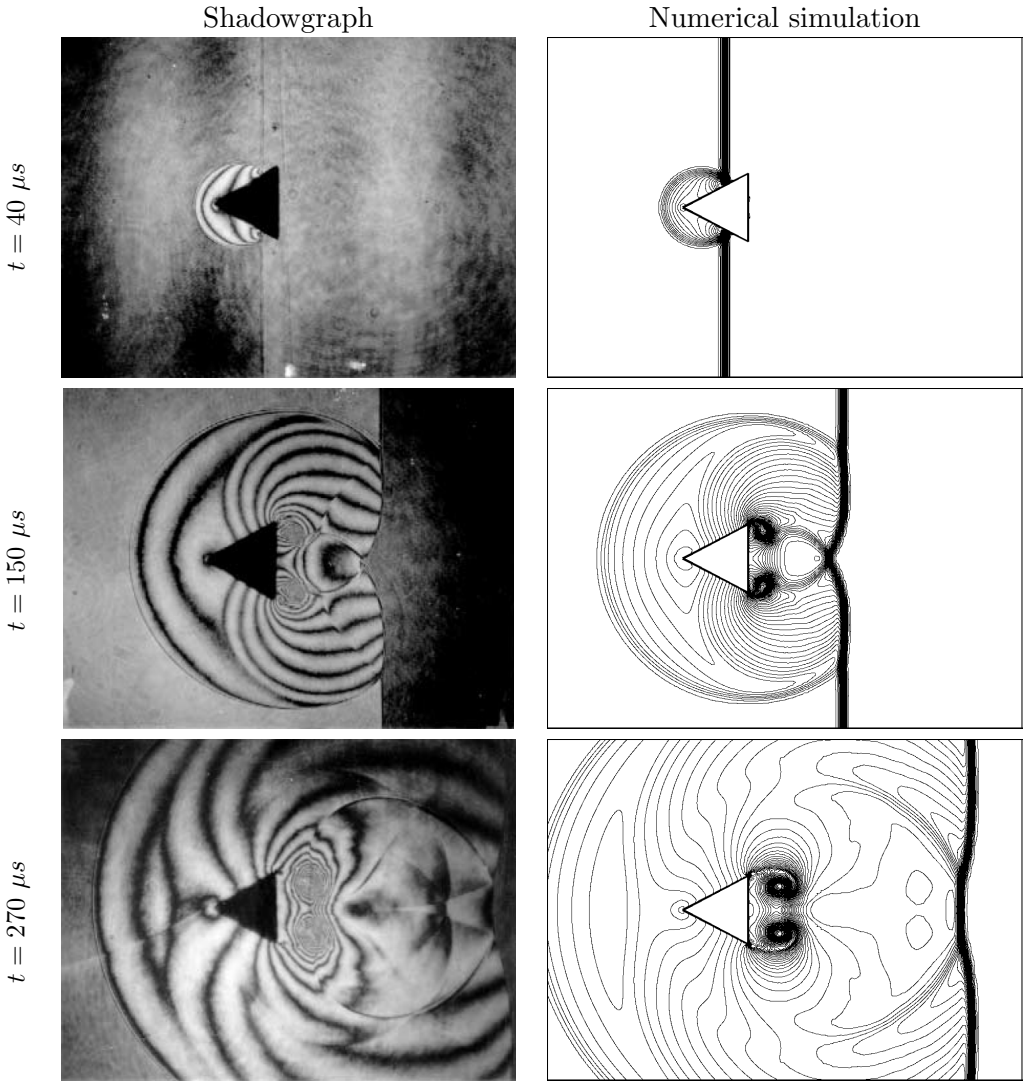

Figure B.8: Density fields for the Schardin's problem

B.4 Shock wave propagation in a square cavity

We focus now on the interaction between a planar shock wave and a square cavity. This test case was first introduced by Igra and Falcovitz in [85] which led experimental investigations on

the shock tube of the Ernst mach Institute in Freiburgn Germany. Here, we use the shadowgraphs they have obtained in order to evaluate the computed results. The numerical experience is characterized by $(M_s, P_0, \rho_0) = \left(1.3, 98285\ Pa, 1.2\ kg.m^{-3}\right)$ where M_s is the Mach number of the incident shock wave, P_0 the initial pressure and ρ_0 the initial density.

Here again, we use a piston-like condition to generate the shock wave. We impose an incoming velocity to the left side equal to $\mathbf{U}^* = (u^*, 0)$ where u^* still computed thanks to Rankine-Hugoniot conditions with $u^* = -149.77\ m.s^{-1}$, corresponding to an incident shock moving at the velocity $Dc = 440,2\ m.s^{-1}$. The domain, schematized on FIG. B.9, is initially paved with a grid composed of 15748 square cells.

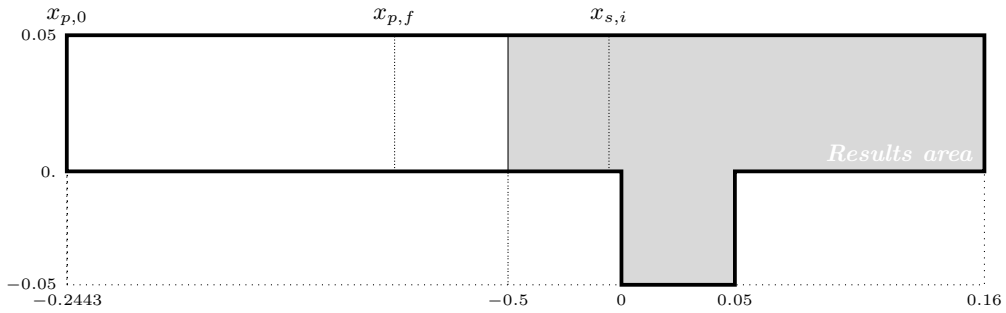

Figure B.9: Square cavity configuration with $x_{p,0} = -0.2443$ the initial lagrangian position of the piston, $x_{p,f} = -0.1$ the final position of the piston and $x_{s,0} = -0.0055$ the position of the incident shock.

Similarly to the Schardin's problem, we represent on FIG. B.10 the fact that ReALE strategy allows connectivity changes as square cells turn into polygonal cells all along the simulation.

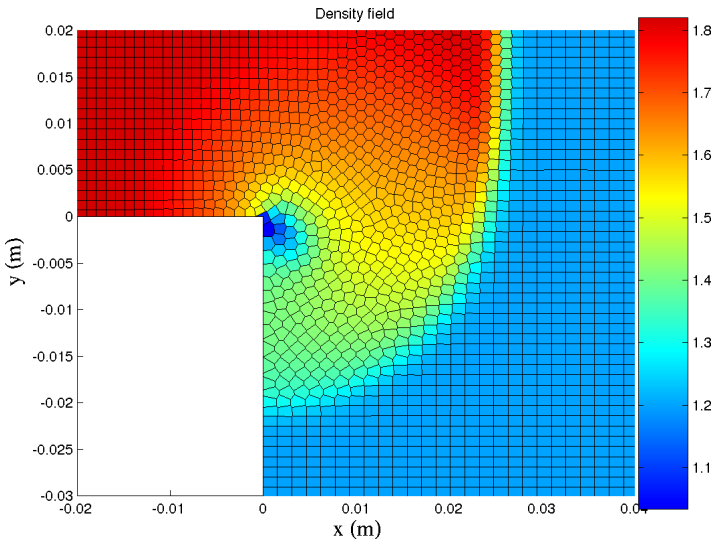

Figure B.10: Visualization of the reconnected mesh and the density field $(kg.m^{-3})$ at $t = 70\mu s$

The FIG. B.11 shows the evolution of the various waves resulted from the interaction of the incident shock wave S_1 with the square cavity. Computed isopycnic are represented using lines of constant density separated from each other by a ratio $\Delta\rho/\rho_0$ equal to 0.054. This value is chosen to compare our results with [85]. In the shadowgraph at $t = 40\ \mu s$, the incident shock is shown a short time after it has reached the left-upper corner of the cavity. S_1 starts

diffracting around this point and gives birth to a vortex. The propagation of S_1 continues until S_1 hits the upper-right corner of the cavity. At $t = 140\mu s$, the mean shock wave has split into a transmitted S_1 and a reflected S_{r1} shock waves. During the propagation of S_1, we observe that the size of the vortex has increased while its center has slowly moved to the right of the cavity. At $t = 280\ \mu s$, the reflected shock wave $S_{r'1}$ has appeared at the right-bottom of the cavity because of the coalescence of S_{r1} and the reflection of S_1 in the left-bottom corner of the cavity. At the end of the simulation, it becomes complicated to interpret wave patterns efficiently as multiple interactions have occurred among the waves and between the waves and the geometry.

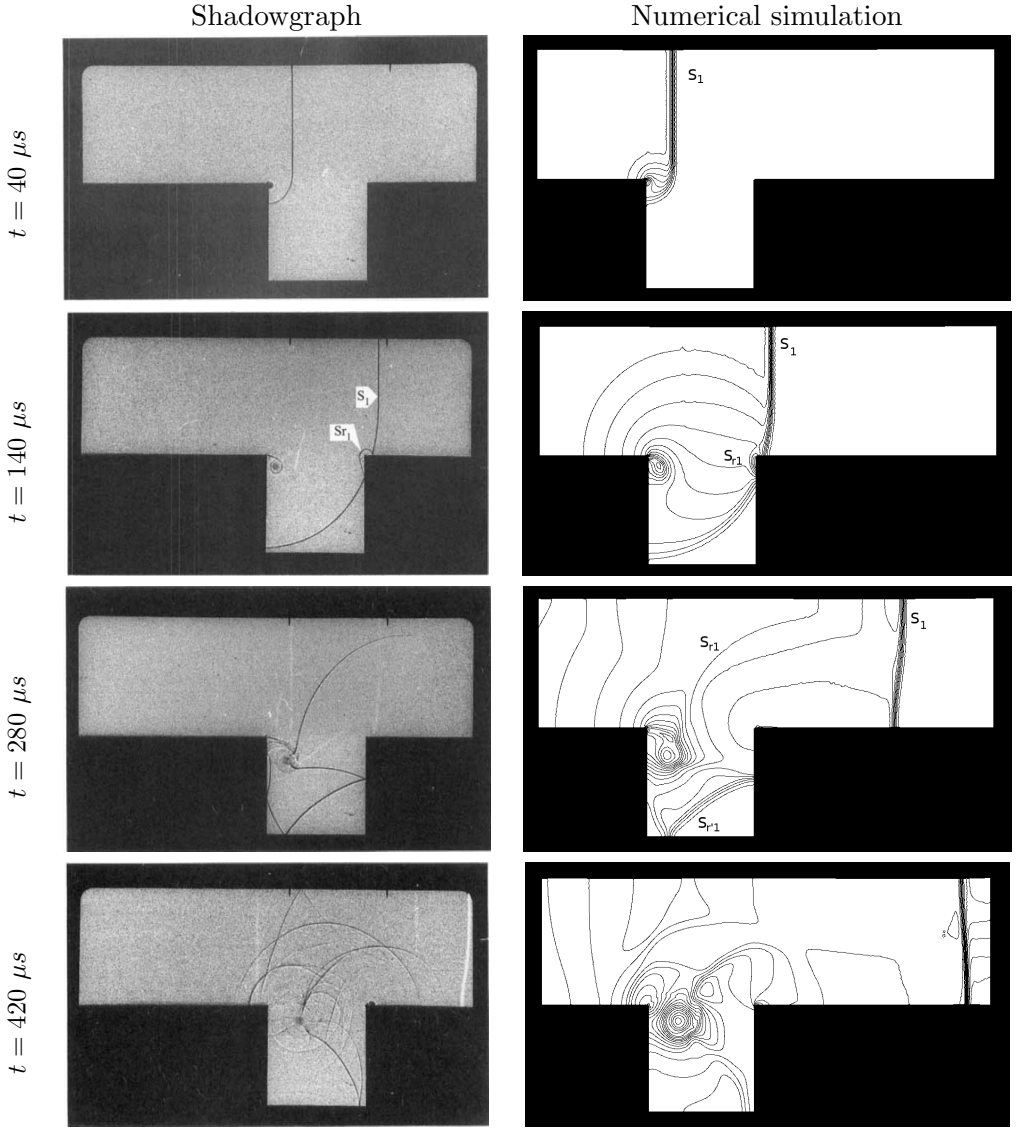

Figure B.11: Wave pattern during the interaction of a planar shock wave with a square cavity. Shadowgraphs extracted from [85] (on the left) are compared to computational results (on the right)

Finally, the simulations performed using ReALE strategy show a good agreement between shadowgraphs and numerical results. This numerical experiment constitutes a validation of the ReALE strategy by demonstrating its capabilities of producing physically accurate simulations of complex shock wave structures.

B.5 Reflexion of a shock wave on a double wedge

Here we consider the reflection of a shock wave from a double wedge [21]. The surface of the second wedge is parallel to the incident shock front as depicted on FIG. B.12. This case deals with an incident shock propagating into air at a Mach number $M_s = 1.488$ considering a wedge angle equal to $\theta = 55°$. The computational domain is composed by 29355 generators and initial conditions for the fluid are $(M_s, \rho_0, P_0) = \left(1.488, 1.2\ kg.m^{-3}, 98500\ Pa\right)$. Here again, we use a piston-like condition to generate the shock wave. We impose an incoming velocity to the left side equal to $\mathbf{U}^* = (u^*, 0)$ with $u^* = -230.5\ m.s^{-1}$ which corresponds to an incident shock moving at the velocity $Dc = 504.4\ m.s^{-1}$. The initial position of the shock is $x = 0.0536\ m$.

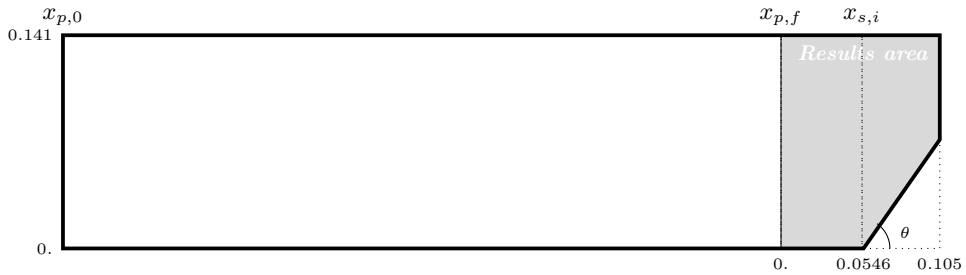

Figure B.12: Schardin's problem configuration with $x_{p,0,lag} = -0.475$ the initial lagrangian position of the piston, $x_{p,f} = 0.$ the final position of the piston and $x_{s,0} = 0.0536$ the position of the incident shock.

Considering the experimental and computed isopycnic depicted on FIG. B.13, it appears that three types of reflected shock coexist at $t = 206\ \mu s$. Here again, we represent 50 isopycnic from the lowest to the highest value of the density. First, the incident shock is reflected on the first wedge and create a regularly-reflected curved shock. Then, the incident shock is reflected on the shock tube end wall which engenders a planar shock segment parallel to the end wall. These two fronts are linked by a short oblique shock segment whose endpoints can be considered as 'triple points' in a Mach reflection. In other terms, each one of these points characterize the intersection of three shocks and a slip surface, as it is clearly visible on both experimental and computational maps. Those observations make sure that there is a close agreement between the experimental and the computed isopycnic lines.

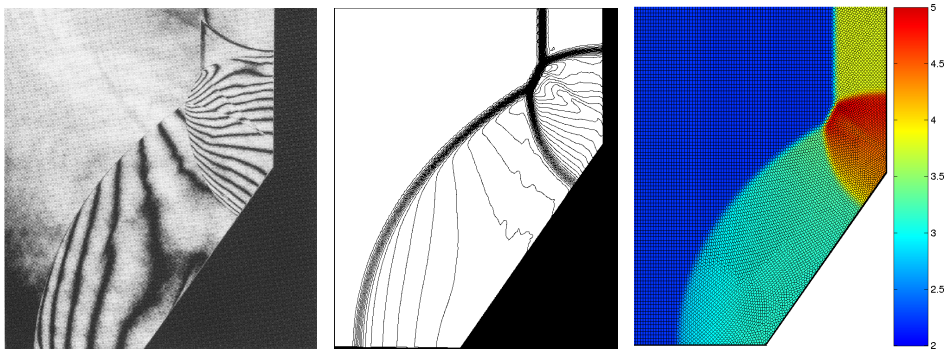

(a) (b) (c)

Figure B.13: Results obtained for the double wedge configuration at $t = 206\ \mu s$. (a) Experimental shadowgraph [21], (b) computed isopycnic and (c) density $(kg.m^{-3})$ and mesh

B.6 Transient shock wave in tubes

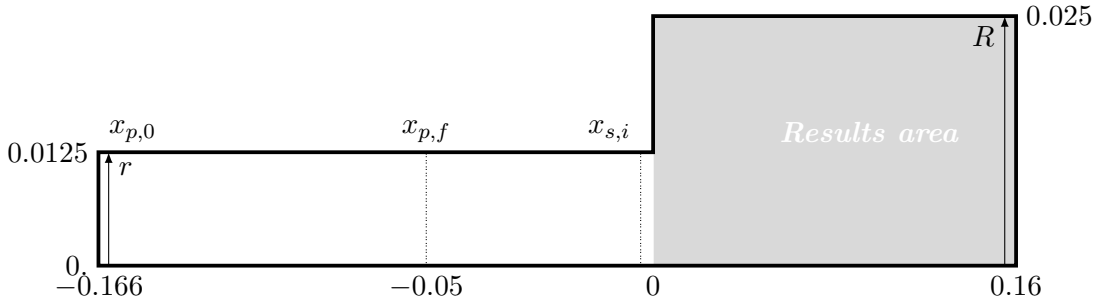

Figure B.14: Transient shock wave in tubes configuration with $x_{p,0} = -0.166\ m$ the initial Lagrangian position of the piston, $x_{p,f} = -0.05\ m$ the final position of the piston and $x_{s,i} = 0.0\ m$ the position of the incident shock at the beginning of the interaction time. $r = 0.0125m$ is the radius of the tube where the shock is generated and $R = 0.0250m$ is the radius of the tube of interaction cavity.

Here we consider the interaction of a shock generated in a tube with sudden area change in cross-section. This test case is based on an experiment presented in [87]. The fluid considered here is characterized by $(\rho_0, P_0, \gamma) = \left(1.2\ kg.m^{-3}, 98285\ Pa, 1.4\right)$ where ρ_0 is the initial density, P_0 the initial pressure and γ is the polytropic index of a diatomic gas.
For the first computation, we focus on the interaction of the cylindrical cavity with an incident shock wave of Mach number $M_s = 1.3$. The shock is generated by a piston-like condition imposed to the left boundary with an imposed velocity equal to $\mathbf{U}^* = (u^*, 0)$. The horizontal velocity $u^* = -149.77\ m.s^{-1}$ is obtained thanks to Rankine-Hugoniot conditions, corresponding to an incident shock moving at the velocity $Dc = 440,2\ m.s^{-1}$. The final time is given by $t_f = t_i + t_s$ where $t_i = 341\mu s$ is the time required by the shock to reach the position $x_{s,i}$ and $t_s = 341\mu s$ correspond to the interaction time of the shock with the cylindrical cavity. The domain represented on Fig. B.14 is initially paved with a grid composed of 24264 square cells. The ALE method is not suitable for this test case because of the complex geometry. Indeed, the fixed topology that characterized the ALE method can not deal with such configuration whereas the ReALE strategy will leads progressively to a polygonal mesh which can handle the sudden change in cross section.
The Fig. B.16 shows the evolution of the incident shock with the larger cylindrical tube. We observe that the incident shock diffracts into spherical shape (Fig. B.16(a)). The shock is reflected on the inside wall (Fig. B.16(b)), interact with the vortex ring and finally converge in the center of the tube (Fig. B.16(c)). This lead the Mach disc to move faster downstream (Fig. B.16(d)-(e)) and reach the first incident shock. During all the computation the vortex ring initially created by the incident shock move inside the cavity (Fig. B.16(f)). We compare our ReALE method with experimental results from [87] where the Mach number $M_s = 1.3$ and the ratio of cross section is $R/r = 2$. The comparison are presented in Fig. B.15 and the computation faithfully reproduces the main flow structure.

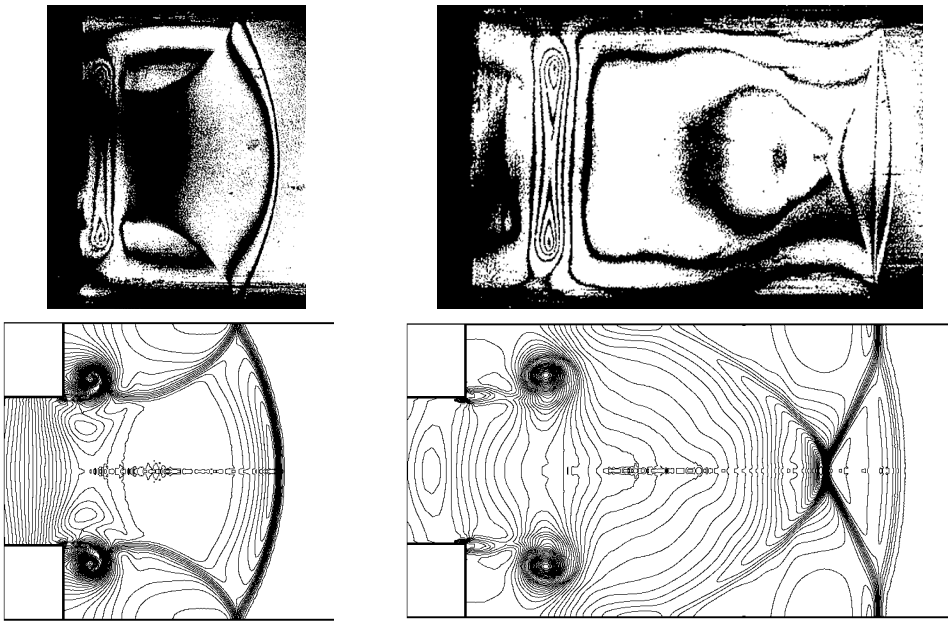

Figure B.15: Transient shock wave in tubes. Comparison between experimental interferogram and isopycnic computed from density at $t = 120\mu s$ and $t = 220\mu s$.

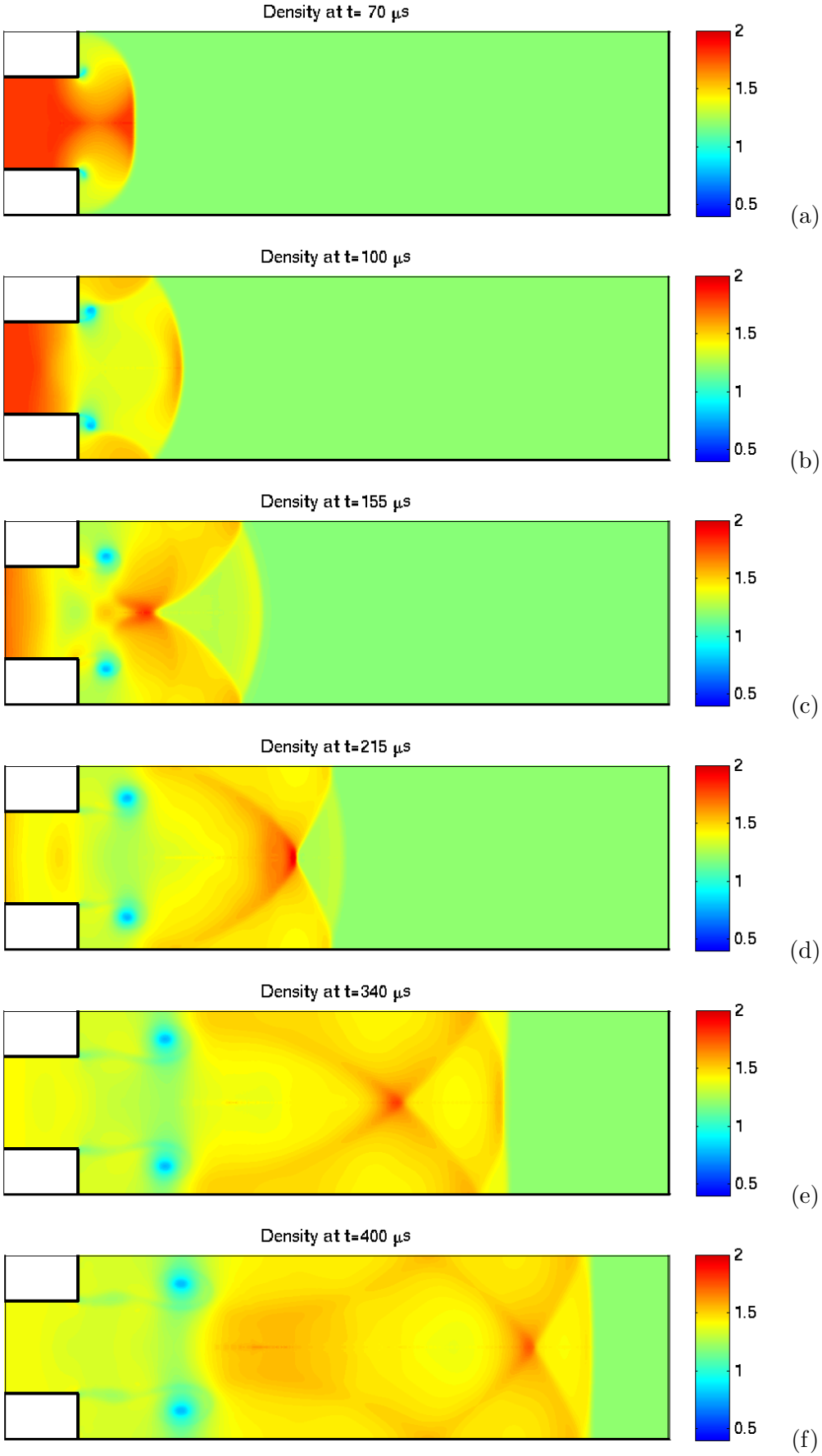

Figure B.16: Transient shock wave in tubes. Density plot ($kg.m^{-3}$) for the Mach number $M_s = 1.3$ and the ratio of cross section is $R/r = 2$.

Appendix C

Irradiation study for HiPER project

C.1 Introduction

Irradiation nonuniformities are directly connected to the laser device. Such nonuniformities produce low mode perturbation which needs to be accurately known in order to investigate the consequences on hydrodynamic target stability. The specific illumination 3D code, CECLAD, developed and validated in CELIA calculates target irradiation by multi-laser beams to optimize illumination on complex geometries. We use this tool to define the baseline specifications of the HIPER project.Several configurations of laser beams (size, energy balance, pointing, centering) and target (shape, position, size) has been tested. The irradiation uniformity has been optimized (σ_{rms} and the energy balance η_B). A Legendre polynomial expansion of the illumination has been performed to compute the amplitudes of the main modes. The robustness of the solution is then studied.

C.2 The CECLAD irradiation code

C.2.1 model presentation

In order to evaluate the irradiation of the target with complex geometry (spherical target with petawatt cone for example) we discretize the target using a surface mesh based on quad or triangle cells. On this mesh we have for each cell ($i = 1, \ \dots \ , \ I$) the local normal $\boldsymbol{N}_i$ and the local surface dS_i. thus $S = \sum_{i=1,\ I} dS_i$ is the total surface of the target.

The intensity envelope of the beams is a super-Gaussian of order m :

$f(x,y) = \exp(-\left(\frac{x^2+y^2}{a^2}\right)^m)$ where x and y are the coordinates in the focal plane, a is the half width at $1/\exp$ and m is the order of the super-Gaussian. This envelope can be reduce or increase on each beam j using the balance b_j. The beam direction is given by the normal $\boldsymbol{S}_j$.

We compute the intensity on the cell target i due to the irradiation of the beam j using the formula (see FIG. C.1) :

$I_i, j = \boldsymbol{N}_i \cdot \boldsymbol{S}_j f(x,y) b_j$

The total incident intensity on a cell i is the sum of all the beam contributions I_i. The root mean square deviation or σ_{rms} is then defined by :

$$\sigma_{rms} = \sqrt{\frac{1}{S}\left(\sum_{i=1,I}\left(\frac{I_i}{\bar{I}} - 1\right)^2 \ dS_i\right)}$$

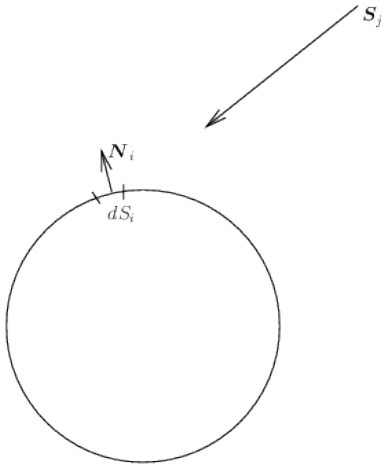

Figure C.1: Beam intensity on the target.

where $\bar{I}$ is the average intensity on the target $\bar{I} = \frac{1}{S} \sum_{i=1,\ I} I_i dS_i$.
As we deal here with geometries where we have axisymmetric symmetry we integrate the flux on the latitude φ and we get an intensity depending on θ :

$$I(\theta) = \frac{1}{\int_{-\pi}^{\pi} r\ d\varphi} \int_{-\pi}^{\pi} I(\theta, \varphi)\ r\ d\varphi$$

This can be expanded in Legendre polynomials :

$$\tilde{I}(\theta) = \bar{I}(1 + \sum_{k=1}^{\infty} a_k P_k(\cos\theta))$$

where k is the Legendre mode and a_k is calculated using

$$a_k = \frac{2k+1}{2} \int_{-1}^{1} \frac{I(\theta)}{\bar{I}} P_k(\cos(\theta))\ d(\cos(\theta))$$

a_k is here the normalized Legendre mode coefficient.
From this we can characterize the laser facility and get some information on the low mode that will be generated in the target (see [42]).

C.2.2 Validation

We compare here our code with some analytical solution for configurations of perfectly uniform irradiation of spherical laser fusion targets (see [164]).
For this case we use a special beam profile that provide an intensity on the spherical target of

$$I_j(\gamma_j) = \sum_{m=0}^{M} I_0 \cos^{2m} \gamma_k$$

where $\cos\gamma_k = \boldsymbol{N}_i \cdot \boldsymbol{S}_j$
M is provided for each case such that $\sigma_{rms} = 0$ can be obtained for any configuration of even number of beams N_b.
We test here only a few configurations $N_b = 42,\ 46,\ 48\ and\ 60$ on a mesh of 180×180.

N_b	L	N_i	θ_i (deg)	ϕ_i (deg)	M	σ_{rms}
42	5	5 10 12	25.14 57.33 90.		2	2.46 10^{-2} %
46	4	8 15	30.55 70.12		3	1.5 10^{-4} %
48	12	4	21.23	0.	3	1.77 10^{-5} %
		8(4+4)	47.03	±23.36		
		12(4+4+4)	74.95	0. ±29.83		
60	12	5	21.44	0.	3	2.88 10^{-5} %
		5	41.98	0.		
		10(5+5)	58.84	±23.97		
		10(5+5)	81.27	±12.55		

Table C.1: Description of the 42, 46, 48 and 60 beams configurations.

In Tab. C.1 N_b is the number of beams, L is the total number of rings and N_i is the number of beams on each rings. θ_i are the angle of each rings and ϕ_i are the angle on the ring when they are not aligned.

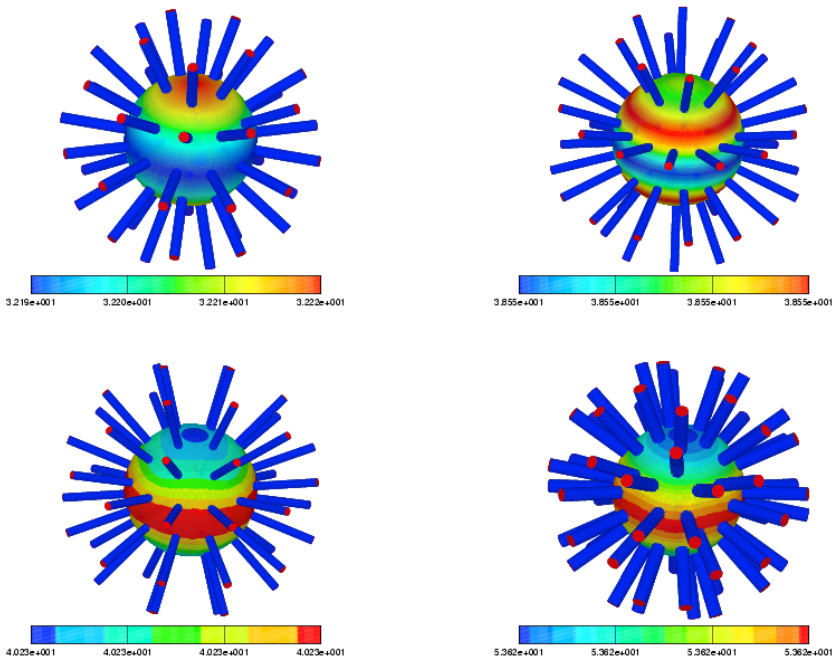

Figure C.2: Intensity and beams positions for the perfect configuration 42 (Top left), 46 (top right), 48 (bottom left) and 60 (bottom right).

C.3 Compression beams configurations

The nominal specification for the fuel assembly is given by a wavelength of 0.35 microns, an energy of 250 kJ during 10 ns (0.6 TW foot, 50 TW max) with or without picket. The foot-to-main contrast aspect ratio required is about 80% and the pulse shaping accuracy about 100 *ps*. HiPER specifications are ≈ 50 beams with 15 kJ per beams at 1 ω (6 kJ at 3 ω) [60].

Several symmetric configurations are considered and a procedure of optimization on the parameters (a,m) of the beams has led to illegible configurations of illumination.

We present in the Tab. C.2 all the configurations we have studied. From the requirement of HIPER and regarding the different configurations studied we will focus on the 32, 42, 46 and 48 configurations.

Beams	m	a	σ_{rms}	Energy budget	Legendre Modes
6	1.63	1.02	1.73%	78%	8,10,14
8	1.66	1.01	0.96%	79%	10,16,20
12	1.415	0.76	0.37%	93%	12,16,10
20	1.39	0.79	0.17%	91%	16,18,10
32	1.33	0.83	0.21%	87%	12,18,10
42	1.9	0.79	0.18%	94%	10,12,2
46	1.11	0.63	0.11%	95%	8,10,12
48	1.02	0.61	0.15%	94%	16,18,12
60	1.067	0.567	0.05%	97%	16,12,10
60 (Ω)	1.08	0.63	0.08%	94%	16,18,12

Table C.2: σ_{rms}, Energy budget and principal Legendre Modes for the different configurations studied

We now give the details of the 32, 42, 46 and 48 beams pattern. In Fig. C.3 the angle $\theta$of the cone and the number of beams on each cone are given. In Fig. C.5 we give the angles of the different cone. On Fig. C.4 and Fig. C.6 we show a 3D representation of the target with all the beams impinging on it. The field represented on the target is the intensity.

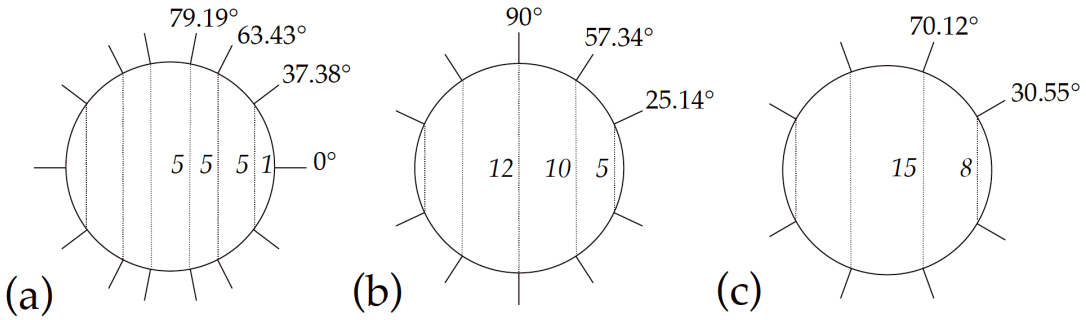

Figure C.3: The polar angle of 32 (a) 42 (b) 46 (c) patterns.

On Fig.C.7 and Fig.C.8 we represent the optimization of the σ_{rms} as a function of (a,m) for the 32, 42, 46 and 48 beams configurations.

Fig. C.9 and Fig. C.10 represent the Legendre mode for the 32, 42, 46 and 48 beams configurations.

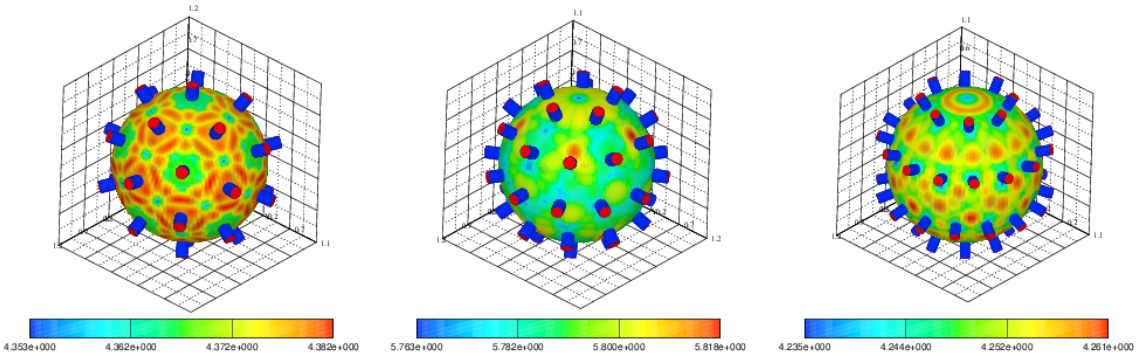

Figure C.4: Nominal irradiation of 32 (left) 42 (middle) and 46 (right) patterns.

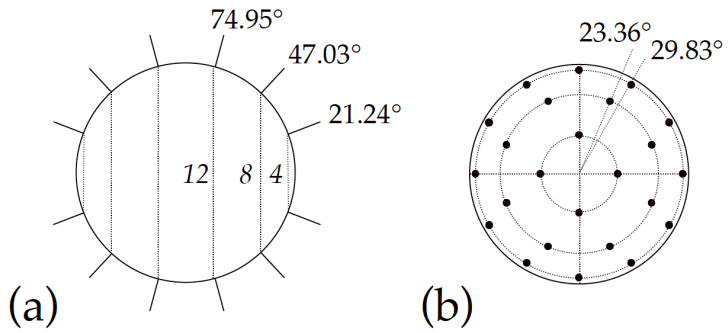

Figure C.5: The polar (a) and azimuth angles (b) of the 48 pattern.

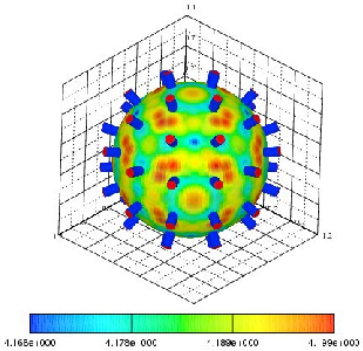

Figure C.6: Nominal irradiation of the 48 pattern.

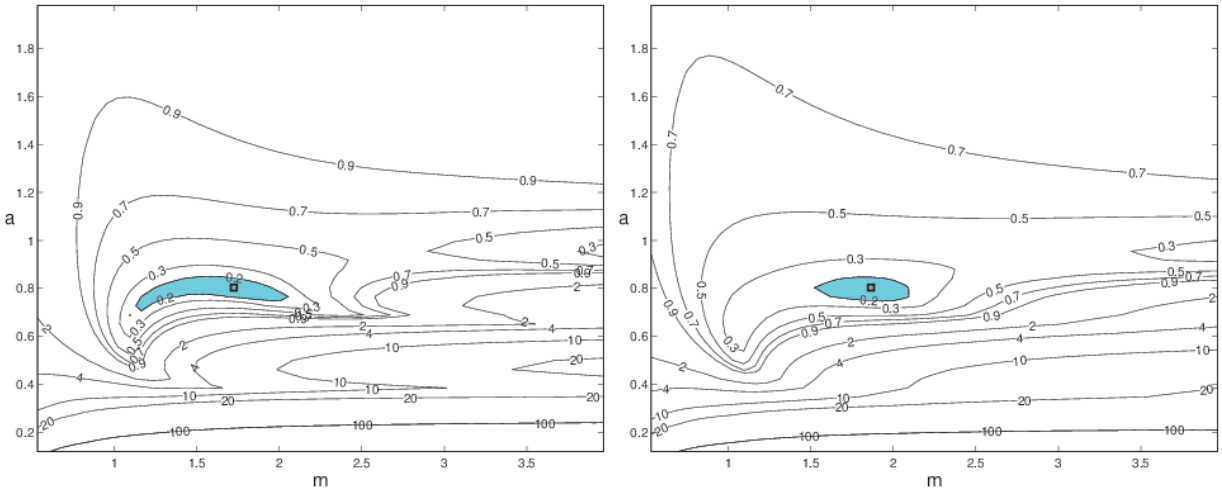

Figure C.7: σ_{rms} optimization as a function of (a,m) for the 32 (left) and 42 (right) beams configurations.

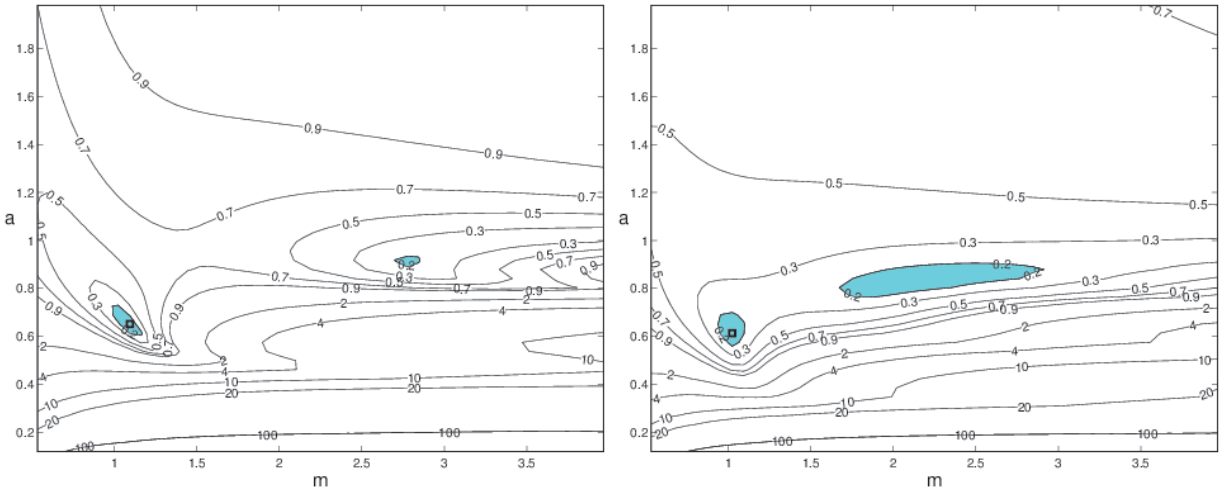

Figure C.8: σ_{rms} optimization as a function of (a,m) for the 46 (left) and 48 (right) beams configurations.

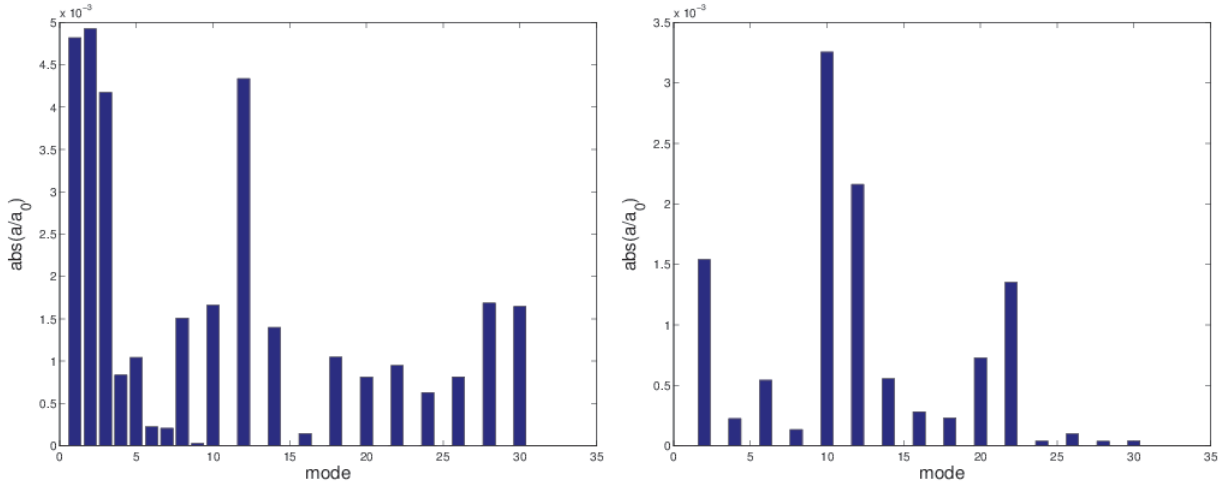

Figure C.9: Legendre analysis of the 32 (left) and 42 (right) beams configuration.

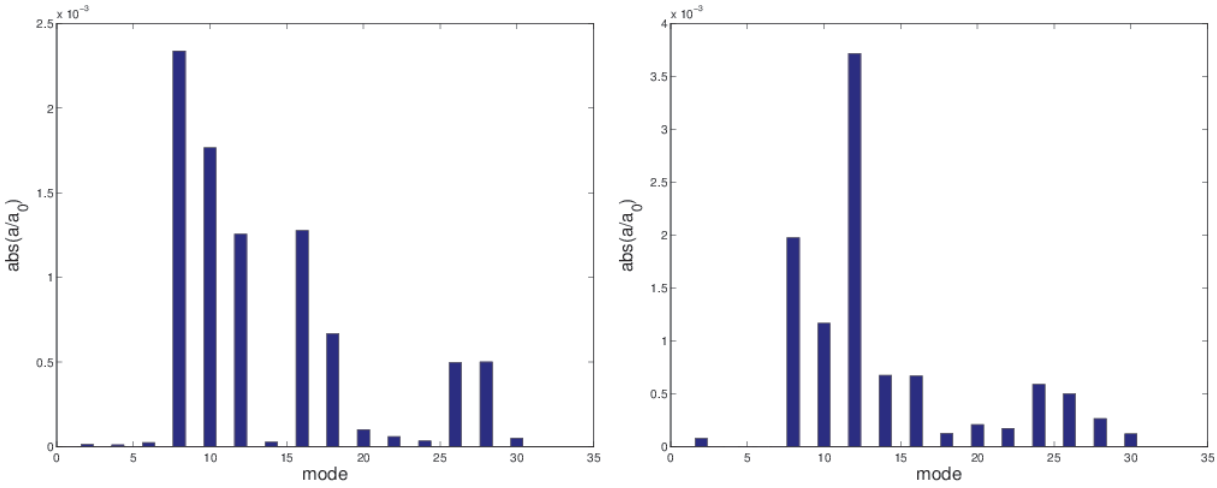

Figure C.10: Legendre analysis of the 46 (left) and 48 (right) beams configuration.

C.4 Inserting a cone

In the fast ignition schemes for inertial confinement fusion one of the solution is to insert a cone in the spherical target. On this scheme nanosecond beans are used to compress the spherical target which should slide on the cone. At the end of the compression phase a petawatt laser is shot inside the cone to ignite the hot spot at the tip of the cone. To achieve all this different step the initial conditions should be suitable for ignition. In this study an angle of 30 degree has been used. This angle is imposed by the petawatt laser ([91]). The intensity on the spherical target should be uniform and intensity on the cone must be kept as low as possible. The beams should not enter inside the cone to avoid the ablation and formation of plasma inside the cone. Different configurations has been tested 42, 46 and 48 (see Fig. C.12, Fig. C.13 and Fig. C.14). The advantage of the 46 is that no beams should be turn off instead of 4 and 8 for the 48 and 42 configurations. The intensity on the target is uniform in comparison with 42 and 48 configurations. In all the case intensity on the external cone is the almost the same. About the energy inside (Fig. C.15) the cone, the configuration with 46 beams seems to be very bad but in fact if we add a cylinder on the base of the cone we can protect and avoid beams to enter inside the cone.

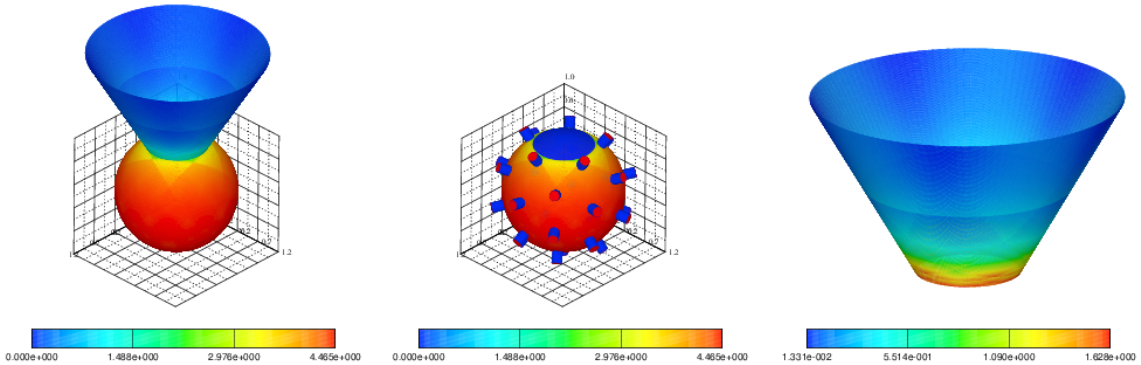

Figure C.11: Irradiation of fast ignition target with cone for the 32 beams configuration.

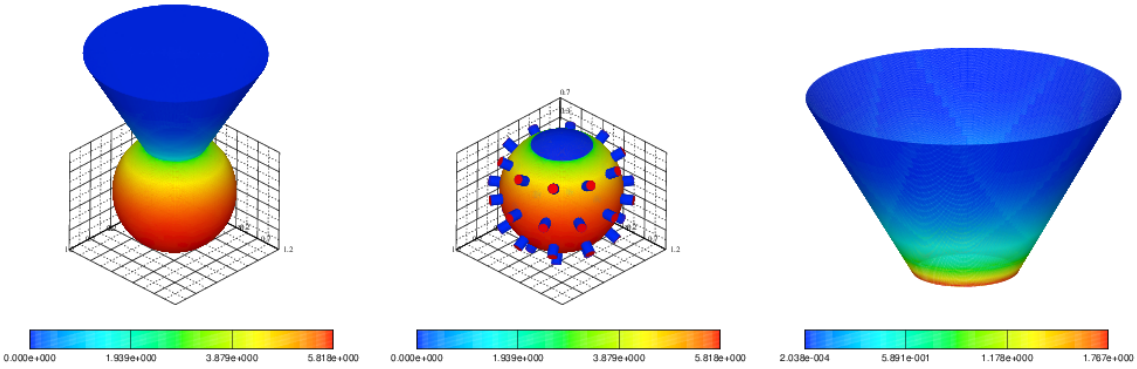

Figure C.12: Irradiation of fast ignition target with cone for the 42 beams configuration.

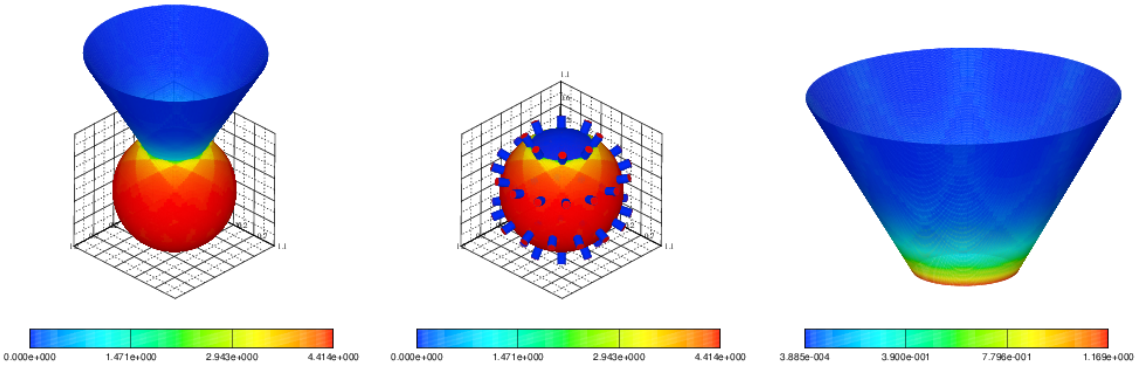

Figure C.13: Irradiation of fast ignition target with cone for the 46 beams configuration.

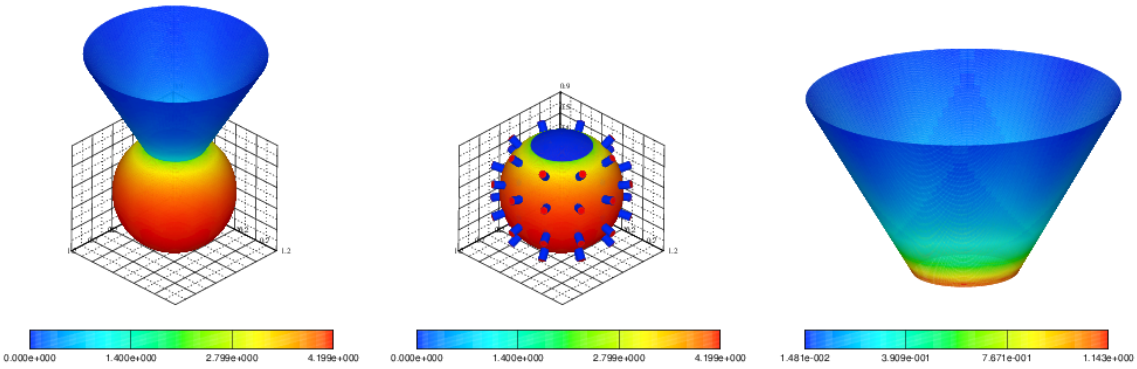

Figure C.14: Irradiation of fast ignition target with cone for the 48 beams configuration.

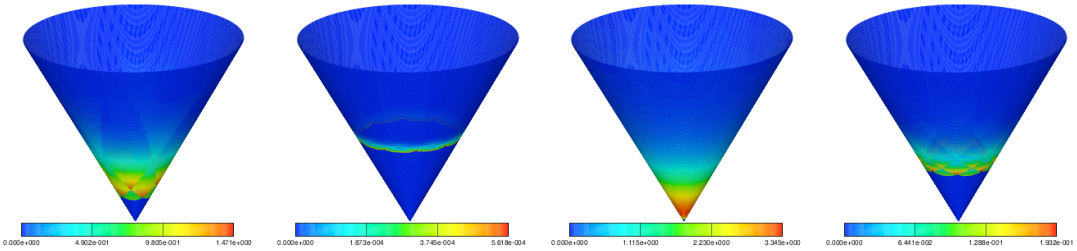

Figure C.15: Energy inside the cone for the 32,42, 46, and 48 configurations

C.5 Intrinsic symmetry and robustness for different beam arrangements

The requirement of irradiation symmetry is given by $\sigma_{rms} < 1\%$. This may be different according to the ignition scheme. This is probably more stringent during the foot (i.e. the drive of the first shock) than during the main drive (acceleration). The effect on fuel assembly strongly depends on spectrum. To achieve this requirement, the beam geometry, the focal spots and the random deviations have to be controlled.
Those parameters will define the figure of merit of the chosen irradiation pattern.
The trade off is given by the following alternative. If many beams pattern are chosen, the configuration will be robust and less energy will be required per beam. Contrariwise, a few beams pattern will be simplest but will generate lower Legendre modes.
To study the robustness of configurations, different control parameters has been tuned FIG. C.16 for the 48 beams configurations. Laser imperfections can induce power imbalance, pointing and centering errors. Random deviations following normal distribution around the nominal configuration are led. We examine their consequences on the mode spectrum.

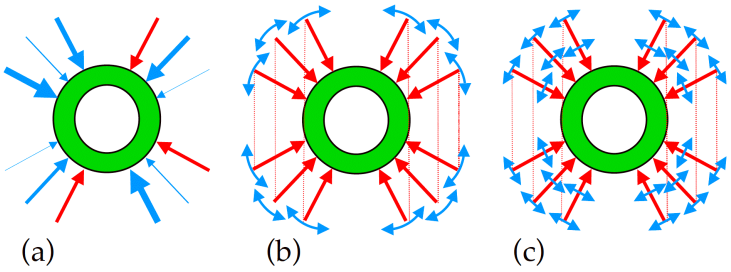

Figure C.16: Beam to beam imbalance (a), Beams pointing (b), Beams centring (c).

The imperfection of the laser system generates a distribution of beam following a Gaussian law centered on the nominal value. Each parameter induces a mean value for the σ_{rms} and the generation of new low modes. 100000 realizations are led. A normal repartition of the beam to beam imbalance (10%), of the beam pointing (5%), and of the beam centering 2% have been used separately and have been also combine all together to study the stability off the configurations. In the table we compare the case where we study the variation of all the parameters with the quadratic mean or L_2 norm:

$$\sigma_{L_2 norm} = \sqrt{\sigma^2_{balance} + \sigma^2_{centering} + \sigma^2_{pointing}} \tag{C.1}$$

In FIG. C.17 results for the σ_{rms} robustness and Legendre mode study for the beams balance are presented for the 48 beams configurations. In FIG. C.18 results for the σ_{rms} robustness and Legendre mode study for the beams pointing are presented for the 48 beams configurations. In FIG. C.19 results for the σ_{rms} robustness and Legendre mode study for the beams centering are presented for the 48 beams configurations. In FIG. C.20 results for the σ_{rms} robustness and Legendre mode study for all the parameters are presented for the 48 beams configurations. The results of the different studies are respectively resume in TAB. C.3 for the 48 beams configurations.

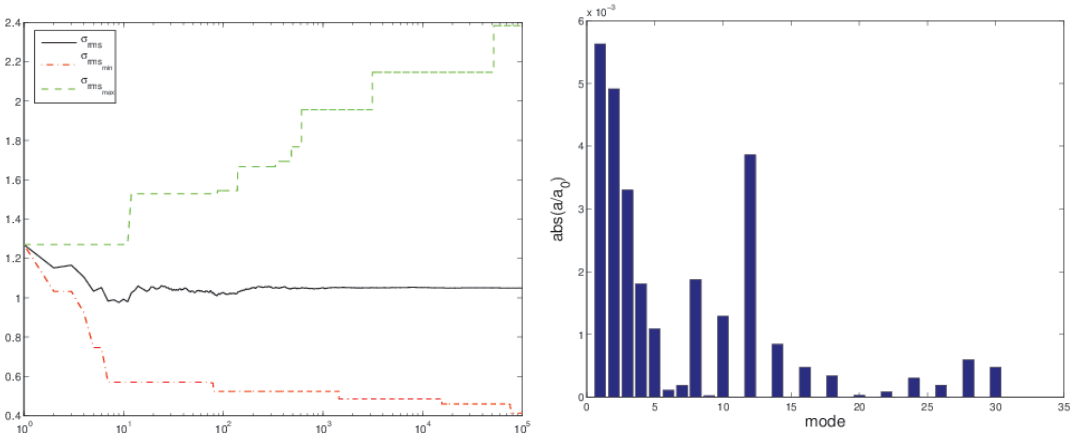

Figure C.17: σ_{rms} robustness and Legendre mode study for variation of the 48 beams configurations balance.

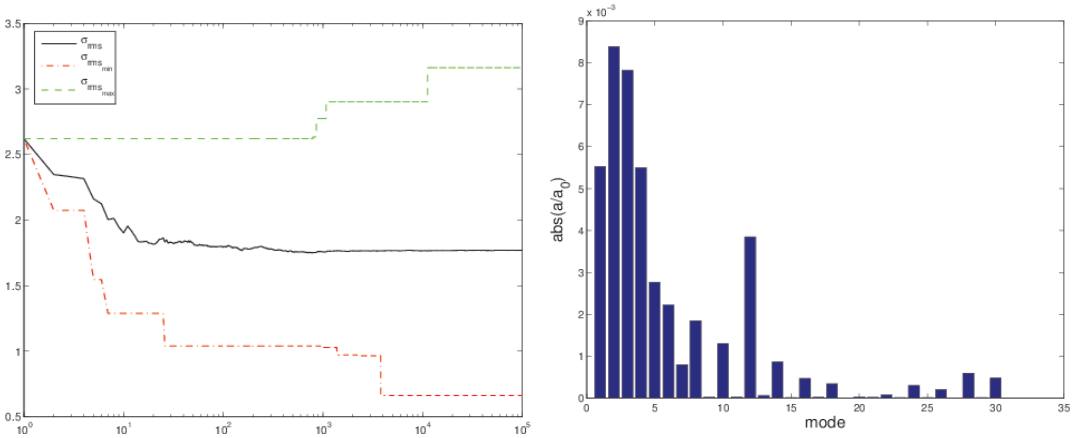

Figure C.18: σ_{rms} robustness and Legendre mode study for variation of the 48 beams configurations pointing.

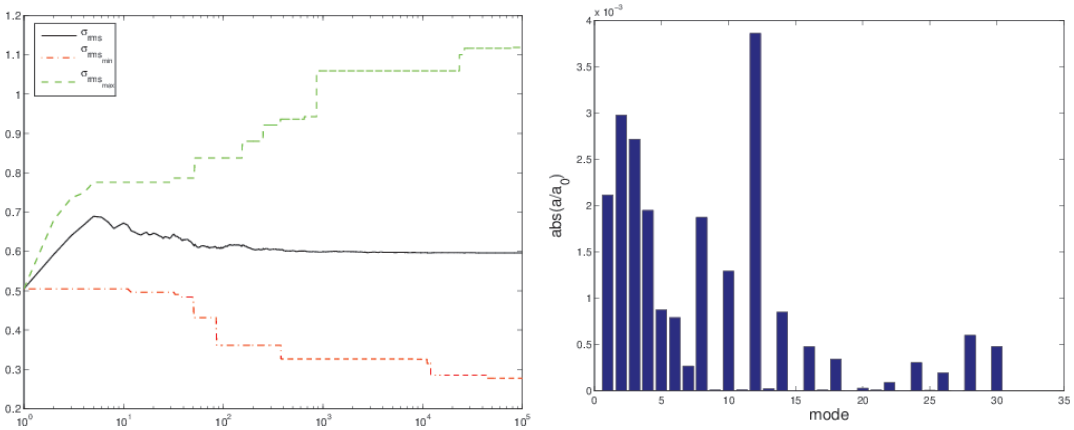

Figure C.19: σ_{rms} robustness and Legendre mode study for variation of the 48 beams configurations Centering.

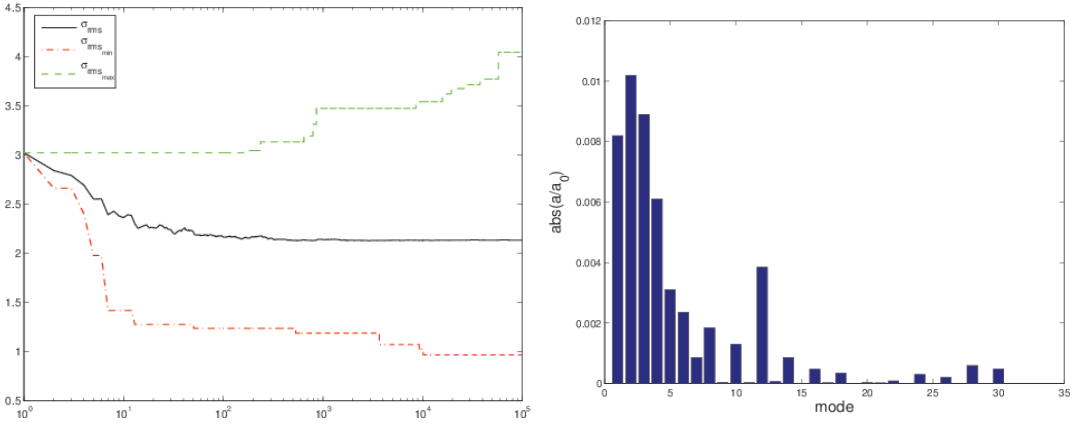

Figure C.20: σ_{rms} robustness and Legendre mode study for variation of all the parameter for the 48 beams configurations.

Variation on	σ_{rms}	$\sigma_{rms_{min}}$	$\sigma_{rms_{max}}$
Balance	1.05	0.41	2.38
Centering	0.59	0.27	1.11
Pointing	1.77	0.66	3.16
all parameters	2.13	0.96	4.04
L_2 norm	2.14	0.82	4.1

Table C.3: converge σ_{rms}, $\sigma_{rms_{min}}$ and $\sigma_{rms_{max}}$ comparison with L_2 norm when all parameters vary for the 48 beams configurations.

C.6 Nominal irradiation configuration

The irradiation pattern for HiPER has been defined by using the geometrical optics code CE-CLAD. HiPER specifications are 50 beams with 15 kJ per beams at 1 ω (6 kJ at 3 ω) [60]. The chosen 48 laser beams configuration [164] is made of 3 rings on each side of the target hemispheres. This configuration seems to be a good trad off compared to the others configurations. We choose a 48 beams configuration pattern [164] made of 3 rings on each side of the target hemispheres (21.23°, 47.03°, 74.95°). The rings have, respectively, 4, 8 and 12 beams. The offsets are 0° for the 4 beams on the first ring, ±23.4° for the 8 (4 + 4) beams of the second ring and 0° and ±29.8° for the 12 (4 + 4 + 4) beams of the last ring (see FIG. C.5). Each beam has a super Gaussian distribution of intensity in the focal spot, in the form $I(r) = exp(-r/a)^{2m}$. Parameters m and a are chosen such as to minimize the irradiation non-uniformity σ_{rms}. According to our computations a minimum $\sigma_{rms} = 0.15\%$ is obtained for $m = 1.02$ and $a = 0.61R_a$, where R_a is the initial outer radius. The implosion dynamics causes the critical radius to decrease in time; however, the symmetry indicator σ_{rms} remains stable during this whole process. The robustness of this pattern with respect to random deviations from nominal was evaluated: the symmetry indicator σ_{rms} remains close to 1% under a normal repartition of the beam to beam imbalance (10%), of the beam pointing (5%), and of the beam centering (2% of initial target radius). In order to give input to low-mode asymmetry studies, a Legendre polynomial expansion has also been carried out. It shows that the main modes of illumination non-uniformity are $l = 12$, 8 and 10, with a maximum relative non-uniformity of 0.5% for mode $l = 12$.

Appendix D

Personal record

Work Experience

- From 2003 to 2015 : Researcher in CELIA laboratory, University of Bordeaux, France. Development and validation of numerical method for a multi-material 2D Lagrangian hydrodynamics code CHIC to simulate ICF (Inertial Confinement Fusion) and plasma physics experiments. Interpretation of plasma physics experiments using simulation tools.
- From 2001 to 2003 : Post doc in National Aerospace Laboratory (JAXA), Tokyo, Japan. Development of a parallel solver for Navier-Stokes equations using specific numerical method (additive Schwartz domain decomposition) on a Linux Cluster with MPI Library.
- From 1997 to 2001 : Phd, TREFLE Laboratory, University of Bordeaux, France. Modelisation of viscous fluid using interface reconstruction method in 2D and 3D. Application to mould filling of Ariane V rocket booster.

Education and Qualifications

- June 2016 : Habilitation à Diriger des Recherches (HDR) in applied Mathematics and computation.
- 2005 : HEDP Summer school at Berkeley University, USA.
- From 2001 to 2003 : Post doc at National Aerospace Laboratory of Japan in Tokyo.
- From 1997 to 2001 : Phd at University of Bordeaux.

Journals with Editorial Board

1. B. Delorme, M. Olazabal-Loumé, A. Casner, Ph. Nicolaï, D.T. Michel, G. Riazuelo, N. Borisenko, J. Breil, S. Fujioka, M. Grech, A. Orekhov, W. Seka, A. Sunahara, D.H. Froula, V. Goncharov, V.T. Tikhonchuk, *Experimental demonstration of laser imprint reduction using underdense foams*, Phys. Plasmas, 23(4), 042701, 2016.
2. G. Gabriel, J. Breil, P.-H. Maire, *A 3D GCL compatible cell-centered Lagrangian scheme for solving gas dynamics equations*, J. Comput. Phys., 305, 921-941, 2016.

3. J. Breil, H. Alcin, P.-H. Maire, *A swept-intersection-based remapping method for axisymmetric ReALE computation*, Int. J. Numer. Meth. Fluids, 77(11), 694-706, 2015.

4. G. Georges, J. Breil, X. Ribeyre, E. Le Bel, *A 3D cell-centered Lagrangian scheme applied to the simulation of 3D non-stationary RayleigheTaylor Instability in supernova remnants*, HEDP, 17, 151-156, 2015.

5. J. Velechovsky, J. Breil, R. Liska, *Flux corrected remapping using piecewise parabolic reconstruction for 2D cell-centered ALE methods*, Int. J. Numer. Meth. Fluids, 76, 575-586, 2014.

6. M. Billaud Friess, J. Breil, P.-H. Maire and. Shashkov, *A multi-material CCALE-MOF approach in cylindrical geometry*, Commun. Comput. Phys., 15, 330-364, 2014.

7. A. Lar'kin, D. Uryupina, K. Ivanov, A. Savel'ev, T. Bonnet, F. Gobet, F. Hannachi, M. Tarisien, M. Versteegen, K. Spohr, J. Breil, B. Chimier, F. Dorchies, C. Fourment, P.-M. Leguay, V. Tikhonchuk, *Microjet formation and hard x-ray production from a liquid metal target irradiated by intense femtosecond laser pulses*, Phys. Plasmas, 21, 9, 093103, 2014.

8. M. Gauthier, A. Lévy, E. d'Humières, M. Glesser, B. Albertazzi, C. Beaucourt, J. Breil, S.-N. Chen, V. Dervieux, J.-L. Feugeas, Ph. Nicolaï, V. Tikhonchuk, H. Pépin, P. Antici, J. Fuchs, *Investigation of longitudinal proton acceleration in exploded targets irradiated by intense short-pulse laser*, Phys. Plasmas, 21, 1, 013102, 2014.

9. J. Breil, T. Harribey, P.-H. Maire, M. Shashkov, *A multi-material ReALE method with MOF interface reconstruction*, Comput. Fluids, 83, 115-125, 2013.

10. M. Olazabal-Loumé, Ph. Nicolaï, G. Riazuelo, M. Grech, J. Breil, S. Fujioka, A. Sunahara, N. Borisenko, V. Tikhonchuk, *Simulations of laser imprint reduction using underdense foams and its consequences on the hydrodynamic instability growth*, New J. Phys., 15 (8), 085033, 2013.

11. T. Harribey, J. Breil, P.-H. Maire, M. Shashkov, *A swept-intersection-based remapping method in a ReALE framework*, Int. J. Numer. Meth. Fluids, 72 (6), 697-708, 2013.

12. P.-H. Maire, R. Abgrall, J. Breil, R. Loubère, B. Rebourcet, *A nominally second-order cell-centered Lagrangian scheme for simulating elastic-plastic flows on two-dimensional unstructured grids*, J. Comput. Phys., 235, 626-665, 2013.

13. P.-H. Maire, J. Breil, *A nominally second-order accurate finite volume cell-centered scheme for anisotropic diffusion on two-dimensional unstructured grids*, J. Comput. Phys., 231 (5), 2259-2299, 2012.

14. J. Breil, S. Galera, P.-H. Maire, *Multi-material ALE computation in inertial confinement fusion code CHIC*, Comput. Fluids, 46, 1, 161-167, 2011.

15. J. Breil, S. Galera, P.-H. Maire, *A two-dimensional VOF interface reconstruction in a multi-material cell-centered ALE scheme*, Int. J. Numer. Meth. Fluids, 65, 11-12, 1351-1364, 2011.

16. S. Galera, J. Breil, P.-H. Maire, *A 2D unstructured multi-material Cell-Centered Arbitrary Lagrangian-Eulerian (CCALE) scheme using MOF interface reconstruction*, Comput. Fluids, 46, 1, 237-244, 2011.

17. M. Kucharik, J. Breil, S. Galera, P.-H. Maire, M. Berndt, M. Shashkov, *Hybrid remap for multi-material ALE*, Comput. Fluids, 46, 1, 293-297, 2011.

18. M. Berndt, J. Breil, S. Galera, M. Kucharik, P.-H. Maire, M. Shashkov, *Two-Step Hybrid Remapping (Conservative Interpolation) for Multimaterial Arbitrary Lagrangian-Eulerian Methods*, J. Comput. Phys., 230, 17, 6664-6687 , 2011.

19. M. Olazabal-Loumé, J. Breil, L. Hallo, X. Ribeyre, *Linear and non-linear high mode perturbations amplification at ablation front in HiPER targets*, Plasma Phys. Control. Fusion, 53, 015015, 2011.

20. X. Ribeyre, V. T. Tikhonchuk, J. Breil, M. Lafon, E. Le Bel, *Analytic criteria for shock ignition of fusion reactions in a central hot spot*, Phys. Plasmas, 18, 102702, 2011.

21. Ph. Nicolaï, J.-L. Feugeas, C. Regan, M. Olazabal-Loumé, J. Breil, B. Dubroca, J.-P. Morreeuw, and V. Tikhonchuk, *Effect of the plasma-generated magnetic field on relativistic electron transport*, Phys. Rev. E, 84, 016402, 2011.

22. Ph. Nicolaï, J.-L. Feugeas, C. Regan, M. Olazabal-Loumé, J. Breil, B. Dubroca, J.-P. Morreeuw, V. Tikhonchuk, *Effect of the plasma-generated magnetic field on relativistic electron transport*, Phys. Rev. E 84, 016402, 2011.

23. E. Falize, B. Loupias, A. Ravasio, C.D. Gregory, A. Dizière, M. Koenig, C. Michaut, C. Cavet, P. Barroso, J.-P. Leidinger, X. Ribeyre, J. Breil, H. Takabe, Y. Sakawa, Y. Kuramitsu, T. Morita, N.C. Woolsey, W. Nazarov, S. Pikuz, *The scalability of the accretion column in magnetic cataclysmic variables: the POLAR project*, Astrophysics and Space Science, 336, 81-85, 2011.

24. E. Lescoute, T. De Rességuier, J.-M. Chevalier, J. Breil, P.-H. Maire, G. Schurtz, *Experimental and numerical study of dynamic fragmentation in laser shock-loaded gold and aluminium targets*, Comput. Mat. Continua, 22 (3), 197, 2011.

25. S. Galera, P.-H. Maire, J. Breil, *A two-dimensional unstructured cell-centered multi-material ALE scheme using VOF interface reconstruction*, J. Comput. Phys., 229, 5755-5787, 2010.

26. R. Loubère, P.-H. Maire, M. Shashkov, J. Breil, S. Galera, *ReALE: A Reconnection-based Arbitrary-Lagrangian-Eulerian Method*, J. Comput. Phys., 229, 12, 4724-4761, 2010.

27. E. Lescoute, T. De Rességuier, J.-M. Chevalier, D. Loison, J.-P. Cuq-Lelandais, M. Boustie, J. Breil, P.-H. Maire, G. Schurtz, *Ejection of spalled layers from laser shock-loaded metals*, J. Appl. Phys. 108, 093510, 2010.

28. S. Atzeni, J.R. Davies, L. Hallo, J.J. Honrubia, P.-H. Maire, M. Olazabal-Loumé, J.-L. Feugeas, X. Ribeyre, A. Schiavi, G. Schurtz, J. Breil, Ph. Nicolaï, *Studies on targets for inertial fusion ignition demonstration at the HiPER facility*, Nucl. Fusion, 49 055008, 2009.

29. X. Ribeyre , M. Lafon , G. Schurtz , M. Olazabal-Loumé , J. Breil , S. Gallera, S. Weber, *Shock ignition: modelling and target design robustness*, Plasma Phys. Control. Fusion, 51, 124030, 2009.

30. C. Mézel, L. Hallo, A. Souquet, J. Breil, D. Hébert, F. Guillemot, *Self-consistent modeling of jet formation process in the nanosecond laser pulse regime*, Phys. Plasmas, 16, 123112, 2009.

31. L. Hallo, M. Olazabal-Loumé, X. Ribeyre, V. Dréan, G. Schurtz, J.-L. Feugeas, J. Breil, Ph. Nicolaï, P.-H. Maire, *Hydrodynamic and symmetry safety factors of HiPER's targets*, Plasma Phys. Control. Fusion, 51, 1, 2009.

32. P.-H. Maire, J. Breil, S. Galera, *A cell-centred arbitrary Lagrangian-Eulerian (ALE) method*, Int. J. Numer. Meth. Fluids, 56, 8, 1161-1166, 2008.

33. P.-H. Maire, J. Breil, *A second-order cell-centered Lagrangian scheme for two-dimensional compressible flow problems*, Int. J. Numer. Meth. Fluids, 56, 8, 1417-1423, 2008.

34. X. Ribeyre, Ph. Nicolaï, G. Schurtz, M. Olazabal-Loumé, J. Breil, P.-H. Maire, J.-L. Feugeas, V. Tikhonchuk, *Compression phase study of the HiPER baseline target*, Plasma Physics and Controlled Fusion 50, 2, 025007, 2008.

35. G. Malka, Ph. Nicolaï, E. Brambrink, J. Santos, M. Aléonard, K. Amthor, P. Audebert, J. Breil, G. Claverie, M. Gerbaux, F. Gobet, F. Hannachi, V. Méot, P. Morel, J.N. Scheurer, M. Tarisien, V. Tikhonchuk, *Fast electron transport and induced heating in solid targets from rear-side interferometry imaging*, Physical Review E, 026408, 2008.

36. P.-H. Maire, R. Abgrall, J. Breil, J. Ovadia, *A cell-centered lagrangian scheme for two-dimensional compressible flow problems*, SIAM J. of Scient. Comput., 29, 4, 1781-1824, 2007.

37. J. Breil, P.-H. Maire, *A cell-centered diffusion scheme on two-dimensional unstructured meshes*, J. Comput. Phys., 224, 2, 785-823, 2007.

38. G. Schurtz, S. Gary, S. Hulin, C. Chenais-Popovics, J.-C. Gauthier, F. Thais, J. Breil, F. Durut, J.-L. Feugeas, P.-H. Maire, Ph. Nicolaï, O. Peyrusse, C. Reverdin, G. Soullié, V. Tikhonchuk, B. Villette, C. Fourment, *Revisiting nonlocal electron-energy transport in inertial-fusion conditions*, Physical Review Letters, 98, 9, 095002, 2007.

39. J. Breil, L. Hallo, P.-H. Maire, M. Olazabal, *Hydrodynamic instabilities in axisymmetric geometry self-similar models and numerical simulations*, Laser and Particle Beams, 23, 2, 155-160., 2005.

40. J.-P. Caltagirone, J. Breil, *A vector projection method for solving the Navier-Stokes equations*, Comptes Rendus de l'Académie des Sciences - Series IIB, 327, 11, 1179-1184, 1999.

Proceedings

1. H. Nagatomo, K. Matsuo, J. Breil, Ph. Nicolaï, J.-L. Feugeas, T. Asahina, A. Sunahara, T. Johzaki, S. Fujioka, T. Sano, K. Mima, *Laser ablation and target acceleration under the strong magnetic field*, APS Meeting Abstracts, 2015.

2. G. Georges, J. Breil, P.-H. Maire, *A 3D symmetric cell-centered Lagrangian scheme based on a multi-dimensional minmod limiter*, Proceedings of the ECCOMAS conference, 5965-5976, 2014.

3. J.-L. Feugeas, Ph. Nicolaï, M. Touati, J. Breil, B. Dubroca, X. Ribeyre, J.J. Santos, V. Tikhonchuk, S. Gus' kov, *New fast and accurate numerical method for laser-produced relativistic electrons beams transport in the context of ICF-Applications to fast and shock ignition*, Plasma Science (ICOPS), 2013.

4. X. Ribeyre, V. Tikhonchuk, J. Breil, M. Lafon, A. Vallet, E. Le Bel, *Analytical criterion for shock ignition of fusion reaction in hot spot*, EPJ Web of Conferences, 59, 2013.

5. T. Harribey, J. Breil, P.-H. Maire, M. Shashkov, *Hydrodynamic applications using ReALE method*, Proceedings of the ECCOMAS conference, 574-587, 2012.

6. T. de Resseguier, E. Lescoute, J.M. Chevalier, P.H. Maire, J. Breil, G. Schurtz, *Experimental and numerical techniques to investigate and to model dynamic fragmentation of laser shock-loaded metals*, APS Shock Compression of Condensed Matter Meeting Abstracts 1, 1002, 2011.

7. J.L. Feugeas, Ph. Nicolaï, C. Regan, B. Dubroca, E. D'Humieres, V. Tikhonchuk, J. Breil, M. Olazabal-Loumé, L. Hallo, *Angular moment model for the charge particle transport in radiation hydrodynamic codes*, APS Meeting Abstracts 1, 5010, 2010.

8. Ph. Nicolaï, J.L. Feugeas, C. Regan, J. Breil, A. Debayle, B. Dubroca, L. Hallo J. Honrubia, M. Olazabal-Loumé, J. Santos, B. Vauzour, V. Tikhonchuk, *Fast ignition studies with an improved transport model implemented in a 2D radiation hydrodynamic code*, APS Meeting Abstracts 1, 6012, 2010.

9. C. Mézel, L. Hallo, A. Souquet, A. Bourgeade, J. Breil, D. Hébert, F. Guillemot, O. Sautd, *Toward a new nanoLIFT transfer process*, AIP Conf. Proc., 1209, 67-70, 2010.

10. R. Liska, R. Loubère, P.-H. Maire, J. Breil, S. Galera, P. Vachal, *Comparison of staggered and cell-centered Lagrangian and ALE hydrodynamical methods*,Hyperbolic Problems: Theory, Numerics and Applications, Proceedings of Symposia in Applied Mathematics, 755-765, 2009.

11. L. Hallo, A. Bourgeade, G. Travaillé, V. Tikhonchuk, B. Nkonga, J. Breil, *Laser produced nanocavities in silica and sapphire: a parametric study*, Journal of Physics: Conference Series, 112, 2008.

12. X. Ribeyre, Ph. Nicolaï, G. Schurtz, M. Olazabal-Loumé, J. Breil, P.-H. Maire, J.-L. Feugeas, L. Hallo, V. Tikhonchuk, *Numerical simulations of the HiPER baseline target*, Journal of Physics: Conference Series, 112, 2008.

13. S. Atzeni, J.R. Davies, L. Hallo, J.J. Honrubia, P.H. Maire, M. Olazabal-Loumé, J.L. Feugeas, X. Ribeyre, A. Schiavi, G. Schurtz, J. Breil, Ph. Nicolaï, *Theoretical and computational studies on targets for inertial fusion ignition demonstration at the HiPER facility*, 22nd IAEA Fusion Energy Conference, Geneva, 2008.

14. J. Breil, P.-H. Maire, Ph. Nicolaï, G. Schurtz, *Modelling of the Magnetic Field Effects in Hydrodynamic Codes Using a Second Order Tensorial Diffusion Scheme*, Journal of Physics: Conference Series, 112, 2008.

15. L. Hallo, M. Olazabal-Loumé, P.-H. Maire, J. Breil, R.-L. Morse, G. Schurtz, *Numerical simulations of hydrodynamic instabilities: Perturbation codes Pansy, Perle, and 2D code Chic applied to a realistic LIL target*, Journal De Physique. IV, 133, 135-139., 2006.

16. P.-H. Maire, J. Breil, L. Hallo, M. Olazabal-Loumé, *Hydrodynamic instabilities in cylindrical geometry self-similar models and numerical simulations*, Proceedings of the 31st EPS Conference on Plasma Physics, London, 2004.

17. J. Breil, J.-P. Caltagirone, E. Giraud, *Comparison between experimental and numerical results of a mould filling with viscous fluid*, ICCFD, 571-576, 2003.

18. J. Breil , R. Marinova, H. Aiso, T. Takahashi, *Fully coupled solver for incompressible Navier-Stokes equations using a domain decomposition Method*, Parallel Computational Fluid Dynamics: New Frontiers and Multi-Disciplinary Applications, 249-256, 2003.

19. J. Breil, J.-P. Caltagirone, *Three dimensional computer simulation of mould filling with N fluids by VOF PLIC and projection methods*, ICCFD, 743-748, 2001.

Bibliography

[1] I. Aavatsmark, T. Barkve, O. Boe, and T. Mannseth. Discretization on unstructured grids for inhomogeneous, anistropic media. Part I: derivation of the methods. *SIAM J. Sci. Comput.*, 19:1700–1716, 1998.

[2] I. Aavatsmark, T. Barkve, O. Boe, and T. Mannseth. Discretization on unstructured grids for inhomogeneous, anistropic media. Part II: discussion and numerical results. *SIAM J. Sci. Comput.*, 19:1717–1736, 1998.

[3] I. Aavatsmark, G.T. Eigestad, B.T. Mallison, and J.M. Nordbotten. A Compact Multipoint Flux Approximation Method with Improved Robustness. *Numer. Methods Partial Differential EQ.*, 24:1329–1360, 2008.

[4] R. Abgrall, R. Loubère, and J. Ovadia. A Lagrangian Discontinuous Galerkin-type method on unstructured meshes to solve hydrodynamics problems. *Int. J. Numer. Meth. Fluids*, 44:645–663, 2004.

[5] H.T. Ahn and M.J. Shashkov. Multi-material interface reconstruction on generalized polyhedral meshes. *J. Comput. Phys.*, 226:2096–2132, 2007.

[6] B. Albertazzi, S.N. Chen, P. Antici, J. Böker, M. Borghesi, J. Breil, V. Dervieux, J.L. Feugeas, L. Lancia, M. Nakatsutsumi, Ph. Nicolaï, L. Romagnagni, R. Shepherd, Y. Sentoku, M. Starodubtsev, M. Swantusch, V. T. Tikhonchuk, O. Willi, E. d'Humières, H. Pépin, and J. Fuchs. Dynamics and structure of self-generated magnetics fields on solids following high contrast, high intensity laser irradiation. *Physics of Plasmas (1994-present)*, 22(12):123108, 2015.

[7] H.R. Anbarlooei and K. Mazaheri. Moment of fluid interface reconstruction method in multi-material arbitrary Lagrangian-Eulerian (MMALE) algorithms. *Comput. Methods Appl. Mech. Engrg.*, 198:3782–3794, 2009.

[8] K. Anderson and R. Betti. Laser-induced adiabat shaping by relaxation in inertial fusion implosions. *Physics of Plasmas*, 11(1):5–8, 2004.

[9] R.W. Anderson, R.B. Pember, and N.S. Elliott. An arbitrary Lagrangian-Eulerian method with local structured adaptive mesh refinement for modeling shock hydrodynamics. In *AIAA paper 2002-0738*, 2002.

[10] S. Atzeni. Laser driven inertial fusion: the physical basis of current and recently proposed ignition experiments. *Plasma Physics and Controlled Fusion*, 51(12):124029, 2009.

[11] S. Atzeni, J. Davies, L. Hallo, J. Honrubia, P.-H. Maire, M. Olazabal-Loumé, J.-L. Feugeas, X. Ribeyre, A. Schiavi, G. Schurtz, J. Breil, and Ph. Nicolaï. Studies on targets for inertial fusion ignition demonstration at the hiper facility. *Nucl. Fusion*, 49:055008, 2009.

[12] S. Atzeni, X. Ribeyre, G. Schurtz, A.J. Schmitt, B. Canaud, R. Betti, and L.J. Perkins. Shock ignition of thermonuclear fuel: principles and modelling. *Nuclear Fusion*, 54(5):054008, 2014.

[13] S. Atzeni and J. Meyer ter Vehn. *The Physics of Inertial Fusion*. Oxford Science Publications, Oxford, 2004.

[14] A. Barlow, R. Hill, and M. Shashkov. Constrained optimization framework for interface-aware sub-scale dynamics closure model for multimaterial cells in lagrangian and arbitrary lagrangian-eulerian hydrodynamics. *Journal of Computational Physics*, 276:92 – 135, 2014.

[15] A.J. Barlow. A compatible finite element multi-material ALE hydrodynamics algorithm. *Int. J. Numer. Meth. Fluids*, 56:953–964, 2008.

[16] A.J. Barlow and P.L. Roe. A cell-centered Lagrangian Godunov scheme for shock hydrodynamics. *Comput. and Fluids*, 46:133–136, 2011.

[17] T.J. Barth and D.C. Jespersen. The design and application of upwind schemes on unstructured meshes. *AIAA Paper, 27th Aerospace Sciences Meeting, Reno, Nevada*, 89-0366, 1989.

[18] D. Batani, M. Koenig, S. Baton, F. Perez, L. A. Gizzi, P. Koester andL. Labate, J. Honrubia, L. Antonelli, A. Morace, L. Volpe, J. Santos, G. Schurtz, S. Hulin, X. Ribeyre, C. Fourment, Ph. Nicolaï, B. Vauzour andL. Gremillet, W. Nazarov, J. Pasley, M. Richetta, K. Lancaster andCh. Spindloe, M. Tolley, D. Neely, M. Kozlov, J. Nejdl, B. Rus, J. Wolowski, J. Badziak, and F. Dorchies. The hiper project for inertial confinement fusion and some experimental results on advanced ignition schemes. *Plasma Physics and Controlled Fusion*, 53(12):124041, 2011.

[19] S. D. Baton, E. Le Bel, D. Batani, J. Breil, S. Brygoo, M. Koenig, D. Raffestin, X. Ribeyre, and C. Rousseau. Preliminary study on shock propagation in the context of polar direct drive shock ignition. *Submitted*, 2016.

[20] S. D. Baton, M. Koenig, E. Brambrink, H. P. Schlenvoigt, C. Rousseaux, G. Debras, S. Laffite, P. Loiseau, F. Philippe, X. Ribeyre, , and G. Schurtz. Experiment in planar geometry for shock ignition studies. *Phys. Rev. Lett.*, 108:195002, 2012.

[21] M. Ben-Artzi and J. Falcovitz. Generalized Riemann problems: from the scalar equation to multidimensional fluid dynamics. In *WSPC Proceedings*, 2008.

[22] D. J. Benson. Computational methods in Lagrangian and Eulerian hydrocodes. *Comp. Meth. in Appl. Mech. and Eng.*, 99:235–394, 1992.

[23] M. Berger, M. Aftosmis, and S. Murman. Analysis of slope limiters on irregular grids. *AIAA Paper, 43th Aerospace Sciences Meeting, Reno, Nevada*, 43, 2005.

[24] M. Berndt, J. Breil, S. Galera, M. Kucharik, P.-H. Maire, and M. Shashkov. Two-step hybrid conservative remapping for multi-material arbitrary Lagrangian-Eulerian methods. *J. Comput. Phys.*, 230:6664–6687, 2011.

[25] R. Betti, V. N. Goncharov, R. L. McCrory, and C. P. Verdon. Growth rates of the ablative Rayleigh-Taylor instability in inertial confinement fusion. *Physics of Plasmas*, 5(5):1446–1454, 1998.

[26] R. Betti, C. D. Zhou, K. S. Anderson, L. J. Perkins, W. Theobald, and A. A. Solodov. Shock ignition of thermonuclear fuel with high areal density. *Phys. Rev. Lett.*, 98:155001, 2007.

[27] M. Billaud-Friess, J. Breil, S. Galera, P.-H. Maire, and M. Shashkov. A multi-material CCALE-MOF approach in cylindrical geometry. *Com. in Comp. Phys.*, 15:330–364, 2014.

[28] W. Bo and M. Shashkov. Adaptive reconnection-based arbitrary lagrangian eulerian method. *Journal of Computational Physics*, 299:902 – 939, 2015.

[29] W. Boscheri and M. Dumbser. A direct Arbitrary-Lagrangian-Eulerian ADER-WENO finite volume scheme on unstructured tetrahedral meshes for conservative and non-conservative hyperbolic systems in 3D. *J. Comput. Phys.*, 275:484–523, 2014.

[30] S.I. Braginskii. Transport Process in a Plasma. In *Reviews of Plasma Physics*, volume I, pages 205–311. Consultants Bureau, New York, 1965.

[31] J. Breil, H. Alcin, and P.-H. Maire. A swept-intersection-based remapping method for axisymmetric ReALE computation. *Int. J. Numer. Meth.*, 77:694–706, 2015.

[32] J. Breil, S. Galera, and P.-H. Maire. A two-dimensional VOF interface reconstruction in a multi-material cell-centered ALE scheme. *Int. J. Numer. Meth. Fluids*, 65:1351–1364, 2011.

[33] J. Breil, S. Galera, and P.-H. Maire. Multi-material ALE computation in Inertial Confinement Fusion code CHIC. *Comput. and Fluids*, 46:161–167, 2011.

[34] J. Breil, L. Hallo, P.-H. Maire, and M. Olazabal-Loumé. Hydrodynamic instabilities in axisymmetric geometry self-similar models and numerical simulations. *Laser Part. Beams*, 23:155–160, 2005.

[35] J. Breil, T. Harribey, P.-H. Maire, and M. Shashkov. A multi-material ReALE method with MOF interface reconstruction. *Comput. and Fluids*, 83:115–125, 2013.

[36] J. Breil and P.-H. Maire. A cell-centered diffusion scheme on two-dimensional unstructured meshes. *J. Comput. Phys.*, 224(2):785–823, 2007.

[37] J. Breil, P.-H. Maire, Ph. Nicolaï, and G. Schurtz. Modelling of the magnetic field effects in hydrodynamic codes using a second order tensorial diffusion scheme. In *Journal of Physics: Conference Series*, volume 112, 2008.

[38] D.E. Burton. Multidimensional discretization of conservation laws for unstructured polyhedral grids. Technical Report UCRL-JC-118306, Lawrence Livermore National Laboratory, 1994.

[39] D.E. Burton, N.R. Morgan, T.C. Carney, and M.A. Kenamond. Reduction of dissipation in Lagrange cell-centered hydrodynamics (CCH) through corner gradient reconstruction (CGR). *J. Comput. Phys.*, 299:229–280, 2015.

[40] J. Campbell and M. Shashkov. A tensor artificial viscosity using a mimetic Finite Difference algorithm. *J. Comput. Phys.*, 172:739–765, 2001.

[41] J.C. Campbell and M.J. Shashkov. A compatible Lagrangian hydrodynamics algorithm for unstructured grids. *Selçuk J. Appl. Math.*, 4(2):53–70, 2003.

[42] B. Canaud, X. Fortin, N. Dague, and J.L. Bocher. Laser mégajoule irradiation uniformity for direct drive. *Physics of Plasmas*, 9(10):4252–4260, 2002.

[43] B. Canaud and M. Temporal. High-gain shock ignition of direct-drive ICF targets for the Laser Mégajoule. *New Journal of Physics*, 12(4):043037, 2010.

[44] E. Caramana and M. Shashkov. Elimination of artificial grid distortion and hourglass-type motions by means of Lagrangian subzonal masses and pressures. *J. Comput. Phys.*, 142:521–561, 1998.

[45] E.J. Caramana, D.E. Burton, M.J. Shashkov, and P.P. Whalen. The construction of compatible hydrodynamics algorithms utilizing conservation of total energy. *J. Comput. Phys.*, 146:227–262, 1998.

[46] E.J. Caramana, C.L. Rousculp, and D.E. Burton. A compatible, energy and symmetry preserving Lagrangian Hydrodynamics algorithm in three-dimensional Cartesian geometry. *J. Comput. Phys.*, 157:89–119, 2000.

[47] E.J. Caramana, M.J. Shashkov, and P.P. Whalen. Formulations of artificial viscosity for multi-dimensional shock wave computations. *J. Comput. Phys.*, 144:70–97, 1998.

[48] G. Carré, S. Del Pino, B. Després, and E. Labourasse. A cell-centered Lagrangian hydrodynamics scheme on general unstructured meshes in arbitrary dimension. *J. Comput. Phys.*, 228:5160–5183, 2009.

[49] S. Clain, S. Diot, and R. Loubère. A high-order finite volume method for systems of conservation laws - Multi-dimensional Optimal Order Detection (MOOD). *J. Comput. Phys.*, 230:4028–4050, 2011.

[50] W. Dai and A. Scannapieco. Second order accurate interface and discontinuity aware diffusion solvers in 2D and 3D. *J. Comput. Phys.*, 281:982–1002, 2015.

[51] R. Dautray and J.-P. Watteau. *La fusion thermonucléaire par laser*, volume II. Eyrolles, 1991.

[52] B. Delorme, M. Olazabal-Loumé, A. Casner, Ph. Nicolaï, D. T. Michel, G. Riazuelo, N. Borisenko, J. Breil, S. Fujioka, M. Grech, A. Orekhov, W. Seka, A. Sunahara, D. H. Froula, V. Goncharov, and V. T. Tikhonchuk. Experimental demonstration of laser imprint reduction using underdense foams. *Physics of Plasmas (1994-present)*, 23(4):042701, 2016.

[53] B. Després and C. Mazeran. Lagrangian gas dynamics in dimension two and Lagrangian systems. *Arch. Ration. Mech. Anal.*, 178:327–372, 2005.

[54] J. Donea, A. Huerta, J.-Ph. Ponthot, and A. Rodriguez-Ferran. *Encyclopedia of Computational Mechanics*, volume 1: Fundamentals. John Wiley and Sons, 2004. Chapter 14: Arbitrary Lagrangian-Eulerian methods.

[55] J.N. Johnson D.P. Starinshak, J.M. Owen. A New Parallel Algorithm for Constructing Voronoi Tessellations from Distributed Input Data. *Computer Physics Communications*, 185(12):3204–3214, 2014.

[56] J. Dukowicz. Caveat: a computer code for fluid dynamics problems with large distortion and internal slip. *Los Alamos National Laboratory Report*, LA-10613-MS, 1986.

[57] J.K. Dukowicz. A general, non-iterative Riemann solver for Godunov's method. *J. Comput. Phys.*, 61:119–137, 1985.

[58] J.K. Dukowicz, M.C. Cline, and F.S. Addessio. A general topology method. *J. Comput. Phys.*, 82:29–63, 1989.

[59] J.K. Dukowicz and B. Meltz. Vorticity errors in multidimensional Lagrangian codes. *J. Comput. Phys.*, 99:115–134, 1992.

[60] M. Dunne, N. Alexander, F. Amiranoff, P. Auger, S. Atzeni, H. Azechi, V. Bagnoud, P. Balcou, J. Badziak, D. Batani, C. Bellei, D. Besnard, R. Bingham, J. Breil, M. Borghesi, S. Borneis, A. Caruso, J. C. Chanteloup, R. J. Clarke, J. L. Collier, J. R. Davies, J.-P. Dufour, P. Estrailler, R. L. Evans, M. Fajardo, R. Fedosejevs, G. Figueria, J. Fils, J. L. Feugeas, M. Galimberti, J.-C. Gauthier, A. Giulietti, L. A. Gizzi, D. Goodin, G. Gregori, S. Guskov, L. Hallo, C. Hermandez-Gomez, D. Hoffman, J. Honrubia, S. Jacquemot, M. Key, J. Kilkenny, R. Kingham, M. Koenig, F. Kovacs, A. McEvoy, P. McKenna, J. T. Mendonca, J. Meyer ter Vehn, K. Mima, G. Morou, S. Moustazis, Z. Najmudin, P. Nickles, D. Neely, P. P. Norreys, M. Olazabal, A. Offenberger, N. Papodogianis, J. M. Perlado, J. Ramirez, R. Ramis, Y. Rhee, X. Ribeyre, A. Robinson, K. Rohlena, S S. Rose, M. Roth, C. Rouyer, C. Rulliere, B. Rus, W. Sandner, A. Schiavi, G. G. Schurtz, A. Sergeev, M. Sherlock, L. Silva, R. Smith, G. Sorasio, C. C. Strangio, H. Takabe, M. Tatarakis, V. Tikhonchuk, M. Tolley, M. Vaselli, P. Velarde, T. Winstone, K. Witte, J. Wolowski, N. Woolsey, B. Wyborn, M. Zepf, , and J. Zhang. HiPER Technical Background and Conceptual Design Report 2007. Technical Report RALTR-2007-008, Rutherford Appleton Laboratory, 2007.

[61] V. Dyadechko and M. Shashkov. Reconstruction of Multi-material Interfaces from Moment Data. *J. Comput. Phys.*, 227:5361–5384, 2008.

[62] M. G. Edwards and C. F. Rogers. Finite volume discretization with imposed flux continuity for the general tensor pressure equation. *Computational Geosciences*, 2:259–290, 1998.

[63] J.-L. Feugeas, J. Breil, Ph. Nicolaï, G. Schurtz, L. Hallo, M. Olazabal-Loumé, X. Ribeyre, P.-H. Maire, V.T. Tikhonchuk, B. Le Garrec, J.-M. Martinez, F. Gaudier, P. Salavatore, and O. Grégoire. Illumination Uniformity Study for the Direct Drive. In *6th Direct Drive and Fast Ignition Workshop, Lisbon*, 2008.

[64] S. Galera, J. Breil, and P.-H. Maire. A 2D unstructured multi-material Cell-Centered Arbitrary Lagrangian-Euleriann (CCALE) scheme using MOF interface reconstruction. *Comput. and Fluids*, 46:1:237–244, 2011.

[65] S. Galera, P.-H. Maire, and J. Breil. A two-dimensional unstructured cell-centered multi-material ALE scheme using VOF interface reconstruction. *J. Comput. Phys.*, 229:5755–5787, 2010.

[66] G. Georges, J. Breil, and P.H. Maire. A 3D GCL compatible cell-centered Lagrangian scheme for solving gas dynamics equations. *J. Comput. Phys.*, 305:921–941, 2016.

[67] J. Glimm, J.W. Grove, X.L. Li, W. Oh, and D.H. Sharp. A critical analysis of Rayleigh-Taylor growth rates. *J. Comput. Phys.*, 169:652–677, 2001.

[68] J. Glimm, J.W. Grove, X.L. Li, K.M. Shyue, Q. Zhang, and Y. Zeng. Three dimensional front tracking. *SIAM J. Sci. Comput.*, 19:703–727, 1998.

[69] E. Godlewski and P.A. Raviart. *Numerical approximation of hyperbolic systems of conservation laws*. Springer, 1995.

[70] S.K. Godunov, A. Zabrodine, M. Ivanov, A. Kraiko, and G. Prokopov. Résolution numérique des problèmes multi-dimensionnels de la dynamique des gaz. *Mir*, 1979.

[71] S.R. De Groot and P. Mazur. *Non-equilibrium thermodynamics*. Dover, 1984.

[72] J.-F. Haas and B. Sturtevant. Interaction of weak shock wave with cylindrical and spherical gas inhomogeneities. *J. Fluid. Mech.*, 181:41–76, 1987.

[73] A. Hadjadj and A. Kudryavtsev. omputation and flow visualization in high-speed aerodynamics. *Journal of Turbulence*, 6:16, 2005.

[74] L. Hallo, M. Olazabal-Loumé, X. Ribeyre, V. Dréan, G. Schurtz, J.-L. Feugeas, J. Breil, Ph. Nicolaï, and P.-H. Maire. Hydrodynamic and symmetry safety factors of HiPER's targets. *Plasma Phys. Control. Fusion*, 51:1:014001, 2009.

[75] T. Harribey, J. Breil, P.-H. Maire, and M. Shashkov. A swept-intersection-based remapping method in a ReALE framework. *Int. J. Numer. Meth. Fluids*, 72:697–708, 2013.

[76] C.W. Hirt, A. Amsden, and J.L. Cook. An arbitrary Lagrangian–Eulerian computing method for all flow speeds. *J. Comput. Phys.*, 14:227–253, 1974.

[77] C.W. Hirt and B.D. Nichols. Volume of fluid (VOF) method for the dynamics of free boundaries. *J. Comput. Phys.*, 39:201–225, 1981.

[78] P. Hoch. An Arbitrary Lagrangian Eulerian strategy to solve compressible fluid flows. HAL : hal-00366858, version 1, 2009. Available at `http://hal.archives-ouvertes.fr/docs/00/36/68/58/PDF/ale2d.pdf`.

[79] M. Hohenberger, W. Theobald, S. X. Hu, K. S. Anderson, R. Betti, T. R. Boehly, A. Casner, D. E. Fratanduono, M. Lafon, D. D. Meyerhofer, R. Nora, X. Ribeyre, T. C. Sangster, G. Schurtz, W. Seka, C. Stoeckl, and B. Yaakobi. Shock-ignition relevant experiments with planar targets on omega. *Physics of Plasmas*, 21(2):022702, 2014.

[80] P.-A. Holstein, M. Andre, M. Casanova, F. Chaland, C. Charpin, C. Cherfils, L. Divol, H. Dumont, D. Galmiche, J. Giorla, L. Hallo, S. Laffite, L. Lours, M.C. Monteil, D. Mourenas, F. Poggi, Y. Saillard, G. Schurtz, M. Valadon, D. Vanderhaegen, and F. Wagon. Target design for the LMJ. *CRAS - IV*, 1(6):693 – 704, 2000.

[81] L.H. Howell and J.A. Greenough. Radiation diffusion for multi-fluid Eulerian hydrodynamics with adaptive mesh refinement. *J. Comput. Phys.*, 184:53–78, 2003.

[82] M.E. Hubbard. Multidimensional slope limiters for MUSCL-type finite volume schemes on unstructured grids. *J. Comput. Phys.*, 155:54–74, 1999.

[83] W. H. Hui, P. Y. Li, and Z. W. Li. A Unified Coordinate System for Solving the Two-Dimensional Euler Equations. *J. Comput. Phys.*, 153:596–637, 1999.

[84] O. A. Hurricane, D. A. Callahan, D. T. Casey, P. M. Celliers, C. Cerjan, E. L. Dewald, T. R. Dittrich, T. Döppner, D. E. Hinkel, L. F. Berzak Hopkins, J. L. Kline, S. Le Pape, T. Ma, A. G. MacPhee, J. L. Milovich, A. Pak, H.-S. Park, P. K. Patel, B. A. Remington, J. D. Salmonson, P. T. Springer, and R. Tommasini. Fuel gain exceeding unity in an inertially confined fusion implosion. *Nature*, 506:343–348, 2014.

[85] O. Igra, Falcovitz, H. Reichenbach, and W. Heilig. Experimental and numerical study of the interaction between a planar shock wave and square cavity. *J. Fluid. Mech.*, 313:105–130, 1996.

[86] P. Jacq, P.-H. Maire, and R. Abgrall. A nominally second-order cell-centered finite volume scheme for simulating three-dimensional anisotropic diffusion equations on unstructured grids. *Com. in Comp. Phys.*, 16:841–891, 2014.

[87] Z. Jiang, K. Takayama, H. Babinsky, and T. Meguro. Transient shock wave flows in tubes with a sudden change in cross section, Shock Waves. *Shock Waves*, 7:151–162, 1997.

[88] J.R. Kamm and F.X. Timmes. On efficient generation of numerically robust Sedov solutions. *Technical report, Los Alamos National Laboratory*, LA-UR-07-2849, 2007.

[89] P. Knupp. Winslow smoothing on two-dimensional unstructured meshes. In *7th International Meshing Roundtable, Sandia National Lab*, pages 449–457, 1998.

[90] P. Knupp. Achieving finite element mesh quality via optimization of the Jacobian matrix norm and associated quantities. Part I– a framework for surface mesh optimization. *Int. J. Numer. Meth. Eng.*, 48:401–420, 2000.

[91] R. Kodama, P. A. Norreys, K. Mima, A. E. Dangor, R. G. Evans, H. Fujita, Y. Kitagawa, K. Krushelnick, T. Miyakoshi, N. Miyanaga, T. Norimatsu, S. J. Rose, T. Shozaki, K. Shigemori, A. Sunahara, M. Tampo, K. A. Tanaka, Y. Toyama, T. Yamanaka, and M. Zepf. Fast heating of ultrahigh-density plasma as a step towards laser fusion ignition. *Nature*, 412:798–802, 2001.

[92] M. Kucharik, J. Breil, S. Galera, P.-H. Maire, M. Berndt, and M. Shashkov. Hybrid remap for multi-material ALE. *Comput. and Fluids*, 46:293–297, 2011.

[93] M. Kucharik, R.V. Garimella, S.P. Schofield, and M.J. Shashkov. A comparative study of interface reconstruction methods for multi-material ALE simulations. *J. Comput. Phys.*, 229:2432–2452, 2010.

[94] M. Kucharik and M. Shashkov. Flux-based approach for conservative remap of multi-material quantities in 2D arbitrary Lagrangian-Eulerian simulations. In J. Fořt, J. Fürst, J. Halama, R. Herbin, and F. Hubert, editors, *Finite Volumes for Complex Applications VI - Problems & Perspectives, Vol. 1*, volume 4 of *Springer Proceedings in Mathematics*, pages 623–631. Springer, 2011.

[95] M. Kucharik, M. Shashkov, and B. Wendroff. An efficient linearity-and-bound-preserving remapping method. *J. Comput. Phys.*, 188:462–471, 2003.

[96] D. Layzer. On the Instability of Superposed Fluids in a Gravitational Field. *Astrophys. J.*, 122:1–12, 1955.

[97] J. D. Lindl. *Inertial Confinement Fusion.* Springer, 1998.

[98] K. Lipnikov, J. Morel, and M. Shashkov. Mimetic finite difference methods for diffusion equations on non-orthogonal non-conformal meshes. *J. Comput. Phys.*, 199:589–597, 2004.

[99] R. Liska, R. Loubère, P.-H. Maire, J. Breil, S. Galera, and P. Vachal. Comparison of staggered and cell-centered Lagrangian and ALE hydrodynamical methods. In *Hyperbolic Problems: Theory, Numerics and Applications, Proceedings of Symposia in Applied Mathematics*, pages 755–765, Washington, 2009.

[100] R. Liska, M. Shashkov, P. Váchal, and B. Wendroff. Optimization-based synchronized flux-corrected conservative interpolation (remapping) of mass and momentum for arbitrary Lagrangian-Eulerian methods. *J. Comput. Phys.*, 229(5):1467–1497, 2010.

[101] R. Liska, M. Shashkov, P. Váchal, and B. Wendroff. Synchronized flux corrected remapping for ALE methods. *Comput. and Fluids*, 46(1):312–317, 2011.

[102] R. Loubère, P.-H. Maire, and M. Shashkov. ReALE: A Reconnection Arbitrary-Lagrangian-Eulerian method in cylindrical geometry. *Comput. and Fluids*, 46:59–69, 2011.

[103] R. Loubère, P.-H. Maire, M. Shashkov, J. Breil, and S. Galera. ReALE: A Reconnection-based Arbitrary-Lagrangian-Eulerian Method. *J. Comput. Phys.*, 229:4724–4761, 2010.

[104] R. Loubère, P.-H. Maire, and P. Vachal. 3D staggered Lagrangian hydrodynamics scheme with cell-centered Riemann solver-based artificial viscosity. *Int. J. Numer. Meth. Fluids*, 72:22–42, 2013.

[105] R. Loubère and M.J. Shashkov. A Subcell Remapping Method on Staggered Polygonal Grids for Arbitrary-Lagrangian-Eulerian Methods. *J. Comput. Phys.*, 23:155–160, 2004.

[106] R. Loubère, M. Staley, and B. Wendroff. The repair paradigm: New algorithms and applications to compressible flow. *J. Comput. Phys.*, 211(2):385–404, 2006.

[107] H. Luo, J.D. Baum, and R. Löhner. On the computation of multi-material flows using ALE formulation. *J. Comput. Phys.*, 194:304–328, 2004.

[108] G. Luttwak and J. Falcovitz. Slope limiting for vectors: A novel vector limiting algorithm. *Int. J. Numer. Meth. Fluids*, 65:1365–1375, 2011.

[109] P.-H. Maire. A high-order cell-centered Lagrangian scheme for compressible fluid flows in two-dimensional cylindrical geometry. *J. Comput. Phys.*, 228:6882–6915, 2009.

[110] P.-H. Maire. A high-order cell-centered Lagrangian scheme for two-dimensional compressible fluid flows on unstructured meshes. *J. Comput. Phys.*, 228:2391–2425, 2009.

[111] P.-H. Maire. *Contribution to the numerical modeling of Inertial Confinement Fusion.* Habilitation à diriger des recherches, Bordeaux University, 2011.

[112] P.-H. Maire. A high-order one-step sub-cell force-based discretization for cell-centered Lagrangian hydrodynamics on polygonal grids. *Comput. and Fluids*, 46(1):341–347, 2011.

[113] P.-H. Maire, R. Abgrall, J. Breil, and J. Ovadia. A cell-centered Lagrangian scheme for two-dimensional compressible flows problems. *SIAM J. Sci. Comput.*, 29:1781–1824, 2007.

[114] P.-H. Maire and J. Breil. A second-order cell-centered Lagrangian scheme for two-dimensional compressible flow problems. *Int. J. Numer. Meth. Fluids*, 56:1417–1423, 2008.

[115] P.-H. Maire and J. Breil. A high-order finite volume cell-centered scheme for anisotropic diffusion on two-dimensional unstructured grids. *J. Comput. Phys.*, 224(2):785–823, 2011.

[116] P.-H. Maire and J. Breil. A nominally second-order accurate finite volume cell-centered scheme for anisotropic diffusion on two-dimensional unstructured grids. *J. Comput. Phys.*, 231:2259–2299, 2012.

[117] P.-H. Maire, J. Breil, and S. Galera. A cell-centered arbitrary Lagrangian-Eulerian (ALE) method. *Int. J. Numer. Meth. Fluids*, 56:1161–1166, 2008.

[118] P.-H. Maire and B. Nkonga. Multi-scale Godunov-type method for cell-centered discrete Lagrangian hydrodynamics. *J. Comput. Phys.*, 228:799–821, 2009.

[119] P.H. Maire, R. Abgrall, J. Breil, R. Loubère, and B. Rebourcet. A nominally second-order cell-centered Lagrangian scheme for simulating elastic-plastic flows on two-dimensional unstructured grids. *J. Comput. Phys.*, 235:626–665, 2013.

[120] L.G. Margolin. Introduction to "An Arbitrary Lagrangian-Eulerian Computing Method for All Flow Speeds". *J. Comput. Phys.*, 135(2):198–202, 1997.

[121] L.G. Margolin and M. Shashkov. Second-order sign-preserving conservative interpolation (remapping) on general grids. *J. Comput. Phys.*, 184(1):266–298, 2003.

[122] B. Mirtich. Fast and accurate computation of polyhedral mass properties. *Journal of Graphics Tools*, 1:31–50, 1996.

[123] J.M. Morrell, P.K. Sweby, and A. Barlow. A cell by cell anisotropic adaptive mesh ALE scheme for the numerical solution of the Euler equations . *Journal of Computational Physics*, 226(1):1152 – 1180, 2007.

[124] H. Nagatomo, K. Matsuo, J. Breil, Ph. Nicolaï, J.L. Feugeas, T. Asahina, A. Sunahara, T. Johzaki, S. Fujioka, T. Sano, and K. Mima. Laser ablation and target acceleration under the strong magnetic field. *Bulletin of the American Physical Society*, 60(19), 2015.

[125] K. Nakajima, H. Nakamura, and T. Tanahashi. Parallel iterative solvers with localized ilu preconditioning. In Bob Hertzberger and Peter Sloot, editors, *High-Performance Computing and Networking*, volume 1225 of *Lecture Notes in Computer Science*, pages 342–350. Springer Berlin Heidelberg, 1997.

[126] Ph. Nicolaï, J.-L. Feugeas, C. Regan, M. Olazabal-Loumé, J. Breil, B. Dubroca, J.-P. Morreeuw, and V. Tikhonchuk. Effect of the plasma-generated magnetic field on relativistic electron transport. *Physical Review E*, 84:016402, 2011.

[127] B. Nkonga. On the conservative and accurate cfd approximations for moving meshes and moving boundaries. *Comput. Methods Appl. Mech. Eng.*, 190(13-14):1801–1825, 2000.

[128] W.F. Noh. Errors for calculations of strong shocks using an artificial viscosity and an artificial heat flux. *J. Comput. Phys.*, 72:78–120, 1987.

[129] M. Olazabal-Loumé, J. Breil, L. Hallo, X. Ribeyre, and J. Sanz. Linear and non-linear amplification of high-mode perturbations at the ablation front in hiper targets. *Plasma Physics and Controlled Fusion*, 53(1):015015, 2011.

[130] M. Olazabal-Loumé, Ph. Nicolaï, G. Riazuelo, M. Grech, J. Breil, S. Fujioka, A. Sunahara, N. Borisenko, and V.T. Tikhonchuk. Simulations of laser imprint reduction using underdense foams and its consequences on the hydrodynamic instability growth. *New Journal of Physics*, 15(8):085033, 2013.

[131] J.S. Park, S.-H. Yoon, and C. Kim. Multi-dimensional limiting process for hyperbolic conservation laws on unstructured grids. *J. Comput. Phys.*, 229:788–812, 2010.

[132] F. Pellegrini. Scotch Web page, 2012. Available at `https://gforge.inria.fr/projects/scotch/`.

[133] R.B. Pember and J.B. Bell. An adaptive Cartesian grid method for unsteady compressible flow in irregular regions. *J. Comput. Phys.*, 120:278–304, 1995.

[134] S. Del Pino. Metric-based mesh adaptation for 2D Lagrangian compressible flows. *J. Comput. Phys.*, 230(5):1793–1821, 2011.

[135] R. Ramis, J. Meyer ter Vehn, and J. Ramírez. MULTI2D - a computer code for two-dimensional radiation hydrodynamics. *Comput. Phys. Com.*, 180:977–994, 2009.

[136] X. Ribeyre, L. Hallo, T. Tikhonchuk, S. Bouquet, and J. Sanz. Non-stationnary Rayleigh-Taylor Instability in supernova ejecta. *Physics of Plasmas*, 14:112902, 2007.

[137] X. Ribeyre, M. Lafon, G. Schurtz, M. Olazabal-Loumé, J. Breil, S. Gallera, and S. Weber. Shock ignition: modelling and target design robustness. *Control. Fusion*, 51:124030, 2009.

[138] X. Ribeyre, G. Schurtz, M. Lafon, S. Galera, and S. Weber. Shock ignition: an alternative scheme for hiper. *Plasma Physics and Controlled Fusion*, 51(1):015013, 2009.

[139] R. D. Richtmyer and K. W. Morton. *Difference methods for initial-value problems.* John Wiley, 1967.

[140] Y. Saillard. Hydrodynamique de l'implosion d'une cible FCI. *C. R. Acad. Sci. Paris Série IV*, 1:705–718, 2000.

[141] S.K. Sambasivan, M.J. Shashkov, and D.E. Burton. Exploration of new limiter schemes for stress tensors in Lagrangian and ALE hydrocodes. *Comput. and Fluids*, 83:98–114, 2013.

[142] S.K. Sambasivan, M.J. Shashkov, and D.E. Burton. A finite volume cell-centered Lagrangian hydrodynamics approach for solids in general unstructured grids. *Int. J. Numer. Meth. Fluids*, 72:770–810, 2013.

[143] J. Sanz, R. Betti, R. Ramis, and J. Ramírez. Nonlinear theory of the ablative Rayleigh-Taylor instability. *Plasma Physics and Controlled Fusion*, 46(12B):B367, 2004.

[144] J. Sanz, J. Ramírez, R. Ramis, R. Betti, and R. P. J. Town. Nonlinear Theory of the Ablative Rayleigh-Taylor Instability. *Phys. Rev. Lett.*, 89:195002, 2002.

[145] H. Schardin. High frequency cinematography in the shock tube. *J. Phot. Sci.*, 5:17–19, 1957.

[146] G. Schurtz, S. Gary, S. Hulin, C. Chenais-Popovics, J.-C. Gauthier, F. Thais, J. Breil, F. Durut, J.-L. Feugeas, P.-H. Maire, Ph. Nicolaï, O. Peyrusse, C. Reverdin, G. Soullié, V. Tikhonchuk, B. Villette, and C. Fourment. Revisiting nonlocal electron-energy transport in inertial-fusion conditions. *Physical review letters*, 98(9):095002, 2007.

[147] L.I. Sedov. *Similarity and Dimensional Methods in Mechanics.* Academic Press, New York, NY, 1959.

[148] M. Shashkov. Closure models for multidimensional cells in Arbitrary Lagrangian-Eulerian hydrocodes. *Int. J. Numer. Meth. Fluids*, 56:1497–1504, 2008.

[149] M. Shashkov and B. Wendroff. The repair paradigm and application to conservation laws. *J. Comput. Phys.*, 198(1):265–277, 2004.

[150] G.A. Sod. A survey of finite difference methods for system of nonlinear conservation laws. *J. Comput. Phys.*, 27:1–31, 1978.

[151] V. Springel. E pur si muove: Galilean-invariant cosmological hydrodynamical simulations on a moving mesh. *Mon. Not. of the R. Astron. Soc.*, 401:791–851, 2009.

[152] W. Theobald, R. Betti, C. Stoeckl, K.S. Anderson, J.A. Delettrez, V.Yu. Glebov, V.N. Goncharov, F.J. Marshall, D.N. Maywar, R.L. McCrory, D.D. Meyerhofer, P.B. Radha, T.C. Sangster, W. Seka, D. Shvarts, V.A. Smalyuk, A.A. Solodov, B. Yaakobi, C.D. Zhou, J.A. Frenje, C.K. Li, F.H. Séguin, R.D. Petrasso, and L.J. Perkins. Initial experiments on the shock-ignition inertial confinement fusion concept. *Physics of Plasmas*, 15(5), 2008.

[153] W. Theobald, R. Nora, W. Seka, M. Lafon, K.S. Anderson, M. Hohenberger, F.J. Marshall, D.T. Michel, A.A. Solodov, C. Stoeckl, D.H. Edgell, B. Yaakobi, A. Casner, C. Reverdin, X. Ribeyre, A. Shvydky, A. Vallet, J. Peebles, F.N. Beg, M.S. Wei, and R. Betti. Spherical strong-shock generation for shock-ignition inertial fusion. *Physics of Plasmas*, 22(5), 2015.

[154] P. Vachal, R.V. Garimella, and M. Shashkov. Untangling of 2D meshes in ALE simulations. *J. Comput. Phys.*, 196:627–644, 2004.

[155] P. Váchal and R. Liska. Sequential flux-corrected remapping for ALE methods. In A. Bermúdez de Castro, D. Gómez, P. Quintela, and P. Salgado, editors, *Numerical Mathematics and Advanced Applications. ENUMATH 2005*, pages 671–679. Springer Berlin Heidelberg New York, 2006.

[156] P. Vachal and P.-H. Maire. Discretizations for weighted condition number smoothing on general unstructured meshes. *Comput. and Fluids*, 46:479–485, 2011.

[157] J. Velechovsky, J. Breil, and R. Liska. Flux corrected remapping using piecewise parabolic reconstruction for 2D cell-centered ALE methods. *Int. J. Numer. Meth. Fluids*, 76(9):575–586, 2014.

[158] J. Velechovsky, M. Kucharik, R. Liska, M. Shashkov, and P. Vachal. Symmetry- and essentially-bound-preserving flux-corrected remapping of momentum in staggered ALE hydrodynamics. *J. Comput. Phys.*, 255:590–611, 2013.

[159] V. Venkatakrishnan. Convergence to steady solutions of the Euler equations on unstructured grids with limiters. *J. Comput. Phys.*, 118:120–130, 1995.

[160] J. von Neumann and R.D. Richtmyer. A method for the numerical calculations of hydrodynamical shocks. *J. Appl. Phys.*, 21:232–238, 1950.

[161] H.A. Van Der Vorst. Bi-CGStab: A fast and smoothly converging variant of Bi-CG for the solution of nonsymmetric linear systems. *SIAM J. Sci. and Stat. Comput.*, 13(2):631–644, 1992.

[162] J. Waltz, N.R. Morgan, T.R. Canfield, M.R.J. Charest, and J.G. Wohlbier. A nodal Godunov method for Lagrangian shock hydrodynamics on unstructured tetrahedral grids. *Int. J. Numer. Meth. Fluids*, 76:129–146, 2014.

[163] M. L. Wilkins. Calculation of elastic plastic flow. *Methods Comput. Phys.*, 3:211–263, 1964.

[164] J. Xiao and B. Lu. Conditions for perfectly uniform irradiation of spherical laser fusion targets. *J. Opt.*, pages 282–286, 1998.

[165] D. L. Youngs. Time dependent multimaterial flow with large fluid distortion. *Numerical Methods for Fluid Dynamics*, pages 273–285, 1982.

[166] D. L. Youngs. Multi-mode implosion in cylindrical 3D geometry. In *11th International Workshop on the Physics of Compressible Turbulent Mixing (IWPCTM11), Santa Fe*, 2008.

[167] D.D. Zeeuw and K.G. Powell. An adaptively refined Cartesian mesh solver for the Euler equations. *J. Comput. Phys.*, 104:56–68, 1993.

[168] YaB. Zel'dovitch and Yup. Raizer. *Physics of shock waves and high-temperature hydrodynamic phenomena*. Academic Press, 1966.